NEUTRINO OSCILLATIONS IN PARTICLE PHYSICS AND ASTROPHYSICS

Memoria de Tesis Doctoral realizada por

Iván Jesús Martínez Soler

presentada ante el Departamento de Física Teórica
de la Universidad Autónoma de Madrid
para optar al título de Doctor en Física Teórica.

Tesis dirigida por el **Prf. D. Michele Maltoni**
Científico titular del Instituto de Física Teórica UAM-CSIC

Departamento de Física Teórica
Universidad Autónoma de Madrid

Instituto de Física Teórica UAM-CSIC

Mayo de 2018

Agradecimientos

Para mí, una tesis doctoral no consiste solamente en los resultados que a continuación se presentan, sino que es un largo e intenso proceso de aprendizaje, en el que un joven estudiante es guiado por su maestro, a través de la consecución de unas pequeñas metas, en el descubrimiento de un vasto universo de conocimiento. Como ya he dicho, este camino no se recorre solo, y para mi fortuna he tenido al mejor guía que podía tener, el Prof. Michele Maltoni. Sin sus enseñanzas, consejos, ayuda e infinita paciencia, recorrer el largo trayecto que me ha traido hasta aquí hubiera sido imposible. Por ello, nada más me gustaría en este momento, que agradecerle todos estos años de máxima felicidad en los que ha llegado a ser más que un profesor para mí.

A lo largo de este tiempo he tenido la gran oportunidad de aprender trabajando junto a físicos increíbles, quienes, además de hacer posible todo lo que aquí se recoge, me han ayudado a comprender mejor el mundo de la física. Solo puedo estar enormemente agradecido a Concha Gonzalez-García y Pilar Coloma por su acogida, dedicación y esfuerzo conmigo, remarco esto último, y porque me han enseñado que incluso a una distancia de miles de kilómetros y varias horas de diferencia, uno puede sentirse como en casa.

Querría también agradecer a todos aquellos con quienes he tenido la oportunidad de colaborar en diferentes proyectos. A Jacobo Lopez-Pavón, Pedro A.N. Machado, Iván Esteban, Hiroshi Nunokawa, Hisakazu Minakata y Ninqiang Song. Una gran parte de este trabajo también es gracias a ellos.

A mis padres, hermanos y abuela, por su constante apoyo y motivación. Quienes han hecho lo imposible para que yo pudiera soñar con este momento. A mis padrinos y a Juan Jesús, por confiar en mí y alentarme en todo este tiempo.

A mis amigos científicos. Por los eternos momentos vividos en cenas, en interminables viajes a Murcia o en infinitas partidas a juegos de mesa. Por las interminables charlas, algunas incluso sobre física, que me han supuesto una fuente inagotable de sabiduría. Me gustaría en especial mencionar a Pedro Fernandez-Ramirez, Nieves Lopez, Pablo Cano, Loles, Alejandro Ruiperez, Oscar Lasso, Margarita, José Angel Romero, Eduardo Ibañez, Manuel Trashorras, Pablo Bueno y Ana Cueto. Y a mis amigos de toda la vida, por todas las "constructivas" discusiones mantenidas.

Y sobre todo a Verónica. Porque a lo largo de una tesis no todos los momentos son buenos ni sencillos, pero ella siempre ha estado a mi lado, sea cual sea la distancia que nos separe, compartiendo todas mis alegrías y haciendo mucho más llevaderos los malos momentos. Porque siempre me ha apoyado en todas las decisiones, por muy difíciles que sean de entender. Porque sin ella no me habría atrevido a dar muchos de los pasos que he dado, ni a comenzar esta aventura. Porque siempre me ha aconsejado seguir y nunca rendirme. En definitiva, por todo.

Abstract

Neutrinos are described in the Standard Model (SM) by three left-handed fermion fields, one for each fermion generation. In the SM, the masses of the fermions arises as a Yukawa interaction between the right-handed and the left-handed fermion fields, and the Higgs doublet. Because of the lack of a right-handed field for neutrinos, these fermions are massless within the SM. Experiments measuring the flavor composition of neutrinos have stablished the oscillation of the flavor along its path. This oscillation can be explained in the scenario of a mixing between neutrino flavor and neutrino mass states. This thesis is devoted to the study of the neutrino flavor oscillations within different mixing models. In particular, it is focused into the physics reach by the new generation of neutrino telescopes, like IceCube and DeepCore.

The low energy part of the atmospheric neutrino flux measured by DeepCore lead a sizable flavor oscillation in the muon disappearance channel ($\nu_\mu \to \nu_\mu$). By combining the latest experimental data collected by this detector (up to 2016) with the results of other oscillation experiments, we have performed a global fits within the three-neutrino mixing framework. In this work has been also discussed the complementarity role played by atmospheric/accelerator and the reactor data on the determination of the atmospheric mass parameter.

IceCube can be also considered as a tool to look for New Physics signals. The minimal extension of the SM to explain the neutrino masses consist of a heavy right-handed neutrino field. The mass of this new fermion is not predicted by any model, it can take any value over a wide range of orders of magnitude. For masses around GeV, we have studied in a different work the detection of the new fermion by looking for "Double-Cascades" events topologies. We have considered two different scenarios where the signal can be created by a heavy neutrino, the mixing of the heavy state with a light neutrino through a NC, and the production of the heavy state via a transition magnetic moment. The results indicate that IceCube improve the current bounds in the scenarios considered for heavy states with masses around 1 GeV.

Another New Physics scenario considered is the so-called Quantum Decoherence, which introduces a damping effect on the flavor oscillation. In a recent work, we have developed a new formalism to study this effect through non-adiabatic matter. By a fit of the atmospheric events measured by IceCube and DeepCore, it is shown that these experiments improve over the current bound from other experiments.

The primary goal of IceCube is the detection of astrophysical neutrinos, what happened in 2013. This energetic events opens the possibility to study New Physics on them. In another, work we have considered the impact of Non-Standard Interactions on the flavor of this events, finding large deviations from the three-neutrino mixing prediction.

Neutrino physics is moving into the precission era, but still a lot of fundamental and exciting problems remain without answer. This converts to this reach area in a very promising field for the near future.

Resumen

Los neutrinos están descritos en el Modelo Estandar (MS) por tres campos fermiónicos zurdos, uno por cada generación de fermiones. En el MS, el término de masa para cada fermión cargado viene dado por una interacción de Yukawa entre los campos zurdos y diestros de dicho fermión, con el campo de Higgs. Debido a que en el SM no hay campo diestro para los neutrinos, estas partículas no poseen masa. Los experimentos que han medido el sabor de los neutrinos han establecido que el sabor de estas partículas oscila a lo largo de su trayectoria. Esta oscilación puede ser explicada por acoplo entre estados de sabor y estados de masa. Esta tesis se centra en el estudio de las oscilaciones de neutrinos para diferentes modelos teóricos que describen este acoplo. En particular, se ha enfocado al estudio de la física que puede ser medida en la nueva generación de telescopios de neutrinos, como IceCube y DeepCore.

La parte de baja energía del espectro de neutrinos atmospféricos medido por DeepCore permite observar las oscilaciones de neutrinos en el canal ($\nu_\mu \to \nu_\mu$). Combinando los últimos resultados experimentales recogidos por este experimento (hasta 2016), junto con los resultados del resto de experimentos de oscilaciones de neutrinos, hemos realizado un ajuste global de los parámetros de oscilación en el modelo de mezcla de tres neutrinos. En este trabajo también ha sido discutida la complementariedad entre las medidas de experimentos atmosféricos/aceleradores con las medidas en reactores en la determinación del parámetro de masas atmosférico.

IceCube también puede ser usado en la búsqueda de señales de nueva física. La mínima extensión del MS necesaria para explicar la masa de los neutrinos consiste en añadir campos diestros para los neutrinos. La masa de estos nuevos fermiones no está fijada por ningún modelo. Hemos estudiado la detección de estos nuevos fermiones con masas entorno al GeV buscando eventos con la topología "Double-Cascade". Para ello, hemos considerado dos escenarios diferentes donde esta señal puede ser creada por la nueva partícula, un acoplo entre los campos diestros y los neutrinos descritos en el MS, y un momento magnético de transición.

Otro escenario de nueva física considerado, en este caso en neutrinos atmosféricos, es el denominado como Decoherencia Quántica, el cual introduce una amortiguación en la oscilación de sabor. A través de un ajuste de los eventos atmosféricos medidos por IceCube y DeepCore, se ha observado una mejora en la precisión con que los efectos de este modelo de nueva física pueden ser medidos.

El objetivo principal de IceCube es la detección de neutrinos astrofísicos, que tuvo lugar en 2013. La observación de estos eventos energéticos ha abierto la posibilidad de buscar en ellos procesos de nueva física. Por ello, en otro trabajo hemos estudiado el impacto que puede tener la existencia de nuevas interacciones en el sabor de estos eventos. Los resultados muestran grandes desviaciones con respecto a lo predicho por el modelo de tres neutrinos.

La física de neutrinos se está encaminando hacia una era de precisión, pero todavía existen problemas excitantes y fundamentales sin resolver. Esto convierte a este área de investigación en un campo muy prometedor para el futuro.

Contents

Chapter1

Introduction

1.1 Historical introduction

The first evidence of neutrino oscillation was observed in the Kamiokande experiment, a detector that which built to discover the proton decay, predicted by the Electroweak Theory. Kamiokande was a water Cherenkov detector located at a depth of 1 km in Kamioka (Japan), which started to take data in 1983 [1]. The charged particles created in the proton decay propagate at relativistic speeds on water, and emit Cherenkov radiation that is detected by the photomultiplier surrounding the water tank. The dominant background was the atmospheric neutrino interactions that were produced by charged leptons.

The interaction of cosmic rays with the atmospheric nuclei produces π and K, that decay mainly in μ and ν_μ. A second particle generation is created after μ decay into ν_μ, e and ν_e. So, ν_μ and ν_e are mainly produced in the atmosphere in a flavor ratio 2:1 ($\nu_\mu : \nu_e$). In 1988, Kamiokande showed a deficit in the number of ν_μ compared with the simulation results, that could not be explained by the systematics detector effects or by the uncertainties in the atmospheric flux prediction [2]. Due to the low precision in the flux calculation, the results were presented in terms of the flavor ratio ν_μ over ν_e. This flavor ratio is theoretically predicted to be around 2, and up-down symmetric for higher energies (multi-GeV). For lower energies (sub-GeV), the magnetic field of the Earth modifies the cosmic ray flux. The results showed the $59 \pm 7\%$ of the expected number for ν_μ [2]. The deficit was also confirmed by another water Cherenkov experiment, IMB [3].

In 1996, a new detector was built with a fiducial volume twenty times larger than Kamiokande volume, what made possible enlarge the statistics by the same factor. The number of photomultipliers used in the new experiment was larger compared with Kamiokande, what allowed the measurement of the neutrino interaction with higher precision. The new experiment was called Super-Kamiokande. In 1998, after two years of data taking, the experiment announced evidence for atmospheric neutrino oscillations with a significance of 6σ [1, 4, 5], Fig 1.1. The results showed a deficit in the up-going ν_μ flux that depended on the zenith angle. For the down-going neutrinos, the prediction agrees with the data. For the ν_e events was observed no deviation from the prediction. A combined analysis of the Kamiokande and Super-Kamiokande measurement showed that neutrino oscillation could consistently explain both results. The results were confirmed by MACRO [6] and Soundan-2 [7], two experiments which also observed a zenith-angle dependence deficit in ν_μ.

1.2 Neutrinos in the SM

The Standard Model (SM) describe the interactions between three generations of fermions, versus gauge bosons and one scalar, the Higgs boson, according to the gauge group

$$SU(3)_C \times SU(2)_L \times U(1)_Y \tag{1.1}$$

Each generation consists of five fermions (Table 1.1), with a different representation under the symmetry group each of them [8]. The fermions have the same charges under the symmetry group in the three generations, but they present different masses. The SM gauge group together with the fermion content present an accidental global symmetry

$$U(1)_B \times U(1)_{L_e} \times U(1)_{L_\mu} \times U(1)_{L_\tau} \tag{1.2}$$

that preserve the baryon number (B) and the three lepton numbers (L_e, L_μ, L_τ), and as a result, the total lepton number $L = L_e + L_\mu + L_\tau$. That global symmetry is a consequence of the SM gauge symmetry and the representation of the physical states.

The subgroup $SU(2) \times U(1)$, called electroweak symmetry group, unifies the electromagnetism and the weak theory and is the only group that acts non-trivially over the neutrino field. These fermions are not affected by strong or electromagnetic interactions, so they are singlets of $SU(3)_c \times U(1)_Q$. The group $SU(2)$, called isospin, acts over the left-handed chiral component of the fermions field, whereas the right-handed components are singlets. It has three generators $I_a (a = 1, 2, 3)$ that verifies the commutation relations $[I_a, I_b] = \imath \epsilon_{abc} I_c$. In a two dimensional representation,

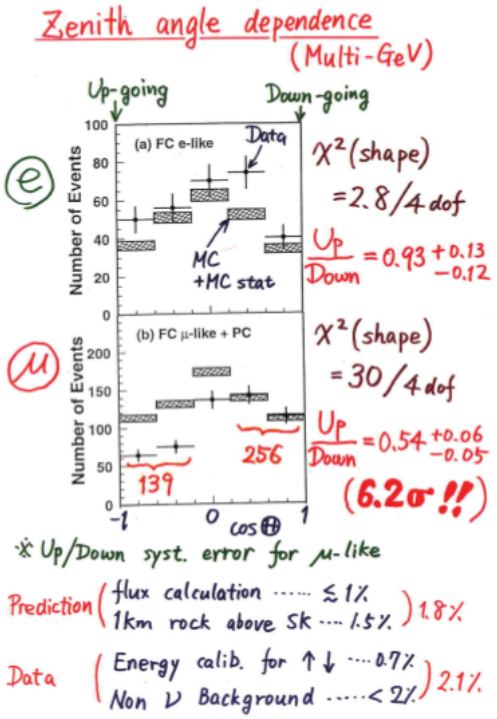

Figure 1.1: Zenith angle distribution events presented by Super-Kamiokande collaboration at the Neutrino '98 [1, 4, 5]

$L_L(1,2,-1/2)$	$Q_L(3,2,1/6)$	$E_R(1,1,-1)$	$U_R(3,1,2/3)$	$D_R(3,1,-1/3)$
$\begin{pmatrix} \nu_e \\ \mathrm{e} \end{pmatrix}_L$	$\begin{pmatrix} \mathrm{u} \\ \mathrm{d} \end{pmatrix}_L$	e_R	u_R	d_R
$\begin{pmatrix} \nu_\mu \\ \mu \end{pmatrix}_L$	$\begin{pmatrix} \mathrm{c} \\ \mathrm{s} \end{pmatrix}_L$	μ_R	c_R	s_R
$\begin{pmatrix} \nu_\tau \\ \tau \end{pmatrix}_L$	$\begin{pmatrix} \mathrm{t} \\ \mathrm{b} \end{pmatrix}_L$	τ_R	t_R	b_R

Table 1.1: The fermion content in SM. The numbers in brackets are the charges under $(SU(3), SU(2), U(1))$ [8].

the generators coincide with the Pauli matrices ($I_1 = \sigma_1/2, \ldots$). The group $U(1)_Y$, called hypercharge, consist of one generator Y. Together with the generator I_3 of $SU(2)$ group, the hypercharge verifies the Gell-Mann-Nishijima relation

$$Q = I_3 + \frac{Y}{2} \tag{1.3}$$

this equation relates weak interactions driven by the operator of the groups $SU(2) \times U(1)$ with the electric charge Q.

1.2.1 Electroweak interaction

The electroweak SM lagrangian for leptons is given by

$$\begin{aligned} \mathscr{L} =& \imath \sum_{\alpha=e,\mu,\tau} \left(\overline{L_{\alpha L}} \not{D} L_{\alpha L} + E_{\alpha R} \not{D} E_{\alpha R} \right) - \frac{1}{4} W_{\mu\nu} W^{\mu\nu} - \frac{1}{4} B_{\mu\nu} B^{\mu\nu} \\ &+ (D_\mu \Phi)^\dagger (D^\mu \Phi)^\dagger - \mu^2 \Phi^\dagger \Phi - \lambda (\Phi^\dagger \Phi)^2 - \sum_{\alpha\beta} \left(Y_{\alpha\beta} \overline{L_{\alpha L}} \Phi E_{\beta R} + Y^*_{\alpha\beta} \overline{E_{\beta R}} \Phi^\dagger L_{\alpha L} \right) \end{aligned} \tag{1.4}$$

in order to ensure the local gauge invariance, the covariant derivatives are defined as

$$D_\mu = \partial_\mu + \imath g I \cdot W_\mu + \imath g' B_\mu Y \tag{1.5}$$

where W_μ and B_μ are the gauge fields associated to $SU(2)$ and $U(1)$ symmetries. The strength of the electroweak interaction is determined by the gauge couplings constants, g and g', associated to the isospin and the hypercharge group, respectively. In the lagrangian, the first row describes the electroweak interactions between the fermions and the gauge bosons, what is obtained by developing the covariant derivative in the lagrangian, and the gauge bosons themselves, which is described by last two terms. Expanding the covariant derivates in the weak isospin representation and keeping just the interaction terms

$$\mathscr{L}_I = - \sum_{\alpha=e,\mu,\tau} \frac{1}{2} \overline{L_{\alpha L}} \left(g \sigma \cdot \not{W} - g' \not{B} \right) L_L + g' \overline{E}_R \not{B} E_R \tag{1.6}$$

where we have used that the hypercharge of the left-handed component of the leptons, $Y L_L = -1/2 L_L$. We can rewrite the interaction terms by introducing new gauge fields $(W^{\mu,+}, W^{\mu,-}, A^\mu, Z^\mu)$, defined as a linear combination of W_i^μ and B^μ:

$$W^{\mu,+} = W_1^\mu - \imath W_2^\mu \quad W^{\mu,-} = W_1^\mu + \imath W_2^\mu \tag{1.7}$$

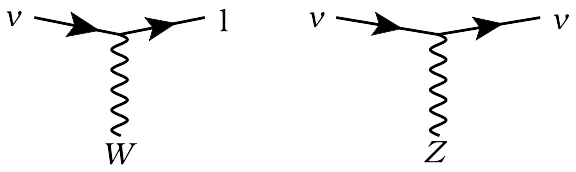

Figure 1.2: Neutrino interaction vertex through CC (left) and NC (right)

$$\begin{pmatrix} A^\mu \\ Z^\mu \end{pmatrix} = \begin{pmatrix} \cos\theta_w & \sin\theta_w \\ -\sin\theta_w & \cos\theta_w \end{pmatrix} \begin{pmatrix} B^\mu \\ W_3^\mu \end{pmatrix} \tag{1.8}$$

where θ_w is the weak mixing angle. The new gauge bosons carry the weak interactions ($W^{\mu,+}, W^{\mu,-}, Z^\mu$) and the electromagnetic interaction (A^μ). In terms of the new gauge bosons, the interaction lagrangian can be written as

$$\begin{aligned}\mathscr{L}_I = -\frac{1}{2}\{&\overline{\nu}_L\gamma_\mu\left(A^\mu(gs_{\theta_w} - g'c_{\theta_w}) + Z_\mu(gc_{\theta_w} + g's_{\theta_w})\right)\nu_L + g\overline{\nu_L}\not{W}^+L_L + g\overline{L_L}\not{W}^-\nu_L \\ &+\overline{L}_L\gamma_\mu\left(A^\mu(gs_{\theta_w} + g'c_{\theta_w}) + Z^\mu(gc_{\theta_w} - g's_{\theta_w})\right)L_L + 2\overline{L}_R\gamma_\mu\left(c_{\theta_w}A^\mu - s_{\theta_w}Z^\mu\right)L_R\}\end{aligned} \tag{1.9}$$

where $c_{\theta_w} = \cos\theta_w$ and $s_{\theta_w} = \sin\theta_w$. Neutrinos are neutral particles, and therefore they are not affected by the electromagnetic interaction, so neutrinos and photons must be decoupled. This condition can be used to fix the weak mixing angle in terms of the coupling constants $\tan\theta_w = g'/g$. The interaction lagrangian becomes

$$\begin{aligned}\mathscr{L}_I = -\frac{1}{2}\Bigg\{&\frac{g}{c_{\theta_w}}\overline{\nu}_L\not{Z}\nu_L + g\overline{\nu_L}\not{W}^+L_L + g\overline{L_L}\not{W}^-\nu_L \\ &+\overline{L}_L\left(2gs_{\theta_w}\not{A} + \frac{g\cos 2\theta_w}{c_{\theta_w}}\not{Z}\right)L_L - 2\overline{L}_R\frac{gs_{\theta_w}}{c_{\theta_w}}\left(c_{\theta_w}\not{A} - s_{\theta_w}\not{Z}\right)L_R\Bigg\}\end{aligned} \tag{1.10}$$

From the interaction lagrangian, neutrinos can interact with a charged lepton through a coupling with a $W^\pm$ boson, what is called Charge Current interaction (CC), or with another neutrino through the coupling to a Z boson, Neutral Current interactions (NC), as shown in Fig 1.2. In addition to the interactions mediated by W and Z boson, the charged leptons can also have interaction mediated by a photon, as shown in the second line of Eq (1.10). The measurement of the Z invisible width determines the number of neutrinos in the SM, N_ν. The results from LEP experiment is $N_\nu = 2.984 \pm 0.008$ [9, 10].

1.2.2 Higgs mechanism

In the SM, the masses of the fermions, the gauge bosons and the scalar are generated through the Higgs mechanism. The Higgs field $\Phi \equiv (\phi^+, \phi^0)^T$ is a scalar doublet, that consist of two scalar field, one of them charged (ϕ^+) and the other one neutral (ϕ^0). The charges of the Higgs field under SM symmetry group are given in the Table 1.2. The second line of Eq (1.4) contains a potential for the Higgs field $V(\Phi) = \mu^2\Phi^\dagger\Phi - \lambda(\Phi^\dagger\Phi)^2$. In quantum field theory, the value of the field at the minimum of the potential correspond to the vacuum state, and the quantum excitations of the lowest state correspond to particle states. In order to preserve the invariance of the vacuum under spatial rotations, the vacuum state of fermions and vector boson, which carry a nonzero spin, must be zero. The same happens for

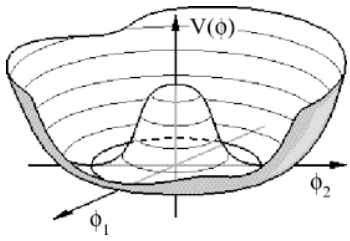

Figure 1.3: Higgs potential. ϕ_1 and ϕ_2 correspond to the real and the imaginary part of ϕ^0

	SU(3)	SU(2)	U(1)
$\Phi = \begin{pmatrix} \phi^+ \\ \phi^0 \end{pmatrix}$	1	2	1/2
ν_s	1	1	0

Table 1.2: Charges under the SM symmetry group of the Higgs field (Φ) and sterile neutrinos (ν_s)

charged scalar fields since the vacuum must be electrically neutral. However, for neutral scalar fields, the vacuum expectation value (vev) can be different from zero. So, the Higgs is the only SM field that can have a vev different from zero.

Considering the Higgs potential, if $\mu^2 > 0$, the minimum is located at zero ($\langle\Phi\rangle = 0$), and the vacuum state is invariant under a gauge transformation. In that case, the vev for the Higgs is zero. For $\mu^2 < 0$, the minimum is fixed to $|\langle\Phi\rangle|^2 = v^2/2$, where $v = \sqrt{-\mu^2/\lambda}$ is the value of the vev. The Higgs is a complex field, so it has two degrees of freedom $\phi^0 = (\phi_1 + \imath\phi_2)/\sqrt{2}$. That can be translated into a degenerate minimum for the potential, there are an infinite number of choices for ϕ_1 and ϕ_2 at the vev, Fig 1.3. Once is selected one of the possible directions, the Higgs field get the vev

$$\langle\Phi\rangle = \frac{1}{\sqrt{2}} \begin{pmatrix} 0 \\ v \end{pmatrix} \tag{1.11}$$

and a mass term for the vector bosons and the Higgs field appear in the lagrangian. That mass terms are obtained by developing the covariant derivative over Φ in the unitary gauge. The election of one vacuum break the Electroweak symmetry into the Quantum Electrodynamics group $SU(2)_L \times U(1)_Y \to U(1)_{\text{QED}}$.

The masses of the fermions arises as a Yukawa interaction between the right-handed and the left-handed fermion fields, and the Higgs doublet ($Y_{\alpha\beta}\bar{L}_{\alpha L}\Phi E_{\beta R}$), this is called a Dirac mass term. Due to the lack of a right-handed field for neutrinos in the SM, these fermions are massless. The only possible mass term (an interaction between a left-handed and a right-handed field) for neutrinos, that can be formed using the fermion content in the SM, is given by the product of the left-handed doublet and its charge conjugated $\bar{L}_L L_L^c$, where $L_L^C = C\overline{L_L}^T$ is obtained after a charge-conjugation operation, and it is called Majorana mass term. That term violates the lepton number by two units and, since the SM symmetry group preserve the total lepton number, it cannot be generated by loop corrections. What means that neutrino is massless in the SM even in the presence of perturbative corrections.

1.3 Neutrino masses

A renormalizable mass term for neutrinos cannot be constructed with the fermion content of the SM and its symmetry group, Eq (1.1). There are only two possible ways to create a neutrino mass term, by introducing new fermions or by breaking the SM symmetries. As seen in the section before, all the fermions mass terms are formed by the Yukawa interaction between the left-handed and the right-handed component of a fermion field and the Higgs boson, Eq (1.4). The minimal extension of SM needed to create a neutrino Dirac mass term is an arbitrary number of right-handed neutrinos (ν_s). These new fermions are defined as having no SM gauge interactions, they are singlets of Eq (1.1) as it is shown in Table 1.2. These new fermions are called sterile. The number of these new fermions that can be used to extend the SM is not constrained by theory, so the minimal extension of right-handed field is one. In the remaining section, we are going to assume an m number of sterile neutrinos. The neutrino Dirac mass term that can be constructed is given by

$$-\mathscr{L}_D = \overline{\nu}_{si} M_{Dij} L_{Lj} + \text{h.c.} = Y^{\nu}_{ij} \overline{\nu}_{si} \tilde{\Phi} L_{Lj} + \text{h.c.} \tag{1.12}$$

where $\tilde{\Phi} = \imath\sigma_2 \Phi^*$ and M_D is a complex $(3 \times m)$ matrix. After the spontaneous symmetry breaking by the Higgs field selecting a vacuum, the neutrino get the mass $M_{Dij} = Y^{\nu}_{ij} v/\sqrt{2}$. That mass preserves the total lepton number.

Breaking gauge invariance, two Majorana mass terms can be constructed, one for the active neutrinos and one for the sterile

$$-\mathscr{L}_M = \frac{1}{2}\overline{\nu_L} M_L \nu_L^c + \frac{1}{2}\overline{\nu_s} M_s \nu_s + h.c. \tag{1.13}$$

where M_L and M_s are 3×3 and $m\times m$ symmetric matrices. Defining the left-handed state $\nu = (\nu_L \;\; \nu_s^c)^T$, the three mass terms can be combined into a single term

$$-\mathscr{L}_{M_\nu} = \frac{1}{2}\overline{\nu} M_\nu \nu^c = \frac{1}{2} \begin{pmatrix} \overline{\nu_L} & \overline{\nu_s^c} \end{pmatrix} \begin{pmatrix} M_L & M_D^T \\ M_D & M_s \end{pmatrix} \begin{pmatrix} \nu_L^c \\ \nu_s \end{pmatrix} + h.c. \tag{1.14}$$

In the case of $M_L = 0$, gauge invariance is recovered because the Majorana term for sterile neutrinos is allowed by the SM symmetries. M_ν is a $(3+m)\times(3+m)$ complex symmetric matrix, so it can be diagonalized using a unitary matrix V_ν

$$V_\nu^\dagger \begin{pmatrix} M_L & M_D^T \\ M_D & M_s \end{pmatrix} V_\nu^* = \text{diag}\{m_1, m_2, \ldots, m_{3+m}\} \tag{1.15}$$

The mass eigenstates are obtained multiplying V_ν by the state ν and ν^c, $\tilde{\nu} = V_\nu^\dagger(\nu_L \;\; \nu_s^c)^T$ and $\tilde{\nu}^c = V_\nu^T(\nu_L^c \;\; \nu_s)^T$, where we have taken into account that the right-hand field transforms under the unitary matrix as $\tilde{\nu}^c = (V_\nu^\dagger \nu)^c$. The left-handed and the right-handed component of the neutrino field in the mass basis can be added to a single state

$$\tilde{\nu}_M = \tilde{\nu} + \tilde{\nu}^c \tag{1.16}$$

which satisfies the Majorana condition, $\tilde{\nu}_M^c = \tilde{\nu}_M$. Majorana states are formed by just one field, which means that they can be described by a two-component spinor. For Dirac state it is needed a four-component spinor. In the mass basis, Eq (1.14)

can be rewriten as

$$-\mathscr{L}_{M_\nu} = \frac{1}{2}\sum_{k=1}^{3+m} m_k \overline{\tilde{\nu}}_{M,k}\tilde{\nu}_{M,k} = \frac{1}{2}\sum_{k=1}^{3+m} m_k(\overline{\tilde{\nu}}_k\tilde{\nu}_k^c + \overline{\tilde{\nu}}_k^c\tilde{\nu}_k) \tag{1.17}$$

where we have used $\overline{\tilde{\nu}^c}\tilde{\nu}^c = -\overline{\tilde{\nu}}\tilde{\nu}$. So, the most general mass term that can be constructed for neutrinos can be written as a Majorana mass term. Unless $V = I_{(3+m)\times(3+m)}$, which is equivalent to a diagonal mass matrix in the interaction basis, the flavor states, identified by the fields in the interaction lagrangian, and the mass states are not identical. That mismatch implies a flavor lepton mixing.

1.3.1 The see-saw mechanism

The scale of M_D should be of the order of the electroweak symmetry breaking ($M_D \sim 174$ GeV). Since M_L break gauge invariance in the neutrino mass matrix, we consider it zero ($M_L = 0$). For the third mass matrix, we can expect $M_s >> M_D$ since it is generated by physics beyond the SM. Considering the strong hierarchy between the scales of the mass matrices, M_ν can be diagonalized by blocks up to corrections of the order of $o(M_D/M_s)$

$$V_\nu^\dagger M_\nu V_\nu = \begin{pmatrix} M_{\text{light}} & 0 \\ 0 & M_{\text{heavy}} \end{pmatrix} \tag{1.18}$$

where

$$M_{\text{light}} \simeq -M_D^T M_s^{-1} M_D \qquad\qquad M_{\text{heavy}} \simeq M_s \tag{1.19}$$

and

$$V_\nu \simeq \begin{pmatrix} 1 - \frac{1}{2}M_D^\dagger (M_s^*)^{-1} M_s^{-1} M_D & M_D^\dagger (M_s^*)^{-1} \\ -(M_s)^{-1} M_D & 1 - \frac{1}{2}(M_s)^{-1} M_D M_D^\dagger (M_s^*)^{-1} \end{pmatrix} \tag{1.20}$$

The eigenvalues are in two different scales. The scale of heavier states is of the order of M_s, whereas for the lightest states its mass is suppressed by $M_D^T M_s^{-1}$. This is called the *see-saw mechanism*, which can explain the small values of active neutrino masses just in term of a very heavy sterile neutrino and avoiding very small Yukawa couplings.

1.3.2 Leptonic Mixing

In general, the representation of a field in the interaction basis can be different from the representation in the mass basis. In the SM, neutrinos are massless. Since the flavor is defined in the interaction basis, and because the neutrino flavor coincides with the charged lepton flavor, the interaction basis for neutrinos and charged leptons coincides. Without loss of generality, we can choose the basis where mass and the interaction states for the charged leptons coincide. If the SM is extended by a neutrino mass term, the mass basis for neutrinos and charged leptons do not have to coincide, and this mismatch can lead to a flavor lepton mixing. In order to see clearly where the mixing is coming from, in the following we are going to assume that the flavor and the mass basis for the charged leptons do not coincide. Let consider the mass term for the charged leptons and the neutrinos written in the

interaction basis

$$-\mathscr{L}_{\text{lepton}} = \overline{L_L} M_L E_R + \frac{1}{2}\overline{\nu} M_\nu \nu^c \tag{1.21}$$

we can define two 3×3 unitary matrices V_L and V_R, which diagonalize the mass matrix for the charged leptons $V_L^\dagger M_L V_R = \text{diag}(m_e, m_\mu, m_\tau)$. Using V_ν to diagonalize M_ν as in Eq (1.15), the mass terms for charged leptons and neutrinos can be written in the mass basis as

$$-\mathscr{L}_{\text{lepton}} = \overline{\tilde{L}_L}\text{diag}(m_e, m_\mu, m_\tau)\tilde{E}_R + \frac{1}{2}\overline{\tilde{\nu}}\text{diag}(m_1, \ldots, m_{3+m})\tilde{\nu}^c \tag{1.22}$$

where $\tilde{L}_L = V_L^\dagger L_L$ and $\tilde{E}_R = V_R E_R$. Using V_L and V_ν, the CC interaction Eq (1.10) can be written in the mass basis

$$\begin{aligned}\mathscr{L}_{CC} &= -\frac{g}{2}\sum_\alpha \overline{L_{\alpha L}}\gamma_\mu \nu_{\alpha L} W^{\mu,-} + h.c. \\ &= -\frac{g}{2}\sum_\alpha \sum_{ij} \overline{\tilde{L}_{iL}}\gamma_\mu V_{\alpha i,L} V'^\dagger_{\alpha j,\nu} \tilde{\nu}_{jL} W^{\mu,-} + h.c.\end{aligned} \tag{1.23}$$

where $V_\nu'^\dagger$ is a $3 \times (3+m)$ complex matrix that relates the left-handed flavor states $(\nu_{eL}, \nu_{\mu L}, \nu_{\tau L})$ with the mass states $(\nu_1, \ldots, \nu_{3+m})$, and verifies

$$V_\nu'^\dagger V_\nu' = I_{3\times 3} \qquad\qquad V_\nu' V_\nu'^\dagger \neq I_{(3+m)\times(3+m)} \tag{1.24}$$

$U = V_L V_\nu'^\dagger$ is the mixing matrix in the leptonic sector. The number of independent parameters depends on the nature of neutrinos. For pure Majorana states, U can be parametrize with $3(m+1)$ angles and $3(m+1)$ complex phases. For Dirac neutrinos, U contains $3(m+1)$ angles and $(2m+1)$ phases. There are two particular cases where U is a unitary matrix, for 3 Majorana neutrinos without any additional sterile neutrino, and for 3 Dirac neutrinos. For 3 Majorana neutrinos, U is parametrized by 3 angles and 3 complex phases, U is conventionally written as [10]

$$U = \begin{pmatrix} 1 & 0 & 0 \\ 0 & c_{23} & s_{23} \\ 0 & -s_{23} & c_{23} \end{pmatrix} \begin{pmatrix} c_{13} & 0 & s_{13}e^{-\imath\delta_{cp}} \\ 0 & 1 & 0 \\ -s_{13}e^{-\imath\delta_{cp}} & 0 & c_{13} \end{pmatrix} \begin{pmatrix} c_{12} & s_{12} & 0 \\ -s_{12} & c_{12} & 0 \\ 0 & 0 & 1 \end{pmatrix} \begin{pmatrix} 1 & 0 & 0 \\ 0 & e^{\imath\delta_1^M} & 0 \\ 0 & 0 & e^{\imath\delta_2^M} \end{pmatrix} \tag{1.25}$$

For 3 Dirac neutrinos, the phases δ_1^M and δ_2^M are absorbed in the neutrino states.

1.4 Neutrino flavor oscillations

Neutrino experiments have established the oscillation of the flavor on the neutrino path. The experiments have also measured the wavelength showing a dependence on the distance traveled and the neutrino energy. Most of the signals measured by experiments can be explained in the framework of the three neutrino mixing. In this model, there are three massive neutrinos that can be expressed as a quantum superposition of the flavor states in the SM (Table 1.1) weighted by the lepton mixing matrix

$$\nu_\alpha = \sum_i U_{\alpha i}\nu_i \tag{1.26}$$

where U is given by Eq (1.25). In the following, flavor states are identified by a greek index (ν_α) and mass states by latin index (ν_i). We have chosen the mass basis for the charged lepton as the interaction basis ($V_L = I_{3\times3}$). The Majorana phases δ_1^M and δ_2^M are irrelevant for neutrino oscillation because they enter into the lepton mixing through a diagonal matrix. So, the only parameters of the mixing matrix that can be constrained in neutrino oscillation experiments are the three mixing angles ($\theta_{12}, \theta_{13}, \theta_{23}$) and the complex phase (δ_{CP}). In those experiments cannot be differentiated between the Majorana or Dirac nature of this leptons.

Neutrinos (ν_α) and antineutrinos ($\overline{\nu}_\alpha$) are created in CC interactions together with charged antileptons (l_α^+) and charged leptons (l_α^-) respectively, Eq (1.10). Making a Fourier expansion of the neutrino field in terms of creation and annihiliation operators

$$\nu_{iL}(x) = \int \frac{d^3p}{(2\pi)^3 2E} \sum_{h=\pm1} \left[a_{\nu_k}^{(h)}(p) u_{\nu_{kL}}^{(h)}(p) e^{-\imath px} + b_{\nu_k}^{(h)\dagger}(p) v_{\nu_{kL}}^{(h)}(p) e^{\imath px} \right] \tag{1.27}$$

we find that the neutrino state is created by the charged current

$$j_{W,L}^{\mu} = 2 \sum_{\alpha} \sum_{k} U_{\alpha i}^{\dagger} \overline{\nu}_i \gamma_\mu L_{\alpha L} \tag{1.28}$$

and antineutrinos are created in the Hermitian conjugate charged current. From Eq (1.27), we find that neutrino (antineutrino) flavor states $|\nu_\alpha\rangle$ ($|\overline{\nu}_\alpha\rangle$) and neutrino (antineutrino) mass states $|\nu_i\rangle$ ($|\overline{\nu}_i\rangle$) are related by

$$|\nu_\alpha\rangle = \sum_i U_{\alpha i}^{\dagger} |\nu_i\rangle \qquad\qquad |\overline{\nu}_\alpha\rangle = \sum_i U_{\alpha i} |\overline{\nu}_i\rangle \tag{1.29}$$

1.4.1 Vacuum neutrino oscillations

The evolution of a flavor neutrino state ($|\nu_\alpha\rangle$) in the vacuum is described by the Schördinger equation

$$\imath \frac{d}{dt} |\nu_\alpha(t)\rangle = H_{vac} |\nu_\alpha(t)\rangle \tag{1.30}$$

where H_{vac} is the vacuum hamiltonian in the flavor basis. Since the mass and flavor basis do not coincide, the evolution equation in the flavor basis corresponds to coupled equations between all flavors. In order to solve them, we have to change to the mass basis where the vacuum hamiltonian is diagonal ($\tilde{H}_{vac} = \mathrm{Diag}(E_1, E_2, E_3)$)

$$\imath \frac{d}{dt} |\nu_i(t)\rangle = E_i |\nu_i(t)\rangle \tag{1.31}$$

the resulting equation can be solved analytically by integrating along the neutrino trajectory. Since the hamiltonian is constant, the integral is given by the product of the energy and the time of neutrino travel. Assuming the origin at $t = 0$, $|\nu_i\rangle$ after a time t is

$$|\nu_i(t)\rangle = |\nu_i(t=0)\rangle \, e^{-\imath E_i t} \tag{1.32}$$

Coming back to the flavor basis, we can describe the time evolution of a flavor

state by the superposition of the time evolution of the mass states

$$|\nu_\alpha(t)\rangle = \sum_i U^\dagger_{\alpha i} |\nu_i(t)\rangle = \sum_i U^\dagger_{\alpha i} |\nu_i(t=0)\rangle \, e^{-\imath E_i t} \tag{1.33}$$

The amplitude of the flavor transition $|\nu_\alpha\rangle \to |\nu_\beta\rangle$ after a time t, is given by

$$A_{\alpha\beta}(t) = \langle \nu_\beta | \nu_\alpha(t) \rangle = \sum_i U^\dagger_{\alpha i} U_{\beta i} \exp\left(-\imath E_i t\right) \tag{1.34}$$

The flavor oscillation probability of a flavor $|\nu_\alpha\rangle$ into a flavor $|\nu_\beta\rangle$ after a time t is given by the square of the transition amplitude

$$P_{\alpha\beta}(t) = |A_{\alpha\beta}(t)|^2 = \sum_{ij} U_{\beta i} U^\dagger_{\beta j} U^\dagger_{\alpha i} U_{\alpha i} \exp\left(-\imath (E_i - E_j) t\right) \tag{1.35}$$

For relativistic neutrinos, the energy of every mass state (E_i) can be approximated by

$$E_i = \sqrt{P_i^2 + m_i^2} = |P_i|(1 + m_i^2/2P_i^2 + \cdots) \approx E + m_i^2/2E \tag{1.36}$$

where we have approximated the momentum of the mass state (P_i) with the energy of the flavor state (E). This is a good approximation since the masses of the neutrinos states is very small ($m_i < 0.23$ eV) [11]. Under this approximation, the flavor oscillation probability can be written as

$$P_{\alpha\beta}(t) = \sum_{ij} U_{\beta i} U^\dagger_{\beta j} U^\dagger_{\alpha i} U_{\alpha i} \exp\left(-\imath \frac{\Delta m^2_{ij} t}{2E}\right) \tag{1.37}$$

In neutrino experiments, the time used by the neutrino to travel from the production point to the detector usually is not measured. Instead of that, the distance between the source and the detector (L) is known with high precision, and it is called baseline. We can express the oscillation probability in terms of the baseline using $L \equiv t$. Since the mixing matrix is unitary for 3 massives neutrinos, we can use the unitary relations to separate the contributions to the probability into real and complex part

$$\begin{aligned} P_{\alpha\beta}(L,E) = \delta_{\alpha\beta} - 4 \sum_{i>j} \mathrm{Re}[U_{\alpha i} U^\dagger_{\alpha j} U^\dagger_{\beta i} U_{\beta j}] \sin^2\left(\frac{\Delta m^2_{ij} L}{4E}\right) \\ + 2 \sum_{i>j} \mathrm{Im}[U_{\alpha i} U^\dagger_{\alpha j} U^\dagger_{\beta i} U_{\beta j}] \sin\left(\frac{\Delta m^2_{ij} L}{2E}\right) \end{aligned} \tag{1.38}$$

For the three neutrino mixing, there are three oscillations lengths given by $L^{\mathrm{osc}}_{kj} = 4\pi E/\Delta m^2_{kj}$. The expression obtained verifies the probability conservation for initial and final states

$$\sum_\alpha P_{\alpha\beta} = 1 \qquad\qquad \sum_\beta P_{\alpha\beta} = 1 \tag{1.39}$$

The kinematical properties of antineutrinos are identical to neutrinos. In order to get the oscillation probability for antineutrinos we can follow the same steps as in the neutrino case. The only difference is that the flavor states are related to the mass states through the mixing matrix instead of the hermitian matrix, as shown in Eq (1.29). So, the oscillation probability for antineutrinos has the same expression

as for neutrinos Eq (1.38) up to a minus sign in the imaginary terms.

When the distance between the source and the detector is much larger than the oscillation length ($L \gg L^{\rm osc}_{kj}$) the neutrinos arrive to the detector as an incoherent superposition of mass states[1]. Because of the finite energy resolution of the detectors, the oscillatory terms are averaged by the detector resolution if the baseline is much larger than the oscillation length. The average of the sin function vanishes, whereas the average of $\sin^2$ function is 1/2. From Eq (1.38), we obtain an expression for the flavor transition in terms of the mixing angles and the complex phase

$$P_{\alpha\beta} = \sum_i |U_{\alpha i}|^2 |U_{\beta i}|^2 \tag{1.40}$$

The flavor transition measured for very long baselines is determined just by squares of the mixing matrix elements.

1.4.2 CPT, CP and T transformations

SM is symmetric under the product of the transformations over the charge (C), parity (P) and time (T), CPT. On the other hand, neutrinos and antineutrinos are related under a CP transformation ($\nu_\alpha \xrightarrow{\rm CP} \bar{\nu}_\alpha$). Under this transformation, the oscillation probability for neutrinos become into the probability for antineutrinos ($P_{\nu_\alpha\to\nu_\beta} \xrightarrow{\rm CP} P_{\bar{\nu}_\alpha\to\bar{\nu}_\beta}$). T revert the order of the flavor oscillation ($P_{\nu_\alpha\to\nu_\beta} \xrightarrow{\rm T} P_{\nu_\beta\to\nu_\alpha}$). Because of the symmetry of SM under the CPT transformation the oscillation probability must satisfied

$$P_{\nu_\alpha\to\nu_\beta} = P_{\bar{\nu}_\beta\to\bar{\nu}_\alpha} \tag{1.41}$$

This property can also be observed by looking into the oscillation probability Eq (1.38). From the oscillation probability for antineutrinos, exchanging the mass index ($i \leftrightarrow j$) a minus sign appears from the terms that go with a sin function and compensate the sign due to the complex transformation of the mixing matrix, recovering the neutrino oscillation probability. When neutrinos propagate in matter, the oscillation probability violates the CPT symmetry. The normal matter is composed by particles and not antiparticles, which induce a CP violation on the oscillation probability.

The symmetry under a CPT transformation of $P_{\alpha\beta}$ in vacuum implies that CP and T can be violated separately. The complex phase in the mixing matrix encodes the amount of CP violation. In order to measure that quantity, in neutrino oscillation experiments we need to measure

$$\Delta P^{\rm CP}_{\alpha\beta} = P(\nu_\alpha \to \nu_\beta) - P(\bar{\nu}_\alpha \to \bar{\nu}_\beta) \tag{1.42}$$

note that $\beta \neq \alpha$ since the difference in the probability for neutrinos and antineutrinos comes from the imaginary part that is zero in the case of $P(\nu_\alpha \to \nu_\alpha)$.

1.4.3 2ν approximation

We can consider a simplified model formed just by two mass neutrinos ($|\nu_1\rangle$, $|\nu_2\rangle$) and two flavor states ($|\nu_\alpha\rangle$, $|\nu_\beta\rangle$). In this case, the mixing matrix is given by 2×2

[1] That is the case of neutrinos produced at the Sun or in astrophysical sources

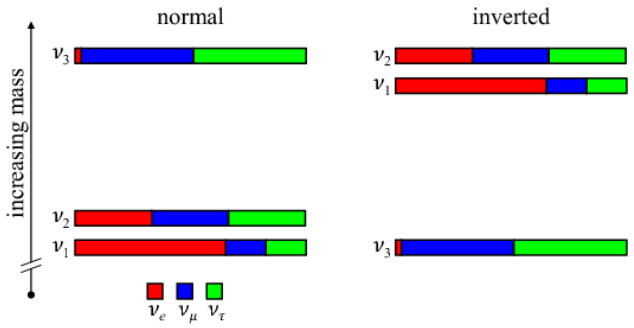

Figure 1.4: Neutrino mass ordering. The colors represent the contribution of every flavor state

rotation matrix without a CP violation phase[2]

$$U(\theta) = \begin{pmatrix} \cos\theta & \sin\theta \\ -\sin\theta & \cos\theta \end{pmatrix} \tag{1.43}$$

To obtain the flavor oscillation probability, We can follow the same steps as for the 3ν case. In this simplified model it is given by

$$P_{\alpha\beta} = \sin^2 2\theta \sin^2\left(\frac{\Delta m^2 L}{4E}\right)^2 \qquad P_{\alpha\alpha} = 1 - \sin^2 2\theta \sin^2\left(\frac{\Delta m^2 L}{4E}\right)^2 \tag{1.44}$$

The amplitude depends on $\sin^2 2\theta$, so it is maximal for $\theta = 45$. The probability is symmetric under the transformations $\theta \to \pi/2 - \theta$ and $\Delta m^2 \to -\Delta m^2$. The octant transformation changes the projection of every mass state in the flavor basis. The change in the sign of the mass parameter corresponds with an interchange between the mass states. After both transformations, the contribution of $|\nu_1\rangle$ and $|\nu_2\rangle$, over $|\nu_\alpha\rangle$ and $|\nu_\beta\rangle$ are the same. Eq (1.44) is not only symmetric under both transformations, but also under each transformation separately. Those transformations implie that there are two different set of parameters, $(\Delta m^2, \theta)$ and $(\Delta m^2, \theta + \pi/2)$, with different physical meaning which cannot be resolved by the flavor oscillation in the vacuum. That degeneracy is solved when neutrinos propagate through matter.

1.4.4 Mass splitting dominance

The data collected by the experiments have shown that there two very well separates mass splittings $\Delta m^2_{21} \sim 10^{-5}\text{eV}^2$ and $|\Delta m^2_{3l}| \sim 10^{-3}\text{eV}^2$, which are called the solar and the atmospheric mass parameters respectively. The sign of the atmospheric mass splitting determines the mass ordering, Fig 1.4. A positive sign corresponds with a heavier neutrino state compared with the other two states. This mass ordering is called normal hierarchy (NH). A negative sign corresponds with two quasi-degenerate mass states and a light one. In this case, the mass ordering is called inverted hierarchy (IH). For a neutrino experiment, the energy of the neutrino beam and the baseline determine the scale of the wavelength where a flavor oscillation can be detected.

[2]The number of CP phases for Dirac neutrinos after rephasing the states is given by $(n-1)(n-2)/2$, where n is the number of neutrino states. CP non-conservation is only possible for $n \geq 3$.

Neutrino oscillation experiments usually are devoted to the measurement of some specific neutrino flavors oscillation over a narrow L/E ratio. Therefore, they are mainly sensitives to one the oscillation wavelengths. In the case of experiments which are sensitives to the atmospheric mass parameter, the following approximation can be used on the oscillation probability $\Delta m^2_{31} \approx \Delta m^2_{32} \equiv \Delta m^2$ and $\Delta m^2_{21} \approx 0$. In that regime, the contribution of the imaginary vanishes in Eq (1.38) and the oscillation probability can be written as

$$P_{\alpha\beta} = \delta_{\alpha\beta} - 4(\delta_{\alpha\beta}|U_{\alpha 3}|^2 - |U_{\alpha 3}|^2|U_{\beta 3}|^2)\sin^2\left(\frac{\Delta m^2 L}{4E}\right) \tag{1.45}$$

$$= \delta_{\alpha\beta} - \sin^2 2\theta^{\text{eff}}_{\alpha\beta}\sin^2\left(\frac{\Delta m^2 L}{4E}\right) \tag{1.46}$$

where

$$\alpha \neq \beta \qquad \sin^2 2\theta^{\text{eff}}_{\alpha\beta} = 4|U_{\alpha 3}|^2|U_{\beta 3}|^2$$
$$\alpha = \beta \qquad \sin^2 2\theta^{\text{eff}}_{\alpha\alpha} = 4|U_{\alpha 3}|^2(1 - |U_{\alpha 3}|^2)$$

Those expressions can be used to describe the flavor oscillation in experiments with atmospheric neutrinos, reactor and long-base lines experiments.

There are other experiments that are mainly sensitives to the solar mass splitting. In that case, the approximation that the imaginary terms vanish cannot be used. In order to obtain a simplified expression, we use the finite detector energy resolution, which average the terms that depend on the atmospheric mass splitting. In this case, for the disappearance channel, the initial and the final states are the same ($\alpha = \beta$), the probability can be written as

$$P_{\alpha\alpha} = 1 - 4|U_{\alpha 2}|^2|U_{\alpha 1}|^2\sin^2\left(\frac{\Delta m^2_{21} L}{4E}\right) - 2\left(|U_{\alpha 3}|^2|U_{\alpha 1}|^2 + |U_{\alpha 2}|^2|U_{\alpha 2}|^2\right) \tag{1.47}$$

This expression are relevant for reactor experiments like KamLAND, where the neutrino energy is of the order of $\sim$ MeV and the baseline is $L \sim 100$ km

1.5 Neutrino oscillation in matter

The matter that form most of the enviorments where neutrino propagation takes place is made of electrons, protons, and neutrons, some examples are the Earth or the Sun. That enviroments are neutral, what implies a coincidence in the number density of protons and electrons. Neutrinos can interact with the quarks and leptons present in the matter through CC and NC, as shown in Eq (1.10), and this can affect neutrino properties. Depending on the energy mediator, the neutrino interactions can be divided into coherent or incoherent. A coherent interaction takes place when the energy mediator goes to zero, and the matter as well as the neutrino kinematical properties are unchanged after the interaction. In an incoherent interaction, the initial and final states are different.

As neutrino energy increases, the total inclusive cross section in a incoherent interaction shows a linear dependence on energy, Fig 1.5 [10]. This is the expected response for a Deep Inelastic Scattering ($E_\nu > 10$ GeV), where neutrinos can scatter off an individual quark inside a nucleon. The total cross section can be approximated

as

$$\sigma \sim \frac{G_F^2 s}{\pi} \sim 10^{-38}\text{cm}^2 \frac{E_\nu M}{\text{GeV}^2} \tag{1.48}$$

where s is the square of the total energy in the center of mass frame. In the laboratory frame, where the target is at rest, the total square energy can be approximated as $s \sim 2E_\nu M$, where M is the mass of the target particle and E_ν is the neutrino energy. At lower energies ($E_\nu < 10$ GeV), the cross section is dominated by Quasi-elastic scattering and the resonance production, changing the energy dependence (Fig 1.5). The mean free path (L_{free}) in a medium with number density N is inversely proportional to the number of scatters

$$L_{\text{free}} \sim \frac{1}{N\sigma} \tag{1.49}$$

For the Earth mantle, with an average density of the order of $\rho \sim 4\text{g/cm}^3$, and for a nucleon target $M \sim 1$ GeV, the mean free path in a DIS process is $L_\oplus \sim 10^{14}/(E/\text{GeV})$ cm. The diameter of the Earth is $2R_\oplus \sim 10^9$ cm. So, the incoherent interaction are the dominant process for atmospheric neutrinos with energies of the order of 10^5 GeV, around four orders of magnitude higher than the maximum energy at which neutrinos oscillate through the Earth. For the Sun, with an average density of $\rho \sim 1.5\text{g/cm}^3$, and for a neutrino energy in the MeV range, the mean free path is $L_\odot \sim 10^{18}/(E/\text{MeV})$ cm, seven orders of magnitude higher than its diameter. So, the incoherent interactions are not relevant in the energy regime where the flavor oscillations take place.

1.5.1 Neutrino coherent interaction

In the limit of an interaction with zero momentum transfer, the momenta and the helicity of the matter and the neutrino remains unchanged, and the neutrino ensemble can coherently interfere in the forward direction. This interaction modifies the flavor propagation of the neutrino ensemble, and can be described by an effective potential which depends on the mediator. The only CC coherent forward scattering in normal matter is due to an $\nu_e - e$ interaction. Because of the zero momentum of

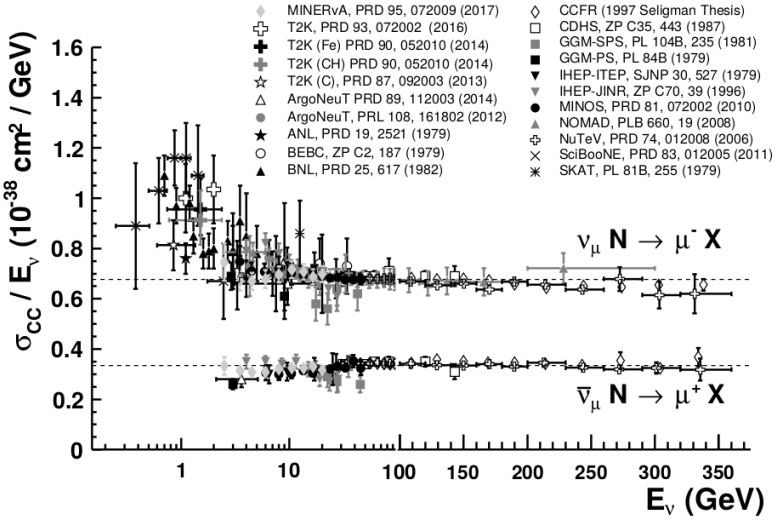

Figure 1.5: Measurement of ν_μ and $\overline{\nu_\mu}$ CC inclusive cross section per nucleon as a function of neutrino energy [10]. The cross section is divided by the neutrino energy.

	g_V^f	g_A^f
e	$-\frac{1}{2} + 2\sin^2\theta_w$	- $\frac{1}{2}$
p	$\frac{1}{2} - 2\sin^2\theta_w$	$\frac{1}{2}$
n	$-\frac{1}{2}$	- $\frac{1}{2}$

Table 1.3: Vector (g_V^f) and axial (g_A^f) couplings for electrons (e), protons (p) and neutrons (n).

the mediator, the process is described by an effective hamiltonian given by

$$H_{\text{eff}}^{CC} = \frac{G_F}{\sqrt{2}}\overline{\nu}_e\gamma^\mu(1-\gamma_5)\nu_e\overline{e}\gamma_\mu(1-\gamma_5)e \tag{1.50}$$

where we have used the Fierz transformation [12] to reorder the field operators. Assuming the electron background is thermally distributed and unpolarized, we can take the average of the hamiltonian over the electron states. The remaining effective hamiltonian can be written as

$$H_{\text{eff}}^{CC} = \sqrt{2}G_F n_e \overline{\nu}_{eL}\gamma^0\nu_{eL} \tag{1.51}$$

where n_e is the electron number density in the medium. This term can be interpreted as a potential energy $V_{CC} = \sqrt{2}G_F n_e$ for ν_{eL} due to the electrons in matter.

We can follow the same steps to derive an effective potential for the NC interactions. Since NC are equal for the three neutrino flavors, the effective potential is flavor independent, and it is composed of the contribution of the three interactions $\nu_\alpha - (e, p, n)$. The effective hamiltonian is given by

$$H_{\text{eff}}^{NC} = \frac{G_F}{\sqrt{2}}\sum_\alpha(\overline{\nu}_\alpha\gamma^\mu(1-\gamma_5)\nu_\alpha)\sum_{f=e,p,n}\overline{f}\gamma^\mu(g_v^f - \gamma_5 g_A^f)f \tag{1.52}$$

where g_v^f and g_A^f are the vector and axial coupling constant for the fermion f (Table 1.3). After the average over the background states, the effective potential due to NC interactions is $V_{NC}^f = \sqrt{2}G_F n_f g_V^f$. In an electrically neutral enviroment ($n_e = n_p$) only neutrons contributes to the potential, $V_{NC} = \sum_f V_{NC}^f = -\sqrt{2}G_F n_n/2$.

As a summary, neutrino evolution is modified by an effective potential once they propagate through matter. In an electrically neutral environment, the effective potential is given by

$$V_\alpha = \sqrt{2}G_F\left(n_e\delta_{\alpha,e} - \frac{n_n}{2}\right) \tag{1.53}$$

For antineutrinos, the potential needs to be replaced by $-V_\alpha$. Considering again the Earth with a matter density of $\rho \sim 4\text{g/cm}^3$, the CC potential is of the order of $V_{CC} \sim 10^{-14}$ eV. We can compare that value with the kinetic energy term which the responsible of the oscillation in vacuum. For a neutrino with energy $E_\nu = 10GeV$ and mass $\Delta m_\nu^2 \sim 10^{-3}\text{eV}^2$, the kinetic term $\Delta m^2/2E_\nu \sim 10^{-14}$ eV, similar to the matter potential.

1.5.2 Flavor oscillation in constant matter

The evolution equation for relativistic neutrinos that propagates in matter is modified by the matter potential term

$$\imath\frac{d}{dt}\begin{pmatrix}|\nu_e\rangle\\|\nu_\mu\rangle\\|\nu_\tau\rangle\end{pmatrix}=\frac{1}{2E}\left[U\begin{pmatrix}m_1^2&0&0\\0&m_2^2&0\\0&0&m_3^2\end{pmatrix}U^\dagger+\begin{pmatrix}A&0&0\\0&0&0\\0&0&0\end{pmatrix}\right]\begin{pmatrix}|\nu_e\rangle\\|\nu_\mu\rangle\\|\nu_\tau\rangle\end{pmatrix} \quad (1.54)$$

where $A=2\sqrt{2}G_F n_e E$ depends on the electron density and the neutrino energy. For the matter potential, we have not included the contribution from NC because it is a diagonal term, which affect in the same way to all flavors. Once the evolution equation is solved, the NC potential contribute to the flavor evolution with a phase, similar for all flavors, that desappear when the oscillation probability is obtained. For the vacuum term, we have approximated the energy of every mass state with the energy of the flavor states, Eq (1.36). We have also removed the contribution of the neutrino energy, which is equal for all mass states. The unitary matrix which multiplies the mass matrix is given by Eq (1.25).

As in vacuum, the mixing matrix in matter can be parameterized in terms of three angles and a complex phase $(\tilde{\theta}_{12},\tilde{\theta}_{13},\tilde{\theta}_{23},\tilde{\delta})$. Without loss of generality, we can rephase the states $|\nu_\tau\rangle\rightarrow|\nu_\tau\rangle\,e^{\imath\delta}$ and $|\nu_3\rangle\rightarrow|\nu_3\rangle\,e^{\imath\delta}$ what is equivalent to define $U=R(\theta_{23},\delta_{CP})R(\theta_{13})R(\theta_{12})P$, where P is a diagonal matrix that contains the Majoranna phases

$$U=\begin{pmatrix}1&0&0\\0&c_{23}&s_{23}e^{-\imath\delta_{cp}}\\0&-s_{23}e^{-\imath\delta_{cp}}&c_{23}\end{pmatrix}\begin{pmatrix}c_{13}&0&s_{13}\\0&1&0\\-s_{13}&0&c_{13}\end{pmatrix}\begin{pmatrix}c_{12}&s_{12}&0\\-s_{12}&c_{12}&0\\0&0&1\end{pmatrix}\begin{pmatrix}1&0&0\\0&e^{\imath\delta_1^M}&0\\0&0&e^{\imath\delta_2^M}\end{pmatrix} \quad (1.55)$$

The evolution can be solved in a intermediate basis related with the flavor basis by $|\nu_i'\rangle=\sum_\alpha U^\dagger_{\alpha i}(23,\delta_{CP})\,|\nu_\alpha\rangle$. Once the equation is solved, the flavor evolution is recovered multiplying by $U(23,\delta_{CP})$. For this reason, θ_{23} and δ_{CP} are not modified by matter evolution, and their value is the same as in vacuum.

To solve the neutrino evolution we have to specify the profile density where neutrino propagates. For an arbitrary density profile, the only exact solution is numerical, but there are some matter scenarios where an analytical solution can be obtained, like the constant density matter. In this case, we can define the neutrino hamiltonian (H) as

$$H=U\begin{pmatrix}m_1^2&0&0\\0&m_2^2&0\\0&0&m_3^2\end{pmatrix}U^\dagger+\begin{pmatrix}A&0&0\\0&0&0\\0&0&0\end{pmatrix} \quad (1.56)$$

and $\tilde{U}$ as the mixing matrix that relates the flavor states with the hamiltonian eigenstates

$$\tilde{U}^\dagger H\tilde{U}=\begin{pmatrix}\lambda_1&0&0\\0&\lambda_2&0\\0&0&\lambda_3\end{pmatrix} \quad (1.57)$$

Following the same steps as in section 1.4.1, we can obtain the oscillation probability

$$P_{\alpha\beta}(L,E) = \delta_{\alpha\beta} - 4\sum_{i>j}\mathrm{Re}[\tilde{U}_{\alpha i}\tilde{U}^{\dagger}_{\alpha j}\tilde{U}^{\dagger}_{\beta i}\tilde{U}_{\beta j}]\sin^2\left(\frac{(\lambda_i-\lambda_j)L}{4E}\right) + 2\sum_{i>j}\mathrm{Im}[\tilde{U}_{\alpha i}\tilde{U}^{\dagger}_{\alpha j}\tilde{U}^{\dagger}_{\beta i}\tilde{U}_{\beta j}]\sin\left(\frac{(\lambda_i-\lambda_j)L}{2E}\right) \tag{1.58}$$

The oscillation probability for a constant density profile coincides with the expression in vacuum replacing $U \to \tilde{U}$ and $E_i \to \lambda_i$.

1.5.3 2ν approximation

In a simplify scenario which consist of two flavor states $|\nu_\alpha\rangle$ and $|\nu_\beta\rangle$, the oscillation is described by the mass difference between two massive states $|\nu_1\rangle$ and $|\nu_2\rangle$, and the mixing matrix U_m is given by the rotation matrix

$$U_m = \begin{pmatrix} \cos\theta_m & \sin\theta_m \\ -\sin\theta_m & \cos\theta_m \end{pmatrix} \tag{1.59}$$

The evolution equation is given by

$$\imath\frac{d}{dx}\begin{pmatrix} |\nu_\alpha\rangle \\ |\nu_\beta\rangle \end{pmatrix} = \frac{1}{2E}\left[U\begin{pmatrix} m_1^2 & 0 \\ 0 & m_2^2 \end{pmatrix}U^{\dagger} + \begin{pmatrix} A_\alpha & 0 \\ 0 & A_\beta \end{pmatrix}\right]\begin{pmatrix} |\nu_\alpha\rangle \\ |\nu_\beta\rangle \end{pmatrix} \tag{1.60}$$

where U is the 2×2 rotation matrix given by Eq (1.43), and $A_\alpha = 2EV_\alpha$. The matter potential for $|\nu_\mu\rangle$ and $|\nu_\tau\rangle$ is due to the NC interactions for both states, so in the evolution equation we can take its value as zero [3], and the evolution for those states is described by the vacuum equation. For any two flavor states, we can use U_m to diagonalize the hamiltonian, the eigenvalues are

$$\lambda_1(x) = \frac{1}{2}\left[m_1^2 + m_2^2 + A_\alpha + A_\beta - \sqrt{(\Delta m^2\sin 2\theta)^2 + (\Delta m^2\cos 2\theta - (A_\alpha - A_\beta))^2}\right] \tag{1.61}$$

$$\lambda_2(x) = \frac{1}{2}\left[m_1^2 + m_2^2 + A_\alpha + A_\beta + \sqrt{(\Delta m^2\sin 2\theta)^2 + (\Delta m^2\cos 2\theta - (A_\alpha - A_\beta))^2}\right] \tag{1.62}$$

and the mixing angle in matter is given by

$$\tan 2\theta_m = \frac{\Delta m^2\sin 2\theta}{\Delta m^2\cos 2\theta - 2E\,(V_\alpha - V_\beta)} \tag{1.63}$$

θ_m depends on the potential, so the relation between the mass and the flavor states change along the neutrino trajectory as the electron density change. If a mass state in vacuum, let say $|\nu_1\rangle$, has a large projection over a flavor state, for example $|\nu_\alpha\rangle$, which means $\theta \simeq 0$ or $\theta \simeq \pi/2$, inside matter that verifies $2E(V_\alpha - V_\beta) \gg \Delta m^2\cos 2\theta$, the projection change and $|\nu_\alpha\rangle$ is dominated by $|\nu_2\rangle$. For some values of the matter potential and the neutrino energy, the denominator of $\tan 2\theta_m$ vanishes

[3] The matter potential is non-zero for any of the three neutrinos defined in the SM because of the electroweak interactions. For the states $|\nu_\mu\rangle$ and $|\nu_\tau\rangle$ the potential comes from the NC, so it has the same value for both states, and it does not play a role in the oscillation probability. If we consider the mixing with sterile neutrinos, since this new fermions are singlets of SM, their matter potential is zero, and we have to include the contribution of the NC to the potential of the left-handed states.

$(2E(V_\alpha - V_\beta) = \Delta m^2 \cos 2\theta)$, and the mixing angle becomes $\theta_m = 45$. At this point, there is maximal mixing, and the contribution of every mass state to every flavor states is the same. The enhancement of the flavor mixing in matter is called MSW effect [13, 14]. The resonance happens for $\theta < \pi/4$ if $A_\alpha - A_\beta$ and Δm^2 has the same sign or $\theta > \pi/4$ in the other case. Therefore, for a given sign of Δm^2 and octant of vacuum mixing angle, the resonance only happens for neutrinos or antineutrinos.

Neutrino wavelength also can change along its path. The energy difference $(\lambda_2 - \lambda_1)$, which correspond to the oscillation wavelength in matter, depends on the matter density and takes its smallest value $(\Delta m^2 \sin 2\theta)$ at the resonant point.

1.5.4 Adiabatic approximation

As in the 3ν mixing, solving the evolution for a constant matter potential and computing the oscillation probability we recover similar expressions as Eq (1.44) by changing $\theta \to \theta_m$ and $\Delta m^2 \to (\lambda_2 - \lambda_1)$. In matter, the symmetry over the mixing angle octant in the 2ν approximation is broken, for a given sign of $A_\alpha - A_\beta$ and Δm^2, θ_m is larger or smaller than in vacuum depending on the octant of θ. For a non-constant profile density, the evolution equation can be written in the mass basis as

$$\imath \frac{d}{dx} \begin{pmatrix} |\nu_1\rangle \\ |\nu_2\rangle \end{pmatrix} = \left[\frac{1}{2E} \begin{pmatrix} \lambda_1(x) & 0 \\ 0 & \lambda_2(x) \end{pmatrix} - \imath U \frac{d}{dx} U^\dagger \right] \begin{pmatrix} |\nu_1\rangle \\ |\nu_2\rangle \end{pmatrix} \tag{1.64}$$

Developing the last term in the previous equation, we find that it correspond to an antisymmetric matrix proportional to $\dot{\theta} \equiv d\theta/dx$. This term implies a mixing between the mass states in the evolution. If $\dot{\theta}/|\lambda_2 - \lambda_1|$ is very small, the evolution of the mass states is independent of each other and is given by the exponential of the integral of λ_i along the neutrino path. That is called adiabatic regime and take place in slowly varying matter potential compared with the oscillation wavelenght, like the Sun. Under that approximation, the oscillation probability becomes

$$P_{\alpha\beta}(L) = \left| \sum_i U_{\beta i}(0) U_{\alpha i}(L) \exp\left\{ -\frac{\imath}{2E} \int_0^L dx \lambda_i(x) \right\} \right|^2 \tag{1.65}$$

We can study the adiabatic neutrino evolution and the oscillation probability in the particular example of neutrinos created in the inner part of the Sun, where the matter potential can be expected to be much higher than its value at the resonace.

The two main mechanisms that create neutrinos in the Sun are the pp chain and CNO cycle, where the overall result of both process is the conversion of 4 protons into a ^4He nucleus, two positrons, two electron neutrinos and energy $(4p \to {}^4He + 2e^+ + 2\nu_e + \gamma)$. So, we can study the evolution of the system $\nu_e - \nu_\beta$, where ν_β is a linear combination of ν_μ and ν_τ.

At the inner part of the Sun, if the matter potential verifies $A_e \gg \Delta m^2 \cos 2\theta$, the mixing angle is $\theta_m \simeq \pi/2$ and the system is mainly composed by $|\nu_2\rangle$. Since the evolution is adiabatic, the system remains in the same mass state along the whole path. As the neutrino moves to smaller density regions, θ_m become smaller and the mixing increase, being the maximal mixing point at the resonance point $\theta_m = \pi/4$. As the neutrino arrive to the outer part of the Sun, the density decrease but now the same happen to the mixing. When neutrino exit from the Sun, the $|\nu_\beta\rangle$ component is fixed by the vacuum mixing angle, θ.

We can compute the disappearance probability (P_{ee}) from Eq (1.65). Notice that $U_{ei}(0)$ correspond to the mixing matrix at the production point and, $U_{ei}(L)$ outside

the sun

$$P_{ee} = \frac{1}{2}\left[1 + \cos 2\theta_m \cos 2\theta + \sin 2\theta_m \sin 2\theta \cos\left(\frac{-\imath}{2E}\int_0^L dx(\lambda_2(x) - \lambda_1(x))\right)\right] \tag{1.66}$$

we have pulled out the phase associated to λ_1. θ_m and θ are the mixing angles at the production point and outside the Sun, respectively. Due to the large radius of the Sun and the small energy of the neutrinos created, the oscillatory term is going to be averaged. Using $\theta_m \simeq \pi/2$ the probability becomes

$$P_{ee} = \sin^2\theta \tag{1.67}$$

After crossing the Sun, the probability to obtain a ν_e can be very small, and it is just determined by the vacuum mixing angle. Since the final probability is independent of the energy and the distance traveled, the ν_e disappearance can be explained by flavor transition rather than a flavor oscillation.

1.6 Atmospheric neutrinos

As it was mentioned at the begining, atmospheric neutrinos are created in the collision of cosmic rays with the atmospheric nuclei. Coming from outside the solar system, their energy range extends from 100 MeV, below which energy the flux of extraterrestrial particles arriving to the Earth is dominated by the solar wind, up to 10^{20} eV, above which the flux is suppressed because of the interaction with the *cosmic microwave background* (cmb). The cosmic rays are mainly protons, electrons and a small fraction of heavy nuclei [15]. After the interactaion with the atmosphere, a second generation of particles is produced, and among the hadrons produced there are many pions and kaons. The spectrum of this secondary flux peaks in the GeV range, and can be approximated by a power-law to higher energies. At energies lower than 100 GeV, the atmospheric neutrino flux is dominated by the π decay, Eq (1.68), whose principal mode corresponds with the decay into a μ and a ν_μ with a branching ratio (Br) of $Br = 99.99\%$ [10]. To higher energies, the K decay contribution dominates. Apart from the K decay into μ and ν_μ Eq (1.68) that correspond to a $Br = 63.56\%$ [10], there are additional contributions from other semileptonic decays like $K^\pm \to \pi^0 + \mu^\pm + \nu_\mu(\overline{\nu_\mu})$ $(K^\pm \to \pi^0 + e^\pm + \nu_e(\overline{\nu_e}))$ with a $Br = 3.35\%(5.07\%)$. There is a secondary neutrino flux generated by the μ decay Eq (1.68) that contribute in the same amount to ν_μ and ν_e fluxes. So, the atmospheric neutrino flux is formed by ν_μ and ν_e in a flavor ratio $(\nu_\mu + \overline{\nu_\mu})/(\nu_e + \overline{\nu_e}) \simeq 2$. At high energies, this flux is suppressed because μ hit the Earth before its decay.

$$\begin{aligned} \pi^\pm &\to \mu^\pm + \nu_\mu(\overline{\nu_\mu}) && Br = 99,99\% \\ K^\pm &\to \mu^\pm + \nu_\mu(\overline{\nu_\mu}) && Br = 63.56\% \\ \mu^\pm &\to e^\pm + \nu_e(\overline{\nu_e}) + \nu_\mu(\overline{\nu_\mu}) && Br = 100\% \end{aligned} \tag{1.68}$$

The first observation of atmospheric neutrinos was carried out in 1960's by the Kolar Gold Field experiment in India [16] and the underground experiments in South Africa [17]. Both experiments measured the horizontal flux because they could not distinguish between the up and down directions. In the following decades, new

experiments were able to measure the atmospheric neutrino flux with high precision, showing a dependence of the flux that arrives at the detector not only with the rate at which they are produced but also with the distance traveled along the Earth.

1.6.1 Atmospheric neutrino flux calculations

A detailed knowledge of the neutrino flux is crucial to determine their oscillation properties. The most recent calculations of the atmospheric neutrino flux are based in 3D-MonteCarlo (MC) simulations, where the motion of all the cosmic rays that penetrate the Earth magnetic field is followed, as well as the subsequent generations of particles, created after their interaction. All the neutrinos generated during the propagation, whose direction cross a specific location in the Earth, are registered.

The MC simulation makes a convolution between the primary cosmic ray spectrum (ϕ_p), the yield (Y) of neutrinos per primary particle and the geomagnetic cutoff (R) [15]

$$\phi_{\nu_i} = \phi_p \otimes R_p \otimes Y_{p\to\nu_i} + \sum_A \phi_A \otimes R_A \otimes Y_{A\to\nu_i} \tag{1.69}$$

where A corresponds to the heavy nuclei present in the arriving cosmic ray flux. ϕ_{ν_i} shows an energy dependence that follows a power law $\phi_{\nu_i} \sim E_\nu^\gamma$ (Fig 1.6), with an spectral index close to $\gamma \approx -3$ in the energy range 1 GeV to 1 TeV. For higher (lower) energies the flux becomes steeper (less marked). About the zenith response, the flux shape depends on the energy and the Earth location where it is computed [18] (Fig 1.6). Those effects are due to:

- Geomagnetic effects over the cosmic ray fluxes. Earth magnetic field modifies the trajectory of the charged cosmic rays once they arrive to the Earth. The effect depends on the impact point over the Earth. Low rigidity particles can only penetrate to the Earth in the parallel direction to the magnetic field. For high rigidity, cosmic rays can enter to Earth from any direction.

- A zenith dependence of the yield. Inclined showers develops in air longer distances before hitting the ground, and therefore they have more time to decay. The atmosphere density increase as the altitude decrease. For the inclined shower, a longer part of the track is developed in high altitudes, which increase the probability that the particles of the showers end in a decay. Those effects are more relevant for high energy neutrinos. For low energies, neutrinos are produced in the decays of low energy mesons and muons, for those who there is no enhancement in the horizontal directions. As a results, the ratio between the flux from horizontal to vertical directions increase with neutrino energy.

- Enhancement of the flux at horizontal directions due to the spherical geometry of the atmosphere. For low energy neutrinos, there is no correlation between neutrino direction and its parent particle, the neutrino emission is isotropic. For an observer which is not at the center of the emission sphere, the center of the Earth, there is an enhancement in the horizontal direction. The effect is stronger as the observer moves away from the center. For high energies, the isotropy emission disappear and the neutrino direction can be approximated by its parent direction, and the enhancement disappears.

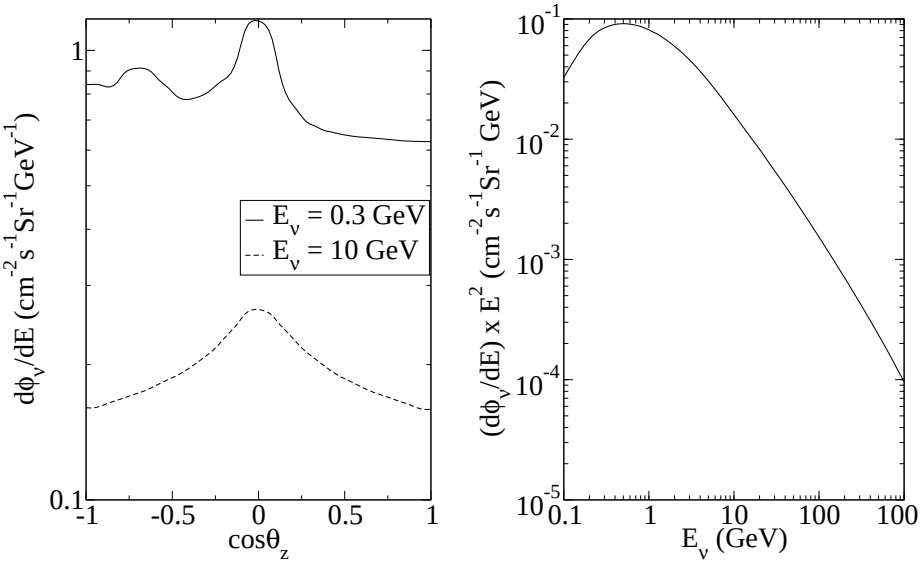

Figure 1.6: Atmospheric muon neutrino flux (ϕ_{ν_μ}) as a function of zenit angle (left) and neutrino energy (right). The dash line in the left pannel has been increase by 3 orders of magnitude. The flux has been obtain from the tables published in [19]

All those effects are presented in the left panel of Fig 1.6, that shows the muon atmospheric neutrino flux for two different energies $E_\nu = 0.3$ GeV (continuous line) and $E_\nu = 10$ GeV (dashed line) as a function of the zenith angle. Due to the stronger energy dependence od the flux, the dash line has been increased by 3 orders of magnitude. For the continuous line, the flux is higher for the horizontal direction because of the atmospheric geometry, and it has different values for the up and down directions due to the geomagnetic effects. For the dashed line, the flux is perfectly symmetric around an axis pointing in the horizontal direction, and the flux is higher for $\cos\theta_z = 0$ because of the zenith dependence of the yield. The flux has been obtained from the tables published in [19]

1.6.2 Flavor oscillation in the Earth

The most accurate description of the Earth density profile is given by Preliminary Reference Earth Model [20] (PREM), Fig 1.7. Based in seismological studies, PREM divides the Earth into eleven concentric spherical layers. In each of them, the density is given in terms of the distance to the center of the Earth by a polynomial function. In that model, the neutron/electron ratio is also fixed to $Y_n = 1.012$ in the mantle and $Y_n = 1.137$ in the Core. Because the Earth matter is electrically neutral, using the density ρ and Y_n can be obtained the electron density $N_e = \rho/(1 + Y_n)$. Apart from the density, PREM also provides values for elastic properties, attenuation and pressure.

Neutrino propagation through the Earth can only be described in the non-adiabatic regime. The Earth profile density present two very well separate density regions, the mantle ($|x| > 0.54$) and the core ($|x| < 0.54$), where the density abruptly change by a factor of two, breaking any possible adiabatic description for the trajectories that cross the core, Fig 1.7. x is the ratio between the distance of the layer to the center of the Earth (R) and the Earth radius $R_\oplus = 6371$ km. Although there are analytic approximations that provide an accurate description of the flavor oscillation in non-adiabatic evolutions [21], we are going to proceed by a

numerical integration in order to describe the flavor evolution.

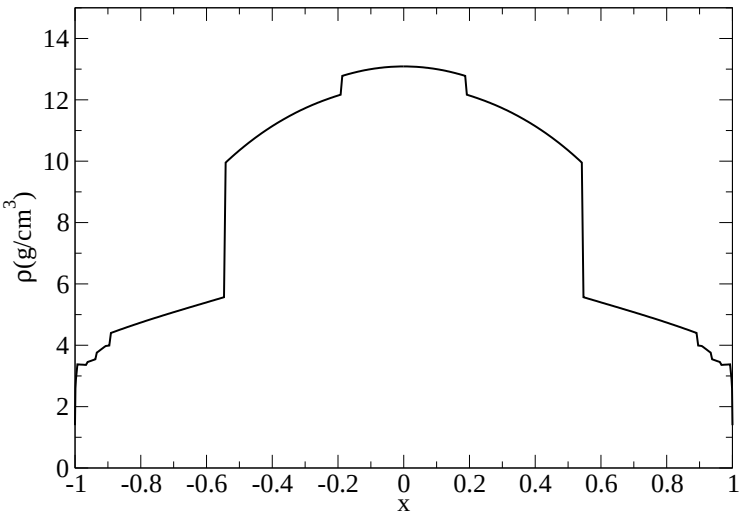

Figure 1.7: Earth density given by PREM [20] as a function of the fractional distance to the Earth center $x = R/R_\oplus$, where R is the distance of the layer to the center of the Earth and $R_\oplus = 6371$ km.

In order to have an overall view of the matter resonances when neutrinos travel through the Earth, we are going to study the electron disappearance channel, $(1 - P_{ee} = P_{\mu e} + P_{\tau e})$, Fig 1.8. Notice that the Earth profile density is symmetric about the midpoint in the neutrino path, so the oscillation probability is invariant under the time ordering operation $P_{\alpha\beta} = P_{\beta\alpha}$. The flavor oscillation along the Earth depends on neutrino energy (E_ν) and the direction of the neutrino trajectory, that is given by the cosine of the zenith angle ($\cos\theta_z$), defined as $\cos\theta_z = -1$ for up-going neutrinos, and $\cos\theta_z = 1$ for down going neutrinos. To present the probability we are going to use the oscillogram, a two dimensional contour plot where every color line corresponds with a value for $1 - P_{ee}$. In this figure, the best fit values of the global fit [22] were used as input for the oscillation parameters. Since we are interested only in the evolution through the Earth, the zenith angle is in the interval $\cos\theta_z \in [-1, 0]$, for positives values the neutrino only crosses the atmosphere. For simplicity, we have assumed that neutrinos are produced at an altitude of 15 km[4]. For the energy, we have considered the range $E_\nu \in [0.05, 100]$ GeV. At the top of the energy range, the flavor oscillation is limited by the atmospheric mass splitting ($\sim 10^{-3}\text{eV}^2$), which produce the first oscillation maximum at $E_\nu \approx 20$ GeV. At the bottom of the energy range, neutrinos never stop oscillating. We can consider as a minimum value, the energy at which the solar mass splitting ($\sim 10^{-5}\text{eV}^2$) produce a complete oscillation for horizontal neutrinos ($\cos\theta_z = 0$) inside the atmosphere is $E_\nu \approx 0.05$ GeV.

[4]Most of the neutrinos are produced at an altitude of 20-10 km [15]. In order to properly treat with the neutrino production at different altitudes, we have to average the oscillation probability along the atmosphere weighted by an altitude distribution function normalized to one. Due to the small size of the atmosphere compared with the Earth, we have fixed its size to an intermediate value of 15 km.

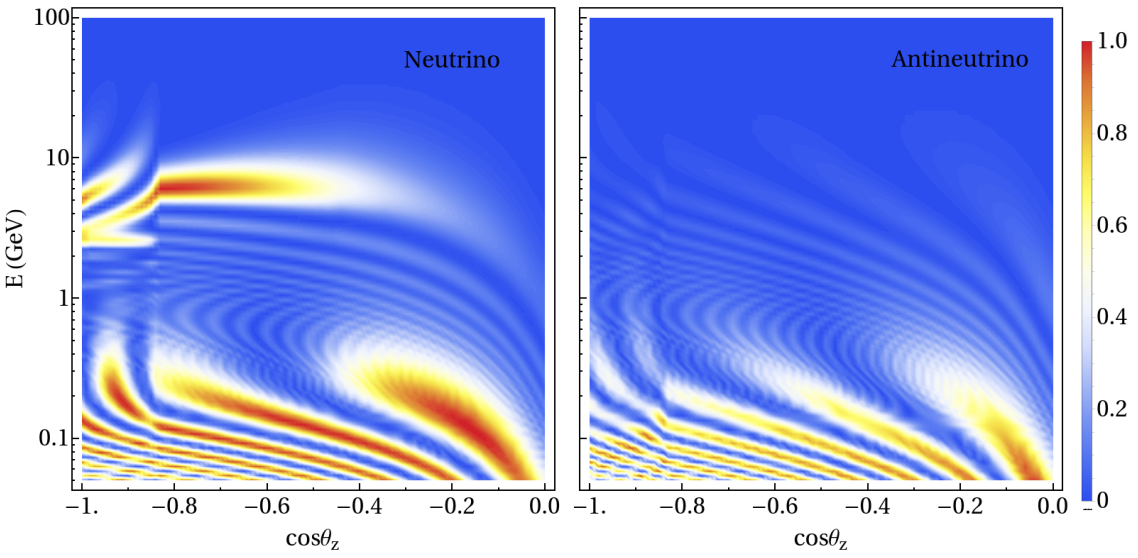

Figure 1.8: $1-P_{ee}$ for atmospheric neutrinos (left) and antineutrinos (right) crossing the Earth.

The neutrino evolution inside the Earth is obtained by solving Eq (1.54) for PREM, Fig 1.7. $1-P_{ee}$ shows two separate regions that correspond to trajectories that cross the Earth core ($cos\theta_z < -0.83$), or trajectories developed just in the mantle. In a 3ν mixing, there are two oscillations wavelengths that compete at different energy scales. For the 1-3 mixing, the MSW resonance is driven by the atmospheric mass parameter ($\Delta m^2_{31} = 2.494\times10^{-3}\text{eV}^2$ NH or $\Delta m^2_{32} = -2.465\times10^{-3}\text{eV}^2$ IH) [22]. A constant density approximation can be used to describe the evolution of trajectories that only cross the mantle [23, 24]. In this case, the resonance condition can be written as

$$2\overline{V_{CC}}E^R_\nu = |\Delta m^2_{3l}|\cos 2\theta_{13} \tag{1.70}$$

where $\overline{V_{CC}}$ is the averaged CC potential along the neutrino path. This expression determines the values of the energy where oscillation amplitude is maximal as a function of the trajectory $E^R_\nu(\theta_z)$. In addition, to get a maximum in the oscillation probability ($1-P_{ee} \simeq 1$), it is needed that the oscillation phase should be proportional to $\pi/2$. From Eq (1.58) we get

$$\frac{(\lambda_3-\lambda_1)L}{4E} = (2k+1)\frac{\pi}{2} \qquad k\in\mathbb{N} \tag{1.71}$$

For an average density of the mantle about $\rho\sim(4-5)\text{g/cm}^3$, both conditions meet at $E^R_\nu \sim 6$ GeV and $\cos\theta_z \sim -0.8$. There is only one point where both conditions meet because of the oscillation length at the resonance, given by

$$L^{\text{OSC}}_R = \frac{L^{\text{OSC}}}{\sin 2\theta_{13}} \tag{1.72}$$

where L^{OSC} is the oscillation vacuum length, which is of the order of the Earth radius. Due to the small value of $\theta_{13} \sim 8.5$ [22], L^{OSC}_R is much longer than Earth size.

For the 1-2 mixing, the resonant amplitude depends on the solar mass parameter, $\Delta m^2_{21} = 7.4\times10^{-5}\text{eV}^2$ [22]. Using the approximation of constant density

matter for the mantle, the resonant energy is about $E_\nu^R \sim 0.1$ GeV. Around that value, there are three directions where there is a total flavor conversion, $\cos\theta_z = \{-0.75, -0.49, -0.15\}$. For the solar mass parameter, the vacuum oscillation length is about half of the Earth radius, so at the resonance $L_R^{\rm OSC} \sim R_\oplus/4$. The neutrino baseline through the Earth can be approximated as $L \simeq 2R_\oplus|\cos\theta_z|$. We can compute the phase ($\phi = \Delta m^2_{21} \sin 2\theta_{21} L/4E$) for the three directions where the maximum transition is obtained, finding

$$\phi(\cos\theta_z = -0.75) \approx 5\pi/2$$
$$\phi(\cos\theta_z = -0.49) \approx 3\pi/2$$
$$\phi(\cos\theta_z = -0.15) \approx \pi/2$$

The three directions corresponding to the first three odd multiples of $\pi/2$. There is another maximum transition point around $\cos\theta_z \simeq -0.92$ and $E_\nu \simeq 0.2$ GeV. That direction crosses the Earth core, so the evolution cannot be described by the constant matter approximation. In spite of that, the resonant energy for the core should be smaller than in mantle since the matter potential is higher in the core. For that reason, a maximum transition point at the core with $E_\nu > 0.1$ GeV cannot be explained as coincident between the resonant amplitude and phase conditions. Instead, this total flavor conversion can be explained by a parametric enhancement of the oscillations [24].

In Fig 1.8 we have used a normal mass ordering, since the best fit points towards that mass distribution, although with small preference over invert hierarchy [22]. Since the mass splittings and the matter potential for antineutrinos have opposite signs, it is not possible to get a resonant amplitude for them. We can repeat the simulation for IH, and we will get the opposite situation, the maximum flavor conversion will take place for antineutrinos. For IH, we can repeat the same discussion as before, but in this case for antineutrinos.

1.6.3 IceCube DeepCore experiment

IceCube is neutrino cherenkov telescope located at the South Pole, whose primary scientific objective is the discovery of astrophysical neutrinos, which was realized in 2013 [25]. The astrophysical flux measured is in the energy range of $\sim$ 30 TeV to PeV, Fig. 1.9. For lower energies, the neutrino flux arriving at the detector is dominated by atmospheric neutrinos. At sufficient low energies, the atmospheric flux can be measured for an L/E ratio relevant for the flavor oscillations, opening the possibility to study this phenomenon for high energy atmospheric neutrinos. Before this experiment, SK was the only statistically significant detector able to measure oscillations through the Earth.

The small neutrino cross section and the expected low flux for astrophysical neutrinos require a detector with a large target mass. IceCube consists of 5160 photomultipliers, called DOMs (Digital Optical Module) distributed over a volume of almost a cubic kilometer below the Antartica surface, which is equivalent to a mass of $\sim$ 1000 MTon. The DOMs are arranged in 86 strings distributed along a hexagonal pattern [27]. Each string contains 60 DOMs and, 78 of them are instrumented from a depth of $\sim$ 1450 km to $\sim$ 2450 km, with a vertical spacing of 17 m between DOM, and a horizontal distance of 125 m to the nearest string. The remaining eight strings are also formed by 60 photomultipliers with 35% higher efficiency. Six of the last

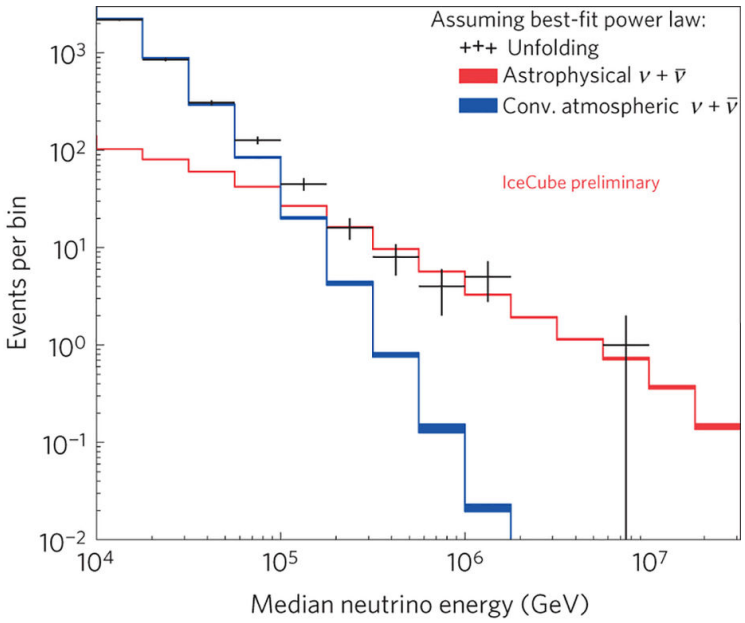

Figure 1.9: Muon event distribution as a function of neutrino energy deposit inside the detector [26]. The neutrino energy is infered by performing of the best-fit of its spectrum. The blue (red) bands correspond to the atmospheric (astrophysical) constribution.

eight strings form a hexagonal distribution surrounding the central IceCube string, with an average horizontal distance of 70 m between them. The remaining two strings are located inside the inner hexagon, with an average horizontal distance of 42 m between them and to the nearest neighbor. The vertical distance between DOMs for this 8 strings is 7 m for the deepest 50 DOMs. Then, there is a gap of 350 m due to a dust layer in the ice, and the remaining 10 DOMs are separated 10 m. To the denser array of DOMs formed by the eight strings with a small DOMs separation, the six that surround them and the central one, is called DeepCore. At the Antartica surface, there is an array of ice filled tanks (IceTop), each of them with two DOMs, that detect cosmic rays by observing the air showers created in its collision with the atmosphere. The layout of IceCube is in Fig 1.10.

The optical properties of the ice affect the trajectories of the photons emitted in the cherenkov radiation ($o(10^5)$ per GeV). By interacting with the ice, the photons can be absorbed or its trajectory can be deviated. In the clearest ice, the transparency of the Antartica ice cap allows an attenuation length larger than the DOMs separation [28]. The refreezed water, that filled the hole containing the DOMs, has optical properties rather different from those of the bulk ice. The new ice induces an additional scattering over the photon propagation due to the high concentration of air bubbles [29].

How does the detector work?

IceCube is an ice cherenkov detector. The charged particles, that move faster than the speed of light in the ice, emits photons with a wavelength in the optical range, [300 - 500]nm (cherenkov radiation). The detector performance is based in the detection of such radiation, together with its arrival time and its location. In order to reduce the noise, once a DOM detect the radiation, it communicates with its nearest and next-to-nearest DOMs to determine if the signal has been also seen by the others, in a time window of $1\mu s$. If two or more DOMs fulfill the criteria, the

event is called Hard Local Coincidence (HLC).

The fundamental trigger used by IceCube is based on the number of DOMs satisfying HLC condition. For IceCube is required at least 8 DOMs within a $5\mu s$ time window, that is called SMT8. For DeepCore are needed at least 3 DOMs in a 2.5μs window (SMT3) [28]. Additional triggers with lower multiplicity can be defined for subsets of DOMs in order to identify specific signals. After the trigger condition is fulfilled the information in the whole detector is saved, and in order to reduce the background are applied different filters.

ν oscillation in IceCube DeepCore

The IceCube geometry determines the energy range at which the atmospheric neutrino flux can be measured, and the event topology used to distinguish between different neutrino flavors. The events at IceCube comes from the neutrino interaction with the nucleons in the ice, and the signals left at the detector depends on the interaction final state. The two main event topologies that can be detected in IceCube are, "tracks" and "cascades". The tracks are produced by the cherenkov radiation in the muon propagation. The cascades, which shows a spherical light pattern inside the detector, are created by the hadronic showers of CC and NC, by the electrons that lose their energy quickly into electromagnetic showers, and by tau decaying into electrons and hadrons. This topology is also called "bang". The only interaction that can be identified in IceCube for low energy atmospheric neutrinos is the ν_μ CC, which leaves a signal in the detector consisting of a track and a cascade [29]. For ν_e CC, due to the quick loss of energy by the electron, the detector cannot to distinguish between the two cascades at the final state. The same

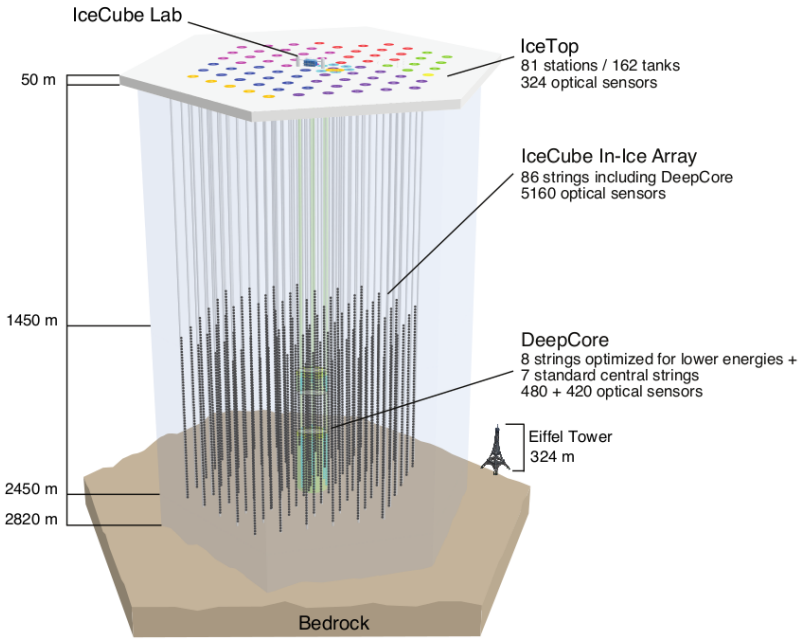

Figure 1.10: IceCube layout [27]. IceCube consist of 5160 DOMs distributed in 86 strings that form a hexagonal pattern. The DOMs are deployed from a depth of 1450 m to 2450 m. At the inner part of the detector, there is a denser array of photomultipliers called DeepCore. Over the Antartica surface, there is an array of ice filled tanks, each of them contains two DOMs.

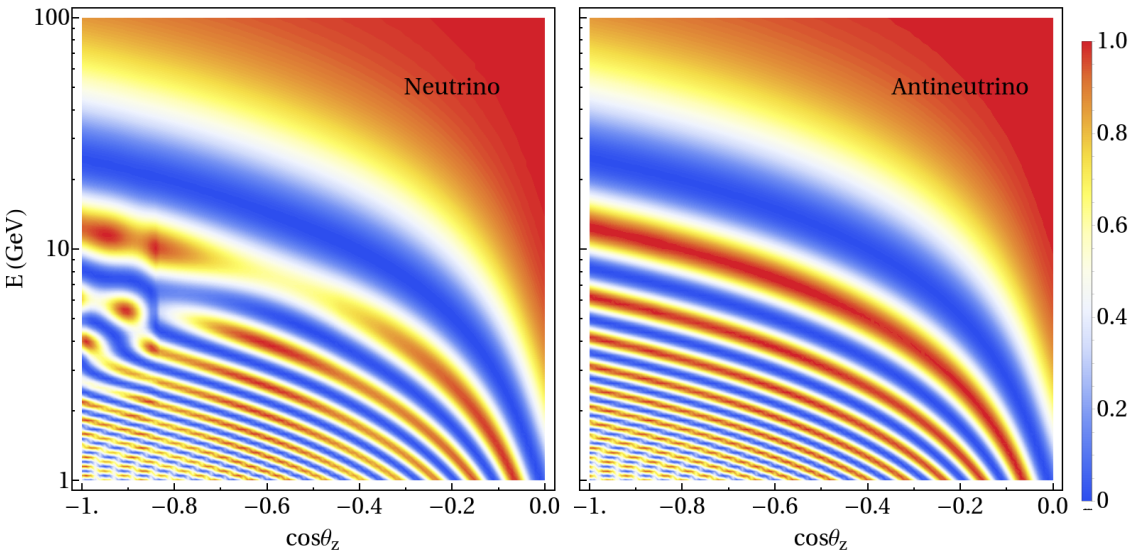

Figure 1.11: $P_{\mu\mu}$ for atmospheric neutrinos (left) and antineutrinos (right) crossing the Earth. The value used for the oscillation parameter has been taken from the best-fit point of the global fit [22]

happens for ν_τ CC at low energies due to the small lifetime of the tau lepton. As the energy of ν_τ increase, the tau is boosted and the two cascades can be separated. As an example, for $E_{\nu_\tau} \sim$ PeV the distance between the showers is ~ 100 m. The NC interaction is independent of the initial flavor, and the signal is only a cascade.

For atmospheric muon neutrinos that cross the whole Earth ($\cos\theta_z = -1$), the maximum energy at which the total flavor conversion happen ($P_{\mu\mu} = 0$) is $E_{\nu_\mu} \sim 23$ GeV, Fig 1.11. Muons with energies lower than 100 GeV lose their energy by ionization [10], and for energies lower than its critical energy ($E_{\mu c} \sim 600$ GeV), the distance traveled before its decay can be approximated as $R_\mu(E) \approx E/(\rho a)$ where $a \approx 2\text{MeV cm}^2/g$ is the electronic stopping power and $\rho \approx 1\text{g/cm}^3$ is the ice density. The distance traveled by the muons before its decay can be approximated by 5m/GeV. The DOM separation and the trigger conditions make DeepCore the only place in IceCube where the flavor oscillation can be measured.

DeepCore is able to measure muon neutrinos and antineutrinos with energies above 5 GeV [30]. Above that energy, the flavor oscillation is driven by the atmospheric mass parameter (Δm^2_{3l}). From 3 GeV to 12 GeV, the matter effects modify the flavor oscillation probability with respect to the vacuum case for neutrinos (antineutrinos) and normal (inverted) mass hierarchy, Fig 1.11. The main background to this signal comes from atmospheric muons that reach to the detector from above.

Chapter2

Fit to three neutrino mixing

Beside a few examples where the events measured can only be explained by a mass parameter much larger than the atmospheric mass splitting [31], the results of the neutrino oscillation experiments can be explained within a 3 neutrino mixing flavor [32]. In this model, the flavor oscillation depends on two mass splittings, the solar ($\Delta m^2_{SOL} \sim 10^{-5}\text{eV}^2$) and the atmospheric mass ($|\Delta m^2_{ATM}| \sim 10^{-3}\text{eV}^2$), three angles ($\theta_{12}$, θ_{13}, θ_{23}), and a complex phase (δ_{CP}). After several years of data taking, the least known among those parameters are the sign of Δm^2_{ATM}, which determine the neutrino mass ordering (Fig 1.4), the octant of θ_{23} and the complex phase δ_{CP}. About the mass ordering, the change of sign induces a detectable effect for matter experiments by comparing the oscillation probability for neutrinos and antineutrinos in the appearance channel, where the actual sensitivity comes from. There is a statistical preference is for NO with a significance of 2σ [22] over IH. θ_{23} can be maximal ($\theta_{23} = 45$), or can be in the first octant ($\theta_{23} < 45$) or in the second octant ($\theta_{23} > 45$). The muon disappearance channel ($P_{\mu\mu}$) can disentangle between maximal or not maximal mixing. To resolve between the octants, only matter experiments measuring in the apperance channel can do it. The recent results indicate a preference for values in the second octant, the best fit is close to 45 [22]. For δ_{CP}, the sensitivity comes from the comparison between the neutrino and antineutrino oscillations probabilities in the appearance channel. The current results exclude an interval of 60° around $\delta_{CP} \simeq 90$ to more than 3σ [22], for both mass ordering.

The sensitivity of the present data to the six parameters that describe the model can only be obtained by a global fit, where all the experiment are included. Neutrino flavor oscillations have been observed in a wide variety of experiments which include different energy neutrino beams, different initial and final flavors, and different baselines. Those characteristics determine the contribution of every experiment into the global fit (Tab 2.1).

Experiment	Dominant	Important
Solar Experiments	θ_{12}	Δm^2_{21} and θ_{13}
Reactor LBL (KamLAND)	Δm^2_{21}	θ_{12} and θ_{13}
Reactor MBL (Daya-Bay, Reno, Double-Chooz)	θ_{13}	$\lvert\Delta m^2_{3l}\rvert$
Atmospheric Experiments	θ_{23}	$\lvert\Delta m^2_{3l}\rvert$, θ_{13} and δ_{CP}
Accelerator LBL ν_μ Disapp (Minos, NOνA,T2K)	$\lvert\Delta m^2_{3l}\rvert$ and θ_{23}	
Accelerator LBL ν_e App (Minos, NOνA,T2K)	δ_{CP}	θ_{23} θ_{13}, sign(Δm^2_{3l})

Table 2.1: Experiment contribution to the oscillation parameter determination

JHEP

Published for SISSA by Springer

Received: November 16, 2016
Revised: January 3, 2017
Accepted: January 14, 2017
Published: January 20, 2017

Updated fit to three neutrino mixing: exploring the accelerator-reactor complementarity

Ivan Esteban,[a] **M.C. Gonzalez-Garcia,**[a,b,c] **Michele Maltoni,**[d] **Ivan Martinez-Soler**[d] **and Thomas Schwetz**[e]

[a] *Departament de Fisíca Quàntica i Astrofísica and Institut de Ciencies del Cosmos, Universitat de Barcelona, Diagonal 647, E-08028 Barcelona, Spain*

[b] *Institució Catalana de Recerca i Estudis Avançats (ICREA), Pg. Lluis Companys 23, 08010 Barcelona, Spain*

[c] *C.N. Yang Institute for Theoretical Physics, State University of New York at Stony Brook, Stony Brook, NY 11794-3840, U.S.A.*

[d] *Instituto de Física Teórica UAM/CSIC, Universidad Autónoma de Madrid, Calle de Nicolás Cabrera 13–15, Cantoblanco, E-28049 Madrid, Spain*

[e] *Institut für Kernphysik, Karlsruher Institut für Technologie (KIT), D-76021 Karlsruhe, Germany*

E-mail: ivan.esteban@fqa.ub.edu, maria.gonzalez-garcia@stonybrook.edu, michele.maltoni@csic.es, ivanj.m@csic.es, schwetz@kit.edu

Abstract: We perform a combined fit to global neutrino oscillation data available as of fall 2016 in the scenario of three-neutrino oscillations and present updated allowed ranges of the six oscillation parameters. We discuss the differences arising between the consistent combination of the data samples from accelerator and reactor experiments compared to partial combinations. We quantify the confidence in the determination of the less precisely known parameters θ_{23}, $\delta_{\rm CP}$, and the neutrino mass ordering by performing a Monte Carlo study of the long baseline accelerator and reactor data. We find that the sensitivity to the mass ordering and the θ_{23} octant is below 1σ. Maximal θ_{23} mixing is allowed at slightly more than 90% CL. The best fit for the CP violating phase is around 270°, CP conservation is allowed at slightly above 1σ, and values of $\delta_{\rm CP} \simeq 90°$ are disfavored at around 99% CL for normal ordering and higher CL for inverted ordering.

Keywords: Neutrino Physics, Solar and Atmospheric Neutrinos

ArXiv ePrint: 1611.01514

Open Access, © The Authors.
Article funded by SCOAP[3].

doi:10.1007/JHEP01(2017)087

JHEP01(2017)087

Contents

1 Introduction

Experiments measuring the flavor composition of solar neutrinos, atmospheric neutrinos, neutrinos produced in nuclear reactors and in accelerators have established that lepton flavor is not conserved in neutrino propagation, but it oscillates with a wavelength depending on distance and energy, because neutrinos are massive and the mass states are admixtures of the flavor states [1, 2], see ref. [3] for an overview.

With the exception of a set of unconfirmed "hints" of possible eV scale mass states (see ref. [4] for a recent review), all the oscillation signatures can be explained with the three flavor neutrinos (ν_e, ν_μ, ν_τ), which can be expressed as quantum superpositions of three massive states ν_i ($i = 1, 2, 3$) with masses m_i. This implies the presence of a leptonic mixing matrix in the weak charged current interactions [5, 6] which can be parametrized as:

$$U = \begin{pmatrix} 1 & 0 & 0 \\ 0 & c_{23} & s_{23} \\ 0 & -s_{23} & c_{23} \end{pmatrix} \cdot \begin{pmatrix} c_{13} & 0 & s_{13}e^{-i\delta_{\rm CP}} \\ 0 & 1 & 0 \\ -s_{13}e^{i\delta_{\rm CP}} & 0 & c_{13} \end{pmatrix} \cdot \begin{pmatrix} c_{12} & s_{12} & 0 \\ -s_{12} & c_{12} & 0 \\ 0 & 0 & 1 \end{pmatrix} \cdot \mathcal{P} \qquad (1.1)$$

where $c_{ij} \equiv \cos\theta_{ij}$ and $s_{ij} \equiv \sin\theta_{ij}$. The angles θ_{ij} can be taken without loss of generality to lie in the first quadrant, $\theta_{ij} \in [0, \pi/2]$, and the phase $\delta_{\rm CP} \in [0, 2\pi]$. Here $\mathcal{P}$ is a diagonal

JHEP01(2017)087

matrix which is the identity if neutrinos are Dirac fermions and it contains two additional phases if they are Majorana fermions, and plays no role in neutrino oscillations [7, 8]. In this convention there are two non-equivalent orderings for the neutrino masses which can be chosen to be: normal ordering (NO) with $m_1 < m_2 < m_3$, and inverted ordering (IO) with $m_3 < m_1 < m_2$. Furthermore the data shows a relatively large hierarchy between the mass splittings, $\Delta m^2_{21} \ll |\Delta m^2_{31}| \simeq |\Delta m^2_{32}|$ with $\Delta m^2_{ij} \equiv m^2_i - m^2_j$. In this work we follow the convention introduced in ref. [9] and present our results in terms of the variable $\Delta m^2_{3\ell}$, with $\ell = 1$ for NO and $\ell = 2$ for IO. Hence, $\Delta m^2_{3\ell} = \Delta m^2_{31} > 0$ for NO and $\Delta m^2_{3\ell} = \Delta m^2_{32} < 0$ for IO, i.e., it corresponds to the mass splitting with the largest absolute value.

In this article, we present an up-to-date (as of fall 2016) global analysis of neutrino data in the framework of three-neutrino oscillations. Alternative recent global fits have been presented in refs. [10, 11]. With current data from the accelerator long-baseline experiments MINOS, T2K, NOνA and modern reactor experiments like Daya-Bay, RENO, and Double-Chooz, their complementarity anticipated more than a decade ago [12–14] has become a reality, and the combined analysis starts to show some sensitivity to subtle effects like the θ_{23} octant or the $\delta_{\rm CP}$ phase (though still at low statistical significance).

The outline of the paper is as follows: in section 2.1 we describe the data samples included in our analysis (see also appendix A for a schematic list). The presently allowed ranges of the six oscillation parameters are given in section 2.2 assuming that $\Delta\chi^2$ follows a χ^2-distribution, while section 2.3 contains the corresponding measures of CP violation in terms of the leptonic Jarlskog invariant and the leptonic unitarity triangle. Deviations from the Gaussian approximation of the confidence intervals for θ_{23} and $\delta_{\rm CP}$ and the confidence level for the mass ordering determination are quantified in section 4. Several issues appearing in the present analysis are discussed in section 3, in particular about the consistent combination of results from long baseline accelerator experiments with reactors results, now that both provide comparable precision in the determination of the relevant mass-squared difference. We also give the updated status on the ongoing tension in the Δm^2_{21} determination from solar experiments versus KamLAND, and comment on the stand-by in the analysis of the Super-Kamiokande atmospheric data. Section 5 contains the summary of our results.

2 Global analysis: determination of oscillation parameters

2.1 Data samples analyzed

In the analysis of solar neutrino data we consider the total rates from the radiochemical experiments Chlorine [15], Gallex/GNO [16] and SAGE [17], the results for the four phases of Super-Kamiokande [18–22], the data of the three phases of SNO included in the form of the parametrization presented in [23], and the results of both Phase-I and Phase-II of Borexino [24–26].

Results from long baseline (LBL) accelerator experiments include the final energy distribution of events from MINOS [27, 28] in ν_μ and $\bar\nu_\mu$ disappearance and ν_e and $\bar\nu_e$ appearance channels, as well as the latest energy spectrum for T2K in the same four channels [29, 30] and for NOνA on the ν_μ disappearance and ν_e appearance neutrino modes [31].

JHEP01(2017)087

Data samples on $\bar{\nu}_e$ disappearance from reactor include the full results of the long baseline reactor data in KamLAND [32], as well as the results from medium baseline reactor experiments from CHOOZ [33] and Palo Verde [34]. Concerning running experiments we include the latest spectral data from Double-Chooz [35] and Daya-Bay [36], while for RENO we use the total rates obtained with their largest data sample corresponding to 800 days of data-taking [37].

In the analysis of the reactor data, the unoscillated reactor flux is determined as described in [38] by including in the fit the results from short baseline reactor data (RSBL) from ILL [39], Gösgen [40], Krasnoyarsk [41, 42], ROVNO88 [43], ROVNO4 [44], Bugey3 [45], Bugey4 [46], and SRP [47].

For the analysis of atmospheric neutrinos we include the results from IceCube/DeepCore 3-year data [48].

The above data sets constitute the samples included in our NuFIT 3.0 analysis. For Super-Kamiokande atmospheric neutrino data from phases SK1–4 we will comment on our strategy in section 3.3. A full list of experiments including the counting of data points in each sample can be found in appendix A.

2.2 Results: oscillation parameters

The results of our standard analysis are presented in figures 1 and 2 where we show projections of the allowed six-dimensional parameter space.[1] In all cases when including reactor experiments we leave the normalization of reactor fluxes free and include data from short-baseline (less than 100 m) reactor experiments. In our previous analysis [9, 50] we studied the impact of this choice versus that of fixing the reactor fluxes to the prediction of the latest calculations [51–53]. As expected, the overall description is better when the flux normalization f_{flux} is fitted against the data. We find $\chi^2(f_{\text{flux}}\ \text{fix}) - \chi^2(f_{\text{flux}}\ \text{fit}) \simeq 6$ which is just another way to quantify the well-known short baseline reactor anomaly to be $\sim 2.5\sigma$. However, the difference in the resulting parameter determination (in particular for θ_{13}) between these two reactor flux normalization choices has become marginal, since data from the reactor experiments with near detectors such as Daya-Bay, RENO and Double-Chooz (for which the near-far comparison allows for flux-normalization independent analysis) is now dominant. Consequently, in what follows we show only the $\Delta\chi^2$ projections for our standard choice with fitted reactor flux normalization.

The best fit values and the derived ranges for the six parameters at the 1σ (3σ) level are given in table 1. For each parameter x the ranges are obtained after marginalizing with respect to the other parameters[2] and under the assumption that $\Delta\chi^2_{\text{marg}}(x)$ follows a χ^2 distribution. Hence the 1σ (3σ) ranges are given by the condition $\Delta\chi^2_{\text{marg}}(x) = 1$ (9). It is known that because of its periodic nature and the presence of parameter degeneracies the statistical distribution of the marginalized $\Delta\chi^2$ for δ_{CP} and θ_{23} (and consequently the

[1] $\Delta\chi^2$ tables from the global analysis corresponding to all 1-dimensional and 2-dimensional projections are available for download at the NuFIT website [49].

[2] In this paper we use the term "marginalization" over a given parameter as synonym for minimizing the χ^2 function with respect to that parameter.

JHEP01(2017)087

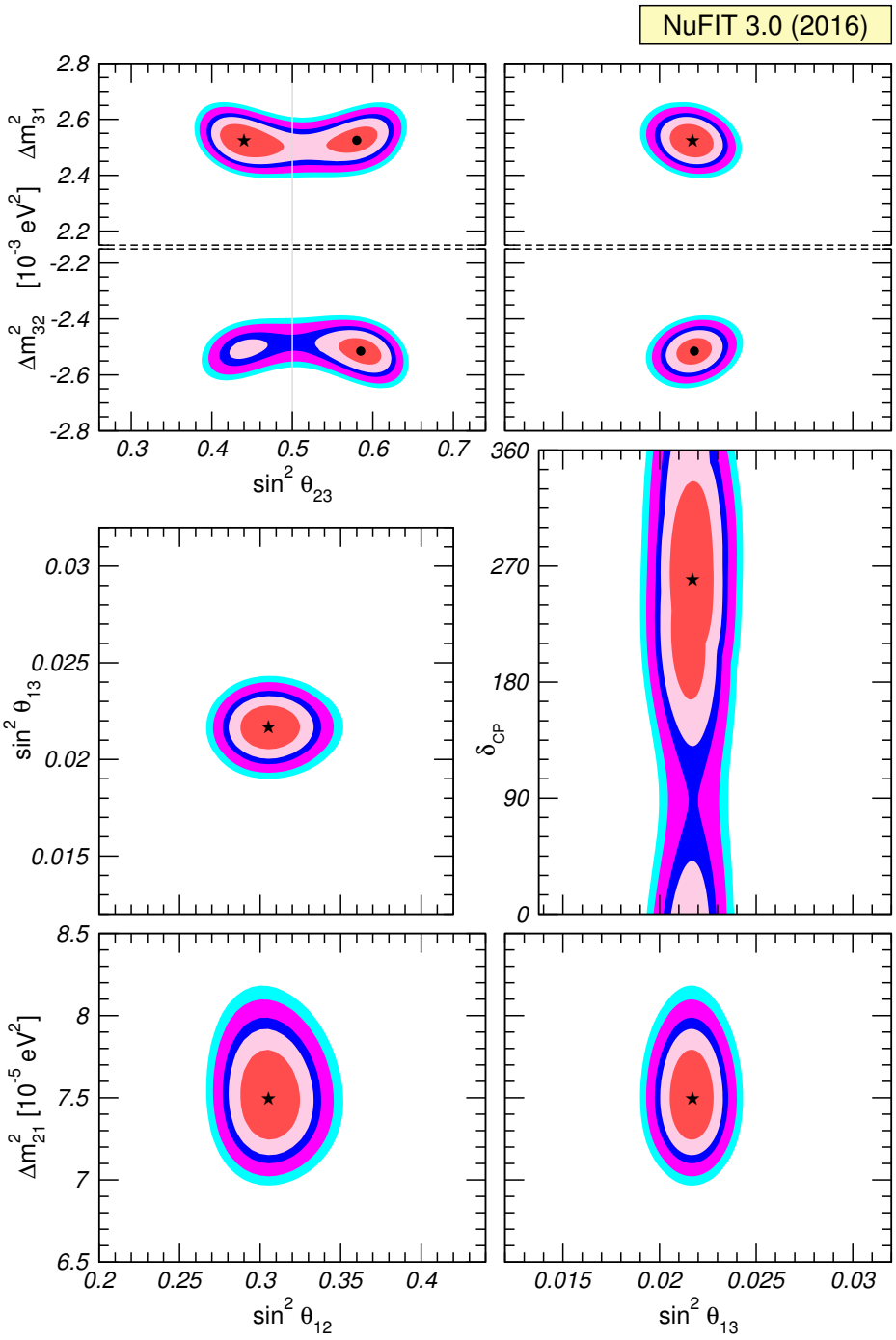

Figure 1. Global 3ν oscillation analysis. Each panel shows the two-dimensional projection of the allowed six-dimensional region after marginalization with respect to the undisplayed parameters. The different contours correspond to 1σ, 90%, 2σ, 99%, 3σ CL (2 dof). The normalization of reactor fluxes is left free and data from short-baseline reactor experiments are included as explained in the text. Note that as atmospheric mass-squared splitting we use Δm^2_{31} for NO and Δm^2_{32} for IO. The regions in the four lower panels are obtained from $\Delta\chi^2$ minimized with respect to the mass ordering.

JHEP01(2017)087

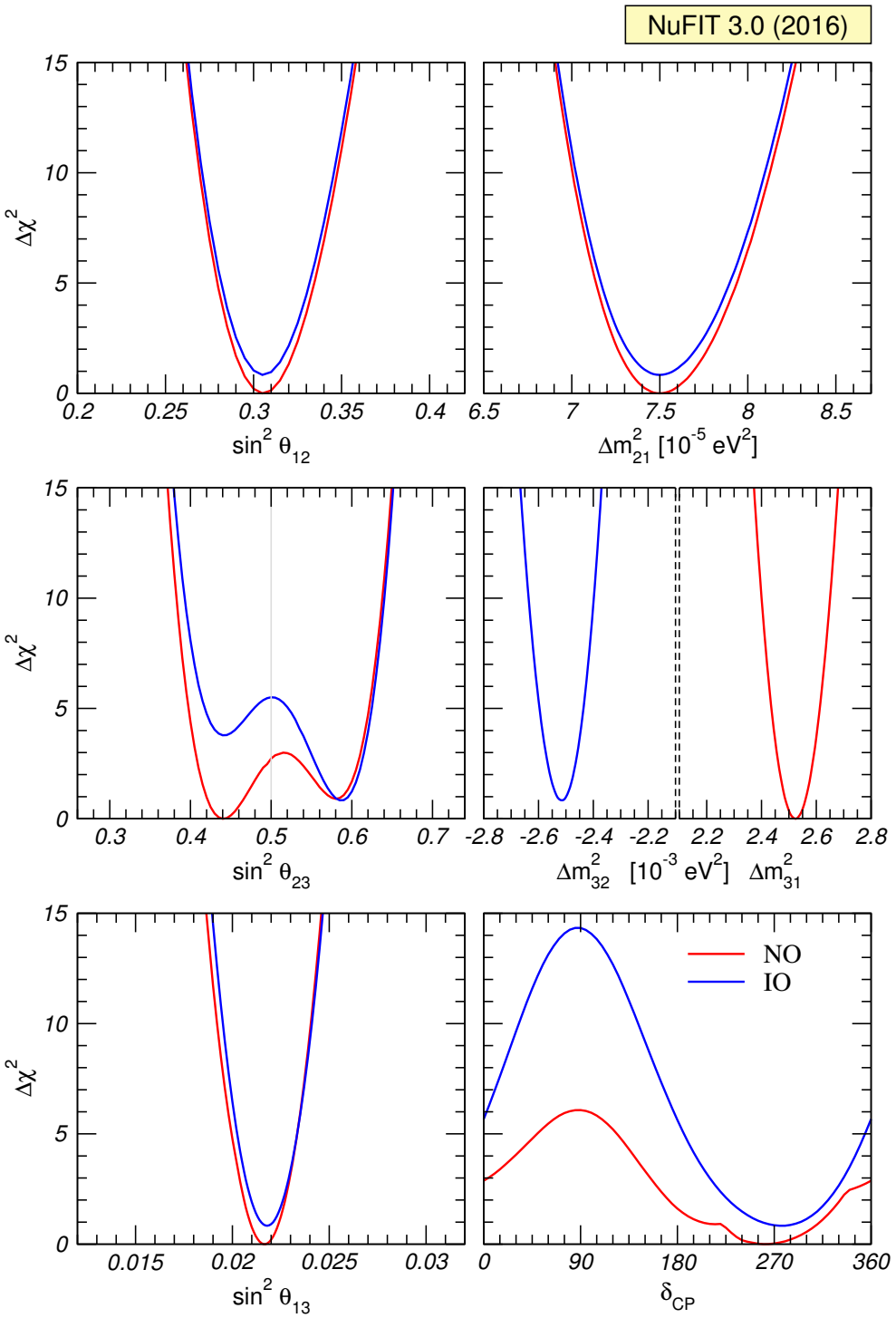

Figure 2. Global 3ν oscillation analysis. The red (blue) curves correspond to Normal (Inverted) Ordering. The normalization of reactor fluxes is left free and data from short-baseline reactor experiments are included. Note that as atmospheric mass-squared splitting we use Δm^2_{31} for NO and Δm^2_{32} for IO.

JHEP01(2017)087

	Normal Ordering (best fit)		Inverted Ordering ($\Delta\chi^2 = 0.83$)		Any Ordering
	bfp $\pm 1\sigma$	3σ range	bfp $\pm 1\sigma$	3σ range	3σ range
$\sin^2\theta_{12}$	$0.306^{+0.012}_{-0.012}$	$0.271 \to 0.345$	$0.306^{+0.012}_{-0.012}$	$0.271 \to 0.345$	$0.271 \to 0.345$
$\theta_{12}/^\circ$	$33.56^{+0.77}_{-0.75}$	$31.38 \to 35.99$	$33.56^{+0.77}_{-0.75}$	$31.38 \to 35.99$	$31.38 \to 35.99$
$\sin^2\theta_{23}$	$0.441^{+0.027}_{-0.021}$	$0.385 \to 0.635$	$0.587^{+0.020}_{-0.024}$	$0.393 \to 0.640$	$0.385 \to 0.638$
$\theta_{23}/^\circ$	$41.6^{+1.5}_{-1.2}$	$38.4 \to 52.8$	$50.0^{+1.1}_{-1.4}$	$38.8 \to 53.1$	$38.4 \to 53.0$
$\sin^2\theta_{13}$	$0.02166^{+0.00075}_{-0.00075}$	$0.01934 \to 0.02392$	$0.02179^{+0.00076}_{-0.00076}$	$0.01953 \to 0.02408$	$0.01934 \to 0.02397$
$\theta_{13}/^\circ$	$8.46^{+0.15}_{-0.15}$	$7.99 \to 8.90$	$8.49^{+0.15}_{-0.15}$	$8.03 \to 8.93$	$7.99 \to 8.91$
$\delta_{\rm CP}/^\circ$	261^{+51}_{-59}	$0 \to 360$	277^{+40}_{-46}	$145 \to 391$	$0 \to 360$
$\frac{\Delta m^2_{21}}{10^{-5}\ \text{eV}^2}$	$7.50^{+0.19}_{-0.17}$	$7.03 \to 8.09$	$7.50^{+0.19}_{-0.17}$	$7.03 \to 8.09$	$7.03 \to 8.09$
$\frac{\Delta m^2_{3\ell}}{10^{-3}\ \text{eV}^2}$	$+2.524^{+0.039}_{-0.040}$	$+2.407 \to +2.643$	$-2.514^{+0.038}_{-0.041}$	$-2.635 \to -2.399$	$\begin{bmatrix} +2.407 \to +2.643 \\ -2.629 \to -2.405 \end{bmatrix}$

Table 1. Three-flavor oscillation parameters from our fit to global data after the NOW 2016 and ICHEP-2016 conference. The numbers in the 1st (2nd) column are obtained assuming NO (IO), i.e., relative to the respective local minimum, whereas in the 3rd column we minimize also with respect to the ordering. Note that $\Delta m^2_{3\ell} \equiv \Delta m^2_{31} > 0$ for NO and $\Delta m^2_{3\ell} \equiv \Delta m^2_{32} < 0$ for IO.

corresponding CL intervals) may be modified [54, 55]. In section 4 we will discuss and quantify these effects.

In table 1 we list the results for three scenarios. In the first and second columns we assume that the ordering of the neutrino mass states is known *a priori* to be Normal or Inverted, respectively, so the ranges of all parameters are defined with respect to the minimum in the given scenario. In the third column we make no assumptions on the ordering, so in this case the ranges of the parameters are defined with respect to the global minimum (which corresponds to Normal Ordering) and are obtained marginalizing also over the ordering. For this third case we only give the 3σ ranges. In this case the range of $\Delta m^2_{3\ell}$ is composed of two disconnected intervals, one containing the absolute minimum (NO) and the other the secondary local minimum (IO).

Defining the 3σ relative precision of a parameter by $2(x^{\rm up} - x^{\rm low})/(x^{\rm up} + x^{\rm low})$, where $x^{\rm up}$ ($x^{\rm low}$) is the upper (lower) bound on a parameter x at the 3σ level, we read 3σ relative precision of 14% (θ_{12}), 32% (θ_{23}), 11% (θ_{13}), 14% (Δm^2_{21}) and 9% ($|\Delta m^2_{3\ell}|$) for the various oscillation parameters.

2.3 Results: leptonic mixing matrix and CP violation

From the global χ^2 analysis described in the previous section and following the procedure outlined in ref. [56] one can derive the 3σ ranges on the magnitude of the elements of the

JHEP01(2017)087

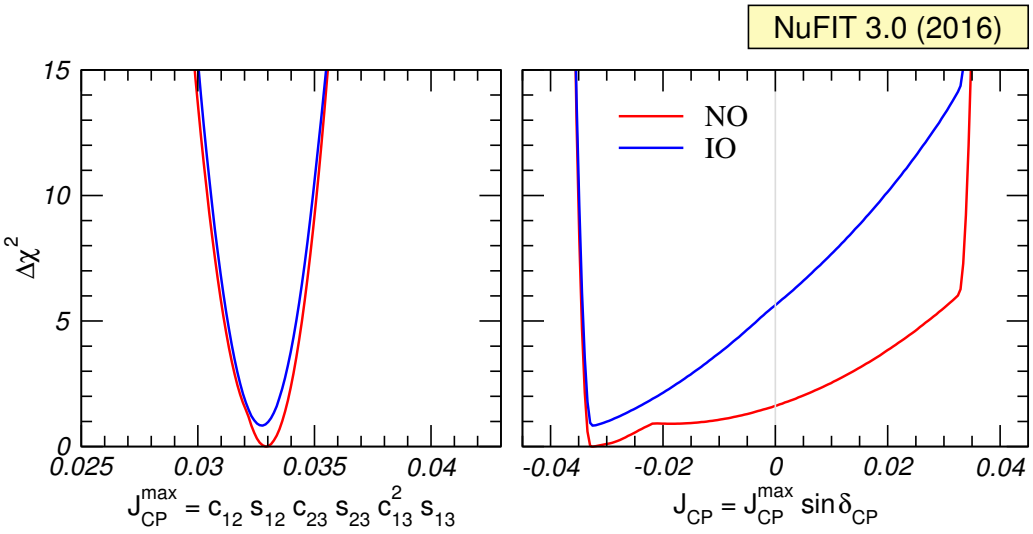

Figure 3. Dependence of the global $\Delta\chi^2$ function on the Jarlskog invariant. The red (blue) curves are for NO (IO).

leptonic mixing matrix:

$$|U| = \begin{pmatrix} 0.800 \to 0.844 & 0.515 \to 0.581 & 0.139 \to 0.155 \\ 0.229 \to 0.516 & 0.438 \to 0.699 & 0.614 \to 0.790 \\ 0.249 \to 0.528 & 0.462 \to 0.715 & 0.595 \to 0.776 \end{pmatrix}. \tag{2.1}$$

Note that there are strong correlations between the elements due to the unitary constraint.

The present status of the determination of leptonic CP violation is illustrated in figure 3. In the left panel we show the dependence of $\Delta\chi^2$ of the global analysis on the Jarlskog invariant which gives a convention-independent measure of CP violation [57], defined as usual by:

$$\mathrm{Im}\left[U_{\alpha i} U^*_{\alpha j} U^*_{\beta i} U_{\beta j}\right] \equiv J_{\mathrm{CP}}^{\mathrm{max}} \sin\delta = \cos\theta_{12}\sin\theta_{12}\cos\theta_{23}\sin\theta_{23}\cos^2\theta_{13}\sin\theta_{13}\sin\delta \tag{2.2}$$

where we have used the parametrization in eq. (1.1). Thus the determination of the mixing angles yields at present a maximum allowed CP violation

$$J_{\mathrm{CP}}^{\mathrm{max}} = 0.0329 \pm 0.0007\,(^{+0.0021}_{-0.0024}) \tag{2.3}$$

at 1σ (3σ) for both orderings. The preference of the present data for non-zero δ_{CP} implies a best fit value $J_{\mathrm{CP}}^{\mathrm{best}} = -0.033$, which is favored over CP conservation with $\Delta\chi^2 = 1.7$. These numbers can be compared with the size of the Jarlskog invariant in the quark sector, which is determined to be $J_{\mathrm{CP}}^{\mathrm{quarks}} = (3.04^{+0.21}_{-0.20}) \times 10^{-5}$ [58].

In figure 4 we recast the allowed regions for the leptonic mixing matrix in terms of one leptonic unitarity triangle. Since in the analysis U is unitary by construction, any given pair of rows or columns can be used to define a triangle in the complex plane. In the figure we show the triangle corresponding to the unitarity conditions on the first and third columns which is the equivalent to the one usually shown for the quark sector.

JHEP01(2017)087

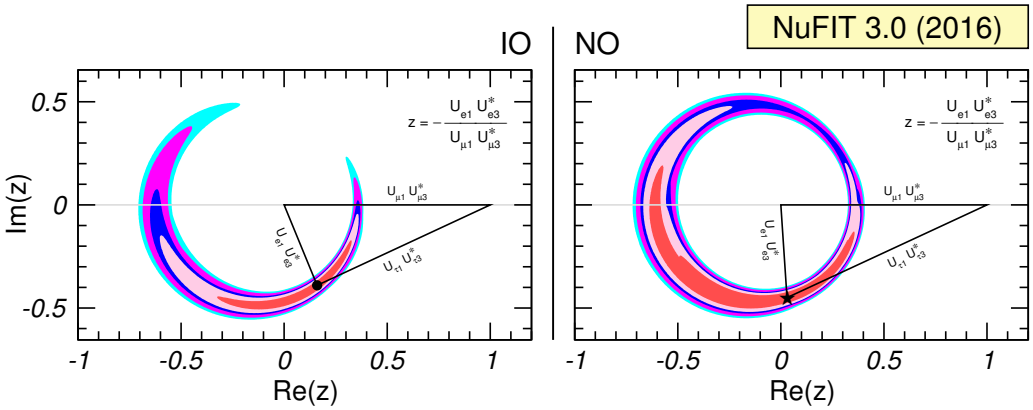

Figure 4. Leptonic unitarity triangle for the first and third columns of the mixing matrix. After scaling and rotating the triangle so that two of its vertices always coincide with $(0,0)$ and $(1,0)$ we plot the 1σ, 90%, 2σ, 99%, 3σ CL (2 dof) allowed regions of the third vertex. Note that in the construction of the triangle the unitarity of the U matrix is always explicitly imposed. The regions for both orderings are defined with respect to the common global minimum which is in NO.

In this figure the absence of CP violation implies a flat triangle, i.e., $\mathrm{Im}(z) = 0$. As can be seen, for NO the horizontal axis crosses the 1σ allowed region, which for 2 dof corresponds to $\Delta\chi^2 \leq 2.3$. This is consistent with the present preference for CP violation, $\chi^2(J_{\mathrm{CP}} = 0) - \chi^2(J_{\mathrm{CP}}\ \text{free}) = 1.7$ mentioned above. We will comment on the statistical interpretation of this number in section 4.

3 Issues in present analysis

The 3ν fit results in the previous section provide a statistically satisfactory description of all the neutrino oscillation data considered. There are however some issues in the determination of some of the parameters which, although not of statistical significance at present, deserve some attention.

3.1 Status of Δm^2_{21} in solar experiments versus KamLAND

The analyses of the solar experiments and of KamLAND give the dominant contribution to the determination of Δm^2_{21} and θ_{12}. It has been a result of global analyses for several years already, that the value of Δm^2_{21} preferred by KamLAND is somewhat higher than the one from solar experiments. This tension arises from a combination of two effects which have not changed significantly over the last lustrum: a) the well-known fact that none of the ^{8}B measurements performed by SNO, SK and Borexino shows any evidence of the low energy spectrum turn-up expected in the standard LMA-MSW [59, 60] solution for the value of Δm^2_{21} favored by KamLAND; b) the observation of a non-vanishing day-night asymmetry in SK, whose size is larger than the one predicted for the Δm^2_{21} value indicated of KamLAND (for which Earth matter effects are very small). In ref. [9] we discussed the differences in the physics entering in the analyses of solar and KamLAND data which are relevant to this tension, and to which we refer the reader for details. Here

JHEP01(2017)087

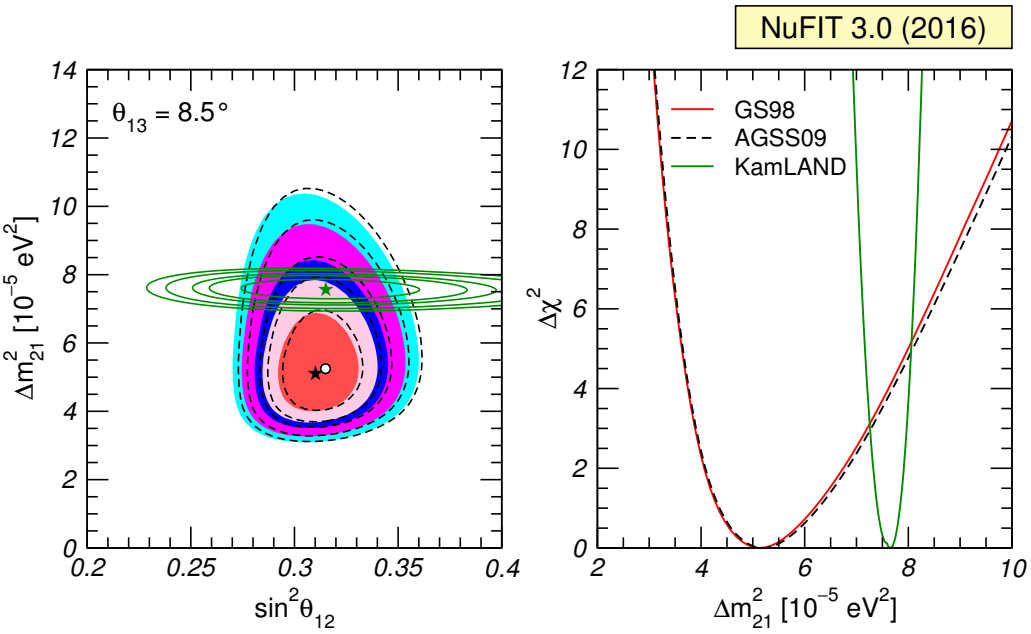

Figure 5. Left: allowed parameter regions (at 1σ, 90%, 2σ, 99% and 3σ CL for 2 dof) from the combined analysis of solar data for GS98 model (full regions with best fit marked by black star) and AGSS09 model (dashed void contours with best fit marked by a white dot), and for the analysis of KamLAND data (solid green contours with best fit marked by a green star) for fixed $\theta_{13} = 8.5°$. Right: $\Delta\chi^2$ dependence on Δm^2_{21} for the same three analyses after marginalizing over θ_{12}.

for sake of completeness we show in figure 5 the quantification of this tension in our present global analysis. As seen in the figure, the best fit value of Δm^2_{21} of KamLAND lays at the boundary of the 2σ allowed range of the solar neutrino analysis.

Also for illustration of the independence of these results with respect to the solar modeling, the solar neutrino regions are shown for two latest versions of the Standard Solar Model, namely the GS98 and the AGSS09 models [61] obtained with two different determinations of the solar abundances [62].

3.2 $\Delta m^2_{3\ell}$ determination in LBL accelerator experiments versus reactors

Figure 6 illustrates the contribution to the present determination of $\Delta m^2_{3\ell}$ from the different data sets. In the left panels we focus on the determination from long baseline experiments, which is mainly from ν_μ disappearance data. We plot the 1σ and 2σ allowed regions (2 dof) in the dominant parameters $\Delta m^2_{3\ell}$ and θ_{23}. As seen in the figure, although the agreement between the different experiments is reasonable, some "tension" starts to appear in the determination of both parameters among the LBL accelerator experiments. In particular we see that the recent results from NOνA, unlike those from T2K, favor a non-maximal value of θ_{23}. It is important to notice that in the context of 3ν mixing the relevant oscillation probabilities for the LBL accelerator experiments also depend on θ_{13} (and on the θ_{12} and Δm^2_{21} parameters which are independently well constrained by solar and KamLAND data). To construct the regions plotted in the left panels of figure 6, we adopt the procedure

JHEP01(2017)087

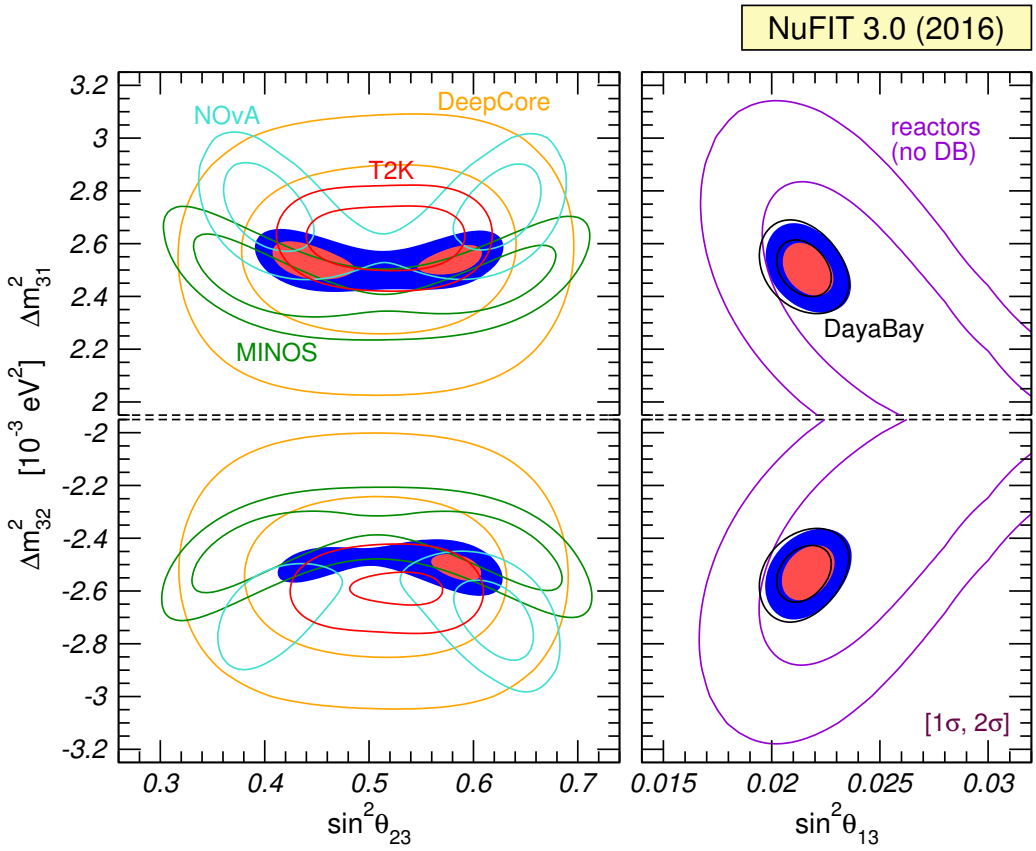

Figure 6. Determination of $\Delta m^2_{3\ell}$ at 1σ and 2σ (2 dof), where $\ell = 1$ for NO (upper panels) and $\ell = 2$ for IO (lower panels). The left panels show regions in the $(\theta_{23}, \Delta m^2_{3\ell})$ plane using both appearance and disappearance data from MINOS (green line), T2K (red lines), NOνA (light blue lines), as well as IceCube/DeepCore (orange lines) and the combination of them (colored regions). In these panels the constraint on θ_{13} from the global fit (which is dominated by the reactor data) is imposed as a Gaussian bias. The right panels show regions in the $(\theta_{13}, \Delta m^2_{3\ell})$ plane using only Daya-Bay (black lines), reactor data without Daya-Bay (violet lines), and their combination (colored regions). In all panels solar and KamLAND data are included to constrain Δm^2_{21} and θ_{12}. Contours are defined with respect to the global minimum of the two orderings.

currently followed by the LBL accelerator experiments: we marginalize with respect to θ_{13}, taking into account the information from reactor data by adding a Gaussian penalty term to the corresponding $\chi^2_{\rm LBL}$. This is not the same as making a combined analysis of LBL and reactor data as we will quantify in section 3.2.1.

Concerning ν_e disappearance data, the total rates observed in reactor experiments at different baselines can provide an independent determination of $\Delta m^2_{3\ell}$ [50, 63]. On top of this, the observation of the energy-dependent oscillation effect due to θ_{13} now allows to further strengthen such measurement. In the right panels of figure 6 we show therefore the allowed regions in the $(\theta_{13}, \Delta m^2_{3\ell})$ plane based on global data on ν_e disappearance. The violet contours are obtained from all the medium-baselines reactor experiments with the exception of Daya-Bay; these regions emerge from the baseline effect mentioned above plus

JHEP01(2017)087

spectral information from Double-Chooz.[3] The black contours are based on the energy spectrum in Daya-Bay, whereas the colored regions show the combination.

By comparing the left and right panels of figure 6 we observe that the combined ν_μ and ν_e disappearance experiments provide a consistent determination of $|\Delta m^2_{3\ell}|$ with similar precision. However when comparing the region for each LBL experiment with that of the reactor experiments we find some dispersion in the best fit values and allowed ranges. This is more clearly illustrated in the upper panels of figure 7, where we plot the one dimensional projection of the regions in figure 6 as a function of $\Delta m^2_{3\ell}$ after marginalization over θ_{23} for each of the LBL experiments and for their combination, together with that from reactor data after marginalization over θ_{13}. The projections are shown for NO(right) and IO(left). Let us stress that the curves corresponding to LBL experiments in the upper panels of figure 7 (as well as those in the upper panels of figures 8 and 9) have been obtained by a partial combination of the information on the shown parameter ($\Delta m^2_{3\ell}$ or θ_{23} or $\delta_{\rm CP}$) from LBL with that of θ_{13} from reactors, because in these plots only the θ_{13} constraint from reactors is imposed while the dependence on $\Delta m^2_{3\ell}$ is neglected. This corresponds to the 1-dim projections of the function:

$$\Delta\chi^2_{\rm LBL+\theta_{13}^{REA}}(\theta_{23},\delta_{\rm CP},\Delta m^2_{3\ell}) = \min_{\theta_{13}}\left[\chi^2_{\rm LBL}(\theta_{13},\theta_{23},\delta_{\rm CP},\Delta m^2_{3\ell}) + \min_{\Delta m^2_{3\ell}}\chi^2_{\rm REA}(\theta_{13},\Delta m^2_{3\ell})\right] - \chi^2_{\rm min}\,. \quad (3.1)$$

However, since reactor data also depends on $\Delta m^2_{3\ell}$ the full combination of reactor and LBL results implies that one must add consistently the χ^2 functions of the LBL experiment with that of reactors evaluated the same value of $\Delta m^2_{3\ell}$, this is

$$\Delta\chi^2_{\rm LBL+REA}(\theta_{23},\delta_{\rm CP},\Delta m^2_{3\ell}) = \min_{\theta_{13}}\left[\chi^2_{\rm LBL}(\theta_{13},\theta_{23},\delta_{\rm CP},\Delta m^2_{3\ell}) + \chi^2_{\rm REA}(\theta_{13},\Delta m^2_{3\ell})\right] - \chi^2_{\rm min}\,. \quad (3.2)$$

We discuss next the effect of combining consistently the information from LBL and reactor experiments in the present determination of θ_{23}, $\delta_{\rm CP}$ and the ordering.

3.2.1 Impact on the determination of θ_{23}, mass ordering, and $\delta_{\rm CP}$

We plot in the lower panels of figures 7–9 the one dimensional projections of $\Delta\chi^2_{\rm LBL+REA}$ for each of the parameters θ_{23}, $\delta_{\rm CP}$, $\Delta m^2_{3\ell}$ (marginalized with respect to the two undisplayed parameters) for the consistent LBL+REA combinations with both the information on θ_{13} and $\Delta m^2_{3\ell}$ from reactors included, eq. (3.2). As mentioned before, the curves in the upper panels for these figures show the corresponding 1-dimensional projections for the partial combination, in which only the θ_{13} constraint from reactors is used, eq. (3.1). For each experiment the curves in these figures are defined with respect to the global minimum of the two orderings, so the relative height of the minimum in one ordering vs the other gives a measure of the ordering favored by each of the experiments.

[3]Recently, RENO has presented a spectral analysis based on an exposure of 500 days [64]. Here we prefer to include from RENO only the total rate measurement, based on the larger exposure of 800 days [37].

JHEP01(2017)087

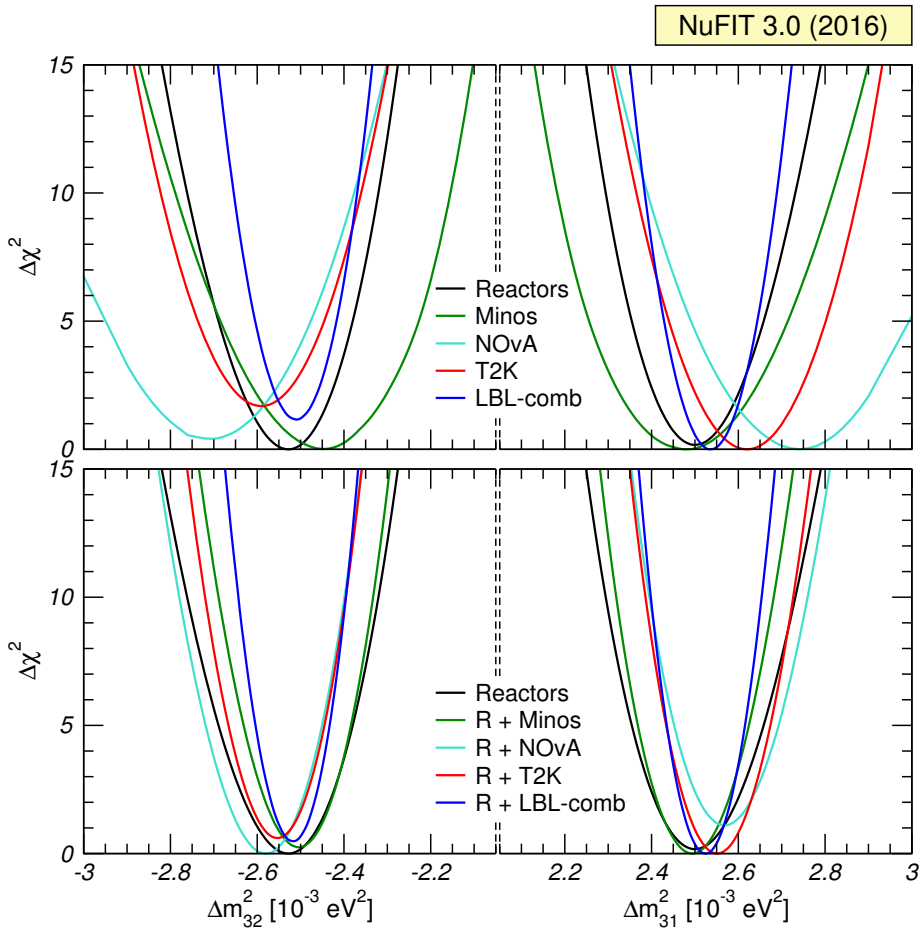

Figure 7. $\Delta m^2_{3\ell}$ determination from LBL accelerator experiments, reactor experiments and their combination. Left (right) panels are for IO (NO). The upper panels show the 1-dim $\Delta\chi^2$ from LBL accelerator experiments after constraining *only* θ_{13} from reactor experiments (this is, marginalizing eq. (3.1) with respect to θ_{23} and $\delta_{\rm CP}$). For each experiment $\Delta\chi^2$ is defined with respect to the global minimum of the two orderings. The lower panels show the corresponding determination when the full information of LBL and reactor experiments is used in the combination (this is, marginalizing eq. (3.2) with respect to θ_{23} and $\delta_{\rm CP}$).

Comparing the upper and lower panels in figures 7, 8 and 9 one sees how the contribution to the determination of the mass ordering, the octant and non-maximality of θ_{23}, and the presence of leptonic CP violation of each LBL experiment in the full LBL+REA combination (eq. (3.2)) can differ from those derived from the LBL results imposing only the θ_{13} constraint from reactors (eq. (3.1)). This is due to the additional information on $\Delta m^2_{3\ell}$ from reactors, which is missing in this last case. In particular:

- When only combining the results of the accelerator LBL experiments with the reactor bound of θ_{13}, both NOνA and T2K favor NO by $\chi^2_{\rm LBL+\theta_{13}^{REA}}({\rm IO}) - \chi^2_{\rm LBL+\theta_{13}^{REA}}({\rm NO}) \simeq 0.4$ (1.7) for LBL = NOνA (T2K). This is in agreement with the analyses shown by the collaborations for example in refs. [29, 31]. However, when consistently combining

JHEP01(2017)087

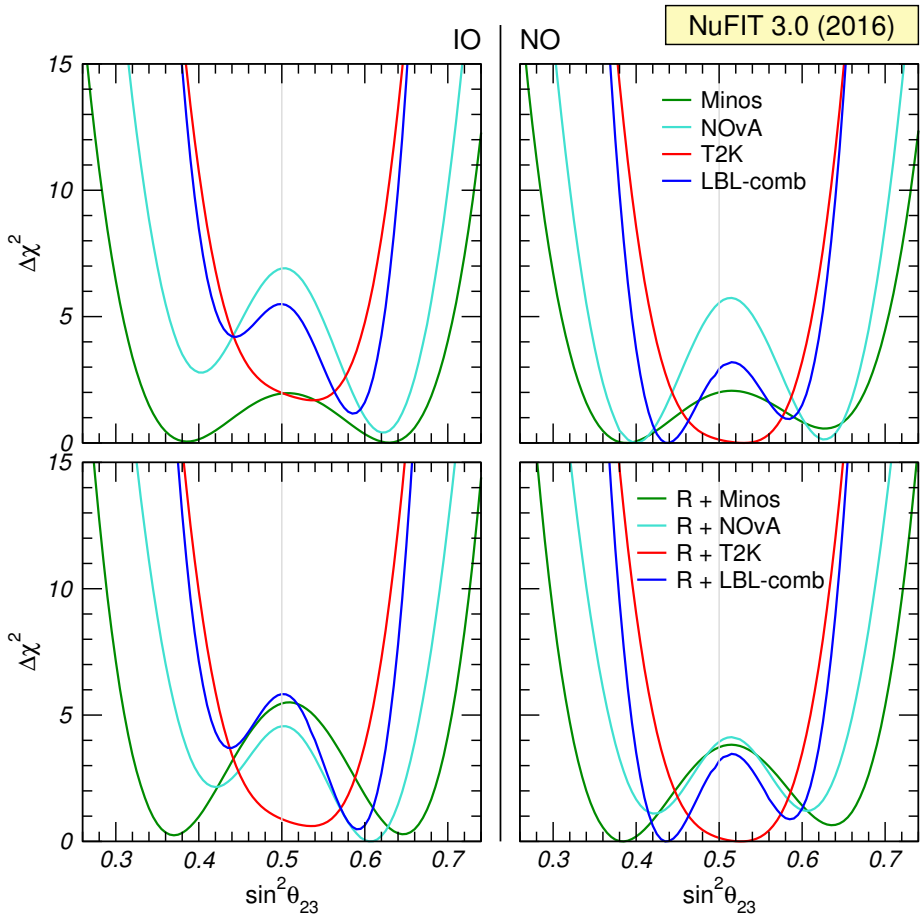

Figure 8. θ_{23} determination from LBL, reactor and their combination. Left (right) panels are for IO (NO). The upper panels show the 1-dim $\Delta\chi^2$ from LBL experiments after constraining *only* θ_{13} from reactor experiments (this is, marginalizing eq. (3.1) with respect to $\Delta m^2_{3\ell}$ and $\delta_{\rm CP}$). For each experiment $\Delta\chi^2$ is defined with respect to the global minimum of the two orderings. The lower panels show the corresponding determination when the full information of LBL accelerator and reactor experiments is used in the combination (this is, marginalizing eq. (3.2) with respect to $\Delta m^2_{3\ell}$ and $\delta_{\rm CP}$).

with the reactor data, we find that the preference for NO by T2K+REA is reduced, and NOνA+REA actually favors IO. This is due to the slightly lower value of $|\Delta m^2_{3\ell}|$ favored by the reactor data, in particular in comparison with NOνA for both orderings, and also with T2K for NO. Altogether we find that for the full combination of LBL accelerator experiments with reactors the "hint" towards NO is below 1σ.

- Figure 8 illustrates how both NOνA and MINOS favor non-maximal θ_{23}. From this figure we see that while the significance of non-maximality in NOνA seems more evident than in MINOS when only the information of θ_{13} is included (upper panels), the opposite holds for the full combination with the reactor data (lower panels). In

JHEP01(2017)087

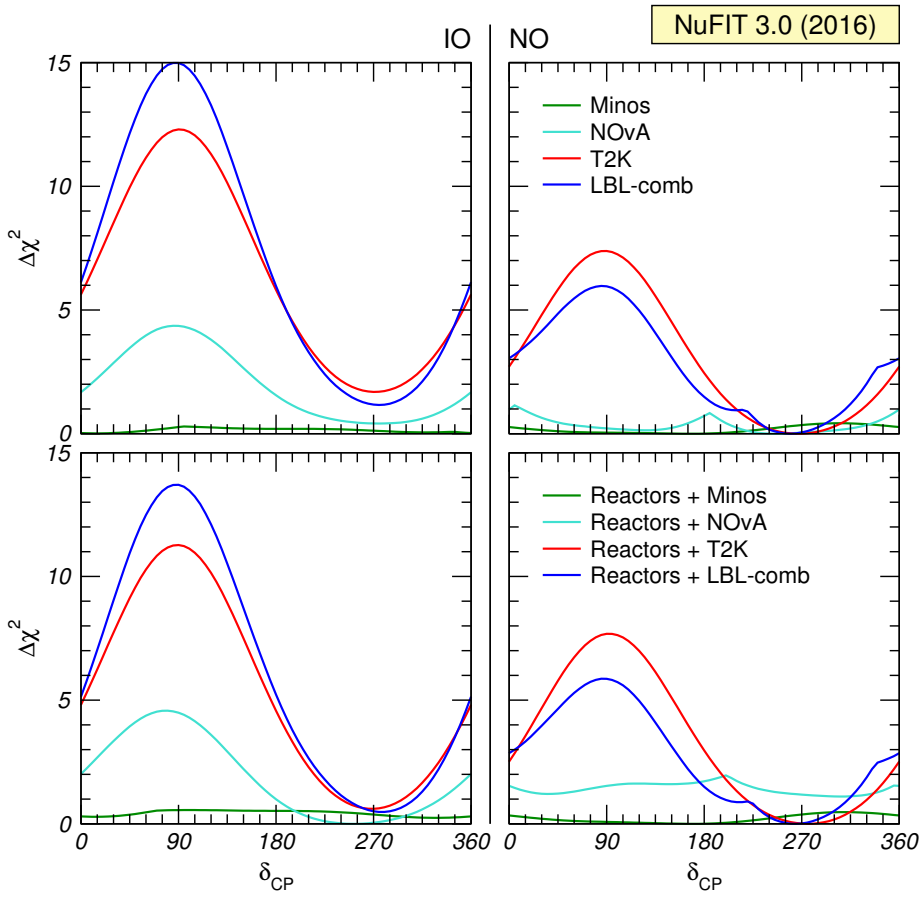

Figure 9. $\delta_{\rm CP}$ determination from LBL, reactor and their combination. Left (right) panels are for IO (NO). The upper panels show the 1-dim $\Delta\chi^2$ from LBL experiments after constraining *only* θ_{13} from reactor experiments (this is, marginalizing eq. (3.1) with respect to $\Delta m^2_{3\ell}$ and θ_{23}). For each experiment $\Delta\chi^2$ is defined with respect to the global minimum of the two orderings. The lower panels show the corresponding determination when the full information of LBL accelerator and reactor experiments is used in the combination (this is, marginalizing eq. (3.2) with respect to $\Delta m^2_{3\ell}$ and θ_{23}).

particular,

$$\begin{aligned}
&\chi^2_{\rm LBL+\theta_{13}^{REA}}(\theta_{23}=45^\circ,{\rm NO}) - \min_{\theta_{23}} \chi^2_{\rm LBL+\theta_{13}^{REA}}(\theta_{23},{\rm NO}) = 5.5\ (2.0)\,,\\
&\chi^2_{\rm LBL+\theta_{13}^{REA}}(\theta_{23}=45^\circ,{\rm IO}) - \min_{\theta_{23}} \chi^2_{\rm LBL+\theta_{13}^{REA}}(\theta_{23},{\rm IO}) = 6.5\ (1.9)\,,\\
&\chi^2_{\rm LBL+REA}(\theta_{23}=45^\circ,{\rm NO}) - \min_{\theta_{23}} \chi^2_{\rm LBL+REA}(\theta_{23},{\rm NO}) = 2.8\ (3.7)\,,\\
&\chi^2_{\rm LBL+REA}(\theta_{23}=45^\circ,{\rm IO}) - \min_{\theta_{23}} \chi^2_{\rm LBL+REA}(\theta_{23},{\rm IO}) = 4.6\ (5.2)\,,
\end{aligned} \tag{3.3}$$

for LBL = NOνA (MINOS). On the other hand T2K results are compatible with $\theta_{23} = 45^\circ$ for any ordering. Altogether we find that for NO the full combination of LBL accelerator experiments and reactors disfavor maximal θ_{23} mixing by $\Delta\chi^2 = 3.2$.

JHEP01(2017)087

- Regarding the octant of θ_{23}, for IO all LBL accelerator experiments are better described with $\theta_{23} > 45^\circ$, adding up to a $\sim 1.8\sigma$ preference for that octant. Conversely, for NO $\theta_{23} < 45^\circ$ is favored at $\sim 1\sigma$.

- From figure 9 we see that the "hint" for a CP phase around 270° is mostly driven by T2K data, with some extra contribution from NOνA in the case of IO. Within the present precision the favored ranges of $\delta_{\rm CP}$ in each ordering by the combination of LBL accelerator experiments are pretty independent on the inclusion of the $\Delta m^2_{3\ell}$ information from reactors.

3.3 Analysis of Super-Kamiokande atmospheric data

In all the results discussed so far we have not included information from Super-Kamiokande atmospheric data. The reason is that our oscillation analysis cannot reproduce that of the collaboration presented in their talks in the last two years (see for example ref. [66] for their latest unpublished results).

Already since SK2 the Super-Kamiokande collaboration has been presenting its experimental results in terms of a growing number of data samples. The rates for some of those samples cannot be predicted (and therefore included in a statistical analysis) without a detailed simulation of the detector, which can only be made by the experimental collaboration itself. Our analysis of Super-Kamiokande data has been always based on the "classical" set of samples for which our simulations were reliable enough: sub-GeV and multi-GeV e-like and μ-like fully contained events, as well as partially contained, stopping and through-going muon data, each divided into 10 angular bins for a total of 70 energy and zenith angle bins (details on our simulation of the data samples and the statistical analysis are given in the appendix of ref. [3]). Despite the limitations, until recently our results represented the most up-to-date analysis of the atmospheric neutrino data which could be performed outside the collaboration, and we were able to reproduce with reasonable precision the oscillation results of the full analysis presented by SK – both for what concerns the determination of the dominant parameters $\Delta m^2_{3\ell}$ and θ_{23}, as well as their rather marginal sensitivity to the subdominant ν_e appearance effects driven by θ_{13} (and consequently to $\delta_{\rm CP}$ and the ordering). Thus we confidently included our own implementation of the Super-Kamiokande χ^2 in our global fit.

However, in the last two years Super-Kamiokande has developed a new analysis method in which a set of neural network based selections are introduced, some of them with the aim of constructing $\nu_e + \bar{\nu}_e$ enriched samples which are then further classified into ν_e-like and $\bar{\nu}_e$-like subsamples, thus increasing the sensitivity to subleading parameters such as the mass ordering and $\delta_{\rm CP}$ [65, 67]. The selection criteria are constructed to exploit the expected differences in the number of charged pions and transverse momentum in the interaction of ν_e versus $\bar{\nu}_e$. With this new analysis method Super-Kamiokande has been reporting in talks an increasing sensitivity to the ordering and to $\delta_{\rm CP}$: for example, the preliminary results of the analysis of SK1–4 (including 2520 days of SK4) [66] in combination with the reactor constraint of θ_{13} show a preference for NO with a $\Delta\chi^2({\rm IO}) = 4.3$ and variation of $\chi^2(\delta_{\rm CP})$ with the CP phase at the level of $\sim 1.7\sigma$.

JHEP01(2017)087

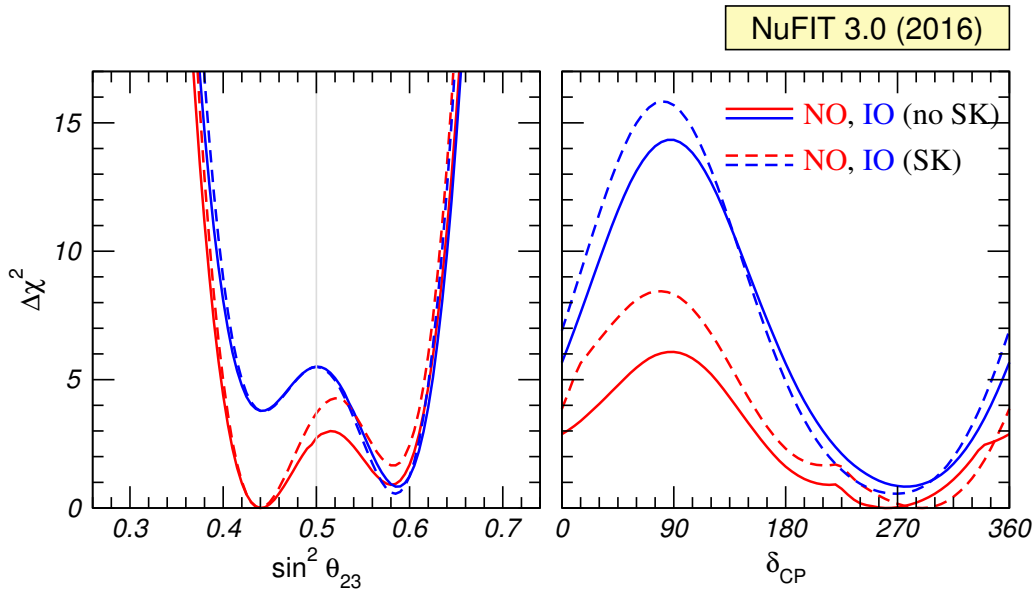

Figure 10. Impact of our re-analysis of SK atmospheric neutrino data [65] (70 bins in energy and zenith angle) on the determination of $\sin^2\theta_{23}$, $\delta_{\rm CP}$, and the mass ordering. The impact on all other parameters is negligible.

	Normal Ordering (best fit)		Inverted Ordering ($\Delta\chi^2 = 0.56$)		Any Ordering
	bfp $\pm 1\sigma$	3σ range	bfp $\pm 1\sigma$	3σ range	3σ range
$\sin^2\theta_{23}$	$0.440^{+0.024}_{-0.019}$	$0.388 \to 0.630$	$0.584^{+0.019}_{-0.022}$	$0.398 \to 0.634$	$0.388 \to 0.632$
$\theta_{23}/^\circ$	$41.5^{+1.4}_{-1.1}$	$38.6 \to 52.5$	$49.9^{+1.1}_{-1.3}$	$39.1 \to 52.8$	$38.6 \to 52.7$
$\delta_{\rm CP}/^\circ$	289^{+38}_{-51}	$0 \to 360$	269^{+40}_{-45}	$146 \to 377$	$0 \to 360$

Table 2. Three-flavor oscillation parameters from our fit to global data, including also our re-analysis of SK1–4 (4581 days) atmospheric data. The numbers in the 1st (2nd) column are obtained assuming NO (IO), i.e., relative to the respective local minimum, whereas in the 3rd column we minimize also with respect to the ordering. The omitted parameters are identical to table 1.

Unfortunately, with publicly available information this analysis is not reproducible outside the collaboration. Conversely our "traditional" analysis based on their reproducible data samples continues to show only marginal dependence on these effects. This is illustrated in figure 10 and table 2 where we show the impact of inclusion of our last re-analysis of SK atmospheric data using the above mentioned 70 bins in energy and zenith angle.[4] We only show the impact on the determination of $\sin^2\theta_{23}$, $\delta_{\rm CP}$, and the mass ordering as the effect on all other parameters is negligible. We observe that $\Delta\chi^2$ for maximal mixing and the second θ_{23} octant receive an additional contribution of about 1 unit in the case of NO, whereas the θ_{23} result for IO is practically unchanged. Values of $\delta_{\rm CP} \simeq 90^\circ$ are slightly more disfavoured, whereas there is basically no effect on the mass ordering discrimination.

[4]We use the same data and statistical treatment as in our previous global fit NuFIT 2.0 [9] as well as in versions 2.1 and 2.2 [49] which is based on 4581 days of data from SK1–4 [65] (corresponding to 1775 days of SK4).

JHEP01(2017)087

In summary, with the information at hand we are not able to reproduce the elements driving the main dependence on the subdominant effects of the official (though preliminary and unpublished) Super-Kamiokande results, while the dominant parameters are currently well determined by LBL experiments. For these reasons we have decided not to include our re-analysis of Super-Kamiokande data in our preferred global fit presented in the previous section. Needless to say that when enough quantitative information becomes available to allow a reliable simulation of the subdominant ν_e-driven effects, we will proceed to include it in our global analysis.

4 Monte Carlo evaluation of confidence levels for θ_{23}, $\delta_{\rm CP}$ and ordering

At present the three least known neutrino oscillation parameters are the Dirac CP violating phase $\delta_{\rm CP}$, the octant of θ_{23} and the mass ordering (which in what follows we will denote by "O"). In order to study the information from data on these parameters one can use two $\Delta\chi^2$ test statistics [55, 68]:

$$\Delta\chi^2\left(\delta_{\rm CP}, \mathrm{O}\right) = \min_{x_1} \chi^2\left(\delta_{\rm CP}, \mathrm{O}, x_1\right) - \chi^2_{\rm min}\,, \tag{4.1}$$

$$\Delta\chi^2\left(\theta_{23}, \mathrm{O}\right) = \min_{x_2} \chi^2\left(\theta_{23}, \mathrm{O}, x_2\right) - \chi^2_{\rm min}\,, \tag{4.2}$$

where the minimization in the first equation is performed with respect to all oscillation parameters except $\delta_{\rm CP}$ and the ordering ($x_1 = \{\theta_{12}, \theta_{13}, \theta_{23}, \Delta m^2_{21}, |\Delta m^2_{3\ell}|\}$), while in the second equation the minimization is over all oscillation parameters except θ_{23} and the ordering ($x_2 = \{\theta_{12}, \theta_{13}, \delta_{\rm CP}, \Delta m^2_{21}, |\Delta m^2_{3\ell}|\}$). Here $\chi^2_{\rm min}$ indicates the χ^2 minimum with respect to all oscillation parameters including the mass ordering.

We have plotted the values of these test statistics in the lower right and central left panels in figure 2. We can use them not only for the determination of $\delta_{\rm CP}$ and θ_{23}, respectively, but also of the mass ordering. For instance, using eq. (4.1) we can determine a confidence interval for $\delta_{\rm CP}$ at a given CL for both orderings. However, below a certain CL no interval will appear for the less favored ordering. In this sense we can exclude that ordering at the CL at which the corresponding interval for $\delta_{\rm CP}$ disappears. Note that a similar prescription to test the mass ordering can be built for any other parameter as well, e.g., for θ_{23} using eq. (4.2).[5]

In section 2 we have presented confidence intervals assuming that the test statistics follow a χ^2-distribution with 1 dof, relying on Wilks theorem to hold [70] (this is what we call the Gaussian limit). However, the test statistics in eqs. (4.1) and (4.2) are expected not to follow Wilks' theorem because of several reasons [68]:

- Sensitivity of current data to $\delta_{\rm CP}$ is still limited, as can be seen in figure 2: all values of $\delta_{\rm CP}$ have $\Delta\chi^2 < 14$, and for NO not even $\Delta\chi^2 = 6$ is attained.
- Regarding θ_{23}, its precision is dominated by ν_μ disappearance experiments. Since the relevant survival probability depends dominantly on $\sin^2 2\theta_{23}$, there is both a

[5] Let us mention that this method to determine the mass ordering is different from the one based on the test statistics T discussed in ref. [69].

JHEP01(2017)087

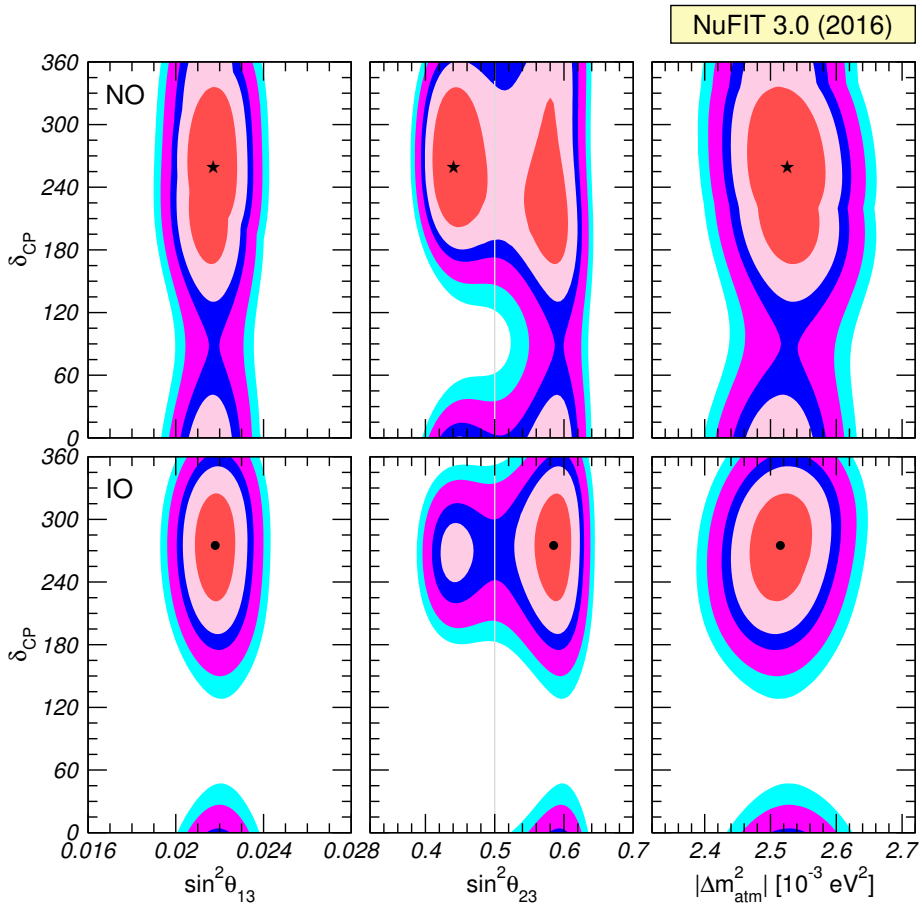

Figure 11. Allowed regions from the global data at 1σ, 90%, 2σ, 99% and 3σ CL (2 dof). We show projections onto different planes with $\delta_{\rm CP}$ on the vertical axis after minimizing with respect to all undisplayed parameters. The lower (upper) panels correspond to IO (NO). Contour regions are derived with respect to the global minimum which occurs for NO and is indicated by a star. The local minimum for IO is shown by a black dot.

physical boundary of their parameter space at $\theta_{23} = 45^\circ$ (because $\sin 2\theta_{23} < 1$), as well as a degeneracy related to the octant.

- The mass ordering is a discrete parameter.
- The dependence of the theoretical predictions on $\delta_{\rm CP}$ is significantly non-linear, even more considering the periodic nature of this parameter. Furthermore, there are complicated correlations and degeneracies between $\delta_{\rm CP}$, θ_{23}, and the mass ordering (see figure 11 for illustration).

Therefore, one may expect deviations from the Gaussian limit of the $\Delta\chi^2$ distributions, and confidence levels for these parameters should be cross checked through a Monte Carlo simulation of the relevant experiments. We consider in the following the combination of the T2K, NOνA, MINOS and Daya-Bay experiments, which are most relevant for the parameters we are interested in this section. For a given point of assumed true values for

JHEP01(2017)087

the parameters we generate a large number (10^4) of pseudo-data samples for each of the experiments. For each pseudo-data sample we compute the two statistics given in eqs. (4.1) and (4.2) to determine their distributions numerically. In ref. [68] it has been shown that the distribution of test statistics for 2-dimensional parameter region (such as for instance the middle panels of figure 11) are more close to Gaussianity than 1-dimensional ones such as eqs. (4.1) and (4.2). Therefore we focus here on the 1-dimensional cases.

First, let us note that in order to keep calculation time manageable one can fix all parameters which are known to be uncorrelated with the three we are interested in (i.e., θ_{23}, $\delta_{\rm CP}$, O). This is certainly the case for Δm^2_{21} and θ_{12} which are determined independently by solar and KamLAND data. As for θ_{13}, presently the most precise information arises from reactor data whose results are insensitive to $\delta_{\rm CP}$ and θ_{23}. Consequently, marginalizing over θ_{13} within reactor uncertainties or fixing it to the best fit value gives a negligible difference in the simulations. Concerning $|\Delta m^2_{3\ell}|$ we observe that there are no strong correlations or degeneracies with $\delta_{\rm CP}$ (see figure 11), and we assume that the distributions of the test statistics do not significantly depend on the assumed true value. Therefore we consider only the global best fit values for each ordering as true values for $|\Delta m^2_{3\ell}|$ to generate pseudo-data. However, since the relevant observables *do* depend non-trivially on its value, it is important to keep $|\Delta m^2_{3\ell}|$ as a free parameter in the fit and to minimize the χ^2 for each pseudo-data sample with respect to it. Hence, we approximate the test statistics in eqs. (4.1) and (4.2) by using

$$\chi^2\left(\delta_{\rm CP}, \mathrm{O}, x_1\right) \equiv \min_{\theta_{23}, |\Delta m^2_{3\ell}|} \chi^2\left(\theta_{23}, \delta_{\rm CP}, \mathrm{O}, |\Delta m^2_{3\ell}|\right) , \tag{4.3}$$

$$\chi^2\left(\theta_{23}, \mathrm{O}, x_2\right) \equiv \min_{\delta_{\rm CP}, |\Delta m^2_{3\ell}|} \chi^2\left(\theta_{23}, \delta_{\rm CP}, \mathrm{O}, |\Delta m^2_{3\ell}|\right) , \tag{4.4}$$

with the other oscillation parameters kept fixed at their best fit points: $\Delta m^2_{21} = 7.5 \times 10^{-5}$ eV^2, $\sin^2\theta_{12} = 0.31$, and $\sin^2\theta_{13} = 0.022$.

4.1 $\delta_{\rm CP}$ and the mass ordering

The value of the test statistics (4.1) is shown in figure 12 for the combination of T2K, NOνA, MINOS and Daya-Bay as a function of $\delta_{\rm CP}$ for both mass orderings. In the generation of the pseudo-data we have assumed three representative values of $\theta_{23,\rm true}$ as shown in the plots. The broken curves show, for each set of true values, the values of $\Delta\chi^2(\delta_{\rm CP}, \mathrm{O})$ which are larger than 68%, 95%, and 99% of all generated data samples.

From the figure we read that if the $\Delta\chi^2$ from real data (solid curve, identical in the three panels) for a given ordering is above the x% CL lines for that ordering for a given value of $\delta_{\rm CP}$, that value of $\delta_{\rm CP}$ and the mass ordering can be rejected with x% confidence. So if the minimum of the $\Delta\chi^2$ curve for one of the orderings (in this case IO is the one with non-zero minimum) is above the x% CL line one infers that that ordering is rejected at that CL.

For the sake of comparison we also show in figure 12 the corresponding 68%, 95% and 99% Gaussian confidence levels as horizontal lines. There are some qualitative deviations from Gaussianity that have already been reported [68]:

JHEP01(2017)087

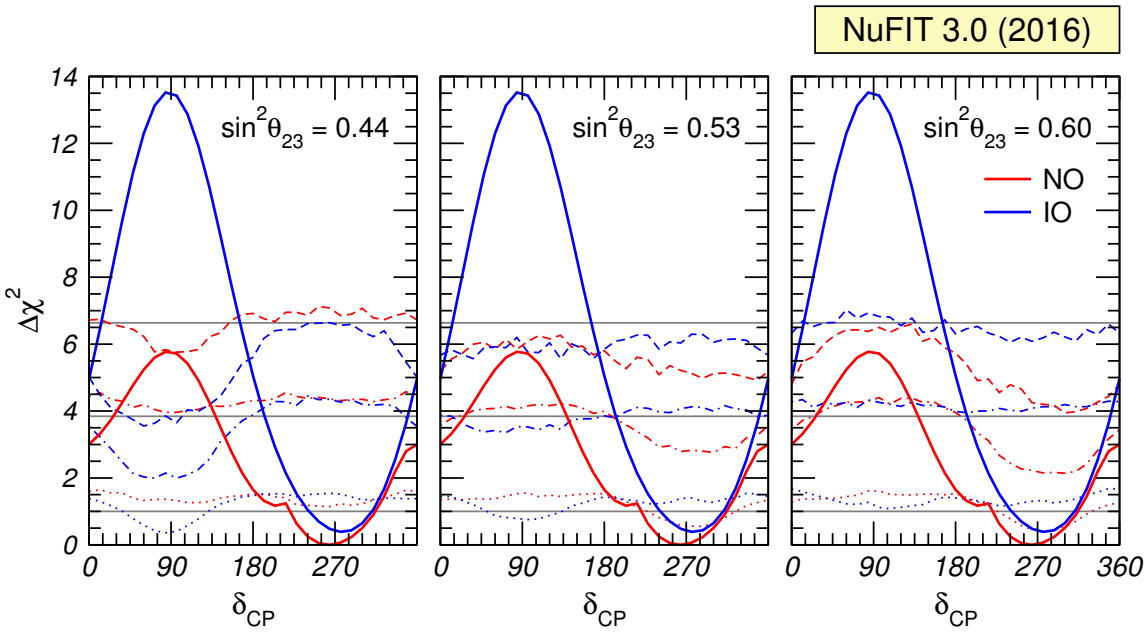

Figure 12. 68%, 95% and 99% confidence levels (broken curves) for the test statistics (4.1) along with its value (solid curves) for the combination of T2K, NOνA, MINOS and reactor data. The value of $\sin^2\theta_{23}$ given in each panel corresponds to the assumed true value chosen to generate the pseudo-experiments and for all panels we take $\Delta m^2_{3\ell,\text{true}} = -2.53 \times 10^{-3}$ eV^2 for IO and $+2.54 \times 10^{-3}$ eV^2 for NO. The solid horizontal lines represent the 68%, 95% and 99% CL predictions from Wilks' theorem.

- For $\theta_{23} < 45°$, $\delta_{\text{CP}} = 90°$, and IO as well as for $\theta_{23} > 45°$, $\delta_{\text{CP}} = 270°$ and NO, the confidence levels decrease. This effect arises because at those points in parameter space the $\nu_\mu \to \nu_e$ oscillation probability has a minimum or a maximum, respectively. Therefore, statistical fluctuations leading to less (or more) events than predicted cannot be accommodated by adjusting the parameters. $\Delta\chi^2$ is small more often and the confidence levels decrease. This is an effect always present at boundaries in parameter space, usually referred to as an effective decrease in the number of degrees of freedom in the model.

- Conversely for $\delta_{\text{CP}} \sim 90°$ for $\theta_{23} > 45°$, and $\delta_{\text{CP}} \sim 270°$ for $\theta_{23} < 45°$, the confidence levels increase. This is associated with the prominent presence of the octant degeneracy. Degeneracies imply that statistical fluctuations can drive you away from the true value, $\Delta\chi^2$ increases, and the confidence levels increase. This is usually referred to as an effective increase in the number of degrees of freedom in the model due to degeneracies.

- Overall we find that with present data confidence levels are clearly closer to Gaussianity than found in refs. [9, 68], where similar simulations have been performed with less data available. For those data sets confidence levels were consistently below their Gaussian limit. This was mainly a consequence of the limited statistics and the cyclic nature of δ_{CP} which lead to an effective decrease in the number of degrees of

JHEP01(2017)087

$\sin^2\theta_{23,\text{true}}$	Ordering	CP cons.	90% CL range	95% CL range
0.44	NO	70%	$[0°, 14°] \cup [151°, 360°]$	$[0°, 37°] \cup [133°, 360°]$
	IO	98%	$[200°, 341°]$	$[190°, 350°]$
0.53	NO	70%	$[150°, 342°]$	$[0°, 28°] \cup [133°, 360°]$
	IO	98%	$[203°, 342°]$	$[193°, 350°]$
0.60	NO	70%	$[148°, 336°]$	$[0°, 28°] \cup [130°, 360°]$
	IO	97%	$[205°, 345°]$	$[191°, 350°]$
Gaussian	NO	80%	$[158°, 346°]$	$[0°, 26°] \cup [139°, 360°]$
	IO	97%	$[208°, 332°]$	$[193°, 350°]$

Table 3. Confidence level with which CP conservation ($\delta_{\text{CP}} = 0, 180°$) is rejected (third column) and 90% and 95% confidence intervals for δ_{CP} (fourth and fifth column) for different sets of true values of the parameters and in the Gaussian approximation. Confidence intervals for δ_{CP} as well as the CL for CP conservation are defined for both orderings with respect to the global minimum (which happens for NO).

freedom. We now find that when the full combination of data currently available is included this effect is reduced, as expected if experiments become more sensitive.

- For all true values considered, IO is not rejected even at 1σ. In particular we find IO disfavored at $30\% - 40\%$ for $\sin^2\theta_{23} = 0.44 - 0.60$.

Quantitatively we show in table 3 the CL at which CP conservation ($\delta_{\text{CP}} = 0, 180°$) is disfavored as well as the 90% and 95% confidence intervals for δ_{CP}. We find that the CL of rejection of CP conservation as well as the allowed ranges do not depend very significantly on $\theta_{23,\text{true}}$. This can be understood from figure 12: the dependence on $\theta_{23,\text{true}}$ occur mostly for $\delta_{\text{CP}} \sim 90°$ and IO, a region discarded with a large CL, and for $\delta_{\text{CP}} \sim 270°$ and NO, a region around the best fit.

Note that in the table the intervals for δ_{CP} are defined for both orderings with respect to the global minimum (which happens for NO). Hence the intervals for IO include the effect that IO is slightly disfavored with respect to NO. They cannot be directly compared to the intervals given in table 1, where we defined intervals relative to the local best fit point for each ordering.

A similar comment applies also to the CL quoted in the table to reject CP conservation. For IO this is defined relative to the best fit point in NO. We find that for NO, CP conservation is allowed at 70% CL, i.e., slightly above 1σ (with some deviations from the Gaussian result of 80% CL), while for IO the CL for CP conservation is above 2σ. Note that values of $\delta_{\text{CP}} \simeq 90°$ are disfavored at around 99% CL for NO, while for IO the rejection is at even higher CL: the $\Delta\chi^2$ with respect to the global minimum is around 14, which would correspond to 3.7σ in the Gaussian limit. Our Monte Carlo sample of 10^4 pseudo-data sets is not large enough to confirm such a high confidence level.

JHEP01(2017)087

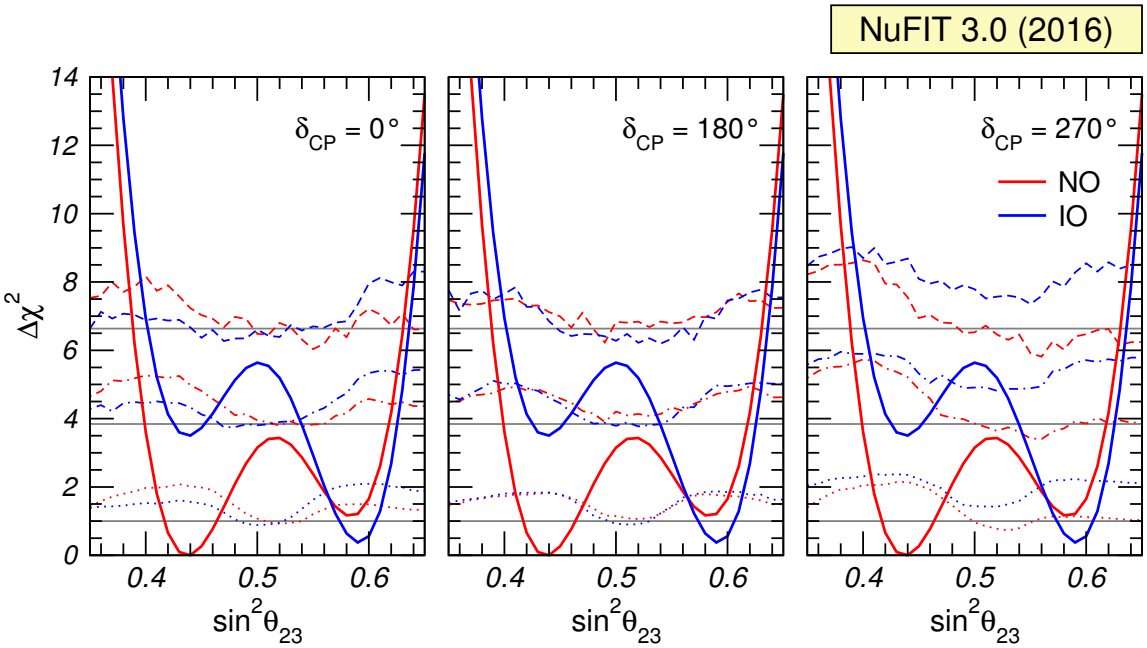

Figure 13. 68%, 95% and 99% confidence levels (broken curves) for the test statistics (4.2) along with its value (solid curves) for the combination of T2K, NOνA, MINOS and reactor data. The value of $\delta_{\rm CP}$ above each plot corresponds to the assumed true value chosen to generate the pseudo-experiments and for all panels we take $\Delta m^2_{3\ell,\rm true} = -2.53 \times 10^{-3}$ eV^2 for IO and $+2.54 \times 10^{-3}$ eV^2 for NO. The solid horizontal lines represent the 68%, 95% and 99% CL predictions from Wilks' theorem.

4.2 θ_{23} and the mass ordering

Moving now to the discussion of θ_{23}, we show the value of the test statistics (4.2) in figure 13 for the combination of T2K, NOνA, MINOS and Daya-Bay experiments as a function of θ_{23}, for both mass orderings. For the generation of the pseudo-data we have assumed three example values $\delta_{\rm CP,true} = 0, 180°, 270°$. We do not show results for $\delta_{\rm CP,true} = 90°$, since this value is already quite disfavored by data, especially for IO.[6] The broken curves show for each set of true values, the values of $\Delta\chi^2(\theta_{23}, \mathrm{O})$ which are larger than 68%, 95%, and 99% of all generated data samples. From the figure we see that the deviations from Gaussianity are not very prominent and can be understood as follows:

- The confidence levels decrease around maximal mixing because of the boundary on the parameter space present at maximal mixing for disappearance data.
- There is some increase and decrease in the confidence levels for $\delta_{\rm CP} = 270°$, in the same parameter region as the corresponding ones in figure 12.

In table 4 we show the CL at which the combination of LBL and reactor experiments can disfavor maximal θ_{23} mixing ($\theta_{23} = 45°$) as well as the 90% and 95% confidence intervals

[6] We are aware of the fact that this choice is somewhat arbitrary and implicitly resembles Bayesian reasoning. In the strict frequentist sense we cannot a priori exclude any true value of the parameters.

JHEP01(2017)087

$\delta_{\mathrm{CP,true}}$	Ordering	$\theta_{23} = 45°$	90% CL range	95% CL range
0°	NO	92%	$[0.40, 0.49] \cup [0.55, 0.61]$	$[0.39, 0.62]$
	IO	98%	$[0.55, 0.62]$	$[0.42, 0.46] \cup [0.54, 0.63]$
180°	NO	91%	$[0.40, 0.50] \cup [0.54, 0.61]$	$[0.40, 0.62]$
	IO	98%	$[0.43, 0.44] \cup [0.55, 0.62]$	$[0.41, 0.46] \cup [0.54, 0.63]$
270°	NO	92%	$[0.40, 0.49] \cup [0.55, 0.61]$	$[0.39, 0.62]$
	IO	97%	$[0.42, 0.45] \cup [0.55, 0.62]$	$[0.41, 0.48] \cup [0.53, 0.63]$
Gaussian	NO	92%	$[0.41, 0.49] \cup [0.55, 0.61]$	$[0.40, 0.62]$
	IO	98%	$[0.56, 0.62]$	$[0.43, 0.45] \cup [0.54, 0.63]$

Table 4. CL for the rejection of maximal θ_{23} mixing (third column), and 90% and 95% CL intervals for $\sin^2\theta_{23}$ for different sets of true parameter values and in the Gaussian approximation (last row).

$\delta_{\mathrm{CP,true}}$	NO/2nd Oct.	IO/1st Oct.	IO/2nd Oct.
0°	62%	91%	28%
180°	56%	89%	32%
270°	70%	83%	27%
Gaussian	72%	94%	46%

Table 5. CL for the rejection of various combinations of mass ordering and θ_{23} octant with respect to the global best fit (which happens for NO and 1st octant). We quote the CL of the local minima for each ordering/octant combination, assuming three example values for the true value of δ_{CP} as well as for the Gaussian approximation (last row).

for $\sin^2\theta_{23}$ for both orderings with respect to the global best fit. We observe from the table that the Gaussian approximation is quite good for both, the CL of maximal mixing as well as for the confidence intervals. We conclude that present data excludes maximal mixing at slightly more than 90% CL. Again we note that the intervals for $\sin^2\theta_{23}$ for IO cannot be directly compared with the ones from table 1, where they are defined with respect to the local minimum in each ordering.

In table 5 we show the CL at which a certain combination of mass ordering and θ_{23} octant can be excluded with respect to the global minimum in the NO and 1st θ_{23} octant. We observe that the CL of the second octant for NO shows relatively large deviations from Gaussianity and dependence on the true value of δ_{CP}. In any case, the sensitivity is very low and the 2nd octant can be reject at most at 70% CL (1σ) for all values of δ_{CP}. The first octant for IO can be excluded at between 83% and 91% CL, depending on δ_{CP}. As discussed above, the exclusion of the IO/2nd octant case corresponds also to the exclusion of the IO, since at that point the confidence interval in IO would vanish. Also in this case we observe deviations from the Gaussian approximation and the CL of at best 32% is clearly less than 1σ (consistent with the results discussed in the previous subsection), showing that the considered data set has essentially no sensitivity to the mass ordering.

JHEP01(2017)087

5 Conclusions

We have presented the results of the updated (as of fall 2016) analysis of relevant neutrino data in the framework of mixing among three massive neutrinos. Quantitatively the present determination of the two mass differences, three mixing angles and the relevant CP violating phase obtained under the assumption that their log-likelihood follows a χ^2 distribution is listed in table 1, and the corresponding leptonic mixing matrix is given in eq. (2.1). We have found that the maximum allowed CP violation in the leptonic sector parametrized by the Jarlskog determinant is $J_{\rm CP}^{\rm max} = 0.0329 \pm 0.0007\,(^{+0.0021}_{-0.0024})$ at 1σ (3σ).

We have studied in detail how the sensitivity to the least-determined parameters θ_{23}, $\delta_{\rm CP}$ and the mass ordering depends on the proper combination of the different data samples (section 3.2). Furthermore we have quantified deviations from the Gaussian approximation in the evaluation of the confidence intervals for θ_{23} and $\delta_{\rm CP}$ by performing a Monte Carlo study of the long baseline accelerator and reactor results (section 4). We can summarize the main conclusions in these sections as follows:

- At present the precision on the determination of $|\Delta m^2_{3\ell}|$ from ν_μ disappearance in LBL accelerator experiments NOνA, T2K and MINOS is comparable to that from ν_e disappearance in reactor experiments, in particular with the spectral information from Daya-Bay. When comparing the region for each LBL experiment with that of the reactor experiments we find some dispersion in the best fit values and allowed ranges.

- The interpretation of the data from accelerator LBL experiments in the framework of 3ν mixing requires using information from the reactor experiments, in particular about the mixing angle θ_{13}. But since, as mentioned above, reactor data also constrain $|\Delta m^2_{3\ell}|$, the resulting CL of presently low confidence effects (in particular the non-maximality of θ_{23} and the mass ordering) is affected by the inclusion of this information in the combination.

- We find that the mass ordering favored by NOνA changes from NO to IO when the information on $\Delta m^2_{3\ell}$ from reactor experiments is correctly included in the LBL+REA combination, and the $\Delta\chi^2$ of NO in T2K is reduced from around 2 to 0.5 (see figure 7). Our MC study of the combination of LBL and reactor data shows that for all cases generated, NO is favored but with a CL of less than 1σ.

- About the non-maximality of θ_{23}, we find that when the information on $\Delta m^2_{3\ell}$ from reactor experiments is correctly included in the LBL+REA combination, it is not NOνA but actually MINOS which contributes most to the preference for non-maximal θ_{23} (see figure 8). Quantitatively our MC study of the combination of LBL and reactor data shows that for all the cases generated the CL for rejection of maximal θ_{23} is about 92% for NO. As seen in figure 13 and table 4, the CL of maximal mixing as well as confidence intervals for $\sin^2\theta_{23}$ derived with MC simulations are not very different from the corresponding Gaussian approximation.

JHEP01(2017)087

- The same study shows that for NO (IO) the favored octant is $\theta_{23} < 45^\circ$ ($\theta_{23} > 45^\circ$). The CL for rejection of the disfavored octant depends on the true value of $\delta_{\rm CP}$ assumed in the MC study and it is generically lower than the one obtained in the Gaussian limit (see table 5). For example, for NO the second octant is disfavored at a confidence level between 0.9σ and 1.3σ depending on the assumed true value of $\delta_{\rm CP}$.

- The present sensitivity to $\delta_{\rm CP}$ is driven by T2K with a minor contribution from NOνA for IO (see figure 9). The dependence of the combined CL of the "hint" towards leptonic CP violation and in particular for $\delta_{\rm CP} \simeq 270^\circ$ on the true value of θ_{23} is shown in figure 12, from which we read that for all cases generated CP conservation is disfavored only at 70% (1.05σ) for NO. Values of $\delta_{\rm CP} \simeq 90^\circ$ are disfavored at around 99% CL for NO, while for IO the rejection is at higher CL ($\Delta\chi^2 \simeq 14$ with respect to the global minimum).

Finally we comment that the increased statistics in SK4 and Borexino has had no major impact in the long-standing tension between the best fit values of Δm^2_{21} as determined from the analysis of KamLAND and solar data, which remains an unresolved $\sim 2\sigma$ effect.

Future updates of this analysis will be provided at the NuFIT website quoted in ref. [49].

Acknowledgments

This work is supported by USA-NSF grant PHY-1620628, by EU Networks FP10 ITN ELUSIVES (H2020-MSCA-ITN-2015-674896) and INVISIBLES-PLUS (H2020-MSCA-RISE-2015-690575), by MINECO grants FPA2013-46570, FPA2012-31880 and MINECO/FEDER-UE grant FPA2015-65929-P, by Maria de Maetzu program grant MDM-2014-0367 of IC-CUB, and the "Severo Ochoa" program grant SEV-2012-0249 of IFT. I.E. acknowledges support from the FPU program fellowship FPU15/03697.

A List of data used in the analysis

Solar experiments.

- Chlorine total rate [15], 1 data point.
- Gallex & GNO total rates [16], 2 data points.
- SAGE total rate [17], 1 data point.
- SK1 full energy and zenith spectrum [18], 44 data points.
- SK2 full energy and day/night spectrum [19], 33 data points.
- SK3 full energy and day/night spectrum [20], 42 data points.
- SK4 2055-day day-night asymmetry [21] and 2365-day energy spectrum [22], 24 data points.
- SNO combined analysis [23], 7 data points.

JHEP01(2017)087

- Borexino Phase-I 740.7-day low-energy data [24], 33 data points.
- Borexino Phase-I 246-day high-energy data [25], 6 data points.
- Borexino Phase-II 408-day low-energy data [26], 42 data points.

Atmospheric experiments.

- IceCube/DeepCore 3-year data [48, 71], 64 data points.

Reactor experiments.

- KamLAND combined DS1 & DS2 spectrum [32], 17 data points.
- CHOOZ energy spectrum [33], 14 data points.
- Palo-Verde total rate [34], 1 data point.
- Double-Chooz FD-I (461 days) and FD-II (212 days) spectra [35], 54 data points.
- Daya-Bay 1230-day spectrum [36], 34 data points.
- Reno 800-day near & far total rates [37], 2 data points (with free normalization).
- SBL reactor data (including Daya-Bay total flux at near detector), 77 data points [38, 72].

Accelerator experiments.

- MINOS 10.71×10^{20} pot ν_μ-disappearance data [27], 39 data points.
- MINOS 3.36×10^{20} pot $\bar{\nu}_\mu$-disappearance data [27], 14 data points.
- MINOS 10.6×10^{20} pot ν_e-appearance data [28], 5 data points.
- MINOS 3.3×10^{20} pot $\bar{\nu}_e$-appearance data [28], 5 data points.
- T2K 7.48×10^{20} pot ν_μ-disappearance data [29, 30], 28 data points.
- T2K 7.48×10^{20} pot ν_e-appearance data [29, 30], 5 data points.
- T2K 7.47×10^{20} pot $\bar{\nu}_\mu$-disappearance data [29, 30], 63 data points.
- T2K 7.47×10^{20} pot $\bar{\nu}_e$-appearance data [29, 30], 1 data point.
- NOνA 6.05×10^{20} pot ν_μ-disappearance data [31], 18 data points.
- NOνA 6.05×10^{20} pot ν_e-appearance data [31], 10 data points.

Open Access. This article is distributed under the terms of the Creative Commons Attribution License (CC-BY 4.0), which permits any use, distribution and reproduction in any medium, provided the original author(s) and source are credited.

References

[1] B. Pontecorvo, *Neutrino Experiments and the Problem of Conservation of Leptonic Charge*, *Sov. Phys. JETP* **26** (1968) 984 [INSPIRE].

JHEP01(2017)087

[2] V.N. Gribov and B. Pontecorvo, *Neutrino astronomy and lepton charge*, *Phys. Lett.* **28B** (1969) 493 [INSPIRE].

[3] M.C. Gonzalez-Garcia and M. Maltoni, *Phenomenology with Massive Neutrinos*, *Phys. Rept.* **460** (2008) 1 [arXiv:0704.1800] [INSPIRE].

[4] C. Giunti, *Light Sterile Neutrinos: Status and Perspectives*, *Nucl. Phys.* **B 908** (2016) 336 [arXiv:1512.04758] [INSPIRE].

[5] Z. Maki, M. Nakagawa and S. Sakata, *Remarks on the unified model of elementary particles*, *Prog. Theor. Phys.* **28** (1962) 870 [INSPIRE].

[6] M. Kobayashi and T. Maskawa, *CP Violation in the Renormalizable Theory of Weak Interaction*, *Prog. Theor. Phys.* **49** (1973) 652 [INSPIRE].

[7] S.M. Bilenky, J. Hosek and S.T. Petcov, *On Oscillations of Neutrinos with Dirac and Majorana Masses*, *Phys. Lett.* **B 94** (1980) 495 [INSPIRE].

[8] P. Langacker, S.T. Petcov, G. Steigman and S. Toshev, *On the Mikheev-Smirnov-Wolfenstein (MSW) Mechanism of Amplification of Neutrino Oscillations in Matter*, *Nucl. Phys.* **B 282** (1987) 589 [INSPIRE].

[9] M.C. Gonzalez-Garcia, M. Maltoni and T. Schwetz, *Updated fit to three neutrino mixing: status of leptonic CP-violation*, *JHEP* **11** (2014) 052 [arXiv:1409.5439] [INSPIRE].

[10] F. Capozzi, E. Lisi, A. Marrone, D. Montanino and A. Palazzo, *Neutrino masses and mixings: Status of known and unknown 3ν parameters*, *Nucl. Phys.* **B 908** (2016) 218 [arXiv:1601.07777] [INSPIRE].

[11] D.V. Forero, M. Tortola and J.W.F. Valle, *Neutrino oscillations refitted*, *Phys. Rev.* **D 90** (2014) 093006 [arXiv:1405.7540] [INSPIRE].

[12] H. Minakata, H. Sugiyama, O. Yasuda, K. Inoue and F. Suekane, *Reactor measurement of theta(13) and its complementarity to long baseline experiments*, *Phys. Rev.* **D 68** (2003) 033017 [*Erratum ibid.* **D 70** (2004) 059901] [hep-ph/0211111] [INSPIRE].

[13] P. Huber, M. Lindner, T. Schwetz and W. Winter, *Reactor neutrino experiments compared to superbeams*, *Nucl. Phys.* **B 665** (2003) 487 [hep-ph/0303232] [INSPIRE].

[14] P. Huber, M. Lindner, M. Rolinec, T. Schwetz and W. Winter, *Prospects of accelerator and reactor neutrino oscillation experiments for the coming ten years*, *Phys. Rev.* **D 70** (2004) 073014 [hep-ph/0403068] [INSPIRE].

[15] B.T. Cleveland et al., *Measurement of the solar electron neutrino flux with the Homestake chlorine detector*, *Astrophys. J.* **496** (1998) 505 [INSPIRE].

[16] F. Kaether, W. Hampel, G. Heusser, J. Kiko and T. Kirsten, *Reanalysis of the GALLEX solar neutrino flux and source experiments*, *Phys. Lett.* **B 685** (2010) 47 [arXiv:1001.2731] [INSPIRE].

[17] SAGE collaboration, J.N. Abdurashitov et al., *Measurement of the solar neutrino capture rate with gallium metal. III: Results for the 2002–2007 data-taking period*, *Phys. Rev.* **C 80** (2009) 015807 [arXiv:0901.2200] [INSPIRE].

[18] SUPER-KAMIOKANDE collaboration, J. Hosaka et al., *Solar neutrino measurements in Super-Kamiokande-I*, *Phys. Rev.* **D 73** (2006) 112001 [hep-ex/0508053] [INSPIRE].

[19] SUPER-KAMIOKANDE collaboration, J.P. Cravens et al., *Solar neutrino measurements in Super-Kamiokande-II*, *Phys. Rev.* **D 78** (2008) 032002 [arXiv:0803.4312] [INSPIRE].

JHEP01(2017)087

[20] Super-Kamiokande collaboration, K. Abe et al., *Solar neutrino results in Super-Kamiokande-III*, *Phys. Rev.* **D 83** (2011) 052010 [arXiv:1010.0118] [INSPIRE].

[21] Y. Nakano, ^{8}B *solar neutrino spectrum measurement using Super-Kamiokande IV*, Ph.D. thesis, Tokyo University, Tokyo, Japan (2016).

[22] Y. Nakano, *Solar neutrino results from Super-Kamiokande*, talk given at the *38th International Conference on High Energy Physics*, Chicago, U.S.A., 3–10 August 2016.

[23] SNO collaboration, B. Aharmim et al., *Combined Analysis of all Three Phases of Solar Neutrino Data from the Sudbury Neutrino Observatory*, *Phys. Rev.* **C 88** (2013) 025501 [arXiv:1109.0763] [INSPIRE].

[24] Borexino collaboration, G. Bellini et al., *Precision measurement of the 7Be solar neutrino interaction rate in Borexino*, *Phys. Rev. Lett.* **107** (2011) 141302 [arXiv:1104.1816] [INSPIRE].

[25] Borexino collaboration, G. Bellini et al., *Measurement of the solar 8B neutrino rate with a liquid scintillator target and 3 MeV energy threshold in the Borexino detector*, *Phys. Rev.* **D 82** (2010) 033006 [arXiv:0808.2868] [INSPIRE].

[26] Borexino collaboration, G. Bellini et al., *Neutrinos from the primary proton-proton fusion process in the Sun*, *Nature* **512** (2014) 383 [INSPIRE].

[27] MINOS collaboration, P. Adamson et al., *Measurement of Neutrino and Antineutrino Oscillations Using Beam and Atmospheric Data in MINOS*, *Phys. Rev. Lett.* **110** (2013) 251801 [arXiv:1304.6335] [INSPIRE].

[28] MINOS collaboration, P. Adamson et al., *Electron neutrino and antineutrino appearance in the full MINOS data sample*, *Phys. Rev. Lett.* **110** (2013) 171801 [arXiv:1301.4581] [INSPIRE].

[29] K. Iwamoto, *Recent Results from T2K and Future Prospects*, talk given at the *38th International Conference on High Energy Physics*, Chicago, U.S.A., 3–10 August 2016.

[30] A. Cervera, *Latest Results from Neutrino Oscillation Experiments*, talk given at the *SUSY 2016 Conference*, Melbourne, Australia, 3–8 July 2016.

[31] P. Vahle, *New results from NOvA*, talk given at the *XXVII International Conference on Neutrino Physics and Astrophysics*, London, U.K., 4–9 July 2016.

[32] KamLAND collaboration, A. Gando et al., *Constraints on θ_{13} from A Three-Flavor Oscillation Analysis of Reactor Antineutrinos at KamLAND*, *Phys. Rev.* **D 83** (2011) 052002 [arXiv:1009.4771] [INSPIRE].

[33] CHOOZ collaboration, M. Apollonio et al., *Limits on neutrino oscillations from the CHOOZ experiment*, *Phys. Lett.* **B 466** (1999) 415 [hep-ex/9907037] [INSPIRE].

[34] Palo Verde collaboration, A. Piepke, *Final results from the Palo Verde neutrino oscillation experiment*, *Prog. Part. Nucl. Phys.* **48** (2002) 113 [INSPIRE].

[35] M. Ishitsuka, *New results of Double Chooz*, talk given at the *Rencontres de Moriond EW 2016*, La Thuile, Italy, 12–19 March 2016.

[36] Z. Yu, *Recent Results from the Daya Bay Experiment*, talk given at the *XXVII International Conference on Neutrino Physics and Astrophysics*, London, U.K., 4–9 July 2016.

[37] S.-H. Seo, *New Results from RENO*, talk given at the *XXVI International Conference on Neutrino Physics and Astrophysics*, Boston, U.S.A., 2–7 June 2014.

JHEP01(2017)087

[38] J. Kopp, P.A.N. Machado, M. Maltoni and T. Schwetz, *Sterile Neutrino Oscillations: The Global Picture*, *JHEP* **05** (2013) 050 [arXiv:1303.3011] [INSPIRE].

[39] H. Kwon, F. Boehm, A.A. Hahn, H.E. Henrikson, J.L. Vuilleumier, J.F. Cavaignac et al., *Search for Neutrino Oscillations at a Fission Reactor*, *Phys. Rev.* **D 24** (1981) 1097 [INSPIRE].

[40] CALTECH-SIN-TUM collaboration, G. Zacek et al., *Neutrino Oscillation Experiments at the Gosgen Nuclear Power Reactor*, *Phys. Rev.* **D 34** (1986) 2621 [INSPIRE].

[41] G.S. Vidyakin, V.N. Vyrodov, I.I. Gurevich, Yu. V. Kozlov, V.P. Martemyanov, S.V. Sukhotin et al., *Detection of Anti-neutrinos in the Flux From Two Reactors*, *Sov. Phys. JETP* **66** (1987) 243 [INSPIRE].

[42] G.S. Vidyakin et al., *Limitations on the characteristics of neutrino oscillations*, *JETP Lett.* **59** (1994) 390 [INSPIRE].

[43] A.I. Afonin, S.N. Ketov, V.I. Kopeikin, L.A. Mikaelyan, M.D. Skorokhvatov and S.V. Tolokonnikov, *A Study of the Reaction $\bar{\nu}_e + P \to e^+ + N$ on a Nuclear Reactor*, *Sov. Phys. JETP* **67** (1988) 213 [INSPIRE].

[44] A.A. Kuvshinnikov, L.A. Mikaelyan, S.V. Nikolaev, M.D. Skorokhvatov and A.V. Etenko, *Measuring the $\bar{\nu}_e + p \to n + e^+$ cross-section and beta decay axial constant in a new experiment at Rovno NPP reactor. (In Russian)*, *JETP Lett.* **54** (1991) 253 [INSPIRE].

[45] Y. Declais et al., *Search for neutrino oscillations at 15-meters, 40-meters and 95-meters from a nuclear power reactor at Bugey*, *Nucl. Phys.* **B 434** (1995) 503 [INSPIRE].

[46] Y. Declais et al., *Study of reactor anti-neutrino interaction with proton at Bugey nuclear power plant*, *Phys. Lett.* **B 338** (1994) 383 [INSPIRE].

[47] Z.D. Greenwood et al., *Results of a two position reactor neutrino oscillation experiment*, *Phys. Rev.* **D 53** (1996) 6054 [INSPIRE].

[48] IceCube collaboration, M.G. Aartsen et al., *Determining neutrino oscillation parameters from atmospheric muon neutrino disappearance with three years of IceCube DeepCore data*, *Phys. Rev.* **D 91** (2015) 072004 [arXiv:1410.7227] [INSPIRE].

[49] NuFIT webpage, http://www.nu-fit.org.

[50] M.C. Gonzalez-Garcia, M. Maltoni, J. Salvado and T. Schwetz, *Global fit to three neutrino mixing: critical look at present precision*, *JHEP* **12** (2012) 123 [arXiv:1209.3023] [INSPIRE].

[51] T.A. Mueller et al., *Improved Predictions of Reactor Antineutrino Spectra*, *Phys. Rev.* **C 83** (2011) 054615 [arXiv:1101.2663] [INSPIRE].

[52] P. Huber, *On the determination of anti-neutrino spectra from nuclear reactors*, *Phys. Rev.* **C 84** (2011) 024617 [*Erratum ibid.* **C 85** (2012) 029901] [arXiv:1106.0687] [INSPIRE].

[53] G. Mention et al., *The Reactor Antineutrino Anomaly*, *Phys. Rev.* **D 83** (2011) 073006 [arXiv:1101.2755] [INSPIRE].

[54] T. Schwetz, *What is the probability that theta(13) and CP-violation will be discovered in future neutrino oscillation experiments?*, *Phys. Lett.* **B 648** (2007) 54 [hep-ph/0612223] [INSPIRE].

[55] M. Blennow, P. Coloma and E. Fernandez-Martinez, *Reassessing the sensitivity to leptonic CP-violation*, *JHEP* **03** (2015) 005 [arXiv:1407.3274] [INSPIRE].

JHEP01(2017)087

[56] M.C. Gonzalez-Garcia and C. Pena-Garay, *Three neutrino mixing after the first results from K2K and KamLAND*, *Phys. Rev.* **D 68** (2003) 093003 [hep-ph/0306001] [INSPIRE].

[57] C. Jarlskog, *Commutator of the Quark Mass Matrices in the Standard Electroweak Model and a Measure of Maximal CP-violation*, *Phys. Rev. Lett.* **55** (1985) 1039 [INSPIRE].

[58] PARTICLE DATA GROUP collaboration, C. Patrignani et al., *Review of Particle Physics*, *Chin. Phys.* **C 40** (2016) 100001 [INSPIRE].

[59] L. Wolfenstein, *Neutrino Oscillations in Matter*, *Phys. Rev.* **D 17** (1978) 2369 [INSPIRE].

[60] S.P. Mikheev and A. Yu. Smirnov, *Resonance Amplification of Oscillations in Matter and Spectroscopy of Solar Neutrinos*, *Sov. J. Nucl. Phys.* **42** (1985) 913 [INSPIRE].

[61] J. Bergstrom, M.C. Gonzalez-Garcia, M. Maltoni, C. Pena-Garay, A.M. Serenelli and N. Song, *Updated determination of the solar neutrino fluxes from solar neutrino data*, *JHEP* **03** (2016) 132 [arXiv:1601.00972] [INSPIRE].

[62] N. Vinyoles et al., *A new Generation of Standard Solar Models*, arXiv:1611.09867 [INSPIRE].

[63] T.J.C. Bezerra, H. Furuta and F. Suekane, *Measurement of Effective Δm^2_{31} using Baseline Differences of Daya Bay, RENO and Double CHOOZ Reactor Neutrino Experiments*, arXiv:1206.6017 [INSPIRE].

[64] H. Seo et al., *Spectral Measurement of the Electron Antineutrino Oscillation Amplitude and Frequency using 500 Live Days of RENO Data*, arXiv:1610.04326 [INSPIRE].

[65] SUPER-KAMIOKANDE collaboration, R. Wendell, *Atmospheric Results from Super-Kamiokande*, *AIP Conf. Proc.* **1666** (2015) 100001 [arXiv:1412.5234] [INSPIRE].

[66] J. Kameda, *Recent results from Super-Kamokande on atmospheric neutrinos and next project: Hyper-Kamioande*, talk given at the *XII Rencontres de Vietnam: NuFact 2016*, Qui Nhon, Vietnam, 21–27 August 2016.

[67] K. P. Lee, *Study of the neutrino mass hierarchy with the atmospheric neutrino data observed in SuperKamiokande*, Ph.D. thesis, The University of Tokyo, Tokyo, Japan (2012).

[68] J. Elevant and T. Schwetz, *On the determination of the leptonic CP phase*, *JHEP* **09** (2015) 016 [arXiv:1506.07685] [INSPIRE].

[69] M. Blennow, P. Coloma, P. Huber and T. Schwetz, *Quantifying the sensitivity of oscillation experiments to the neutrino mass ordering*, *JHEP* **03** (2014) 028 [arXiv:1311.1822] [INSPIRE].

[70] S.S. Wilks, *The Large-Sample Distribution of the Likelihood Ratio for Testing Composite Hypotheses*, *Annals Math. Statist.* **9** (1938) 60.

[71] ICECUBE collaboration, J.P. Yañez et al., *IceCube Oscillations: 3 years muon neutrino disappearance data*, http://icecube.wisc.edu/science/data/nu_osc.

[72] C. Zhang, *Recent Results From Daya Bay*, talk given at the *XXVI International Conference on Neutrino Physics and Astrophysics*, Boston, U.S.A., 2–7 June 2014.

JHEP01(2017)087

Chapter3

Double-Cascades Events from New Physics in IceCube

SM can be considered as low energy effective model, so it can be extended by introducing higher-dimension operators in terms of the SM fields

$$\mathscr{L}_{\text{eff}} = \mathscr{L}_{\text{SM}} + \frac{\mathscr{L}_{d=5}}{\Lambda} + \frac{\mathscr{L}_{d=6}}{\Lambda^2} + \cdots \tag{3.1}$$

where Λ is the cutoff scale of the effective field theory. The lowest dimensional operator that generates Majorana neutrino masses after the Higgs mechanism is the dimensional five operator, called Weinberg operator. Which is the only possible $d = 5$ operator [33]

$$\frac{\mathscr{L}_{d=5}}{\Lambda} = \frac{1}{2} c_{\alpha\beta}^{d=5} \left(\overline{L_{L\alpha}^{c}} \tilde{\Phi}^{*} \right) \left(\tilde{\Phi}^{\dagger} L_{L\beta} \right) \tag{3.2}$$

where L_L is the lepton doublet (Table 1.1), $\tilde{\Phi} = \imath\sigma_2\Phi^*$, σ_2 is the Pauli matrix and $\Phi = (\phi^+, \phi^0)^T$ is the standard Higgs doublet. $c_{\alpha\beta}^{d=5} \sim 1/\Lambda$ is a model independent coefficient of inverse mass dimension, which is suppressed by the scale Λ. After the electroweak symmetry breaking, the neutrino gets a mass of the order $m_\nu \sim \langle\Phi\rangle^2 / \Lambda$. For $o(1)$ couplings, the scale is of the order of the Grand Unified Theory $\Lambda \geq 10^{13}$ GeV.

There are only three ways to generate the Weinberg operator at tree level, they are called the see-saw models [34, 35], (Sec. 1.3.1). In the *Type-I* see-saw, the mediator is a singlet fermion. In the *Type-II* see-saw, a triplet scalar is added into the SM. In the *Type-III* see-saw, a triplet fermion works as a mediator. For each of the three see-saw models, we can obtain a $d = 5$ operator by integrating out the heavy degrees of freedom.

In the next work, we have considered the *Type-I* see-saw with a mediator at the scale of 1 GeV. In order to generate neutrino masses ($<$ eV) [16] it is needed an additional suppression mechanism for the neutrino masses. The most studied are [34]:

- The generation of the neutrino mass by loop corrections [36].
- The additional suppression of the neutrino mass due to a small lepton number violation [37, 38].
- The generation of the neutrino masses by higher dimensional operators [39], where the $d = 5$ operators is suppressed.

Double-Cascade Events from New Physics in Icecube

Pilar Coloma,[1,*] Pedro A. N. Machado,[1,†] Ivan Martinez-Soler,[2,‡] and Ian M. Shoemaker[3,§]
[1]*Theory Department, Fermi National Accelerator Laboratory, Post Office Box 500, Batavia, Illinois 60510, USA*
[2]*Instituto de Fisica Teorica UAM-CSIC, Calle Nicolas Cabrera 13-15, Universidad Autonoma de Madrid, Cantoblanco, E-28049 Madrid, Spain*
[3]*Department of Physics, University of South Dakota, Vermillion, South Dakota 57069, USA*
(Received 18 August 2017; published 16 November 2017)

A variety of new physics models allows for neutrinos to up-scatter into heavier states. If the incident neutrino is energetic enough, the heavy neutrino may travel some distance before decaying. In this work, we consider the atmospheric neutrino flux as a source of such events. At IceCube, this would lead to a "double-bang" (DB) event topology, similar to what is predicted to occur for tau neutrinos at ultrahigh energies. The DB event topology has an extremely low background rate from coincident atmospheric cascades, making this a distinctive signature of new physics. Our results indicate that IceCube should already be able to derive new competitive constraints on models with GeV-scale sterile neutrinos using existing data.

DOI: 10.1103/PhysRevLett.119.201804

Introduction.—Although neutrino physics has rapidly moved into the precision era, a number of fundamental questions remain unanswered. Perhaps the most important among these is the mechanism responsible for neutrino masses. In the most naïve extension of the standard model (SM), neutrino masses and mixing can be successfully generated by adding at least two right-handed neutrinos (N_R), with small Yukawa couplings Y_ν to the left-handed lepton doublets L_L and the Higgs boson ϕ. In this framework, Dirac neutrino masses are generated after electroweak (EW) symmetry breaking, as for the rest of the SM fermions. As singlets of the SM the right-handed neutrinos may also have a Majorana mass term, since it is allowed by gauge symmetry. In this case, the neutrino mass Lagrangian reads

$$\mathcal{L}^{\nu}_{\rm mass} \supset Y_\nu \bar{L}_L \tilde{\phi} N_R + \frac{1}{2} M_R \overline{N^c_R} N_R + \text{H.c.},$$

where $\tilde{\phi} \equiv i\sigma_2 \phi^*$, $N^c_R \equiv C\bar{N}^T_R$ is the charge conjugate of N_R and we have omitted flavor and mass indices. This is the well-known type I seesaw Lagrangian [1–3]. Traditionally, the type I seesaw assumed a very high Majorana mass scale M_R. For $M_R \gg v$ the light neutrino masses are proportional to $m_\nu \propto Y^\dagger_\nu M^{-1}_R Y_\nu v^2$, where v is the Higgs vacuum expectation value, while the right-handed neutrino masses would be approximately $m_N \simeq M_R + \mathcal{O}(m_\nu)$. In this framework the SM neutrino masses are naturally suppressed by the new physics scale and can be much smaller than the charged fermion masses without the need for tiny Yukawa couplings. However, such heavy neutrinos are too heavy to be produced in colliders, and the inclusion of very massive Majorana neutrinos would considerably worsen the hierarchy problem for the Higgs mass [4].

Models with lower values of m_N can lead to a more interesting phenomenology, testable at low-energy experiments, and possibly even solve some of the other problems of the SM. For example, keV neutrinos offer a very good dark matter candidate [5], while Majorana neutrinos with masses $m_N \sim \mathcal{O}(1\text{–}100)$ GeV can successfully generate the matter-antimatter asymmetry of the Universe [6–9]. While right-handed neutrinos with masses above the EW scale are subject to very tight bounds from EW observables and charged lepton flavor violating experiments [10,11], these constraints fade away for lower masses. Indeed, for right-handed neutrinos in the (keV–GeV) range, the strongest constraints come from precision measurements of meson decays [12,13], muon decays, and other EW transitions; see, e.g., Ref. [14] for a review.

In this Letter we point out that IceCube and DeepCore can be used to test models with GeV neutrinos directly. To this end, we consider events with a "double-bang" (DB) topology. A schematic illustration of the event topology can be seen in Fig. 1. In the first interaction, an atmospheric neutrino would up-scatter off a nucleus into a heavier state. This generally leaves a visible shower (or cascade) in the

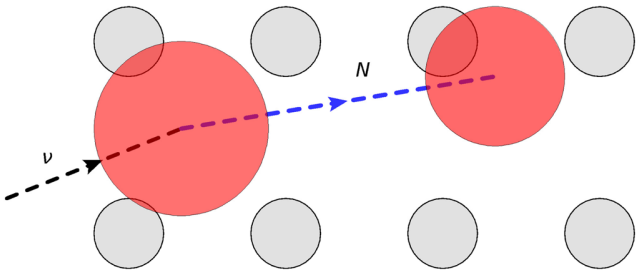

FIG. 1. Schematic illustration of a DB event in IceCube. An incoming active neutrino ν up-scatters into a heavy neutrino N, which then propagates and decays into SM particles. The small circles represent the DOMs while the large circles indicate the positions where energy was deposited.

 © 2017 American Physical Society

detector coming from the hadronic part of the vertex. After traveling a macroscopic distance inside the instrumented ice, the heavy neutrino would decay back to SM particles. The decay will produce a second cascade if the final state involves charged particles or photons which can be detected by IceCube's digital optical modules (DOMs). Thus, the final DB topology would be two cascades (or "bangs") visibly separated, but with no visible track connecting them. A similar topology is predicted to occur in the SM from the production of a τ lepton in ν_τ charged-current (CC) scattering at PeV energies [15], and has already been searched for by the collaboration [16]. In our case, however, the heavy neutrinos will be produced from the atmospheric neutrino flux and thus produce much lower energy DBs.

To illustrate some of the new physics scenarios giving rise to low-energy DB events we consider two basic scenarios depending on the main production or decay mode of the heavy state: (i) through mixing with the light neutrinos, and (ii) through a transition magnetic moment involving the light neutrinos.

Heavy neutrino production via mixing.—The measurement of the invisible decay width of the Z implies that, if additional neutrinos below the EW scale are present, they cannot couple directly to the Z (i.e., they should be "sterile"). For simplicity, let us focus on a scenario where there is sizable mixing with only one heavy neutrino while the others are effectively decoupled. We may write the flavor states ν_α as a superposition of the mass eigenstates as

$$\nu_{\alpha L} = \sum_{i=1}^{3} U_{\alpha i}\nu_{iL} + U_{\alpha 4}N^c_{4R}, \tag{1}$$

where U is the 4×4 unitary mixing matrix that changes between the mass and the flavor bases. For a sterile neutrino with a mass $m_N \sim \mathcal{O}(0.1\text{–}10)$ GeV, its mixing with $\nu_{e,\mu}$ is severely constrained as $|U_{\alpha 4}|^2 \lesssim 10^{-5}\text{–}10^{-8}$ $(\alpha = e,\ \mu)$ [14]. Conversely, the mixing with ν_τ is much more difficult to probe, given the technical challenges of producing and detecting tau neutrinos. For $m_N \sim \mathcal{O}(0.1-10)$ GeV the most stringent bounds are derived from the DELPHI [17] and CHARM [18] experiments. However, a mixing as large as $|U_{\tau 4}|^2 \sim 10^{-2}$ is still allowed for masses around $m_N \sim \mathcal{O}(400)$ MeV [14].

At IceCube, the atmospheric neutrino flux can be used to constrain the values of $U_{\alpha 4}$ directly. Atmospheric neutrinos are produced as a result of the cosmic rays impacting the atmosphere. At the production point, this flux is primarily composed of ν_μ and ν_e. However, for neutrinos crossing Earth a large fraction of the initial ν_μ flux will have oscillated into ν_τ by the time the neutrinos reach the detector. Therefore, here we focus on probing the mixing with ν_τ since this one is much harder to constrain by other means.

To this end, we propose to conduct a search for low-energy DB events. In each event the first cascade is produced from a neutral-current (NC) interaction with a nucleon n, as $\nu n \to N n$. This process is mediated by a Z boson and takes place via mixing between the light and heavy states. Neglecting corrections due to the mass of the heavy neutrino, the up-scattering cross section goes as $\sigma_{\nu_\tau N} \simeq \sigma_\nu^{\rm NC} \times |U_{\tau 4}|^2$, where $\sigma_\nu^{\rm NC}$ is the NC neutrino-nucleon cross section in the SM. Unless the process is quasielastic, it will generally lead to a hadronic shower in the detector. Here we compute the neutrino-nucleon deep-inelastic scattering (DIS) cross section using the parton model, imposing a lower cut on the hadronic shower of 5 GeV so it is observable [19]. In fact, throughout our whole analysis we will assume perfect detection efficiencies above threshold. Although this may be simplistic, we find it adequate to demonstrate the potential of IceCube to search for new physics with low energy DB events. Once the heavy state has been produced, its decay is controlled by kinematics and the SM interactions inherited from the mixing with the active neutrinos. The partial decay widths of a heavy neutrino can be found in Refs. [14,20] and were recomputed here. The decay channels include two-body decays into a charged lepton (active neutrino) and a charged (neutral) meson, and three body decays into charged leptons and light neutrinos. The deposited energy in the second shower is also required to be above 5 GeV. It should be noted that if the N decays into three light neutrinos the second shower will be invisible: those events do not contribute to our signal. As an example, for $m_N = 1$ GeV and $|U_{\tau 4}|^2 = 10^{-3}$, the boosted decay length (for an energy of 10 GeV) is $L_{\rm lab} \sim 20$ m.

The number of DB events from ν_τ mixing with a heavy neutrino, for two cascades taking place within a distance L, is proportional to

$$\int dE_\nu dc_\theta \mathcal{B} \frac{d\phi_{\nu_\mu}}{dE_\nu dc_\theta} P_{\mu\tau}(c_\theta, E_\nu) \frac{d\sigma_{\nu_\tau N}}{dE_\nu} P_d(L) V(L, c_\theta), \tag{2}$$

where E_ν is the incident neutrino energy and $c_\theta \equiv \cos\theta$ is the cosine of its zenith angle. The atmospheric ν_μ flux [21] is given by ϕ_{ν_μ} while $P_{\mu\tau}$ is the oscillation probability in the $\nu_\mu \to \nu_\tau$ channel, which depends on the length of the baseline traveled (inferred from the zenith angle) and the energy. Here, $P_d(L) = e^{-L/L_{\rm lab}}/L_{\rm lab}$ is the probability for the heavy state to decay after traveling a distance L, while $\mathcal{B}$ is its branching ratio into visible final states (i.e., excluding the decay into three light neutrinos). Antineutrino events will give a similar contribution to the total number of events, replacing ϕ_{ν_μ}, $\sigma_{\nu_\tau N}$, and $P_{\mu\tau}$ in Eq. (2) by their analogous expressions for antineutrinos.

In Eq. (2) we have omitted a normalization constant which depends on the number of target nuclei and the data taking period, but we explicitly include an effective volume

$V(L, c_\theta)$. In this work, this was computed using Monte Carlo integration. First, for triggering purposes we require that at least three (four) DOMs detect the first shower simultaneously, if it takes place inside (outside) DeepCore [22]. Once the trigger goes off, all the information in the detector is recorded, and we thus assume that the second shower is always observed as long as it is close enough to a DOM. Eventually, the energy of a cascade determines the distance from which it can be detected by a DOM: the longer the distance, the more energetic the cascade should be so the light can reach the DOM without being absorbed by the ice first. Here we assume that a cascade is seen by a DOM if it takes place within a distance of 36 m, since this is roughly the maximum distance between an event and a DOM inside DeepCore [22]. This is conservative, since showers with energies much above 5 GeV will typically reach a DOM from longer distances. Finally, a minimum separation is required between the two showers so they can be resolved. This ultimately depends on the time resolution of the DOMs. Following Ref. [16], IceCube can distinguish pulses separated by $T \sim 66$ ns. Thus, we require a minimum distance between the two showers of $T/c = 20$ m.

The dominant source of background for DB events is given by two coincident cascades taking place within the same time window Δt. The rate can be estimated as [23] $N_{\rm bkg} \simeq C_{\rm DB}^2 (\Delta t/T)^2$, where $C_{\rm DB}^2 = N_{\rm casc}(N_{\rm casc} - 1)/2$ comes from the number of possible combination of pairs, and $N_{\rm casc}$ is the number of cascade events within a time period T. The number of cascades in the DeepCore volume, with a deposited energy between 5.6 and 100 GeV, is $N_{\rm casc} \simeq 2 \times 10^4$ yr^{-1} [24]. These include CC events with electrons, taus, or low-energy muons in the final state (which do not leave long identificable tracks), as well as NC events. A particle traveling at the speed of light traverses 1 km in $\sim 10^{-5}$ s. Thus, for a conservative time interval $\Delta t = 10^{-3}$ s, we get $N_{\rm bkg} < 10^{-11}$ yr^{-1}.

In view of the negligible background rate, we proceed to determine the region in parameter space where at least one signal event would be expected in six years of data taking at IceCube. This is shown in Fig. 2 as a function of the mass and mixing of the heavy neutrino. The solid line shows the results using the full IceCube volume, while for the dashed line only DeepCore was considered. Our results indicate that IceCube could improve over present bounds between 1 and 2 orders of magnitude, and probe values of the mixing as small as $|U_{\tau 4}|^2 \sim 5 \times 10^{-5}$. According to these results, IceCube could test the proposed solution to the flavor anomalies in the B sector proposed in Ref. [25].

Heavy neutrino production via a transition magnetic moment.—Alternatively, the light neutrinos may interact with the heavy state N through a higher-dimensional operator. As an example, we consider a neutrino transition magnetic moment (NTMM) $\mu_{\rm tr}$:

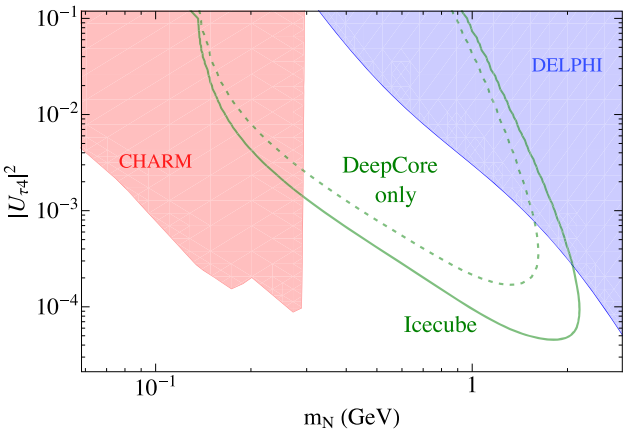

FIG. 2. Expected potential of IceCube to constrain the mixing between ν_τ and a heavy neutrino. In the region enclosed by the solid green contour, more than one DB event is expected during six years of data taking at IceCube. The dashed contour shows the most conservative result, where only the DeepCore volume is considered. The shaded regions are disfavored by CHARM [18] and DELPHI [17] at 90% and 95% C.L., respectively; see Ref. [14].

$$\mathcal{L}_\nu \supset -\mu_{\rm tr} \bar{\nu}_{\alpha L} \sigma_{\rho\sigma} N_{4R} F^{\rho\sigma}, \tag{3}$$

where $F^{\rho\sigma}$ is the electromagnetic field strength tensor and $\sigma_{\rho\sigma} = (i/2)[\gamma_\rho, \gamma_\sigma]$. For simplicity, in this scenario we assume negligible mixing with the light neutrinos, so both the production and decay of the heavy neutrino are controlled by the magnetic moment operator. In the rest frame of N, its decay width reads $\Gamma(N \to \nu\gamma) = \mu_{\rm tr}^2 M^3/(16\pi)$. For $m_N = 100$ MeV, $\mu_{\rm tr} = 10^{-8} \mu_B$ (where μ_B is the Bohr magneton), and a typical energy of 10 GeV this gives a decay length in the lab frame $L_{\rm lab} \sim 14$ m.

Neutrinos with a NTMM could scatter off both electrons and nuclei in the IceCube detector. However, for the range of energies and masses considered in this work, the largest effect comes from scattering on nuclei. In the DIS regime, the cross section for the scattering $\nu n \to N n$ via the operator in Eq. (3) reads [26]

$$\frac{d^2\sigma_{\nu n \to N n}}{dx dy} \simeq 16\pi\alpha\mu_{\rm tr}^2 \left(\frac{1-y}{y}\right) \sum_i e_i^2 f_i(x), \tag{4}$$

where α is the fine structure constant, $f_i(x)$ is the parton distribution function for the parton i, x is the parton momentum fraction, and e_i^2 is its electric charge. Here, $y \equiv 1 - E_N/E_\nu = E_r/E_\nu$, where E_N is the energy of the outgoing heavy neutrino and E_r is the deposited energy. In Eq. (4) we have ignored the impact of the heavy neutrino mass in the cross section, which will be negligible in the region of interest. However, energy and momentum conservation requires

$$E_r^2 - W^2 - [m_N^2 - W^2 - 2xE_\nu m_n - x^2 m_n^2 + 2E_r(xm_n + E_\nu)]^2/4E_\nu^2 > 0, \quad (5)$$

where W^2 is the invariant mass squared of the outgoing hadronic system and m_n is the nucleon mass. Using Eqs. (4) and (5) we can estimate the number of DB events in IceCube using a similar expression to Eq. (2). A 5 GeV lower cut is also imposed on the deposited energy for each shower. Assuming that the decay only takes place via NTMM, the branching ratio to visible final states in this scenario is $\mathcal{B} = 1$.

Before presenting our results, let us discuss first the current constraints on NTMM. Previous measurements of the neutrino-electron elastic scattering cross section can be translated into a bound on NTMM. The corresponding cross section reads

$$\frac{d\sigma_{\nu e\to Ne}}{dE_r} = \mu_{\rm tr}^2\alpha\left[\frac{1}{E_r} - \frac{m_N^2}{2E_\nu E_r m_e}\left(1 - \frac{E_r}{2E_\nu} + \frac{m_e}{2E_\nu}\right) - \frac{1}{E_\nu} + \frac{m_N^4(E_r - m_e)}{8E_\nu^2 E_r^2 m_e^2}\right], \quad (6)$$

where m_e is the electron mass. Moreover, for given E_ν and E_r, the maximum m_N allowed by kinematics is

$$m_{N,\rm max}^2 = 2[E_\nu\sqrt{E_r(E_r + 2m_e)} - E_r(E_\nu + m_e)]. \quad (7)$$

Several experiments can be used to derive constraints from their measurement of neutrino-electron scattering. DONUT derived a constraint on the ν_τ magnetic moment, $\mu_\tau < 3.9\times10^{-7}\mu_B$ at 90% C.L. [27]. For NOMAD [28], Primakoff conversion $\nu_\mu + X \to \nu_s + X(+\gamma)$ (where X is a nucleus) constrains NTMM [29]. Recently, the Borexino collaboration reported the limit $\mu_\nu < 2.8\times10^{-11}\mu_B$ at 90% C.L. [30], valid for all neutrino flavors. For CHARM-II we have derived an approximate limit on the magnetic moment of ν_μ requiring the NTMM cross section in Eq. (6) to be below the reported precision on the measurement of the neutrino-electron cross section (Bounds on NTMM from neutrino-nucleus scattering are less competitive. For example, using NuTeV data [31] we find an approximate bound $\mu_{\rm tr} \lesssim 10^{-4}\mu_B$.), assuming $\langle E_\nu\rangle \sim 24$ and $\langle E_r\rangle \sim 5$ GeV.

The ALEPH constraint on the branching ratio $\mathrm{BR}(Z \to \nu N \to \nu\nu\gamma) < 2.7\times10^{-5}$ [32] translates into the bound $|U_{\alpha 4}|^2(\mu_{\rm tr}/\mu_B)^2 < 1.9\times10^{-16}$ [33], $\alpha \equiv e,\ \mu,\ \tau$. Saturating the bound from direct searches on the mixing $|U_{\tau 4}|^2$ gives the strongest possible constraint from ALEPH data, which is competitive in the mass region $m_N \gtrsim 5$–10 GeV.

Additional bounds on $\mu_{\rm tr}$ can also be derived from cosmology. In the SM, neutrino decoupling takes places at temperatures $T \sim 2$ MeV. However, the additional interaction between photons and neutrinos induced by a magnetic moment may lead to a delayed neutrino decoupling. This imposes an upper bound on $\mu_{\rm tr}$ (see, e.g., Ref. [34] for analogous active limits).

Our results for the NTMM scenario are shown in Fig. 3. The shaded regions are disfavored by past experiments as outlined above. These, however, fade away for heavy neutrino masses above the maximum value allowed by kinematics in each case, given by Eq. (5). [To derive $m_{N,\rm max}$ for Borexino, DONUT, and CHARM-II, we have used the following typical values of $(\langle E_\nu\rangle, \langle E_r\rangle)$: (420, 230 keV), (100, 20 GeV), and (24, 5 GeV), respectively.] The solid contours, on the other hand, indicate the regions where more than one DB event would be expected at IceCube, for six years of data taking. The left panel shows the results for a NTMM between N and ν_τ. Our results indicate that IceCube has the potential to improve more than 2 orders of magnitude over current constraints for NTMM, for $m_N \sim 1$ MeV–1 GeV. The right panel, on the other hand, shows the results for a NTMM between N and ν_μ. In this case, the computation of the number of events is identical as for $\nu_\tau - N$ transitions, replacing the oscillation probability

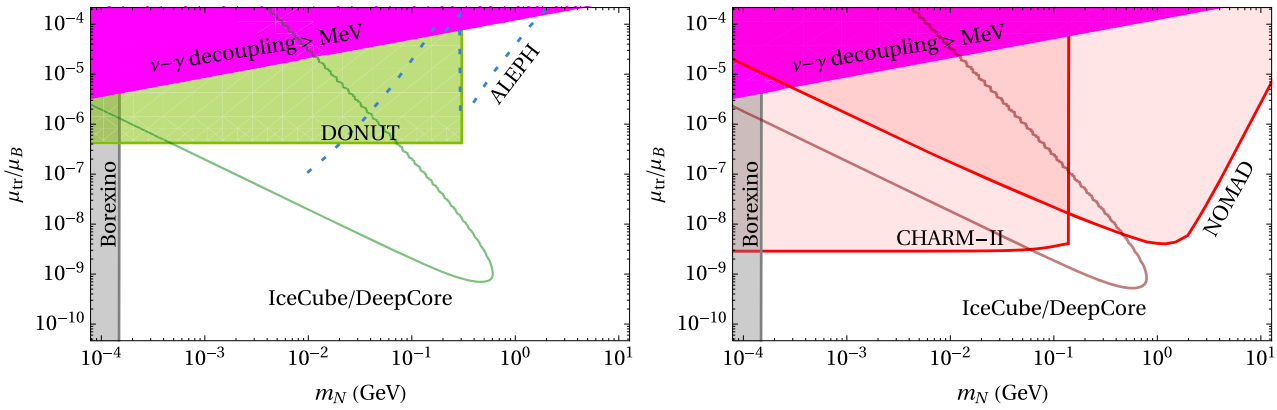

FIG. 3. Expected potential to constrain magnetic moments leading to the transitions $\nu_\tau - N$ (left panel) and $\nu_\mu - N$ (right panel) at IceCube. In the region enclosed by the solid contours, at least one DB event would be expected at IceCube, for a data taking period of six years. The shaded regions are disfavored by previous experiments; see text for details.

$P_{\mu\tau}$ by $P_{\mu\mu}$ in Eq. (2). Even though current constraints are stronger for ν_μ, we also find that IceCube could significantly improve over present bounds.

Conclusions.—In this Letter, we have studied the potential of the IceCube detector to look for new physics using low-energy DB events. The collaboration has already performed searches for events with this topology at ultrahigh energies, which are expected in the SM from the CC interactions of PeV tau neutrinos. In this work we have shown how very simple new physics scenarios with GeV-scale right-handed neutrinos would lead to a similar topology, with two low-energy cascades that could be spatially resolved in the detector. We find that IceCube may be able to improve by orders of magnitude the current constraints on the two scenarios considered here. A DB search may also be sensitive to nonminimal dark matter models, such as the one proposed in Ref. [35].

We warmly thank Tyce de Young for useful discussions on the IceCube detector performance. We are very grateful as well for insightful discussions with Kaladi Babu, Enrique Fernandez-Martinez, Jacobo Lopez-Pavon, Kohta Murase, and Josef Pradler. This work received partial support from the European Union through the Elusives (H2020-MSCA-ITN-2015-674896) and InvisiblesPlus (H2020-MSCA-RISE-2015-690575) grants. I. M.-S. is very grateful to the University of South Dakota for its support. I. M-S. acknowledges support through the Spanish Grants No. FPA2015-65929-P (MINECO/FEDER, UE) and the Spanish Research Agency (Agencia Estatal de Investigación) through the Grants IFT "Centro de Excelencia Severo Ochoa" SEV-2012-0249 and SEV-2016-0597, and would like to thank the Fermilab theory department for their kind hospitality during his visits, where this work was started. This manuscript has been authored by Fermi Research Alliance, LLC under Contract No. DE-AC02-07CH11359 with the U.S. Department of Energy, Office of Science, Office of High Energy Physics. The publisher, by accepting the article for publication, acknowledges that the United States Government retains a non-exclusive, paid-up, irrevocable, world-wide license to publish or reproduce the published form of this manuscript, or allow others to do so, for United States Government purposes.

*pcoloma@fnal.gov
†pmachado@fnal.gov
‡ivanj.m@csic.es
§ian.shoemaker@usd.edu

[1] P. Minkowski, Phys. Lett. **67B**, 421 (1977).
[2] M. Gell-Mann, P. Ramond, and R. Slansky, Conference Proceedings **C790927**, 315 (1979).
[3] R. N. Mohapatra and G. Senjanovic, Phys. Rev. Lett. **44**, 912 (1980).
[4] F. Vissani, Phys. Rev. D **57**, 7027 (1998).
[5] A. Kusenko, Phys. Rep. **481**, 1 (2009).
[6] T. Asaka, S. Blanchet, and M. Shaposhnikov, Phys. Lett. B **631**, 151 (2005).
[7] T. Asaka and M. Shaposhnikov, Phys. Lett. B **620**, 17 (2005).
[8] P. Hernández, M. Kekic, J. López-Pavón, J. Racker, and J. Salvado, J. High Energy Phys. 08 (2016) 157.
[9] P. Hernández, M. Kekic, J. López-Pavón, J. Racker, and N. Rius, J. High Energy Phys. 10 (2015) 067.
[10] S. Antusch and O. Fischer, J. High Energy Phys. 10 (2014) 094.
[11] E. Fernandez-Martinez, J. Hernandez-Garcia, and J. Lopez-Pavon, J. High Energy Phys. 08 (2016) 033.
[12] R. E. Shrock, Phys. Lett. **96B**, 159 (1980).
[13] R. E. Shrock, Phys. Rev. D **24**, 1232 (1981).
[14] A. Atre, T. Han, S. Pascoli, and B. Zhang, J. High Energy Phys. 05 (2009) 030.
[15] J. G. Learned and S. Pakvasa, Astropart. Phys. **3**, 267 (1995).
[16] M. G. Aartsen *et al.* (IceCube Collaboration), Phys. Rev. D **93**, 022001 (2016).
[17] P. Abreu *et al.*, Z. Phys. C **74**, 57 (1997); **75**, 580E (1997).
[18] J. Orloff, A. N. Rozanov, and C. Santoni, Phys. Lett. B **550**, 8 (2002).
[19] M. G. Aartsen *et al.* (IceCube Collaboration), arXiv: 1707.07081.
[20] D. Gorbunov and M. Shaposhnikov, J. High Energy Phys. 10 (2007) 015; 11 (2013) 101E.11 (2013) 101(E).
[21] M. Honda, M. S. Athar, T. Kajita, K. Kasahara, and S. Midorikawa, Phys. Rev. D **92**, 023004 (2015).
[22] M. G. Aartsen *et al.* (IceCube Collaboration), J. Instrum. **12**, P03012 (2017).
[23] S.-F. Ge, M. Lindner, and W. Rodejohann, Phys. Lett. B **772**, 164 (2017).
[24] J. Hignight, *Measurements of atmospheric NuMu disappearance with IceCube-DeepCore* (2017), talk given at the Lake Louise Winter Institute 2017, https://indico.cern.ch/event/531113/contributions/2430431/.
[25] G. Cvetič, F. Halzen, C. S. Kim, and S. Oh, arXiv: 1702.04335.
[26] See Supplemental Material at http://link.aps.org/supplemental/10.1103/PhysRevLett.119.201804 for details on the computation of the cross section for the scattering $\nu n \to Nn$ via a transition magnetic moment.
[27] R. Schwienhorst *et al.* (DONUT Collaboration), Phys. Lett. B **513**, 23 (2001).
[28] J. Altegoer *et al.* (NOMAD Collaboration), Nucl. Instrum. Methods Phys. Res., Sect. A **404**, 96 (1998).
[29] S. N. Gninenko and N. V. Krasnikov, Phys. Lett. B **450**, 165 (1999).
[30] M. Agostini *et al.* (Borexino Collaboration), arXiv: 1707.09355.
[31] G. P. Zeller *et al.* (NuTeV Collaboration), Phys. Rev. Lett. **88**, 091802 (2002); **90**, 239902E (2003).
[32] D. Decamp *et al.* (ALEPH Collaboration), Phys. Rep. **216**, 253 (1992).
[33] S. N. Gninenko, Phys. Rev. D **83**, 015015 (2011).
[34] N. Vassh, E. Grohs, A. B. Balantekin, and G. M. Fuller, Phys. Rev. D **92**, 125020 (2015).
[35] D. Kim, J.-C. Park, and S. Shin, Phys. Rev. Lett. **119**, 161801 (2017).

Chapter4

Non-standard neutrino interactions in the Earth and the flavor of astrophysical neutrinos

In the expansion of the SM lagrangian with higher dimensional operators (eq (3.1)), the operators with $d = 5$ correspond to a neutrino mass term, called Weinberg operator. For $d = 6$, there are some operators that lead the so-called Non-Standard Interactions (NSI) in the neutrino sector [40]

$$(\overline{\nu}_\alpha \gamma^\rho P_L \nu_\beta) \left(\overline{f} \gamma_\rho P f\right) \tag{4.1}$$

$$(\overline{\nu}_\alpha \gamma^\rho P_L l_\beta) \left(\overline{f'} \gamma_\rho P f\right) \tag{4.2}$$

where f and f' correspond to charged fermion fields. $P_L = (1 - \gamma_5)/2$ is the left-handed projector, while P can be either P_L or P_R (right-handed projector). These operators introduce a modification of the neutrino interaction with the charged fermions, which affect to the neutrino production and detection by a new charged-current interaction Eq (4.2), and a new neutral-current interaction Eq (4.1). At zero momentum transfer, the NSI-NC can modify the matter potential that describes the neutrino evolution through the matter, and their effect can be enhanced when neutrinos travel long distances through the matter. This is the case of atmospheric neutrinos experiments. As we are going to see in the following work, the new matter potential can also have an observable effect on the flavor of astrophysical neutrinos.

The operators Eqs (4.2) (4.1) are not singlets of the SM symmetry group Eq (1.1). In order to promote them to a gauge invariant operator, for instance, we can replace the fermion fields by the $SU(2)$ doublets. In this case, the operators Eqs (4.2) (4.1) could be obtained from

$$(\overline{L_{\alpha L}} \gamma^\rho L_{\beta L})(\overline{L_{\gamma L}} \gamma^\rho L_{\delta L}) \tag{4.3}$$

$$(\overline{L_{\alpha L}} \gamma^\rho L_{\beta L})(\overline{Q_{\gamma L}} \gamma^\rho Q_{\delta L}) \tag{4.4}$$

In addition to the new interaction for neutrinos, the gauge invariant operators bring new interactions between the charged fermions like $\mu \to 3e$ that are tight constrained [41, 10]. In the order to avoid these constraints it is needed cancellations among the different higher-dimensional operators [42, 43].

Astroparticle Physics 84 (2016) 15–22

Contents lists available at ScienceDirect

Astroparticle Physics

journal homepage: www.elsevier.com/locate/astropartphys

Non-standard neutrino interactions in the earth and the flavor of astrophysical neutrinos

M.C. Gonzalez-Garcia[a,b,c], Michele Maltoni[d,*], Ivan Martinez-Soler[d], Ningqiang Song[a]

[a] C.N. Yang Institute for Theoretical Physics, SUNY at Stony Brook, Stony Brook, NY 11794-3840, USA
[b] Institució Catalana de Recerca i Estudis Avançats (ICREA), Pg. Lluis Companys 23, 08010 Barcelona, Spain
[c] Departament de Física Quàntica i Astrofísica and ICC-UB, Universitat de Barcelona, Diagonal 647, E-08028 Barcelona, Spain
[d] Instituto de Física Teórica UAM/CSIC, Calle de Nicolás Cabrera 13–15, Universidad Autónoma de Madrid, Cantoblanco, E-28049 Madrid, Spain

ARTICLE INFO

Article history:
Received 7 June 2016
Accepted 9 July 2016
Available online 2 August 2016

Keywords:
Astrophysical neutrinos
Non-standard neutrino interactions
Neutrino oscillations

ABSTRACT

We study the modification of the detected flavor content of ultra high-energy astrophysical neutrinos in the presence of non-standard interactions of neutrinos with the Earth matter. Unlike the case of new physics affecting the propagation from the source to the Earth, non-standard Earth matter effects induce a dependence of the flavor content on the arrival direction of the neutrino. We find that, within the current limits on non-standard neutrino interaction parameters, large deviations from the standard 3ν oscillation predictions can be expected, in particular for fluxes dominated by one flavor at the source. Conversely they do not give sizable corrections to the expectation of equalized flavors in the Earth for sources dominated by production via pion-muon decay-chain.

© 2016 Elsevier B.V. All rights reserved.

1. Introduction

The detection of ultra-high energy neutrinos of astrophysical origin in IceCube [1–4] marks the begin of high energy neutrino astronomy. From the point of view of astronomy, the main open question resides in finding the sources of such neutrinos, an issue to which many suggestions have been contributed (for a recent review see Ref. [5]). More on the astrophysical front, one also questions what type of mechanisms are at work in those sources to produce such high energy neutrino flux. To address this question the measurement of the flavor composition of the observed neutrinos acquires a special relevance. For example, for the pion-muon decay chain, which is the most frequently considered, one expects $\phi^s_\mu = 2\phi^s_e$ while $\phi^s_\tau = 0$ [6] (denoting by ϕ^s_α the neutrino flux of flavor ν_α at source). Alternatively, if some of the muons lose energy very rapidly one would predict a single μ-flavor flux while $\phi^s_e = \phi^s_\tau = 0$ [7–11]. If neutrino production is dominated by neutron decay one expects also a single flavor flux but of electron neutrinos [8] so in this case $\phi^s_\mu = \phi^s_\tau = 0$. Decay of charm mesons contribute a flux with equal amounts of electron and muon neutrinos, $\phi^s_e = \phi^s_\mu$ and $\phi^s_\tau = 0$. If several of the above processes in the source compete, arbitrary flavor compositions of ϕ^s_e and ϕ^s_μ are possible but still with $\phi_\tau = 0$ [10]. If, in addition, ν_τ are also produced in the source [12–14], then generically $\phi^s_\alpha \neq 0$ for $\alpha = e, \mu, \tau$.

Neutrino oscillations modify the flavor composition of the neutrino flux by the time they reach the Earth. In the context of the well established framework of 3ν oscillations these modifications are well understood and quantifiable given the present determination of the neutrino oscillation parameters. Because of this several studies to quantify the flavor composition of the IceCube events, even with the limited statistics data available, have been presented [15–23] but the results are still inconclusive.

It is well-known that new physics (NP) effects beyond 3ν oscillations in the neutrino propagation can alter the predicted flavor composition of the flux reaching the Earth, thus making the task of elucidating the production mechanism even more challenging. Examples of NP considered in the literature include Lorentz or CPT violation [24], neutrino decay [25,26], quantum decoherence [27,28] pseudo-Dirac neutrinos [29,30], sterile neutrinos [31], non-standard neutrino interactions with dark matter [32], or generic forms of NP in the propagation from the source to the Earth parametrized by effective operators [33]. Besides modifications of the flavor ratios many of these NP effects also induce a modification of the energy spectrum of the arriving neutrinos.

In this paper we consider an alternative form of NP, namely the possibility of non-standard interactions (NSI) of the neutrinos in the Earth matter. Unlike the kind of NP listed above, this implies

* Corresponding author.
E-mail addresses: maria.gonzalez-garcia@stonybrook.edu (M.C. Gonzalez-Garcia), michele.maltoni@csic.es (M. Maltoni), ivanj.m@csic.es (I. Martinez-Soler), ningqiang.song@stonybrook.edu (N. Song).

http://dx.doi.org/10.1016/j.astropartphys.2016.07.001
0927-6505/© 2016 Elsevier B.V. All rights reserved.

that neutrinos reach the Earth surface in the expected flavor combinations provided by the "standard" 3ν vacuum oscillation mechanism: in other words, NSI in the Earth affect only the flavor evolution of the neutrino ensemble from the entry point in the Earth matter to the detector. The goal of this paper is to quantify the modification of the neutrino flavor composition at the detector because of this effect within the presently allowed values of the NSI parameters. To this aim we briefly review in Section 2 the formalism employed and derive the relevant flavor transition probabilities from the source to the detector including the effect of NSI in the Earth. We show that the resulting probabilities are energy independent while they depend on the zenith angle arrival direction of the neutrinos, in contrast with NP affecting propagation from the source to the Earth. Our quantitative results are presented in Section 3, where in particular we highlight for which source flavor composition the Earth-matter NSI can be most relevant. Finally in Section 4 we draw our conclusions.

2. Formalism

Our starting point is the initial neutrino (antineutrino) fluxes at the production point in the source which we denote as ϕ^s_α ($\bar\phi^s_\alpha$) for $\alpha = e, \nu, \tau$. The corresponding fluxes of a given flavor at the Earth's surface are denoted as $\phi^\oplus_\alpha$ ($\bar\phi^\oplus_\alpha$) while the fluxes arriving at the detector after traversing the Earth are ϕ^d_α ($\bar\phi^d_\alpha$). They are generically given by

$$\phi^\oplus_\beta(E) = \sum_\alpha \int dE' \mathcal{P}^{s\to\oplus}_{\alpha\beta}(E,E')\phi^s_\alpha(E'),$$
$$\phi^d_\beta(E) = \sum_\alpha \int dE' \mathcal{P}^{s\to d}_{\alpha\beta}(E,E')\phi^s_\alpha(E') \tag{1}$$

and correspondingly for antineutrinos. $\mathcal{P}$ is the flavor transition probability including both coherent and incoherent effects in the neutrino propagation.

2.1. Coherent effects

Let us start by considering first only the coherent evolution of the neutrino ensemble. In this case, the flavor transition probabilities from the source (s) to the Earth entry point ($\oplus$) and to the detector (d) can be written as

$$\mathcal{P}^{s\to\oplus}_{\alpha\beta}(E,E') = P^{s\to\oplus}_{\alpha\beta}(E)\,\delta(E-E'), \quad \text{with} \quad P^{s\to\oplus}_{\alpha\beta}(E) = \left|A^{s\to\oplus}_{\alpha\beta}(E)\right|^2 \tag{2}$$

$$\mathcal{P}^{s\to d}_{\alpha\beta}(E,E') = P^{s\to d}_{\alpha\beta}(E)\,\delta(E-E'), \quad \text{with}$$
$$P^{s\to d}_{\alpha\beta}(E) = \left|A^{s\to d}_{\alpha\beta}(E)\right|^2 = \left|\sum_\gamma A^{s\to\oplus}_{\alpha\gamma}A^{\oplus\to d}_{\gamma\beta}\right|^2, \tag{3}$$

where we have introduced the flavor transition amplitude from the source to the Earth surface $A^{s\to\oplus}$ and from the Earth surface to the detector $A^{\oplus\to d}$.

Generically these amplitudes are obtained by solving the neutrino and antineutrino evolution equations for the flavor wave function $\vec\nu(x) = \{\nu_e(x), \nu_\mu(x), \nu_\tau(x)\}^T$

$$i\frac{d\vec\nu(x)}{dx} = H^{s\to\oplus}_\nu\,\vec\nu(x), \qquad i\frac{d\vec{\bar\nu}(x)}{dx} = H^{s\to\oplus}_{\bar\nu}\,\vec{\bar\nu}(x) \tag{4}$$

for evolution between the source and the Earth surface and

$$i\frac{d\vec\nu(x)}{dx} = H^{\oplus\to d}_\nu\,\vec\nu(x), \qquad i\frac{d\vec{\bar\nu}(x)}{dx} = H^{\oplus\to d}_{\bar\nu}\,\vec{\bar\nu}(x), \tag{5}$$

for evolution in the Earth matter.

In this work we are interested in standard vacuum oscillation dominating the propagation from the source to the detector but allowing for new physics in the interactions of the neutrinos in the Earth matter. In this case

$$H^{s\to\oplus}_\nu = (H^{s\to\oplus}_{\bar\nu})^* = H_{\rm osc} = UD_{\rm vac}U^\dagger \quad \text{with}$$
$$D_{\rm vac} = \frac{1}{2E}\,\text{diag}(0, \Delta m^2_{21}, \Delta m^2_{31}) \tag{6}$$

and U is the leptonic mixing matrix [34,35]. While

$$H^{\oplus\to d}_\nu \simeq H_{\rm mat}, \qquad H^{\oplus\to d}_{\bar\nu} \simeq -H^*_{\rm mat} \tag{7}$$

where the $\simeq$ corresponds to neglecting vacuum oscillations inside the Earth which is a very good approximation for the relevant neutrino energies ($\gtrsim$ 1 TeV).

The standard theoretical framework for the NP considered here is provided by non-standard interactions affecting neutrino interactions in matter [36]. They can be described by effective four-fermion operators of the form

$$\mathcal{L}_{\rm NSI} = -2\sqrt{2}G_F\varepsilon^{fP}_{\alpha\beta}(\bar\nu_\alpha\gamma^\mu\nu_\beta)(\bar f\gamma_\mu Pf), \tag{8}$$

where f is a charged fermion, $P = (L, R)$ and $\varepsilon^{fP}_{\alpha\beta}$ are dimensionless parameters encoding the deviation from standard interactions. NSI enter in neutrino propagation only through the vector couplings, so in the most general case the non-standard matter Hamiltonian can be parametrized as [37]

$$H_{\rm mat} = \sqrt{2}G_F N_e(r)\begin{pmatrix}1&0&0\\0&0&0\\0&0&0\end{pmatrix} + \sqrt{2}G_F\sum_{f=e,u,d}N_f(r)\begin{pmatrix}\varepsilon^f_{ee} & \varepsilon^f_{e\mu} & \varepsilon^f_{e\tau}\\ \varepsilon^{f*}_{e\mu} & \varepsilon^f_{\mu\mu} & \varepsilon^f_{\mu\tau}\\ \varepsilon^{f*}_{e\tau} & \varepsilon^{f*}_{\mu\tau} & \varepsilon^f_{\tau\tau}\end{pmatrix}. \tag{9}$$

The standard model interactions are encoded in the non-vanishing ee entry in the first term of Eq. (9), while the non-standard interactions with fermion f are accounted by the $\varepsilon^f_{\alpha\beta}$ coefficients with $\varepsilon^f_{\alpha\beta} = \varepsilon^{fL}_{\alpha\beta} + \varepsilon^{fR}_{\alpha\beta}$. Here $N_f(r)$ is the number density of fermions f in the Earth matter. In practice, the PREM model [38] fixes the neutron/electron ratio to $Y_n = 1.012$ in the Mantle and $Y_n = 1.137$ in the Core, with an average $Y_n = 1.051$ all over the Earth. Thus we get an average up-quark/electron ratio $Y_u = 3.051$ and down-quark/electron ratio $Y_d = 3.102$. We can therefore define:

$$\varepsilon_{\alpha\beta} \equiv \sum_{f=e,u,d}\left\langle\frac{Y_f}{Y_e}\right\rangle\varepsilon^f_{\alpha\beta} = \varepsilon^e_{\alpha\beta} + Y_u\,\varepsilon^u_{\alpha\beta} + Y_d\,\varepsilon^d_{\alpha\beta} \tag{10}$$

so that the matter part of the Hamiltonian can be written as:

$$H_{\rm mat} = \sqrt{2}G_F N_e(r)\begin{pmatrix}1+\varepsilon_{ee} & \varepsilon_{e\mu} & \varepsilon_{e\tau}\\ \varepsilon^*_{e\mu} & \varepsilon_{\mu\mu} & \varepsilon_{\mu\tau}\\ \varepsilon^*_{e\tau} & \varepsilon^*_{\mu\tau} & \varepsilon_{\tau\tau}\end{pmatrix} \equiv WD_{\rm mat}W^\dagger \tag{11}$$

where

$$D_{\rm mat} = \sqrt{2}G_F N_e(r)\,\text{diag}(\varepsilon_1, \varepsilon_2, \varepsilon_3). \tag{12}$$

where W is a 3×3 unitary matrix containing six physical parameters, three real angles and three complex phases. So without loss of generality the matter potential contains eight parameters, five real and three phases (as only difference of ε_i enter the flavor transition probabilities, only differences in the $\varepsilon_{\alpha\alpha}$ are physically relevant for neutrino oscillation data).

Altogether the flavor transition probabilities from a source at distance L are

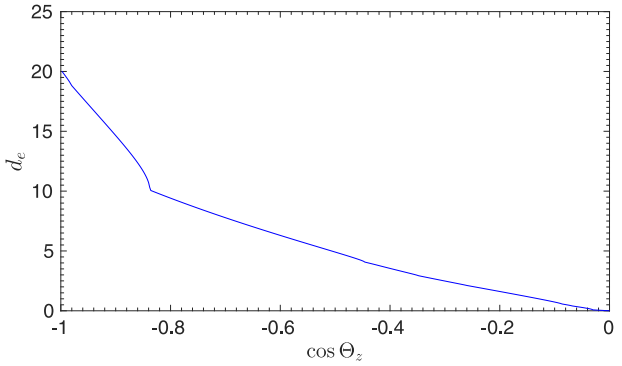

Fig. 1. The normalized density integral d_e along the neutrino path as a function of the neutrino arrival zenith angle.

$$P^{s\to d}_{\alpha\beta}(E) = \sum_{\gamma\eta kl} W_{\beta k} W^*_{\beta l} W_{\gamma l} W^*_{\eta k} \exp(-i d_e \Delta\varepsilon_{kl}) \times \sum_{ij} U_{\eta i} U^*_{\gamma j} U_{\alpha j} U^*_{\alpha i} \exp\left(-i \frac{\Delta m^2_{ij}}{2E} L\right), \tag{13}$$

$$P^{s\to\oplus}_{\alpha\beta}(E) = \sum_{ij} U_{\beta i} U^*_{\beta j} U_{\alpha j} U^*_{\alpha i} \exp\left(-i \frac{\Delta m^2_{ij}}{2E} L\right) \tag{14}$$

where $\Delta\varepsilon_{kl} = \varepsilon_k - \varepsilon_l$. Since for astrophysical neutrinos the propagation distance L is much longer than the oscillation wavelength, we can average out the vacuum oscillation terms:

$$P^{s\to d}_{\alpha\beta}(E) = \sum_i |U_{\alpha i}|^2 |U_{\beta i}|^2 - 2 \sum_{\gamma\eta kli} \mathrm{Re}\left(W_{\beta k} W^*_{\beta l} W_{\gamma l} W^*_{\eta k} U_{\eta i} U^*_{\gamma i} |U_{\alpha i}|^2\right) \times \sin^2\left(d_e \frac{\Delta\varepsilon_{kl}}{2}\right) + \sum_{\gamma\eta kli} \mathrm{Im}\left(W_{\beta k} W^*_{\beta l} W_{\gamma l} W^*_{\eta k} U_{\eta i} U^*_{\gamma i} |U_{\alpha i}|^2\right) \sin(d_e \Delta\varepsilon_{kl}), \tag{15}$$

$$P^{s\to\oplus}_{\alpha\beta}(E) = \sum_i |U_{\alpha i}|^2 |U_{\beta i}|^2. \tag{16}$$

In these expressions we have introduced the dimensionless normalization for the matter potential integral along the neutrino trajectory in the Earth

$$d_e(\Theta_z) \equiv \int_0^{2R\cos(\pi-\Theta_z)} \sqrt{2} G_F N_e(r) dx, \quad \text{with} \quad r = \sqrt{R^2_\oplus + x^2 + 2R_\oplus x \cos\Theta_z}, \tag{17}$$

which we plot in Fig. 1. The integral includes both the effect of the increase length of the path in the Earth and the increase average density which is particular relevant for trajectories crossing the core and leads to the higher slope of the curve for $\cos\Theta_z \lesssim -0.84$.

We notice that the total coherent flavor transition probability remains energy independent even in the presence of NSI. Also the last term in Eq. (15) does not change sign for antineutrinos since both the imaginary part of the combination of mixing matrices and the phase of the oscillating sin change sign for antineutrinos.[1] In other words, there is no CP violation even if all the phases in U and W are kept different from zero. These two facts render the flavor composition of the fluxes at the detector independent of the energy spectrum and the neutrino/antineutrino ratio at the source, as long as the flavor composition at the source is the same for both neutrinos and antineutrinos. This is just as the case for standard 3ν oscillations in the absence of NP.[2]

In brief, the effect of NSI in the Earth is to modify the flavor composition at the detector as compared to the standard case, in a way which depends on the zenith angle of the arrival direction of the neutrinos. Also, as expected, the effect only appears in presence of additional flavor mixing during propagation in the Earth, *i.e.*, for $W_{\alpha i} \neq C\delta_{\alpha i}$, which occurs only if some off-diagonal $\varepsilon_{\alpha\beta}$ (with $\alpha \neq \beta$) is different from zero.

2.2. Incoherent effects

In addition to the coherent effects discussed so far, high-energy neutrinos propagating through the Earth can also interact inelastically with the Earth matter either by charged current or by neutral current interactions. As a consequence of these inelastic processes the neutrino flux is attenuated, its energy is degraded, and secondary fluxes are generated from the decay of the charged leptons (in particular $\tau^\pm$) produced in charged current interactions. In some new physics scenario attenuation and other decoherence effects can also occur in the travel from the source to the Earth, but they are not relevant for this work.

For simplicity, let us first neglect NSI and focus only on the usual 3ν oscillation framework. In the standard scenario, attenuation and regeneration effects can be consistently described by a set of coupled partial integro-differential cascade equations (see for example [41] and references therein). In this case the fluxes at the arrival point in the Earth are given by Eqs. (1) and (2) while for the fluxes at the detector we have:

$$\text{SM:} \qquad \mathcal{P}^{s\to d}_{\alpha\beta}(E, E') = \sum_\gamma P^{s\to\oplus}_{\alpha\gamma}(E) F^{\oplus\to d}_{\gamma\beta}(E, E'), \tag{18}$$

where $F^{\oplus\to d}_{\gamma\beta}(E, E')$ is the function accounting for attenuation and regeneration effects, which depends on the trajectory of the neutrino in the Earth matter (*i.e.*, it depends on Θ_z). Attenuation is the dominant effect and for most energies is only mildly flavor dependent. So the dominant incoherent effects verify

$$\text{SM:} \qquad F^{\oplus\to d}_{\gamma\beta}(E, E') \simeq \delta_{\gamma\beta} F^{\oplus\to d}_{\text{att}}(E) \delta(E - E'). \tag{19}$$

When considering NSI in the Earth the simple factorization of coherent and incoherent effects introduced in Eq. (18) does not hold, since NSI-induced oscillations, attenuation, and regeneration occur simultaneously while the neutrino beam is traveling across the Earth's matter. In order to properly account for all these effects we need to replace the evolution equation in the Earth (5) with a more general expression including also the incoherent components. This can be done by means of the density matrix formalism, as illustrated in Ref. [42] (see also Ref. [43]). However, if one neglects the subleading flavor dependence of these effects and focus only on the dominant attenuation term, as we did in Eq. (19) for the standard case, it becomes possible to write even in the presence of NSI-oscillations:

$$\text{NSI:} \qquad \mathcal{P}^{s\to d}_{\alpha\beta}(E, E') \simeq P^{s\to d}_{\alpha\beta}(E) F^{\oplus\to d}_{\text{att}}(E) \delta(E - E') \tag{20}$$

with $P^{s\to d}_{\alpha\beta}(E)$ given in Eq. (15). In other words, although the presence of NSI affects the flavor composition at the detector through a modification of the *coherent* part of the evolution in the Earth, the *incoherent* part is practically the same in both the standard and the non-standard case and does not introduce relevant flavor distortions.

[1] Indeed this term preserves CP but violates time reversal, as it is well known that Earth matter effects violate CPT.

[2] Relaxing the assumption of equal flavor composition for neutrinos and antineutrinos at the source can lead to additional interesting effects even in the case of standard oscillations as discussed in Ref. [39,40].

In the next section we quantify our results taking into account the existing bounds on NSI. For simplicity we will consider only NSI with quarks and we further assume that the NSI Hamiltonian is real. At present the strongest model-independent constraints on NSI with quarks relevant to neutrino propagation arise from the global analysis of oscillation data [37,44] (see also [45]) in combination with some constraints from scattering experiments [46,47] such as CHARM [48,49], CDHSW [50] and NuTeV [51]. As shown in Ref. [37] neutrino oscillations provide the stronger constraints on NSI, with the exception of some large $\varepsilon_{ee} - \varepsilon_{\mu\mu}$ terms which are still allowed in association with a flip of the octant of θ_{12}, the so-called "dark-side" solution (or LMA-D) found in Ref. [45]. However, these large NSI's are disfavored by scattering data [45]. A fully consistent analysis of both oscillation and scattering data covering the LMA-D region is still missing, so here we conservatively consider only NSI's which are consistent with oscillations within the LMA regions. The corresponding allowed ranges read (we quote the most constraining of both u and d NSI's):

	90% CL	3σ CL
$\varepsilon^q_{ee} - \varepsilon^q_{\mu\mu}$	$[+0.02, +0.51]$	$[-0.09, +0.71]$
$\varepsilon^q_{\tau\tau} - \varepsilon^q_{\mu\mu}$	$[-0.01, +0.03]$	$[-0.03, +0.19]$
$\varepsilon^q_{e\mu}$	$[-0.09, +0.04]$	$[-0.16, +0.11]$
$\varepsilon^q_{e\tau}$	$[-0.13, +0.14]$	$[-0.38, +0.29]$
$\varepsilon^q_{\mu\tau}$	$[-0.01, +0.01]$	$[-0.03, +0.03]$

(21)

where for each NSI coupling the ranges are shown after marginalization over all the oscillations parameters and the other NSI couplings.

3. Results

Flavor composition of the astrophysical neutrinos are usually parametrized in terms of the flavor ratios at the source and at the Earth surface, defined as:

$$\xi^s_\alpha \equiv \frac{\phi^s_\alpha(E)}{\sum_\gamma \phi^s_\gamma(E)}, \qquad \xi^\oplus_\beta \equiv \frac{\phi^\oplus_\beta(E)}{\sum_\gamma \phi^\oplus_\gamma(E)} = \sum_\alpha P^{s\to\oplus}_{\alpha\beta}(E)\xi^s_\alpha \tag{22}$$

and it has become customary to plot them in ternary plots. Experimentally $\xi^\oplus_\beta$ are *reconstructed* from the measured neutrino fluxes in the detector ϕ^d_α by *deconvoluting* the incoherent effects due to SM interactions in the Earth matter:

$$\xi^{\oplus,\mathrm{rec}}_\beta \equiv \frac{\phi^{\oplus,\mathrm{rec}}_\beta(E)}{\sum_\gamma \phi^{\oplus,\mathrm{rec}}_\gamma(E)} \quad \text{with}$$

$$\phi^{\oplus,\mathrm{rec}}_\beta(E) \equiv \sum_\gamma \int dE' G^{\oplus\leftarrow d}_{\gamma\beta}(E,E')\phi^d_\gamma(E') \tag{23}$$

where the function $G^{\oplus\leftarrow d}_{\alpha\beta}(E,E')$ is the inverse of the Earth attenuation + degradation + regeneration function $F^{\oplus\to d}_{\alpha\beta}(E,E')$ introduced in the previous section:

$$\sum_\gamma \int dE'' F^{\oplus\to d}_{\gamma\beta}(E,E'')\, G^{\oplus\leftarrow d}_{\alpha\gamma}(E'',E') = \delta_{\alpha\beta}\,\delta(E-E') \tag{24}$$

Under the approximation described in Eq. (19) $G^{\oplus\leftarrow d}_{\alpha\beta}(E,E')$ reduces to:

$$G^{\oplus\leftarrow d}_{\alpha\beta}(E,E') \simeq \delta_{\alpha\beta}\frac{1}{F^{\oplus\to d}_{\mathrm{att}}(E)}\delta(E-E') \tag{25}$$

so that

$$\xi^{\oplus,\mathrm{rec}}_\beta \simeq \frac{\phi^d_\beta(E)\,/\,F^{\oplus\to d}_{\mathrm{att}}(E)}{\sum_\gamma \phi^d_\gamma(E)\,/\,F^{\oplus\to d}_{\mathrm{att}}(E)} = \frac{\phi^d_\beta(E)}{\sum_\gamma \phi^d_\gamma(E)} \equiv \xi^d_\beta \tag{26}$$

where we have introduced the flavor ratios at the detector ξ^d_β. Thus we have shown that the reconstructed flavor ratios at the surface of the Earth ($\xi^{\oplus,\mathrm{rec}}_\beta$) are well approximated by the measured flavor ratios at the detector (ξ^d_β). This conclusion depends only on the validity of the approximation (19), and therefore applies both for standard oscillations and in the presence of new physics such as Earth NSI. It should be noted, however, that in the standard case $\xi^{\oplus,\mathrm{rec}}_\beta$ really coincides with the actual flavor ratios $\xi^\oplus_\beta$ defined in Eq. (22), whereas in the presence of NSI this is no longer the case.

In what follows we will present our results in terms of flavor ratios at the detector ξ^d_β, since, as we have just seen, they are good estimators of the reconstructed quantities $\xi^{\oplus,\mathrm{rec}}_\beta$ usually shown by the experimental collaborations. It is easy to show that:

$$\xi^d_\beta = \sum_\alpha P^{s\to d}_{\alpha\beta}(E)\xi^s_\alpha \tag{27}$$

where $P^{s\to d}_{\alpha\beta}(E)$ is obtained from Eq. (15). In principle, one may expect that the flavor ratios ξ^d_β would depend on the neutrino energy, either through the oscillation probability $P^{s\to d}_{\alpha\beta}(E)$ or though the intrinsic energy dependence of the flavor ratios at the source ξ^s_α. However, as we have seen in the previous section the expression in Eq. (15) is independent of E, and moreover we will assume (as it is customary to do) that the ratios ξ^s_α do *not* depend on the neutrino energy even though the fluxes $\phi^s_\alpha(E)$ do. Hence, the flavor ratios ξ^d_β are independent of energy and they can be conveniently plotted in a ternary plot.

Let us now discuss the results of our fit, starting with the simpler case of standard oscillations. In the absence of new physics effects the present determination of the leptonic mixing matrix from the measurements of neutrino oscillation experiments allows us to determine the astrophysical neutrino flavor content at detection given an assumption of the neutrino production mechanism. For completeness and reference we show in Fig. 2 the allowed regions of the flavor ratios at the Earth as obtained from the projection of the six oscillation parameter χ^2 function of the global NuFIT analysis of oscillation data [52,53] in the relevant mixing combinations (see also [16,33,40]). We stress that in our plots the correlations among the allowed ranges of the oscillation parameters in the full six-parameter space are properly taken into account. The results are shown after marginalization over the neutrino mass ordering and for different assumptions of the flavor content at the source as labeled in the figure. Fig. 2 illustrates the well-known fact [6] that during propagation from the source neutrino oscillations lead to flavor content at the Earth close to $(\xi^\oplus_e : \xi^\oplus_\mu : \xi^\oplus_\tau) = (\frac{1}{3} : \frac{1}{3} : \frac{1}{3})$, with largest deviations for the case when the flavor content at the source is (1: 0: 0) [54] and (0: 1: 0).

As discussed in the previous section NSI in the Earth modify these predictions and, unlike for NP effects in the propagation from the source, such Earth-induced modifications are a function of the arrival zenith angle of the neutrino. As illustration we show in Fig. 3 the variation of the flavor ratios at the detector as a function of the zenith angle of the neutrino for some values of the $\varepsilon_{\alpha\beta}$ well within the presently allowed 90% CL ranges. In our convention $\cos\Theta_z = -1$ corresponds to vertically upcoming neutrinos (which have crossed the whole Earth before reaching the detector) while $\cos\Theta_z = 0$ corresponds to horizontally arriving neutrinos (for which effectively no Earth matter is crossed so that $\xi^d_\beta(\cos\Theta_z = 0) = \xi^\oplus_\beta$). From Fig. 3 we can observe the main characteristics of the effect of NSI in the Earth matter. Deviations are sizable for flavor α as long as $\varepsilon_{\beta\neq\alpha}$ is non-zero and ξ^s_α or ξ^s_β are non-zero. Larger effects are expected for source flavor compositions for which vacuum oscillations from the source to the Earth lead to "less equal" ratios at the Earth surface: (1: 0: 0) and (0: 1: 0). Finally the increase in frequency for almost vertical neutrino direction is a consequence of the increase of the integral density d_e for core crossing trajectories (see Fig. 1).

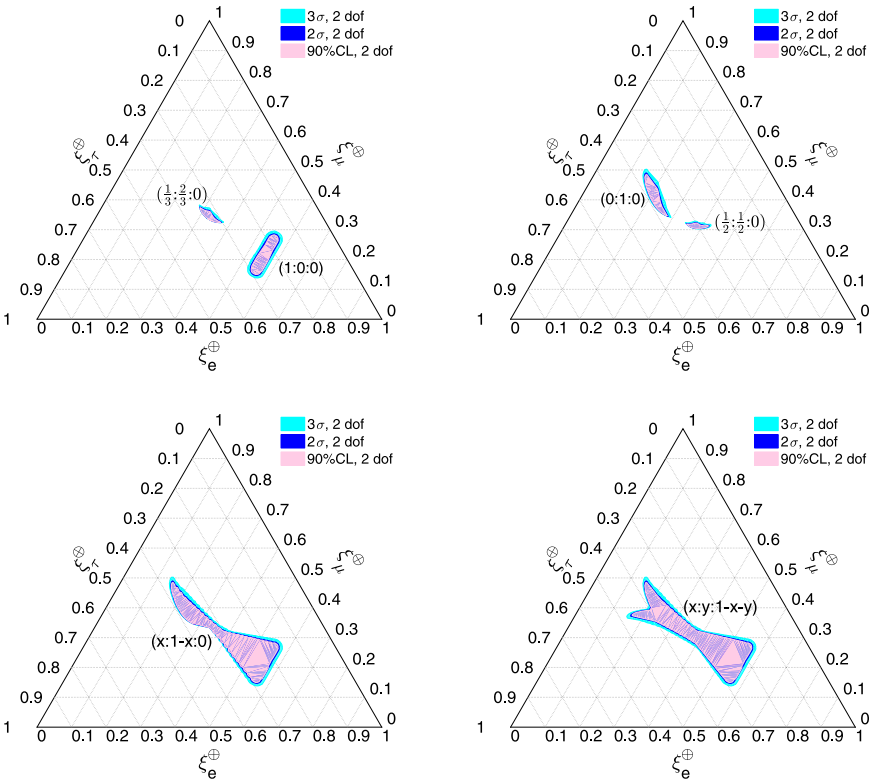

Fig. 2. Two-dimensional projections of the allowed regions from the global analysis of oscillation data from Ref. [52] in the relevant combinations giving the flavor content at the Earth. The allowed regions are shown at 90%, 95% and 3σ CL. In the upper panels we show the regions for four initial flavor compositions $(\xi_e^s : \xi_\mu^s : \xi_\tau^s) = (\frac{1}{3} : \frac{2}{3} : 0)$, (1: 0: 0), (0: 1: 0), and $(\frac{1}{2} : \frac{1}{2} : 0)$. In the lower panel the regions are shown for the more general scenarios, $(\xi_e^s : \xi_\mu^s : \xi_\tau^s) = (x : 1-x : 0)$ for $0 \le x \le 1$, and $(\xi_e^s : \xi_\mu^s : \xi_\tau^s) = (x : y : 1-x-y)$ for $0 \le x, y \le 1$.

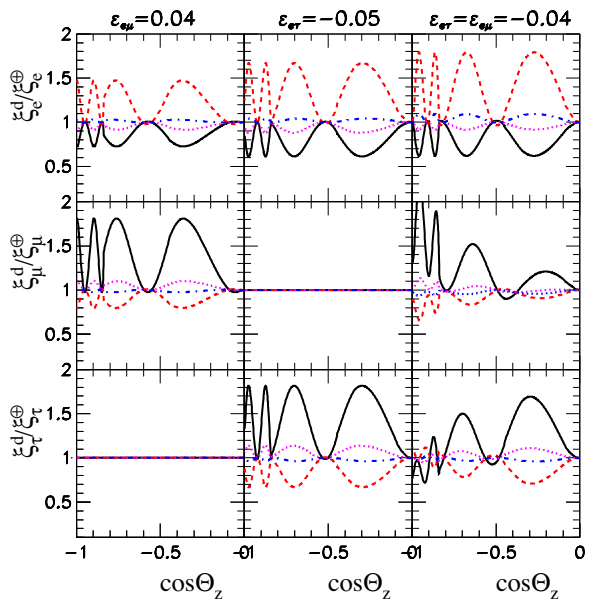

Fig. 3. Flavor ratios at the detector as a function of the zenith angle of the neutrino normalized to the expectation in the absence of NSI and for oscillation parameters at the best fit of the global analysis ($\sin^2\theta_{12} = 0.305$, $\sin^2\theta_{13} = 0.0219$, $\sin^2\theta_{23} = 0.579$, and $\delta_{CP} = 254^\circ$). For the left (central) [right] panels the only non-vanishing NSI parameters are $\varepsilon_{e\mu} = 0.04$ ($\varepsilon_{e\tau} = -0.05$) [$\varepsilon_{e\mu} = \varepsilon_{e\tau} = -0.04$]. The different curves correspond to different flavor composition at the source: $(\xi_e^s : \xi_\mu^s : \xi_\tau^s) = (1 : 0 : 0)$ (full black), (0: 1: 0) (dashed red), $(\frac{1}{2} : \frac{1}{2} : 0)$ (dotted purple), and $(\frac{1}{3} : \frac{2}{3} : 0)$ (dash-dotted blue). (For interpretation of the references to colour in this figure legend, the reader is referred to the web version of this article.)

Next we show how the allowed regions in the ternary plots shown in Fig. 2 are modified when including the effect of the NSI presently allowed at given CL. In order to do so we project the χ^2 of the global analysis of oscillation data in the presence of arbitrary NSI on the relevant combinations entering in the flavor ratios within a given CL. The results are shown in Figs. 4, 5 and 6 for the flavor compositions at source $(\xi_e^s : \xi_\mu^s : \xi_\tau^s) = (1 : 0 : 0)$, (0: 1: 0) and $(\frac{1}{3} : \frac{2}{3} : 0)$, respectively. The results are shown averaged over four zenith angular directions.

Comparing the allowed regions in Figs. 4 and 5 with the corresponding ones for (1: 0: 0) and (0: 1: 0) compositions in the case of standard 3ν oscillations given in Fig. 2 we see that the flavor ratios can take now much wider range of values in any of the zenith angle ranges considered. Moreover, although sizable deviations from $(\xi_e^d : \xi_\mu^d : \xi_\tau^d) = (\frac{1}{3} : \frac{1}{3} : \frac{1}{3})$ are possible, the allowed regions now extend to include $(\frac{1}{3} : \frac{1}{3} : \frac{1}{3})$ at CL of 3σ or lower. We also see that the larger CL region becomes smaller for most vertical arrival directions (see the relative size of the light blue regions in the two lower triangles on these figures). This is so because at those CL for the larger values of ε allowed the NSI-induced oscillations are fast enough to be averaged out $\langle \sin^2(\Delta\varepsilon_{ij}\frac{d_e}{2})\rangle \sim \frac{1}{2}$ for those trajectories while the value in the second most vertical angular bin can be in average larger than 1/2. For contrast, as illustrated in Fig. 6, for the case of flavor composition at the source $(\xi_e^s : \xi_\mu^s : \xi_\tau^s) = (\frac{1}{3} : \frac{2}{3} : 0)$ NSI in the Earth never induce sizable modifications of the expectation $(\xi_e^d : \xi_\mu^d : \xi_\tau^d) = (\frac{1}{3} : \frac{1}{3} : \frac{1}{3})$.

4. Conclusions

The measurement of the flavor composition of the detected ultra-high energy neutrinos can be a powerful tool to learn about the mechanisms at work in their sources. Such inference, however,

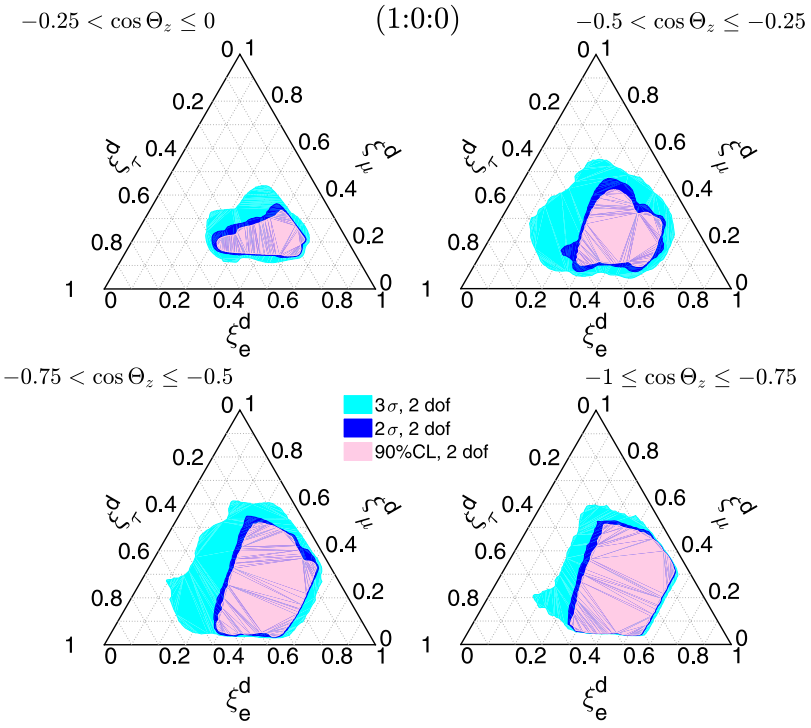

Fig. 4. Allowed regions for the flavor ratios in the presence of NSI in the Earth at 90, 95% and 3σ CL for an initial flavor $(\xi^s_e : \xi^s_\mu : \xi^s_\tau) = (1 : 0 : 0)$. The four triangles correspond to averaging over neutrinos arriving with directions given in the range $0 \geq \cos\Theta_z > -0.25$ (upper left), $-0.25 \geq \cos\Theta_z > -0.5$ (upper right) $-0.5 \geq \cos\Theta_z > -0.75$ (lower left), and $-0.75 \geq \cos\Theta_z \geq -1$ (lower right).

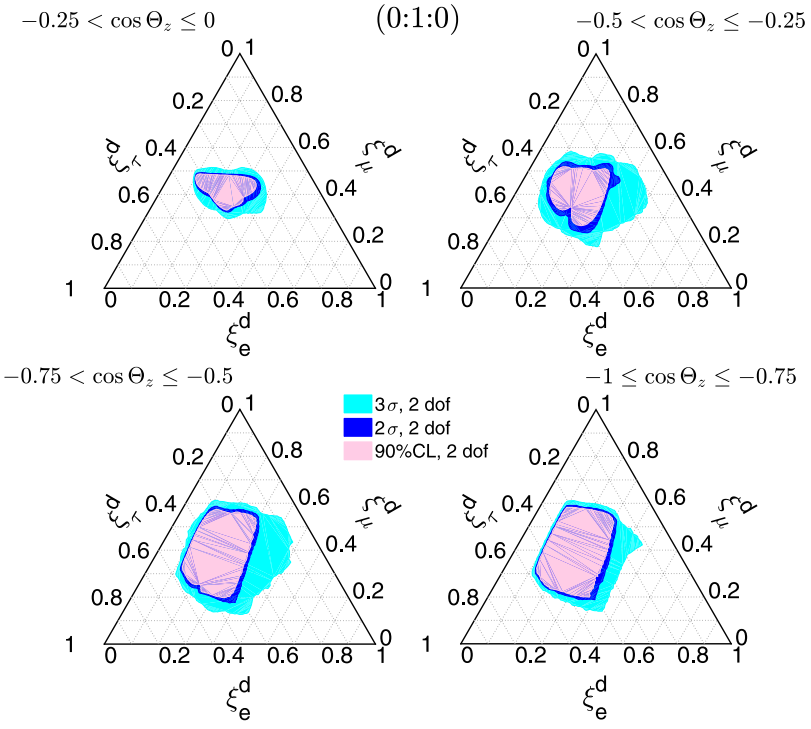

Fig. 5. Same as Fig. 4 for $(\xi^s_e : \xi^s_\mu : \xi^s_\tau) = (0 : 1 : 0)$.

relies on the understanding of the particle physics processes relevant to the neutrino propagation from the source to the detector. The presence of NP effects beyond those of the well established mass-induced 3ν oscillations alter the flavor composition at the detector and can therefore affect the conclusions on the dominant production mechanism.

In this work we have focused on NP effects associated with NSI of the neutrinos in the Earth matter. The relevant flavor transition probabilities accounting from oscillations from the source to the Earth plus NSI in the Earth are energy independent but depend on the zenith angle of the arrival direction of the neutrinos, which is a characteristic feature of this form of NP. Quantitatively, we have

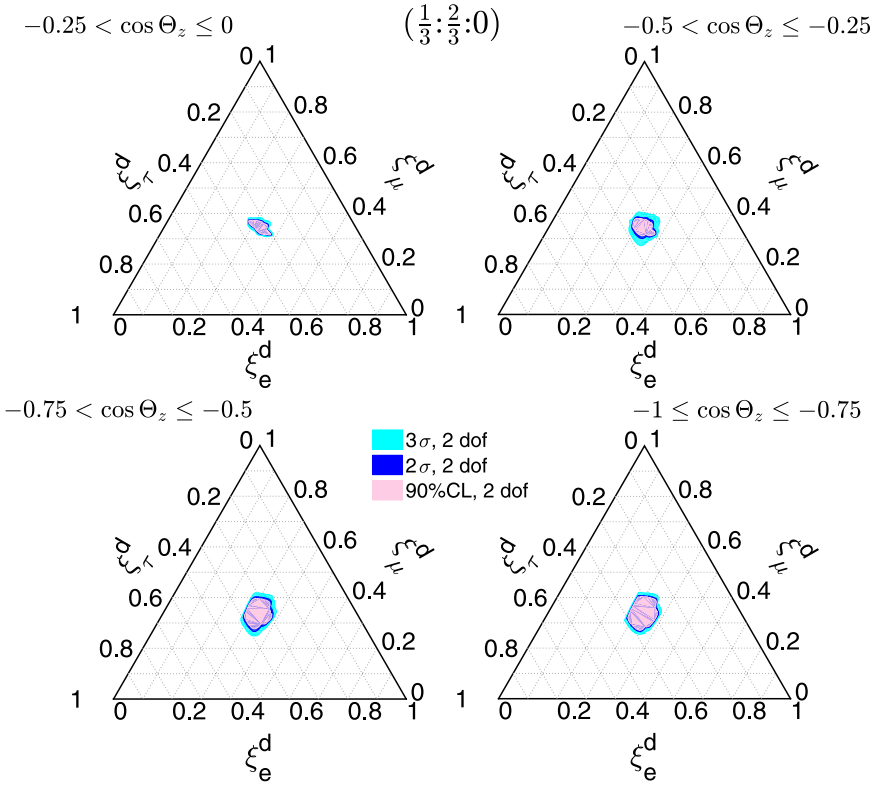

Fig. 6. Same as Fig. 4 for $(\xi^s_e : \xi^s_\mu : \xi^s_\tau) = (\frac{1}{3} : \frac{2}{3} : 0)$.

shown that within the presently allowed range of NSI large deviations from the standard 3ν oscillation predictions for the detected flavor composition can be expected, in particular for fluxes dominated by one flavor at the source. On the contrary we find that the expectation of equalized flavors in the Earth for sources dominated by production via pion-muon decay-chain is robust even in the presence of this form of NP.

Acknowledgments

I.M.S. thanks YITP at Stony Brook Univ. for their kind hospitality during the visit that lead to this work. This work is supported by USA-NSF grant PHY-13-16617, by EU Networks FP7 ITN INVISIBLES (PITN-GA-2011-289442), FP10 ITN ELUSIVES (H2020-MSCA-ITN-2015-674896) and INVISIBLES-PLUS (H2020-MSCA-RISE-2015-690575). M.C.G-G. also acknowledges support by MINECO grants 2014-SGR-104, FPA2013-46570, and “Maria de Maetzu” program grant MDM-2014-0367 of ICCUB. M.M. and I.M-S. also acknowledge support by MINECO grants FPA2012-31880, FPA2012-34694 and by the “Severo Ochoa” program grant SEV-2012-0249 of IFT.

References

[1] M.G. Aartsen, First observation of pev-energy neutrinos with icecube, Phys. Rev. Lett. 111 (2013) 021103. 1304.5356, doi:10.1103/PhysRevLett.111.021103.
[2] M.G. Aartsen, et al., Evidence for high-energy extraterrestrial neutrinos at the icecube detector, Science 342 (2013) 1242856. 1311.5238, doi:10.1126/science.1242856.
[3] M.G. Aartsen, Observation of high-energy astrophysical neutrinos in three years of icecube data, Phys. Rev. Lett. 113 (2014) 101101. 1405.5303, doi:10.1103/PhysRevLett.113.101101.
[4] M.G. Aartsen, et al., Evidence for astrophysical muon neutrinos from the northern sky with icecube, Phys. Rev. Lett. 115 (8) (2015) 081102. 1507.04005, doi:10.1103/PhysRevLett.115.081102.
[5] L.A. Anchordoqui, et al., Cosmic neutrino pevatrons: A brand new pathway to astronomy, astrophysics, and particle physics, JHEAp 1–2 (2014) 1–30. 1312.6587, doi:10.1016/j.jheap.2014.01.001.
[6] J.G. Learned, S. Pakvasa, Detecting tau-neutrino oscillations at pev energies, Astropart. Phys. 3 (1995) 267–274. hep-ph/9405296, doi:10.1016/0927-6505(94)00043-3.
[7] T. Kashti, E. Waxman, Flavoring astrophysical neutrinos: Flavor ratios depend on energy, Phys. Rev. Lett. 95 (2005) 181101. astro-ph/0507599, doi:10.1103/PhysRevLett.95.181101.
[8] P. Lipari, M. Lusignoli, D. Meloni, Flavor composition and energy spectrum of astrophysical neutrinos, Phys. Rev. D75 (2007) 123005. 0704.0718, doi:10.1103/PhysRevD.75.123005.
[9] M. Kachelriess, S. Ostapchenko, R. Tomas, High energy neutrino yields from astrophysical sources. 2. magnetized sources, Phys. Rev. D77 (2008) 023007. 0708.3047, doi:10.1103/PhysRevD.77.023007.
[10] S. Hummer, M. Maltoni, W. Winter, C. Yaguna, Energy dependent neutrino flavor ratios from cosmic accelerators on the hillas plot, Astropart. Phys. 34 (2010) 205–224. 1007.0006, doi:10.1016/j.astropartphys.2010.07.003.
[11] W. Winter, Describing the observed cosmic neutrinos by interactions of nuclei with matter, Phys. Rev. D90 (10) (2014) 103003. 1407.7536, doi:10.1103/PhysRevD.90.103003.
[12] C. Lunardini, A.Y. Smirnov, High-energy neutrino conversion and the lepton asymmetry in the universe, Phys. Rev. D64 (2001) 073006. hep-ph/0012056, doi:10.1103/PhysRevD.64.073006.
[13] S. Razzaque, A.Y. Smirnov, Flavor conversion of cosmic neutrinos from hidden jets, JHEP 03 (2010) 031. 0912.4028, doi:10.1007/JHEP03(2010)031.
[14] S. Sahu, B. Zhang, Effect of resonant neutrino oscillation on tev neutrino flavor ratio from choked GRBs, Res. Astron. Astrophys. 10 (2010) 943–949. 1007.4582, doi:10.1088/1674-4527/10/10/001.
[15] O. Mena, S. Palomares-Ruiz, A.C. Vincent, Flavor composition of the high-energy neutrino events in icecube, Phys. Rev. Lett. 113 (2014) 091103. 1404.0017, doi:10.1103/PhysRevLett.113.091103.
[16] M. Bustamante, J.F. Beacom, W. Winter, Theoretically palatable flavor combinations of astrophysical neutrinos, Phys. Rev. Lett. 115 (16) (2015) 161302. 1506.02645, doi:10.1103/PhysRevLett.115.161302.
[17] A. Palladino, G. Pagliaroli, F.L. Villante, F. Vissani, What is the flavor of the cosmic neutrinos seen by icecube? Phys. Rev. Lett. 114 (17) (2015) 171101. 1502.02923, doi:10.1103/PhysRevLett.114.171101.
[18] S. Palomares-Ruiz, A.C. Vincent, O. Mena, Spectral analysis of the high-energy icecube neutrinos, Phys. Rev. D91 (10) (2015) 103008. 1502.02649, doi:10.1103/PhysRevD.91.103008.
[19] A. Watanabe, The spectrum and flavor composition of the astrophysical neutrinos in icecube, JCAP 1508 (2015) 030. 1412.8264, doi:10.1088/1475-7516/2015/08/030.
[20] C.-Y. Chen, P.S.B. Dev, A. Soni, Two-component flux explanation for the high energy neutrino events at icecube, Phys. Rev. D92 (7) (2015) 073001. 1411.5658, doi:10.1103/PhysRevD.92.073001.

[21] N. Kawanaka, K. Ioka, Neutrino flavor ratios modified by cosmic ray secondary acceleration, Phys. Rev. D92 (8) (2015) 085047. 1504.03417, doi:10.1103/PhysRevD.92.085047.
[22] M.G. Aartsen, et al., A combined maximum-likelihood analysis of the high-energy astrophysical neutrino flux measured with icecube, Astrophys. J. 809 (1) (2015) 98. 1507.03991, doi:10.1088/0004-637X/809/1/98.
[23] A.C. Vincent, S. Palomares-Ruiz, O. Mena, Analysis of the 4-year icecube HESE data, (2016). arXiv:1605.01556.
[24] D. Hooper, D. Morgan, E. Winstanley, Lorentz and CPT invariance violation in high-energy neutrinos, Phys. Rev. D72 (2005) 065009. hep-ph/0506091, doi:10.1103/PhysRevD.72.065009.
[25] J.F. Beacom, N.F. Bell, D. Hooper, S. Pakvasa, T.J. Weiler, Decay of high-energy astrophysical neutrinos, Phys. Rev. Lett. 90 (2003) 181301. hep-ph/0211305, doi:10.1103/PhysRevLett.90.181301.
[26] P. Baerwald, M. Bustamante, W. Winter, Neutrino decays over cosmological distances and the implications for neutrino telescopes, JCAP 1210 (2012) 020. 1208.4600, doi:10.1088/1475-7516/2012/10/020.
[27] L.A. Anchordoqui, H. Goldberg, M.C. Gonzalez-Garcia, F. Halzen, D. Hooper, S. Sarkar, T.J. Weiler, Probing planck scale physics with icecube, Phys. Rev. D72 (2005) 065019. hep-ph/0506168, doi:10.1103/PhysRevD.72.065019.
[28] D. Hooper, D. Morgan, E. Winstanley, Probing quantum decoherence with high-energy neutrinos, Phys. Lett. B609 (2005) 206–211. hep-ph/0410094, doi:10.1016/j.physletb.2005.01.034.
[29] J.F. Beacom, N.F. Bell, D. Hooper, J.G. Learned, S. Pakvasa, T.J. Weiler, Pseudodirac neutrinos: A challenge for neutrino telescopes, Phys. Rev. Lett. 92 (2004) 011101. hep-ph/0307151, doi:10.1103/PhysRevLett.92.011101.
[30] A. Esmaili, Pseudo-dirac neutrino scenario: Cosmic neutrinos at neutrino telescopes, Phys. Rev. D81 (2010) 013006. 0909.5410, doi:10.1103/PhysRevD.81.013006.
[31] H. Athar, M. Jezabek, O. Yasuda, Effects of neutrino mixing on high-energy cosmic neutrino flux, Phys. Rev. D62 (2000) 103007. hep-ph/0005104, doi:10.1103/PhysRevD.62.103007.
[32] P.F. de Salas, R.A. Lineros, M. Tórtola, Neutrino propagation in the galactic dark matter halo, (2016). arXiv:1601.05798.
[33] C.A. Argüelles, T. Katori, J. Salvado, New physics in astrophysical neutrino flavor, Phys. Rev. Lett. 115 (2015) 161303. 1506.02043, doi:10.1103/PhysRevLett.115.161303.
[34] Z. Maki, M. Nakagawa, S. Sakata, Remarks on the unified model of elementary particles, Prog. Theor. Phys. 28 (1962) 870–880, doi:10.1143/PTP.28.870.
[35] M. Kobayashi, T. Maskawa, CP violation in the renormalizable theory of weak interaction, Prog. Theor. Phys. 49 (1973) 652–657, doi:10.1143/PTP.49.652.
[36] L. Wolfenstein, Neutrino oscillations in matter, Phys. Rev. D17 (1978) 2369–2374, doi:10.1103/PhysRevD.17.2369.
[37] M.C. Gonzalez-Garcia, M. Maltoni, Determination of matter potential from global analysis of neutrino oscillation data, JHEP 09 (2013) 152. 1307.3092, doi:10.1007/JHEP09(2013)152.
[38] A. Dziewonski, D. Anderson, Preliminary reference earth model, Phys. Earth Planet. Interiors 25 (1981) 297–356, doi:10.1016/0031-9201(81)90046-7.
[39] I.M. Shoemaker, K. Murase, Probing BSM neutrino physics with flavor and spectral distortions: Prospects for future high-energy neutrino telescopes, Phys. Rev. D93 (8) (2016) 085004. 1512.07228, doi:10.1103/PhysRevD.93.085004.
[40] H. Nunokawa, B. Panes, R.Z. Funchal, How unequal fluxes of high energy astrophysical neutrinos and antineutrinos can fake new physics, (2016). arXiv:1604.08595.
[41] J. Jones, I. Mocioiu, M.H. Reno, I. Sarcevic, Tracing very high-energy neutrinos from cosmological distances in ice, Phys. Rev. D69 (2004) 033004. hep-ph/0308042, doi:10.1103/PhysRevD.69.033004.
[42] M.C. Gonzalez-Garcia, F. Halzen, M. Maltoni, Physics reach of high-energy and high-statistics icecube atmospheric neutrino data, Phys. Rev. D71 (2005) 093010. hep-ph/0502223, doi:10.1103/PhysRevD.71.093010.
[43] C.A.A. Delgado, J. Salvado, C.N. Weaver, A simple quantum integro-differential solver (SQuIDS), Comput. Phys. Commun. 196 (2015) 569–591. 1412.3832, doi:10.1016/j.cpc.2015.06.022.
[44] M.C. Gonzalez-Garcia, M. Maltoni, J. Salvado, Testing matter effects in propagation of atmospheric and long-baseline neutrinos, JHEP 05 (2011) 075. 1103.4365, doi:10.1007/JHEP05(2011)075.
[45] O. Miranda, M. Tórtola, J. Valle, Are solar neutrino oscillations robust? JHEP 0610 (2006) 008. hep-ph/0406280, doi:10.1088/1126-6708/2006/10/008.
[46] S. Davidson, C. Pena-Garay, N. Rius, A. Santamaria, Present and future bounds on nonstandard neutrino interactions, JHEP 0303 (2003) 011. hep-ph/0302093.
[47] C. Biggio, M. Blennow, E. Fernandez-Martinez, General bounds on non-standard neutrino interactions, JHEP 0908 (2009) 090. 0907.0097, doi:10.1088/1126-6708/2009/08/090.
[48] J. Dorenbosch, et al., Experimental verification of the universality of electron-neutrino and muon-neutrino coupling to the neutral weak current, Phys. Lett. B180 (1986) 303, doi:10.1016/0370-2693(86)90315-1.
[49] J. Allaby, et al., A precise determination of the electroweak mixing angle from semileptonic neutrino scattering, Z. Phys. C36 (1987) 611, doi:10.1007/BF01630598.
[50] A. Blondel, P. Bockmann, H. Burkhardt, F. Dydak, A. Grant, et al., Electroweak parameters from a high statistics neutrino nucleon scattering experiment, Z.Phys. C45 (1990) 361–379, doi:10.1007/BF01549665.
[51] G. Zeller, et al., A precise determination of electroweak parameters in neutrino nucleon scattering, Phys. Rev. Lett. 88 (2002) 091802. hep-ex/0110059, doi:10.1103/PhysRevLett.88.091802.
[52] M.C. Gonzalez-Garcia, M. Maltoni, T. Schwetz, Updated fit to three neutrino mixing: status of leptonic CP violation, JHEP 11 (2014) 052. 1409.5439, doi:10.1007/JHEP11(2014)052.
[53] M. Gonzalez-Garcia, M. Maltoni, T. Schwetz, Nufit 2.0, 2014, http://www.nu-fit.org.
[54] A. Palladino, F. Vissani, The natural parameterization of cosmic neutrino oscillations, Eur. Phys. J. C75 (2015) 433. 1504.05238, doi:10.1140/epjc/s10052-015-3664-6.

Chapter5

Decoherence in neutrino propagation through matter, and bounds from IceCube/DeepCore

The description of the neutrino evolution done in the Introduction section, is based in the assumption that neutrinos are plane waves, the neutrino field cover all the space in a periodic way. Under this approximation cannot be described localized events, like the neutrino production and the detection, which take place in a finite space-time region, called coherence region. By the uncertainty principle, the uncertainty in the space (σ_x) is related to an uncertainty in the neutrino momentum (σ_p) by $\sigma_p \sigma_x \sim 1/2$. In quantum mechanics, the real localized particles are described by wave packets, which are a superposition of plane waves.

The neutrino flavor state $|\nu_\alpha(t,\vec{x})\rangle$ distributed according to the wave packet $\psi(t,\vec{x})$ is given, in terms of the massive states, by Eq (1.29)

$$|\nu_\alpha(t,\vec{x})\rangle = \sum_j U^\dagger_{\alpha j}\psi_j(t,\vec{x})\,|\nu_j\rangle \tag{5.1}$$

A convenient way to study the neutrino flavor evolution is to use the density matrix formalism. The 1-particle density operator is defined as

$$\hat{\rho}^\alpha(t,\vec{x}) = |\nu_\alpha(t,\vec{x})\rangle\,\langle\nu_\alpha(t,\vec{x})| = \sum_{jk} U^\dagger_{\alpha j}U_{\alpha k}\psi_j(t,\vec{x})\psi^*_k(t,\vec{x}) \tag{5.2}$$

The evolution equation in the density formalism is given by

$$\frac{d\hat{\rho}^\alpha}{dt} = -[H,\hat{\rho}^\alpha] \tag{5.3}$$

where H is the standard hamiltonian. In the following, we are going to study the evolution in vacuum ($H = H_{vac}$). In matter, we have to include the matter density potential as we did in section 1.5.

We need to make an assumption about the wave packet function $\psi(t,\vec{x})$ to solve the evolution equation. One of the most studied wave packet distributions, and the one that we are going to assume in the following, is the Gaussian wave-packet in the momentum space [44, 45]

$$\psi_k(\vec{p}) = \frac{1}{(2\pi\sigma_p)^{3/4}}\exp\left\{-\frac{(\vec{p}-\vec{p}_k)^2}{4\sigma_p^2}\right\} \tag{5.4}$$

where p_k is the average momentum and σ_p is the uncertainty associated to the momentum. The plane wave limit is recovered for $\sigma_p \to 0$, where the wave packet becomes a delta function $\psi_k(p) \approx \delta^3(\vec{p} - \vec{p}_k)$. In the coordinate space, the wave packet is obtained by making the Fourier transform

$$\psi_k(t, \vec{x}) = \int \frac{d^3p}{(2\pi)^{3/2}} \psi(\vec{p}) \exp\{\imath(\vec{p}\vec{x} - E_k(p)t)\} \tag{5.5}$$

Making a Taylor expansion of the energy of the neutrino state $|\nu_k\rangle$ over the momentum p_k, at first order in approximation we obtain $E_k(p) = \sqrt{p^2 + m_k^2} \approx E_k + p_k/E_k$, where $E_k = \sqrt{p_k^2 + m_k^2}$, and the wave packet in the coordinate space become

$$\psi_k(t, \vec{x}) = \frac{1}{2\pi\sigma_x^2} \exp\left\{\imath(\vec{p}_k\vec{x} - E_k t) - \frac{(\vec{x} - v_k t)^2}{4\sigma_x^2}\right\} \tag{5.6}$$

where we have used $\sigma_x = 1/2\sigma_p$, which is the size of the wave packet, and $v_k = p_k/E_k$ is the group velocity of the kth state.

The density matrix is averaged over the local volume where the propagation take place. The size of the volume is small compared with scale at which the system significantly change, but is very large compared with the size of the neutrino wave packet [45]. Making an integration of $\hat{\rho}^\alpha$ over an infinity volume, we obtain

$$\begin{aligned}\hat{\rho}^\alpha(t) = \int d^3x \hat{\rho}^\alpha(t, \vec{x}) \\ \sum_{jk} U_{\alpha j}^* U_{\alpha k} \exp\left\{-\imath\frac{\Delta m_{jk}^2 t}{2E} - \frac{(\vec{v}_j - \vec{v}_k)^2 t^2}{8\sigma_x^2}\right\}\end{aligned} \tag{5.7}$$

where we have used the ultra-relativistic limit ($E \simeq E_j \simeq E_k$, and $\Delta E - (\partial E/\partial p)\Delta\vec{p} = \Delta m^2/2E$). We have removed terms that goes like $(\vec{p}_j - \vec{p}_k)^2/\sigma_p^2$, since we can expect them to be very small in the ultra-relativistic limit. On the other hand, we keep the term $(\vec{v}_j - \vec{v}_k)^2 t^2$ since it going to be important as the evolution happen. We can compute now $P_{\alpha\beta}$ by taking the trace with the density operator $\hat{\rho}^\beta$. Defining the coherence length as

$$L_{coh} = \frac{2\sqrt{2}\sigma_x}{\vec{v}_j - \vec{v}_k} \tag{5.8}$$

The oscillation probability can be writen as

$$P_{\alpha\beta} = \sum_{jk} U_{\alpha j}^* U_{\alpha k} U_{\beta k}^* U_{\beta k} \exp\left\{-\imath\frac{\Delta m_{jk}^2 t}{2E} - \frac{t^2}{L_{coh}^2}\right\} \tag{5.9}$$

The expression obtained is very similar to Eq (1.37) with an extra term, which introduces a damping factor for the non-diagonal elements. The last term is just a consequence en the different velocities of the wave packets, and it introduces a decoherence in the neutrino propagation. When neutrinos travel for a long time, the damping factor suppresses the oscillations, and the oscillation probability only depends on the mixing matrix. In the next work, we are going to study the decoherence introduced by New Physics when neutrinos propagate through matter.

Prepared for submission to JHEP

CERN-TH-2018-041
IFT-UAM/CSIC-18-022
FERMILAB-PUB-18-067-T

arXiv:1803.04438v1 [hep-ph] 12 Mar 2018

Decoherence in neutrino propagation through matter, and bounds from IceCube/DeepCore

Pilar Coloma, Jacobo Lopez-Pavon, Ivan Martinez-Soler, Hiroshi Nunokawa

Theory Department, Fermi National Accelerator Laboratory, P.O. Box 500, Batavia, IL 60510, USA

Theoretical Physics Department, CERN, 1211 Geneva 23, Switzerland

Instituto de Física Teórica UAM-CSIC, Calle Nicolas Cabrera 13-15

Departamento de Física, Pontifícia Universidade Católica do Rio de Janeiro, C. P. 38097, 22451- 900, Rio de Janeiro, Brazil

E-mail: pcoloma@fnal.gov, jacobo.lopez.pavon@cern.ch, ivanj.m@csic.es, nunokawa@puc-rio.br

Abstract: We revisit neutrino oscillations in matter considering the open quantum system framework which allows to introduce possible decoherence effects generated by New Physics in a phenomenological manner. We assume that the decoherence parameters γ_{ij} may depend on the neutrino energy, as $\gamma_{ij} = \gamma_{ij}^0 (E/\text{GeV})^n$ ($n = 0, \pm 1, \pm 2$). The case of non-uniform matter is studied in detail, both within the adiabatic approximation and in the more general non-adiabatic case. In particular, we develop a consistent formalism to study the non-adiabatic case dividing the matter profile into an arbitrary number of layers of constant densities. This formalism is then applied to explore the sensitivity of IceCube and DeepCore to this type of effects. Our study is the first atmospheric neutrino analysis where a consistent treatment of the matter effects in the three-neutrino case is performed in presence of decoherence. We show that matter effects are indeed extremely relevant in this context. We find that IceCube is able to considerably improve over current bounds in the solar sector (γ_{21}) and in the atmospheric sector (γ_{31} and γ_{32}) for $n = 0, 1, 2$ and, in particular, by several orders of magnitude (between 3 and 9) for the $n = 1, 2$ cases. For $n = 0$ we find $\gamma_{32}, \gamma_{31} < 4.0 \cdot 10^{-24} (1.3 \cdot 10^{-24})$ GeV and $\gamma_{21} < 1.3 \cdot 10^{-24} (4.1 \cdot 10^{-24})$ GeV, for normal (inverted) mass ordering.

Contents

1 Introduction

The accurate measurement of the mixing angle θ_{13} by reactor neutrino experiments [1], with a small uncertainty comparable to that for θ_{12}, has initiated a precision era for neutrino physics. In the standard three-family framework, the main remaining issues are the possible observation of leptonic CP violation, the determination of the ordering of neutrino masses and probing the Dirac or Majorana nature of neutrinos. Some hints currently exist in the latest data collected by NOvA and T2K which seem to point to maximal CP violation in the neutrino sector, but the statistical significance is still low [2, 3]. Likewise, a global fit to neutrino oscillation data seems to show a mild preference for a normal mass ordering (see for instance [4, 5]), which needs to be confirmed as more data become available.

At the same time, and in view of the precision of present and near future neutrino facilities, it is of key importance to verify if neutrinos have unexpected properties caused by New Physics (NP) beyond the standard three-family framework. In this work we study one of the possible windows to NP, the so-called quantum decoherence

in neutrino oscillations, and update the existing bounds by analyzing IceCube and DeepCore data on atmospheric neutrinos. In particular, we are interested in a kind of decoherence effects in neutrino oscillations studied, for example, in [6–13] and, more recently, in [14–19]. These decoherence effects differ from the standard decoherence caused by the separation of wave packets (see e.g. [20]) and might arise, instead, from quantum gravity effects [21–23]. Throughout this work, for brevity, we will refer to such non-standard decoherence simply as decoherence.

The authors of Ref. [7] derived some of the strongest available constraints on neutrino decoherence in neutrino oscillations up to date, using atmospheric neutrino data from the Super-Kamiokande (SK) experiment [24–27]. Moreover, they considered the general case in which the decoherence parameters could depend on the neutrino energy via a power law, $\gamma = \gamma_0 (E/\mathrm{GeV})^n$, where $n = 0, -1, 2$. Nevertheless, these limits were obtained within a simplified two-family framework and without taking into account the matter effects in the neutrino propagation. Moreover, only a reduced subset of SK data (taken, in fact, almost 20 years ago now) was analyzed [24–27].

In this work, we show that performing a three-flavour analysis which includes the matter effects is essential in order to correctly interpret such constraints. In particular, it is not obvious to which γ_{ij} parameter the SK bounds derived in two families [7] would actually apply. We will show that it strongly depends on the neutrino mass ordering and on whether the sensitivity is dominated by the neutrino or antineutrino channels: for neutrinos the decoherence effects at high energies are mainly driven by γ_{21} (γ_{31}) for normal (inverted) ordering, while in the antineutrino channel they are essentially controlled by γ_{32} (γ_{21}) for normal (inverted) ordering. Concerning the solar sector, the authors of Ref. [15] obtained strong constraints on γ_{21} from an analysis of KamLAND data, for $n = 0, \pm 1$.[1] Finally, the authors of Ref. [29] derived several bounds on the atmospheric decoherence parameters γ_{32} and γ_{31} from an analysis of MINOS data.

Non-standard decoherence has been invoked several times in the literature in order to decrease the tension in the parameter space among different sets of neutrino oscillation data. For example, in Refs. [13, 14] a solution to the LSND anomaly based on quantum decoherence, compatible with global neutrino oscillation data, was proposed. More recently, in [17] it was shown that the $\sim 2\sigma$ tension between T2K and NOvA on the measurement of the atmospheric mixing angle θ_{23} could be alleviated through the inclusion of decoherence effects in the atmospheric neutrino sector, namely, $\gamma_{23} = (2.3 \pm 1.1) \cdot 10^{-23}$ GeV. Such value of γ_{23} would be close to the SK bound from Ref. [7], $\gamma < 3.5 \cdot 10^{-23}$ GeV (90% CL), but still allowed.

[1] It should be mentioned that, in [12], very strong bounds on dissipative effects were derived from solar neutrino data, for $n = 0, \pm 1, \pm 2$ and in a two-family approximation. However, such limits do not apply to the case in which only decoherence effects are included, as pointed out in [15, 28]. This will be further clarified in section 2.2.

This topic has recently brought the attention of a part of the community. In fact, several analyses of decoherence effects on present and future long-baseline neutrino oscillation experiments have been recently performed (albeit at the probability level only), see e.g. Refs. [16, 18, 19]. We note however that, according to the latest results reported by NOvA, the significance of the tension has been reduced to less than 1σ [3]. In this work we will show that the reference value for γ_{23} considered in [17] is indeed already excluded by IceCube data. Moreover, we find that IceCube and DeepCore data are able to improve significantly over most of the constraints in past literature, both for solar and atmospheric decoherence parameters, in some cases by several orders of magnitude.

The paper is structured as follows. In section 2 we present the formalism and discuss the effects of decoherence on the oscillation probabilities. We first review the case of constant matter density profile, and then proceed to discuss the case of non-uniform matter. In particular we show that, within the adiabatic approximation, no significant bounds on the decoherence parameters can be extracted from solar neutrino data. We then proceed to develop a formalism which permits a consistent treatment of the decoherence effects on neutrino propagation in non-uniform matter when the adiabaticity condition is not fulfilled, as is the case of atmospheric neutrino experiments. In Section 3 we apply this formalism to the computation of the relevant oscillation probabilities in the atmospheric neutrino case, discussing the main features arising in presence of decoherence. Section 4 summarizes the main features of the IceCube and DeepCore experiments, the data sets considered in our analysis, and the details of our numerical simulations. Our results are then presented and discussed in section 5. Finally, we summarize and draw our conclusions in section 6. Appendices A and B discuss technical details regarding some of the approximations used in our numerical calculations.

2 Quantum decoherence: Density matrix formalism

The evolution of the density matrix ρ in the neutrino system can be described as

$$\frac{d\rho}{dt} = -i\left[H, \rho\right] - \mathcal{D}\left[\rho\right], \tag{2.1}$$

where H is the Hamiltonian of the neutrino system and the second term $\mathcal{D}\left[\rho\right]$ parameterizes the decoherence effects. In vacuum, the diagonal elements of the Hamiltonian are given by $h_i = m_i^2/(2E)$, where m_i $(i = 1, 2, 3)$ are the masses of the three neutrinos and E is the neutrino energy. Here ρ is defined in the flavour basis, with matrix elements $\rho_{\alpha\beta}$. Throughout this work, we will use Greek indices for flavor $(\alpha, \beta = e, \mu, \tau)$, and Latin indices for mass eigenstates $(i, j = 1, 2, 3)$.

A notable simplification of eq. (2.1) can be achieved via the following set of assumptions. First, assuming complete positivity, the decoherence term $\mathcal{D}\left[\rho\right]$ can be

written in the so-called Lindblad form [30, 31]

$$\mathcal{D}\left[\rho\right] = \sum_m \left[\left\{\rho, D_m D_m^\dagger\right\} - 2 D_m \rho D_m^\dagger\right], \tag{2.2}$$

where D_m is a general complex matrix. Second, avoiding unitarity violation, which is equivalent to imposing the condition $d\,\mathrm{Tr}[\rho]/dt = 0$, requires D_m to be Hermitian. Moreover, $D_m = D_m^\dagger$ implies that the entropy $S = \mathrm{Tr}[\rho \ln \rho]$ increases with time. Finally, a key assumption is the average energy conservation of the neutrino system, which is satisfied when $[H, D_m] = 0$. In presence of matter effects, the Hamiltonian is diagonalized by the unitary mixing matrix $\tilde{U}$. Therefore, after imposing the condition $[H, D_m] = 0$, we get

$$\begin{aligned} H &= \tilde{U}\,\mathrm{diag}\left\{\tilde{h}_1, \tilde{h}_2, \tilde{h}_3\right\}\tilde{U}^\dagger \equiv \tilde{U} H_d \tilde{U}^\dagger, \\ D_m &= \tilde{U}\,\mathrm{diag}\left\{d_m^1, d_m^2, d_m^3\right\}\tilde{U}^\dagger \equiv \tilde{U} D_m^d \tilde{U}^\dagger. \end{aligned} \tag{2.3}$$

This condition implies that the averaged energy is conserved along the whole neutrino propagation. Note that we consider the standard definition for the relation between the mass and flavour eigenstates used in neutrino oscillations[2]. Moreover, throughout this paper, in our notation the presence of a tilde denotes that a quantity is affected by matter effects.

From a model-independent point of view, the d_m^j are free parameters that could a priori depend on the matter effects. The most common assumption in the literature is to assume that the d_m^j are independent of the matter density even in presence of matter effects. In order to be consistent with most previous studies and to compare the bounds obtained in our analysis with the constraints derived in previous publications, we will also assume that this is the case. Notice that this assumption does not imply that the matter effects are not relevant when neutrino propagation is affected by decoherence: it just implies that the d_m^j are assumed to be constant during neutrino propagation in the Earth.

2.1 Neutrino propagation in uniform matter

Performing the following change of basis

$$\tilde{\rho} = \tilde{U}^\dagger \rho \tilde{U}, \tag{2.4}$$

eq. (2.1) can be rewritten as

$$\frac{d\tilde{\rho}}{dt} = -i\left[H_d, \tilde{\rho}\right] - \sum_m \left[\left\{\tilde{\rho}, (D_m^d)^2\right\} - 2 D_m^d\, \tilde{\rho}\, D_m^d\right] - \tilde{U}^\dagger \frac{d\tilde{U}}{dt}\tilde{\rho} - \tilde{\rho}\frac{d\tilde{U}^\dagger}{dt}\tilde{U}. \tag{2.5}$$

[2]For field operators, $\nu_\alpha = \sum_i U_{\alpha i}\nu_i$. For one-particle states, $|\nu_\alpha\rangle = \sum_i U_{\alpha i}^* |\nu_i\rangle$.

If the matter profile is constant along the neutrino path, the system of equations becomes diagonal in $\tilde{\rho}_{ij}$

$$\frac{d\tilde{\rho}_{ij}}{dt} = -\left[\gamma_{ij} - i\Delta\tilde{h}_{ij}\right]\tilde{\rho}_{ij}, \tag{2.6}$$

where we have defined

$$\gamma_{ij} \equiv \sum_m \left(d_m^i - d_m^j\right)^2 = \gamma_{ji} > 0\,; \qquad \Delta\tilde{h}_{ij} = \tilde{h}_i - \tilde{h}_j. \tag{2.7}$$

Therefore, the solution of eq. (2.1) for constant matter is simply given by

$$\rho_{\alpha\beta}(t) = \left[\tilde{U}\tilde{\rho}(t)\tilde{U}^\dagger\right]_{\alpha\beta}, \tag{2.8}$$

with

$$\tilde{\rho}_{ij}(t) = \tilde{\rho}_{ij}(0)\, e^{-\left[\gamma_{ij} - i\Delta\tilde{h}_{ij}\right]t}, \tag{2.9}$$

where $\tilde{\rho}_{ij}(0)$ is determined by the initial conditions of the system. For instance, if the neutrino source flux is made only of the flavor ν_α ($\alpha = e, \mu, \tau$) the initial conditions are given by

$$\tilde{\rho}_{ij}(0) = \tilde{U}^*_{\alpha i}\tilde{U}_{\alpha j}\,. \tag{2.10}$$

As a result, the oscillation probabilities in presence of decoherence (for a constant matter profile) read

$$\begin{aligned} P_{\alpha\beta} \equiv P(\nu_\alpha \to \nu_\beta) &= \mathrm{Tr}\left[\hat{\rho}^{(\alpha)}(t)\hat{\rho}^{(\beta)}(0)\right] = \mathrm{Tr}\left[\hat{\rho}^{(\alpha)}(t)|\nu_\beta\rangle\langle\nu_\beta|\right] = \langle\nu_\beta|\hat{\rho}^{(\alpha)}(t)|\nu_\beta\rangle = \\ &= \sum_{i,j} \tilde{U}_{\beta i}\tilde{U}^*_{\beta j}\,\tilde{\rho}_{ij}(t) \\ &= \sum_{i,j} \tilde{U}^*_{\alpha i}\tilde{U}_{\beta i}\tilde{U}_{\alpha j}\tilde{U}^*_{\beta j} e^{-\left[\gamma_{ij} - i\Delta\tilde{h}_{ij}\right]t}\,. \end{aligned} \tag{2.11}$$

Finally, after some manipulation the above equation can be rewritten in the more familiar form

$$\begin{aligned} P_{\alpha\beta} = \delta_{\alpha\beta} &- 2\sum_{i<j} \mathrm{Re}\left[\tilde{U}^*_{\alpha i}\tilde{U}_{\beta i}\tilde{U}_{\alpha j}\tilde{U}^*_{\beta j}\right]\left(1 - e^{-\gamma_{ij}L}\cos\tilde{\Delta}_{ij}\right) \\ &- 2\sum_{i<j} \mathrm{Im}\left[\tilde{U}^*_{\alpha i}\tilde{U}_{\beta i}\tilde{U}_{\alpha j}\tilde{U}^*_{\beta j}\right] e^{-\gamma_{ij}L}\sin\tilde{\Delta}_{ij}, \end{aligned} \tag{2.12}$$

where

$$\tilde{\Delta}_{ij} \equiv \frac{\Delta\tilde{m}^2_{ij}L}{2E}, \qquad \gamma_{ij} = \gamma_{ji} \equiv \gamma^0_{ij}\left(\frac{E}{\mathrm{GeV}}\right)^n, \tag{2.13}$$

where $\Delta\tilde{m}^2_{ij} \equiv \tilde{m}^2_i - \tilde{m}^2_j$ are the effective mass squared differences of neutrinos in matter and we have used the approximation $L \approx t$, L being the distance traveled by the neutrino as it propagates. Note that the power law dependence on the neutrino energy given by eq. (2.13) breaks Lorentz invariance except for the case with $n = -1$

which gives similar effects to the neutrino decay (see e.g. [32]). However, the effect encoded in γ_{ij} only suppresses the oscillatory terms in the oscillation probability while a neutrino decay would also affect the non oscillatory terms. Therefore, in the framework considered in this work the total sum of the probabilities adds up to 1, while this is not the case for neutrino decay.

From eqs. (2.12) and (2.13), one would expect to have a sizable effect in neutrino oscillations for $\gamma_{ij}L \sim 1$. This condition gives an estimate of the values of γ_{ij} for which an effect may be experimentally observable:

$$\gamma_{ij}^0 \sim 1.7 \cdot 10^{-19} \left(\frac{L}{\text{km}}\right)^{-1} \left(\frac{E}{\text{GeV}}\right)^{-n} \text{ GeV}. \tag{2.14}$$

Nevertheless, we would like to remark that fulfilling this condition is not enough to have sensitivity to decoherence effects, as we will discuss in the next subsection.

Even though in our simulations we will numerically compute the exact oscillation probabilities, in order to understand qualitatively the impact of decoherence on the oscillation pattern it is useful to derive approximate analytical expressions. In this work, we will be focusing on the study of atmospheric neutrino oscillations, for which the oscillation channel $P_{\mu\mu}$ is most relevant. Recently, in [33, 34] approximated but very accurate analytical expressions for the standard oscillation probabilities in presence of constant matter density were derived. For the $\nu_\mu \to \nu_\mu$ oscillation channel including decoherence effects, using the same parametrization as in Ref. [34], we find:

$$\begin{aligned} P_{\mu\mu} = 1 &- A_{21}\left[1 - e^{-\gamma_{21}L}\cos\tilde{\Delta}_{21}\right] - A_{32}\left[1 - e^{-\gamma_{32}L}\cos\tilde{\Delta}_{32}\right] \\ &- A_{31}\left[1 - e^{-\gamma_{31}L}\cos\tilde{\Delta}_{31}\right], \end{aligned} \tag{2.15}$$

where

$$A_{ij} \equiv A_{ij}(\theta_{23}, \tilde{\theta}_{12}, \tilde{\theta}_{13}, \delta) = 2|U_{\mu i}(\theta_{23}, \tilde{\theta}_{12}, \tilde{\theta}_{13}, \delta)|^2 |U_{\mu j}(\theta_{23}, \tilde{\theta}_{12}, \tilde{\theta}_{13}, \delta)|^2, \tag{2.16}$$

and the effective mass splittings and mixing angles in matter can be expressed as [34]:

$$\begin{aligned} \cos 2\tilde{\theta}_{13} &= \frac{\cos 2\theta_{13} - a/\Delta m^2_{ee}}{\sqrt{(\cos 2\theta_{13} - a/\Delta m^2_{ee})^2 + \sin^2 2\theta_{13}}}, \\ \cos 2\tilde{\theta}_{12} &= \frac{\cos 2\theta_{12} - a'/\Delta m^2_{21}}{\sqrt{(\cos 2\theta_{12} - a'/\Delta m^2_{21})^2 + \sin^2 2\theta_{12}\cos^2(\tilde{\theta}_{13} - \theta_{13})}}, \\ \Delta\tilde{m}^2_{21} &= \Delta m^2_{21}\sqrt{(\cos 2\theta_{12} - a'/\Delta m^2_{21})^2 + \sin^2 2\theta_{12}\cos^2(\tilde{\theta}_{13} - \theta_{13})}, \\ \Delta\tilde{m}^2_{31} &= \Delta m^2_{31} + (a - \frac{3}{2}a') + \frac{1}{2}(\Delta\tilde{m}^2_{21} - \Delta m^2_{21}), \\ \Delta\tilde{m}^2_{32} &= \Delta\tilde{m}^2_{31} - \Delta\tilde{m}^2_{21}. \end{aligned} \tag{2.17}$$

Here, $a \equiv 2\sqrt{2}G_F n_e E$, where G_F is the Fermi constant and n_e is the electron density along the neutrino path, $\Delta m^2_{ee} \equiv \cos^2\theta_{12}\Delta m^2_{31} + \sin^2\theta_{12}\Delta m^2_{32}$, and $a' = a\cos^2\tilde{\theta}_{13} +$

$\Delta m^2_{ee} \sin^2(\tilde{\theta}_{13} - \theta_{13})$. The corresponding probability for antineutrinos is obtained simply replacing $a \to -a$ and $\delta \to -\delta$, where δ denotes the Dirac CP phase.

2.2 Neutrino propagation in non-uniform matter: adiabatic regime

Eq. (2.12) applies for constant density profiles (which is a very good approximation in the case of long-baseline neutrino oscillation experiments such as T2K or NOvA), but if the matter density is not constant the analysis becomes more complicated. Nevertheless, when the adiabaticity condition $d\tilde{U}/dt \ll 1$ is fulfilled, as in the solar neutrino case, the solution of the evolution equations given by eqs. (2.8) and (2.9) is still a good approximation. In such a case, the oscillation probability is given by

$$P_{\alpha\beta} = \langle \nu_\beta | \hat{\rho}^{(\alpha)}(t) | \nu_\beta \rangle = \sum_{i,j} \tilde{\rho}^{(\alpha)}_{ij}(0) e^{-\left[\gamma_{ij} - i\Delta\tilde{h}_{ij}\right]t} \langle \nu_\beta | \tilde{\nu}^{eff}_i \rangle \langle \tilde{\nu}^{eff}_j | \nu_\beta \rangle, \tag{2.18}$$

where ν^{eff}_i denotes the effective mass eigenstates at time t. In the case of solar neutrinos, the initial flux of ν_e is produced in the solar core and the initial conditions are given by:

$$\tilde{\rho}^{(e)}_{ij}(0) = \tilde{U}^{0*}_{ei} \tilde{U}^0_{ej}, \tag{2.19}$$

where $\tilde{U}^0$ denotes the effective mixing matrix at the production point. On the other hand, since the evolution is adiabatic, when the neutrinos come out from the Sun we have $|\tilde{\nu}^{eff}_i\rangle = |\nu_i\rangle$ and thus

$$\begin{aligned} P_{e\beta} &\approx \sum_{i,j} \tilde{U}^{0*}_{ei} U_{\beta i} \tilde{U}^0_{ej} U^*_{\beta j} e^{-\left[\gamma_{ij} - i\Delta\tilde{h}_{ij}\right]t} \\ &= \sum_i |\tilde{U}^0_{ei}|^2 |U_{\beta i}|^2 \\ &+ 2 \sum_{i<j} \mathrm{Re}\left[\tilde{U}^{0*}_{ei} U_{\beta i} \tilde{U}^0_{ej} U^*_{\beta j}\right] e^{-\gamma_{ij} t} \cos\tilde{\Delta}_{ij} - 2 \sum_{i<j} \mathrm{Im}\left[\tilde{U}^{0*}_{ei} U_{\beta i} \tilde{U}^0_{ej} U^*_{\beta j}\right] e^{-\gamma_{ij} t} \sin\tilde{\Delta}_{ij}. \end{aligned} \tag{2.20}$$

Finally, for solar neutrinos observed at the Earth we obtain, after averaging over the oscillating phase:

$$P_{e\beta} \approx \sum_i |\tilde{U}^0_{ei}|^2 |U_{\beta i}|^2, \tag{2.21}$$

which coincides with the standard three neutrino result. In other words, the decoherence effects encoded in γ_{ij} can not be bounded by solar neutrino oscillation experiments. This is due to the standard loss of coherence in the propagation from the Sun to the Earth, which strongly suppresses the oscillating terms. Notice that high energy astrophysical neutrinos at IceCube are not sensitive either to decoherence due to the averaged oscillations of neutrinos which are produced in distant astrophysical sources.

2.3 Neutrino propagation in non-uniform matter: layers of constant density

In the atmospheric neutrino case, the matter profile can not be considered constant since the neutrinos propagate through the Earth crust, mantle and core, which have different densities. The adiabaticity condition is not fulfilled either. In this case, eq. (2.5) should be solved including the non-adiabatic terms, which give non-diagonal contributions. Even though this can be done numerically, we will show that dividing the matter profile into layers of constant density considerably simplifies the analysis and reduces the computational complexity of the problem. In particular, this is crucial in the case of atmospheric neutrino oscillation experiments, for which numerical studies are already computationally demanding even in the standard three-family scenario. Dividing the matter profile into layers of different constant densities has proved to be a very good approximation in the standard three-family scenario and, therefore, we expect the same level of accuracy in presence of decoherence. Since the matter is constant in each layer, the evolution equations can be solved for each layer M as in section 2.1:

$$\begin{aligned}\rho^M_{\alpha\beta}(t_M) &= \left[\tilde{U}^M \tilde{\rho}^M(t_M)(\tilde{U}^M)^\dagger\right]_{\alpha\beta},\\ \tilde{\rho}^M_{ij}(t_M) &= \tilde{\rho}^M_{ij}(t_{M,0})\, e^{-\left[\gamma_{ij}-i\Delta\tilde{h}^M_{ij}\right]\Delta t_M},\end{aligned} \tag{2.22}$$

where $\Delta t_M \equiv t_M - t_{M,0}$, and $t_{M,0}$ and t_M denote the initial and final time for the propagation along layer M, respectively. Now the problem of computing the probability is just reduced to performing properly the matching among the evolution on the different layers. Let us first consider the simplest case of two layers A and B. The oscillation probability when the neutrino exits the second layer (at time t_B) is given by

$$P_{\alpha\beta} = \langle\nu_\beta|\hat{\rho}^{(\alpha)}(t_B)|\nu_\beta\rangle = \sum_{i,j} \tilde{U}^B_{\beta i}\,\tilde{U}^{B*}_{\beta j}\,\tilde{\rho}^B_{ij}(t_{B,0})\, e^{-\left[\gamma_{ij}-i\Delta\tilde{h}^B_{ij}\right]\Delta t_B}. \tag{2.23}$$

The key point here is that the matching should be done between the solutions of eq. (2.1) at the frontier between the two layers and in the flavor basis, as

$$\rho^A_{\alpha\beta}(t_A) = \rho^B_{\alpha\beta}(t_{B,0}). \tag{2.24}$$

After imposing the matching condition, the elements of the density matrix in the second layer at $t_{B,0}$ can be written in the matter basis as:

$$\begin{aligned}\tilde{\rho}^B_{ij}(t_{B,0}) &= \left[(\tilde{U}^B)^\dagger\tilde{U}^A\tilde{\rho}^A(t_A)(\tilde{U}^A)^\dagger\tilde{U}^B\right]_{ij}\\ &= \tilde{U}^{B*}_{\delta i}\tilde{U}^A_{\delta l}\tilde{\rho}^A_{ln}(t_{A,0})e^{-\left[\gamma_{ln}-i\Delta\tilde{h}^A_{ln}\right]\Delta t_A}\tilde{U}^{A*}_{\gamma n}\tilde{U}^B_{\gamma j}\\ &= \tilde{U}^{B*}_{\delta i}\tilde{U}^A_{\delta l}\tilde{U}^{A*}_{\alpha l}\tilde{U}^A_{\alpha n}e^{-\left[\gamma_{ln}-i\Delta\tilde{h}^A_{ln}\right]\Delta t_A}\tilde{U}^{A*}_{\gamma n}\tilde{U}^B_{\gamma j},\end{aligned} \tag{2.25}$$

where we have considered that the initial flux is made of ν_α as initial condition for the first layer, and $t_{A,0} = 0$. After substituting this result into eq. (2.23) we finally obtain

$$P_{\alpha\beta} = \sum_{\delta,\gamma,i,j,l,n} \tilde{U}^B_{\beta i}\tilde{U}^{B*}_{\delta i}\tilde{U}^B_{\gamma j}\tilde{U}^{B*}_{\beta j} e^{-\left[\gamma_{ij} - i\Delta\tilde{h}^B_{ij}\right]\Delta t_B} \times \tilde{U}^A_{\delta l}\tilde{U}^{A*}_{\alpha l}\tilde{U}^A_{\alpha n}\tilde{U}^{A*}_{\gamma n} e^{-\left[\gamma_{ln} - i\Delta\tilde{h}^A_{ln}\right]\Delta t_A} . \tag{2.26}$$

It can be easily checked that, in the limit $\gamma_{ij} \to 0$, the standard oscillation probability is recovered. In the three-layer case, following the same procedure we find

$$\begin{aligned} P_{\alpha\beta} = & \sum_{\delta,\gamma,\theta,\phi,i,j,l,n,m,k} \tilde{U}^C_{\beta i}\tilde{U}^{C*}_{\delta i}\tilde{U}^C_{\gamma j}\tilde{U}^{C*}_{\beta j} e^{-\left[\gamma_{ij} - i\Delta\tilde{h}^C_{ij}\right]\Delta t_C} \\ & \times \tilde{U}^B_{\delta l}\tilde{U}^{B*}_{\theta l}\tilde{U}^B_{\phi n}\tilde{U}^{B*}_{\gamma n} e^{-\left[\gamma_{ln} - i\Delta\tilde{h}^B_{ln}\right]\Delta t_B} \\ & \times \tilde{U}^A_{\theta m}\tilde{U}^{A*}_{\alpha m}\tilde{U}^A_{\alpha k}\tilde{U}^{A*}_{\phi k} e^{-\left[\gamma_{mk} - i\Delta\tilde{h}^A_{mk}\right]\Delta t_A} . \end{aligned} \tag{2.27}$$

The procedure can be easily generalized to an arbitrary number of layers. Indeed, under the approximation $L \approx t$, and defining

$$\tilde{\mathcal{A}}^M_{\alpha\beta\gamma\delta} \equiv \sum_{i,j} \tilde{U}^M_{\alpha i}\tilde{U}^{M*}_{\beta i}\tilde{U}^M_{\gamma j}\tilde{U}^{M*}_{\delta j} e^{-\left[\gamma_{ij} - i\Delta\tilde{m}^{M2}_{ij}/2E\right]\Delta L_M} , \tag{2.28}$$

the probabilities can be written in a more compact way as

$P_{\alpha\beta} = \sum_{\delta,\gamma} \tilde{\mathcal{A}}^B_{\beta\delta\gamma\beta}\tilde{\mathcal{A}}^A_{\delta\alpha\alpha\gamma}$ for two layers,

$P_{\alpha\beta} = \sum_{\delta,\gamma,\theta,\phi} \tilde{\mathcal{A}}^C_{\beta\delta\gamma\beta}\tilde{\mathcal{A}}^B_{\delta\theta\phi\gamma}\tilde{\mathcal{A}}^A_{\theta\alpha\alpha\phi}$ for three layers, and

$P_{\alpha\beta} = \sum_{\delta,\gamma,\theta,\phi,\ldots,\xi,\omega,\varphi,\rho} \tilde{\mathcal{A}}^N_{\beta\delta\gamma\beta}\tilde{\mathcal{A}}^{N-1}_{\delta\theta\phi\gamma}\ldots\tilde{\mathcal{A}}^B_{\xi\varphi\rho\omega}\tilde{\mathcal{A}}^A_{\varphi\alpha\alpha\rho}$ for N layers.

3 Atmospheric oscillation probabilities with decoherence

Atmospheric neutrino oscillations take place in a regime where matter effects are significant and can even dominate the oscillations. The relevance of matter effect increases with neutrino energy and is very different for neutrinos and antineutrinos, as the sign of the matter potential changes between the two cases. Matter effects also depend strongly on the neutrino mass ordering. In order to understand better the numerical results shown in this paper, it is useful to derive approximate expressions for the oscillations in the $\nu_\mu \to \nu_\mu$ and $\bar{\nu}_\mu \to \bar{\nu}_\mu$ channels in the presence of strong matter effects.

From the results obtained in Refs. [33, 34], for neutrino energies $E \gtrsim 15$ GeV matter effects drive the effective mixing angles in matter $\tilde{\theta}_{12}$ and $\tilde{\theta}_{13}$ to either 0 or $\pi/2$, depending on the channel (neutrino/antineutrino) and the mass ordering. It is

easy to show that, in this regime, the oscillation probabilities in eq. (2.15) can be approximated as:

$$P^{\rm NO}_{\mu\mu} \approx 1 - \frac{1}{2}\sin^2 2\theta_{23}\left(1 - e^{-\gamma_{21}L}\cos\tilde{\Delta}_{21}\right) \text{ for neutrinos,} \tag{3.1}$$

$$P^{\rm NO}_{\bar{\mu}\bar{\mu}} \approx 1 - \frac{1}{2}\sin^2 2\theta_{23}\left(1 - e^{-\gamma_{32}L}\cos\tilde{\Delta}_{32}\right) \text{ for antineutrinos,} \tag{3.2}$$

assuming a normal ordering (NO). For inverted ordering (IO) we get instead

$$P^{\rm IO}_{\mu\mu} \approx 1 - \frac{1}{2}\sin^2 2\theta_{23}\left(1 - e^{-\gamma_{31}L}\cos\tilde{\Delta}_{31}\right) \text{ for neutrinos,} \tag{3.3}$$

$$P^{\rm IO}_{\bar{\mu}\bar{\mu}} \approx 1 - \frac{1}{2}\sin^2 2\theta_{23}\left(1 - e^{-\gamma_{21}L}\cos\tilde{\Delta}_{21}\right) \text{ for antineutrinos.} \tag{3.4}$$

From eqs. (3.1)-(3.4) it is easy to see that the approximated oscillation probabilities for an inverted mass ordering can be obtained from the corresponding ones for normal mass ordering, just performing the following transformation:

$$\gamma_{21}, \tilde{\Delta}_{21} \to \gamma_{31}, \tilde{\Delta}_{31}, \tag{3.5}$$

$$\gamma_{32}, \tilde{\Delta}_{32} \to \gamma_{21}, \tilde{\Delta}_{21}. \tag{3.6}$$

Moreover, note that since the three decoherence parameters and the three mass splittings are related (see eqs. (2.7) and (2.13)), these two transformations automatically imply that

$$\gamma_{31}, \tilde{\Delta}_{31} \to \gamma_{32}, \tilde{\Delta}_{32}. \tag{3.7}$$

Eqs. (3.1)-(3.4) illustrate why a proper consideration of the matter effects in the context of three families is of key importance in order to correctly interpret the bounds extracted within a simplified two-flavour approximation (as done in e.g. Ref. [7]). According to our analytical results, which will be confirmed numerically below, the constraints obtained from SK in a two-family approximation cannot be simply applied to γ_{31} or γ_{32}, contrary to the naive expectation. In fact, the interpretation of such limits depends strongly on the ordering of neutrino masses and on whether the sensitivity is dominated by the neutrino or antineutrino channels: for neutrinos the decoherence effects at high energies would be mainly driven by γ_{21} (γ_{31}) for normal (inverted) ordering. Conversely, in the antineutrino channel decoherence effects are essentially controlled by γ_{32} (γ_{21}) for normal (inverted) ordering. Therefore, we conclude that in order to avoid any misinterpretation of the bounds from atmospheric neutrinos, a three-family approach including matter effects should be considered.

Figure 1 shows the numerically obtained $\nu_\mu \to \nu_\mu$ (top panels) and $\overline{\nu}_\mu \to \overline{\nu}_\mu$ (bottom panels) oscillation probabilities for NO (left panels) and IO (right panels), with and without decoherence, as a function of the neutrino energy for a three-layer model (details on the accuracy of our three-layer model and the specific parameters

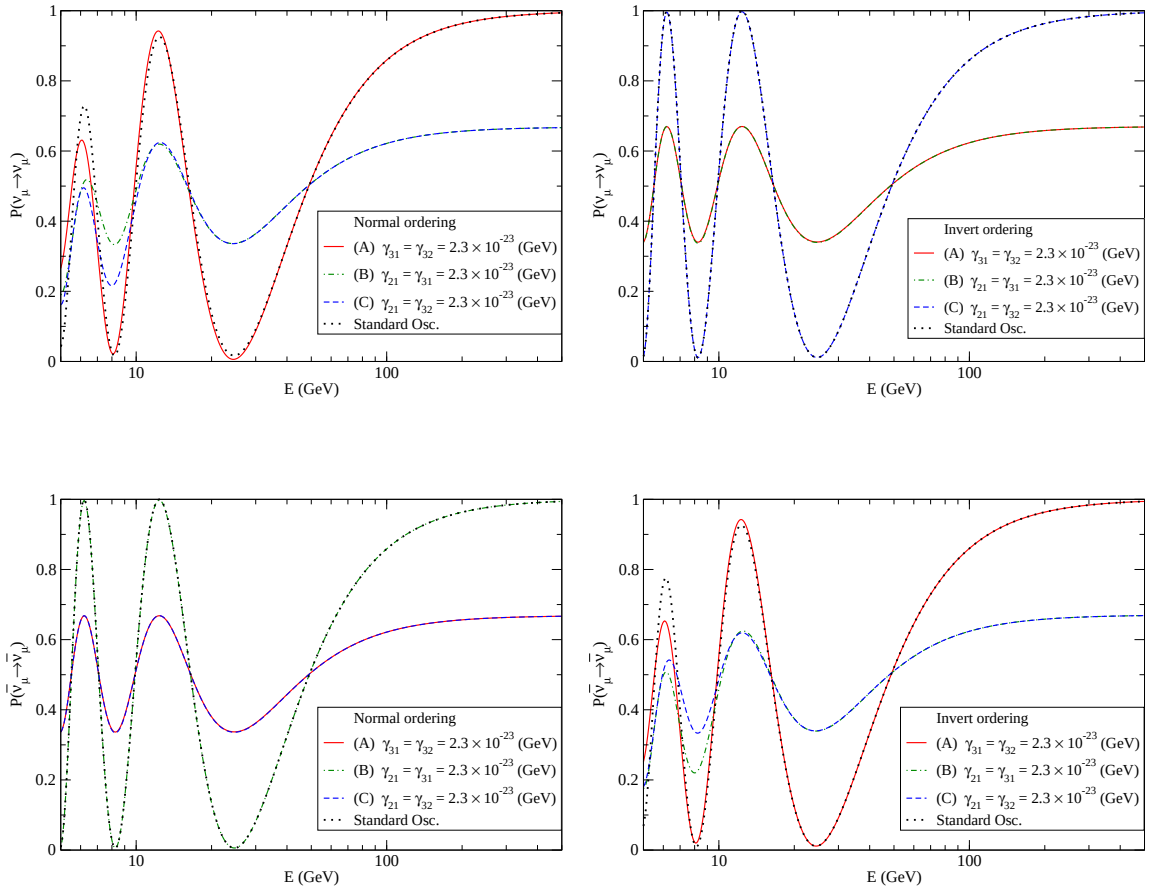

Figure 1: The $\nu_\mu \to \nu_\mu$ (top panels) and $\overline{\nu}_\mu \to \overline{\nu}_\mu$ (bottom panels) oscillation probabilities with $(n = 0)$ and without decoherence effects as a function of the neutrino energy. The probabilities have been computed for normal (left panels) and inverted (right panels) neutrino mass ordering, using the three-layer model for the Earth matter density profile, and correspond to the case in which the neutrinos cross the center of the Earth core, namely, $\cos\theta_z = -1$.

used in our simulations can be found in Appendix A). For the sake of simplicity, in this section we focus on the case $n = 0$, where the γ_{ij} do not depend on the neutrino energy (the results for different values of n show a similar qualitative behavior). The standard oscillation parameters have been fixed to the best fit values given in [4, 5].

Figure 1 clearly shows how the decoherence tends to damp the oscillatory behavior, in qualitative agreement with eq. (2.15) and the corresponding approximated expressions given by eqs. (3.1)-(3.4). Nevertheless, we should stress that eq. (2.15) has been obtained under several approximations, in particular only one layer with constant matter density. Therefore, even though eq. (2.15) is useful to understand the general damping effect of the oscillation and which terms are expected to dom-

inate the sensitivity, it may not explain all the features observed in the DeepCore and IceCube analysis presented in section 5, which has been performed numerically using the exact probability considering three layers (see appendix A for details).

Since the three γ_{ij} are not completely independent from one another (see eq. (2.7)), in view of equations (3.1)-(3.4) and in order to simplify the analysis, hereafter we will distinguish three different representative cases, where the decoherence effects are dominated by just one parameter:

(A) Atmospheric limit: $\gamma_{21} = 0$ ($\gamma_{32} = \gamma_{31}$),

(B) Solar limit I: $\gamma_{32} = 0$ ($\gamma_{21} = \gamma_{31}$),

(C) Solar limit II: $\gamma_{31} = 0$ ($\gamma_{21} = \gamma_{32}$).

In appendix B, we will show that the bounds derived in these limits correspond to the most conservative bounds that can be extracted in the general case. As a reference value for the decoherence parameters in this section, we have considered $\gamma = 2.3 \cdot 10^{-23}$ GeV, for each of the three limiting cases listed above.

The results in figure 1 show that, for neutrinos with a NO (top left panel), the impact of decoherence is essentially controlled by γ_{21}, in good agreement with eq. (3.1): no significant effects are seen in the atmospheric limit (A), while a similar impact is obtained in the solar limits I (B) and II (C). Conversely, for IO (top right panel) the effects are dominated by γ_{31} instead: no effect is observed for the solar limit II (C), while in scenarios (A) and (B) the effect is very similar. This can be qualitatively understood from the approximate probability derived in eq. (3.3), which only depend on the decoherence parameter γ_{31}. On the other hand, in the antineutrino case for NO (bottom left panel) no observable decoherence effects take place in case (B), while cases (A) and (C) show a similar behavior, in agreement with eq. (3.2). Conversely, for IO (bottom right panel) decoherence effects are essentially controlled by γ_{21} as shown in eq. (3.4): therefore, no significant effects are observed in case (A) while a similar impact is obtained for case (B) and (C).

Moreover, it should be pointed out that the transformations listed in Eqs. (3.5)-(3.7) automatically imply the following equivalence for the results obtained in the three limiting cases listed above:

$$\begin{aligned} (\mathrm{A})^{\mathrm{NO}} &\longleftrightarrow (\mathrm{C})^{\mathrm{IO}}, \\ (\mathrm{B})^{\mathrm{NO}} &\longleftrightarrow (\mathrm{A})^{\mathrm{IO}}, \\ (\mathrm{C})^{\mathrm{NO}} &\longleftrightarrow (\mathrm{B})^{\mathrm{IO}}. \end{aligned} \tag{3.8}$$

This is confirmed at the numerical level as it can be easily seen by comparing the different lines shown in the left (NO) and right (IO) panels in figure 1 for the three limiting cases.

It is also remarkable that, for both normal and inverted hierarchy, even when the standard oscillations turn off (at very high energies), there is still a large effect on the probability due to decoherence effects, that could potentially be tested with neutrino telescopes like IceCube. In particular, for $E \gtrsim 200$ GeV one can approximate $\cos\tilde{\Delta}_{ij} \approx 1$, $\forall i, j$. Therefore, in the standard case (with $\gamma_{ij} = 0$) the last three terms in eq. (2.15) approximately vanish, leading to $P_{\mu\mu} \approx 1$. However, in presence of decoherence those terms will not vanish completely, as $e^{-\gamma_{ij}L}\cos\tilde{\Delta}_{ij} \neq 1$. This leads to a depletion of $P_{\mu\mu}$, which is no longer equal to 1 in this case. The size of the effect will of course depend on the baseline of the experiment. Since at high energies the oscillation probability does no longer depend on the neutrino energy, at oscillation experiments with a fixed baseline the effect may be hindered by the presence of any systematic errors affecting the normalization of the signal event rates. However, at atmospheric experiments this effect can be disentangled from a simple normalization error by comparing the event rates at different nadir angles.

The dependence of the neutrino probabilities with the zenith angle θ_z is illustrated in figure 2, assuming a normal mass ordering and fixing the standard oscillation parameters to the best fit values given in [4, 5]. The results are shown as a neutrino oscillogram (see for instance [35]), which represents the oscillation probability in the $P_{\mu\mu}$ channel as a function of neutrino energy and zenith angle θ_z (which can be related to the distance traveled by the neutrino). Figure 2 shows the oscillation probability $P_{\mu\mu}$ in the three limiting cases described above, comparing it to the results in the standard scenario ($\gamma_{ij} = 0$). As expected, the effects depend on the direction of the incoming neutrino and they are more relevant in the region $-1 \lesssim \cos\theta_z \lesssim -0.4$, this is, for very long baselines. This was to be expected, since the decoherence effects are driven by $e^{-\gamma_{ij}L}$. In addition, the dependence of the oscillation probability with the zenith angle at very high energies ($E > 100$ GeV) is clearly visible in the bottom panels of figure 2. As we will show in section 5, this will lead to an impressive sensitivity for the IceCube setup. Finally, note that the results for inverted ordering show similar features to those in figure 2, once the mapping in eq. (3.8) is applied, and are therefore not shown here.

4 IceCube/DeepCore simulation details and data set

The IceCube neutrino telescope, located at the South Pole, is composed of 5160 DOMs (Digital Optical Module) deployed between 1450m and 2450m below the ice surface along 86 vertical strings [36]. In the inner core of the detector, a subset of these DOMs were deployed deeper than 1750m and closer to each other than in the rest of IceCube. This subset of strings is called DeepCore. Due to the shorter distance between its DOMs, the neutrino energy threshold in DeepCore (~ 5 GeV) is lower than in IceCube (~ 100 GeV). This allows DeepCore to observe neutrino

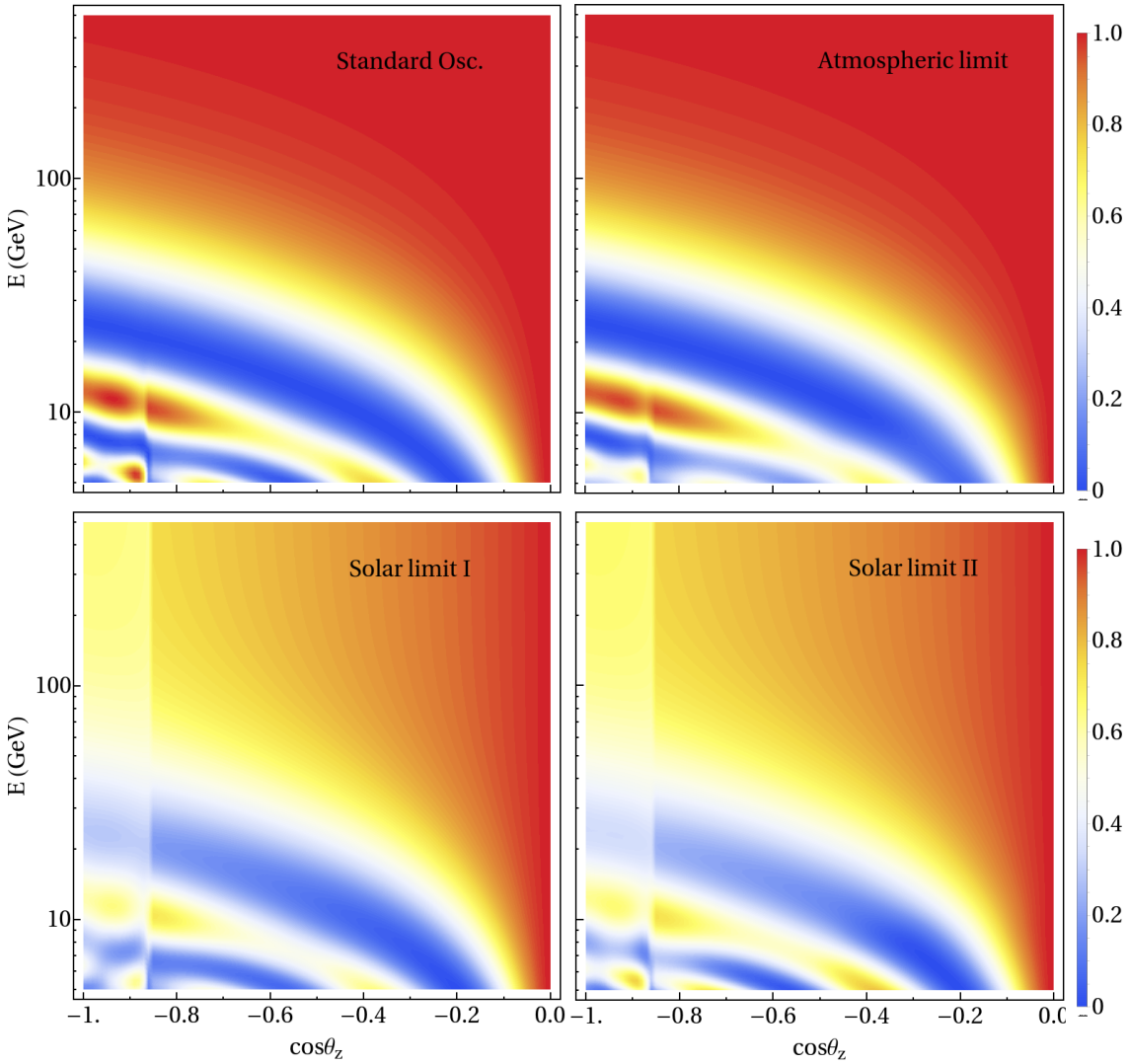

Figure 2: Oscillograms for the neutrino oscillation probability $P_{\mu\mu}$, assuming normal mass ordering. The top-left panel corresponds to the case of no decoherence $\gamma_{ij} = 0$ whereas the rest of the panels correspond to the three limiting cases mentioned in the text: (A) $\gamma_{32} = \gamma_{31}$ (top-right), (B) $\gamma_{31} = \gamma_{21}$ (bottom-left) and (C) $\gamma_{32} = \gamma_{21}$ (bottom-right). In all cases, the size of the decoherence parameters that are turned on is set to a constant value, $\gamma = 2.3 \cdot 10^{-23}$ GeV.

events in the energy region where atmospheric oscillations take place, see figure 1, whereas IceCube only observes high-energy atmospheric neutrino events.

As outlined in section 2, for high energy astrophysical neutrinos the effect of non-standard decoherence in the probability would be completely erased by the time they reach the detector. Therefore, in this work we will focus on the observation of atmospheric neutrino events at both IceCube and DeepCore, in the energy range ~ 10 GeV to ~ 1 PeV. In particular, we have used the three-year DeepCore data on

atmospheric neutrinos with energies between ~ 10 GeV and ~ 1 TeV, taken between May 2011 and April 2014 [37], and the one-year IceCube data taken between 2011-2012 [38–40], corresponding to neutrinos with energies between 200 GeV and 1 PeV.

At IceCube and DeepCore, events are divided according to their topology into "tracks" and "cascades" [41]. Tracks are produced by the Cherenkov radiation of muons propagating in the ice. In atmospheric neutrino experiments, muons are typically produced by two main mechanisms: (1) via charged-current (CC) interactions of ν_μ with nuclei in the detector, and (2) as decay products of mesons (typically pions and kaons) originated when cosmic rays hit the atmosphere. Conversely, cascades are created in CC interactions of ν_e or ν_τ[3]: in this case, the rapid energy loss of electrons as they move through the ice is the origin of an electromagnetic shower. At IceCube/DeepCore, cascades are also observed as the product of hadronic showers generated in neutral current (NC) interactions for neutrinos of all flavors. Our analysis considers only track-like events observed at both IceCube and DeepCore although, as we will see, some small contamination from cascade events can be expected (especially at low energies).

4.1 IceCube simulation details

For IceCube, the observed event rates are provided in a grid of 10×21 [39], using 10 bins for the reconstructed energy (logarithmically spaced, ranging from 400 GeV to 20 TeV), and 21 bins for the reconstructed neutrino direction (linearly spaced, between $\cos\theta_z^{rec} = -1.02$ to $\cos\theta_z^{rec} = 0.24$). The muon energy is reconstructed with an energy resolution $\sigma_{\log_{10}(E_\mu/\mathrm{GeV})} \sim 0.5$ [38], while the zenith angle resolution is in the range $\sigma_{\cos\theta_z} \in [0.005, 0.015]$, depending on the scattering muon angle.

The number of events in each bin is computed as:

$$N_i(E^{rec}, \theta_z^{rec}) = \sum_{\pm} \int dE \; d\cos\theta_z \, \phi^{\mathrm{atm}}_{\mu,\pm}(E,\theta_z) P^{\pm}_{\mu\mu}(E,\theta_z) A^{\mathrm{eff}}_{i,\pm,\mu}(E,\theta_z,E^{rec},\theta_z^{rec}) e^{-X(\theta_z)\sigma^{\pm}(E)}, \tag{4.1}$$

where E, θ_z denote the true values of energy and zenith angle, while E^{rec}, θ_z^{rec} refer to their reconstructed quantities. Here, $\phi^{\mathrm{atm}}_{\mu,\pm}$ is the atmospheric flux for muon neutrinos (+) and anti-neutrinos (-), $P^{\pm}_{\mu\mu}(E,\theta_z)$ is the neutrino/antineutrino oscillation probability given by eq. (2.27), and $A^{\mathrm{eff}}_{i,\pm,\mu}(E,\theta_z)$ is the effective area encoding the detector response in neutrino energy and direction (which relates true and reconstructed variables), the interaction cross section and a normalization constant, and has been integrated over the whole data taking period. In our IceCube simulations,

[3]Technically, a CC ν_τ event could be distinguished from a ν_e CC event, e.g., by the observation of two separates cascades connected by a track from the τ propagation [42]. However, for atmospheric neutrino energies the distance between the cascades cannot be resolved by the DOMs at IceCube/DeepCore, leaving in the detector a signal similar to a single cascade.

we have used the unpropagated atmospheric flux (HondaGaisser) provided by the collaboration [38, 43], and for the effective area we have used the nominal detector taken from Refs. [38, 43]. On the other hand, the exponential factor takes into account the absorption of the neutrino flux by the Earth, which increases with the neutrino energy. Here, $X(\theta_z)$ is the column density along the neutrino path and $\sigma^{\pm}(E)$ is the total inclusive cross section for ν_μ or $\bar{\nu}_\mu$. Note that in eq. (4.1) no contamination from cascade events is considered since the mis-identification rate is expected to be negligible at these energies [44]. Similarly, the number of atmospheric muons that pass the selection cuts can also be neglected, given the extremely good angular resolution at these energies [38].

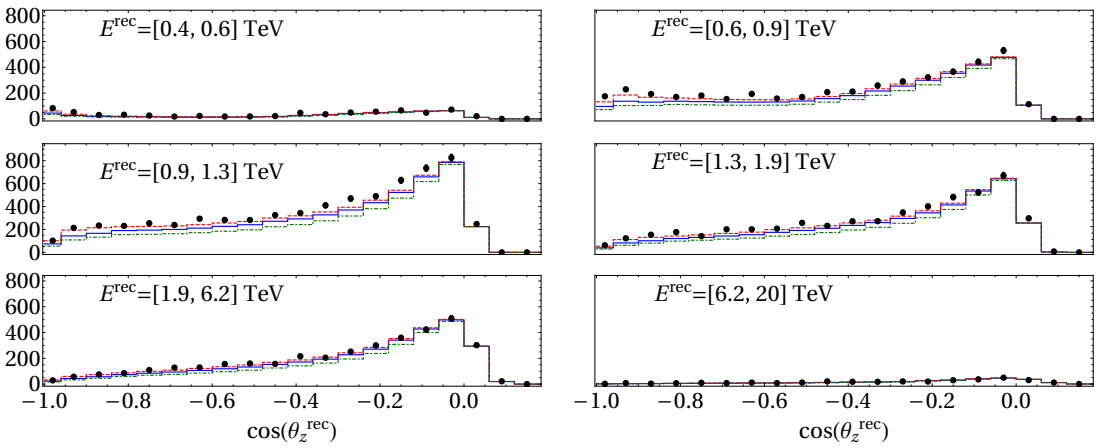

Figure 3: Event distributions obtained for IceCube in our numerical simulations as a function of the reconstructed value of the cosine of the zenith angle, for neutrinos in different reconstructed energy ranges. The lines have been obtained assuming a normal mass ordering, for the following values for the decoherence parameters: $\gamma_{21} = \gamma_{31} = 2.3 \cdot 10^{-23}$ GeV (solid blue line), $\gamma_{21} = \gamma_{31} = 10^{-22}$ GeV (dashed green line) and without decoherence (dashed red line). The observed data points [39] are represented by the black dots, and the error bars indicate the statistical uncertainties for each bin.

Figure 3 shows the expected number of events for IceCube from our numerical simulations including decoherence, for $\gamma_{21} = \gamma_{31} = 2.3 \cdot 10^{-23}$ GeV (solid blue lines) and $\gamma_{21} = \gamma_{31} = 10^{-22}$ GeV (dashed green lines), as a function of $\cos\theta_z^{rec}$, for events in different reconstructed energy ranges. For simplicity, we have considered the $n = 0$ case (that is, γ_{ij} independent of the neutrino energy). The expected result without decoherence is also shown for comparison (dashed red lines), while the observed data are shown by the black dots.

For the analysis of the IceCube data we have performed a Poissonian log-likelihood analysis doing a simultaneous fit on the following parameters: Δm^2_{32}, θ_{23} and γ_{ij}. The

Source of uncertainty	Value
Flux - normalization	Free
Flux - π/K ratio	10%
Flux - energy dependence as $(E/E_0)^\eta$	$\Delta\eta = 0.05$
Flux - $\bar{\nu}/\nu$	2.5%
DOM efficiency	5%
Photon scattering	10%
Photon absorption	10%

Table 1: The most relevant systematic errors used in our analysis of IceCube data, taken from Refs. [38, 40, 43].

rest of the oscillation parameters have been kept fixed to their current best-fit values from Ref. [4]. The most relevant systematic errors used in the fit are summarized in Table 1, and have been taken from Ref. [38, 40, 43]. For each systematic uncertainty a pull term is added to the χ^2 following the values listed in the table, except in the cases indicated as "Free" (when the corresponding nuisance parameter is allowed to float freely in the fit).

4.2 DeepCore simulation details

In the case of DeepCore, the observed event rates are provided in a grid of 8×8 bins, using 8 bins for the reconstructed neutrino energy and 8 bins for the reconstructed neutrino direction. The energy resolution $\sigma_{E/\mathrm{GeV}}$ is in the range of 30%-20% while the zenith angle resolution improves with the energy, from $\sigma_{\theta_z} = 12^\circ$ at $E_\nu = 10$ GeV to $\sigma_{\theta_z} = 5^\circ$ at $E_\nu = 40$ GeV [37]. In each bin, the number of events is computed as

$$N_i(E^{rec}, \theta_z^{rec}) = \sum_{\pm,\alpha,\beta} \int dE\, d\cos\theta_z\, \phi^{\mathrm{atm}}_{\alpha,\pm}(E,\theta_z)\, P^{\pm}_{\alpha\beta}(E,\theta_z)\, A^{\mathrm{eff}}_{i,\pm,\beta}(E,\theta_z,E^{rec},\theta_z^{rec}) + N_{i,\mu}(E^{rec},\theta_z^{rec}). \tag{4.2}$$

Unlike for IceCube, at DeepCore muon tracks can be produced from $\nu_\mu \to \nu_\mu$ and $\nu_e \to \nu_\mu$ events[4]. Moreover, the track-like event distributions at DeepCore will also receive a partial contributions from cascades which are mis-identified as tracks: hence the sum over $\beta = e, \mu, \tau$ in eq. (4.2). Therefore, here $\phi^{\mathrm{atm}}_{\alpha,\pm}$ stands for the atmospheric flux for neutrinos/antineutrinos of flavor α (where we have used the fluxes from Ref. [45]), and $P^{\pm}_{\alpha\beta}$ refers to the neutrino/antineutrino oscillation probability in the channel $\nu_\alpha \to \nu_\beta$ for neutrinos (+) (or $\bar{\nu}_\alpha \to \bar{\nu}_\beta$, for antineutrinos (-)). The rejection efficiencies for the contamination are included in the detector response function $A^{\mathrm{eff}}_{i,\pm,\beta}$, which now depends on the flavor β of the interacting neutrino. Finally, an

[4]The flux from ν_τ can be considered negligible at these energies.

estimate of the atmospheric muons that overcome the selection criteria (taken from Ref. [37, 43]) is also added for each bin in reconstructed variables, $N_{i,\mu}$.

Figure 4 shows the expected number of events for DeepCore obtained from our numerical simulations including decoherence, for $\gamma_{21} = \gamma_{31} = 2.3 \cdot 10^{-23}$ GeV (solid blue lines) and $\gamma_{21} = \gamma_{31} = 10^{-22}$ GeV (dashed green lines), as a function of $\cos\theta_z^{rec}$, for events in different reconstructed energy ranges. For simplicity, we have considered the $n = 0$ case (that is, γ_{ij} independent of the neutrino energy). The expected result without decoherence is also shown for comparison (dashed red lines), while the observed data are shown by the black dots.

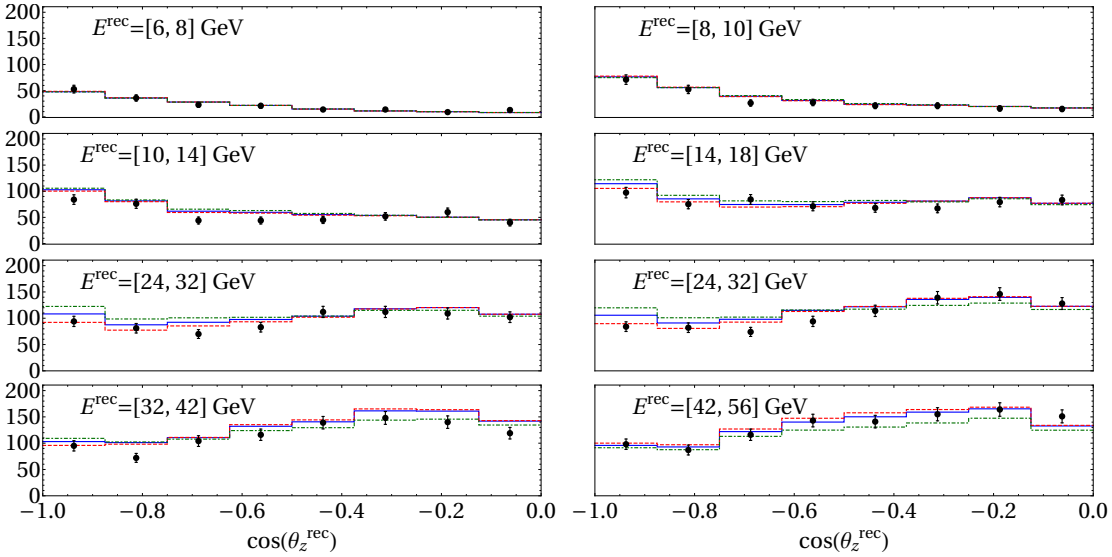

Figure 4: Event distributions obtained for DeepCore in our numerical simulations as a function of the reconstructed values of the cosine of the zenith angle, for neutrinos in different reconstructed energy ranges. The lines have been obtained assuming a normal mass ordering, for the following values for the decoherence parameters: $\gamma_{21} = \gamma_{31} = 2.3 \cdot 10^{-23}$ GeV (solid blue line), $\gamma_{21} = \gamma_{31} = 10^{-22}$ GeV (dashed green line) and without decoherence (dashed red line). The observed data points [37] are represented by the black dots, and the error bars indicate the statistical uncertainties for each bin.

In this work a Gaussian maximum likelihood is used to analyze the DeepCore data, performing a simultaneous fit on the following parameters: Δm^2_{32}, θ_{23} and γ_{ij}. The rest of the oscillation parameters have been kept fixed to their current best-fit values from Ref. [4]. The systematics used in the fit are those associated with the flux, the detector response and the atmospheric muons given in Ref. [37] and are summarized in Table 2. For each systematic uncertainty a pull term is added to the χ^2 following the values listed in the table, except in the cases indicated as "Free" (when the corresponding nuisance parameter is allowed to float freely in the fit). We

Source of uncertainty	Value
Flux - normalization	Free
Flux - energy dependence as $(E/E_0)^\eta$	$\Delta\eta = 0.05$
Flux - $(\nu_e + \bar{\nu}_e)/(\nu_\mu + \bar{\nu}_\mu)$ ratio	20%
Background - normalization	Free
DOM efficiency	10%
Optical properties of the ice	1%

Table 2: Systematic errors used in our analysis of DeepCore data, taken from Refs. [37, 41].

have checked that our analysis reproduces the confidence regions in the $\Delta m^2_{32} - \theta_{23}$ plane obtained by the DeepCore collaboration in Ref. [37] to a very good level of accuracy.

Finally, it should be noted that our fit does not include the latest atmospheric data recently published by the DeepCore collaboration [46]. The new analysis uses a different data set (from April 2012 to May 2015) and a new implementation of systematic errors, which lead to smaller confidence regions in the $\Delta m^2_{32} - \theta_{23}$ plane. However, the detector response parameters and systematic errors used in the latest release have not been published yet. In view of the better results obtained for the standard three-family oscillation scenario, a similar improvement is to be expected if the analysis performed in this work were to be repeated using the latest DeepCore data.

5 Results

Following the procedure described in section 4 we have obtained the χ^2 for every point in the parameter space. Marginalizing over the relevant mixing and mass parameters, namely, Δm^2_{32} and θ_{23}, the sensitivity of the data to γ_{ij} parameters is determined by evaluating the $\sqrt{\Delta\chi^2}$, with $\Delta\chi^2 \equiv \chi^2 - \chi^2_{\rm min}$, where $\chi^2_{\rm min}$ is the value at the global minimum. The rest of the standard mixing parameters have been fixed to their best-fit values from Refs. [4, 5].

In this section we will only show the results obtained for normal neutrino mass ordering, since we have checked that extremely similar results are obtained for IO after applying the mapping given in eq. (3.8). Nevertheless, in Sec. 6 we will also provide the 95% CL bounds obtained in our numerical analysis for the IO case. The bounds obtained are in very good agreement with the mapping given in eq. (3.8).

Figure 5 shows the obtained $\sqrt{\Delta\chi^2}$ as a function of γ_0 for the three limiting cases defined in Sec. 3: (A) atmospheric limit, $\gamma_0 = \gamma^0_{32} = \gamma^0_{31}$ (red curve); (B) solar limit I, $\gamma_0 = \gamma^0_{21} = \gamma^0_{31}$ (green curve); and (C) solar limit II, $\gamma_0 = \gamma^0_{21} = \gamma^0_{32}$ (blue curve). In

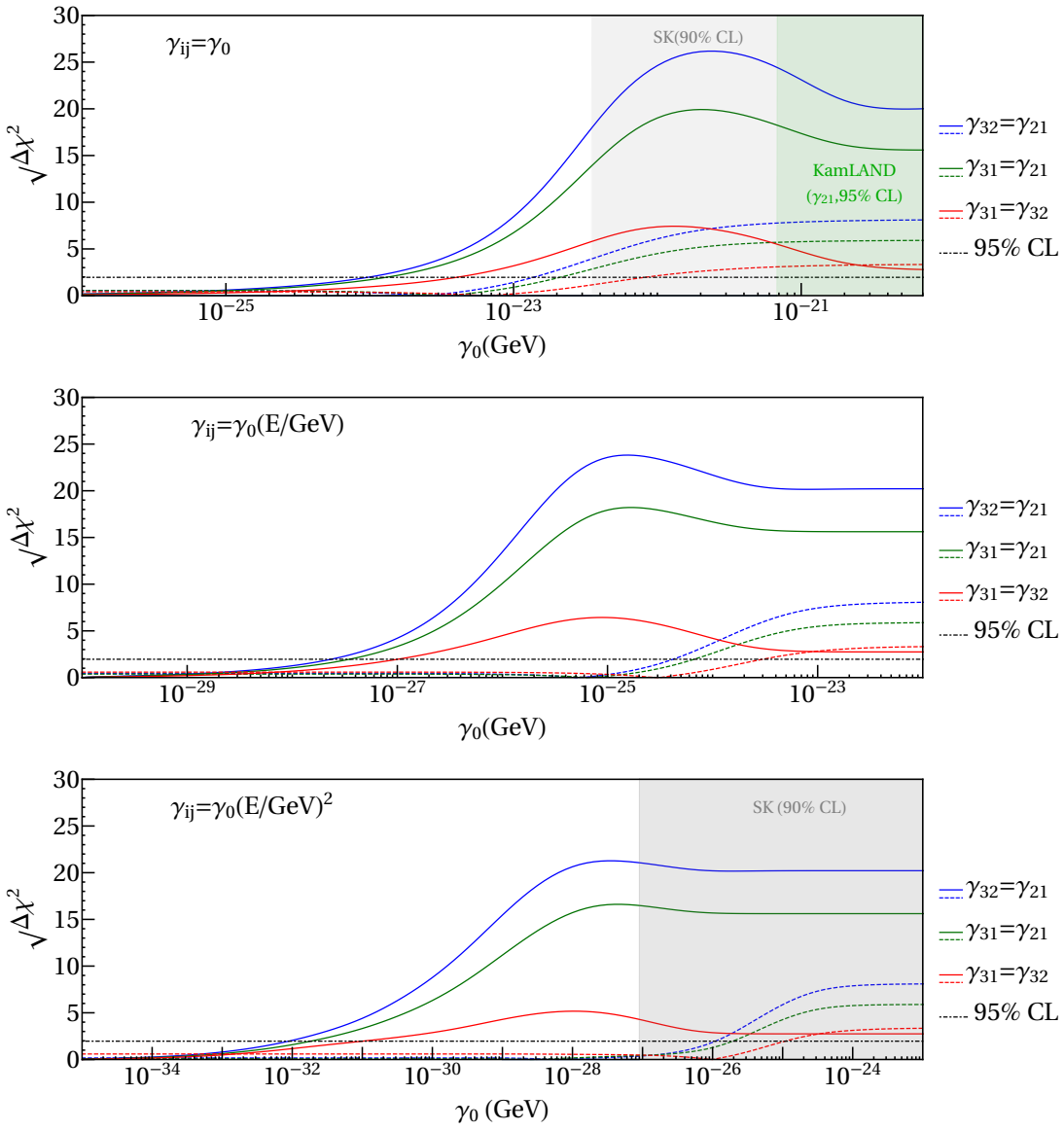

Figure 5: Values of the $\sqrt{\Delta\chi^2}$ as a function of the decoherence parameter for the Atmospheric limit (red), Solar limit I (green) and Solar limit II (blue) defined in Sec. 3. The results obtained from our analysis of IceCube (DeepCore) data are denoted by the solid (dashed) lines. The three panels have been obtained for NO, assuming a different dependence on the neutrino energy: $n = 0$ (top panel), $n = 1$ (middle panel) and $n = 2$ (bottom panel). The shaded regions are disfavored by previous analysis of SK [7] and KamLAND [15] data, see text for details. The horizontal black line indicates the value of the $\sqrt{\Delta\chi^2}$ corresponding to 95% CL for 1 degree of freedom.

all cases, the solid (dashed) lines correspond to the results obtained from our analysis of the IceCube (DeepCore) data, and each panel shows the results obtained assuming

a different energy dependence for the decoherence parameters, see eq. (2.13): $n = 0$ (top panel), $n = 1$ (middle panel) and $n = 2$ (bottom panel). The shaded regions are disfavored by previous analysis of SK [7] (90% CL) and KamLAND [15] data (95% CL). As explained in section 3, the KamLAND constraints derived in [15] apply to γ_{12}^0 (solar limits) while it is not clear to which γ_{ij} the bounds from SK obtained in [7] would apply, since this depends on the true neutrino mass ordering (which is yet unknown).

Figure 5 shows that for both DeepCore and IceCube the best sensitivity is achieved for the solar limits (B) and (C) while the weakest limit is obtained in the atmospheric limit (A). In particular, the strongest bound is obtained for (C). This is in agreement with the behaviour of the oscillation probability in presence of strong matter effects, discussed in section 3. On one hand, as shown in section 3, for NO the decoherence effects are mainly driven by γ_{21} in the neutrino channel and γ_{32} in the antineutrino channel. On the other hand, the number of antineutrino events is going to be suppressed with respect to the neutrino case, due to the smaller cross section and flux. Hence, the best sensitivity is expected for case (C), where $\gamma_0 = \gamma_{21}^0 = \gamma_{32}^0$, since both neutrinos and antineutrinos are sensitive to decoherence effects. Conversely, in case (B), where $\gamma_0 = \gamma_{21}^0 = \gamma_{31}^0$, only neutrinos are sensitive to decoherence effects, and therefore some sensitivity is lost with respect to the results for case (C). Finally, in case (A), with $\gamma_0 = \gamma_{32}^0 = \gamma_{31}^0$, the bounds come mainly from the impact of decoherence on the antineutrino event rates and, since these are much smaller than in the neutrino case, the obtained bounds are much weaker when compared to the results obtained in case (B).

Figure 5 shows a flat asymptotic feature of the $\sqrt{\Delta\chi^2}$ for large values of γ_0, where the sensitivity becomes independent of γ_0. In fact, for IceCube there is a decrease in sensitivity for values of γ above a certain range: for example, for $n = 0$ the best sensitivity is achieved for $\gamma_0 \sim \mathcal{O}(10^{-22})$ GeV while it decreases for higher values. This behaviour can be understood as follows. For the neutrino energies observed at IceCube (above 100 GeV) the oscillation phases do not develope and the probabilities do not depend on the energy ($\cos\tilde{\Delta}_{ij} \approx 1$ in eq. (2.15)). Therefore, at IceCube the sensitivity to the decoherence effects comes from the observation of a non-standard behaviour of the number of events with the zenith angle. Naively, eq. (2.14) gives the values of L and γ that yield a large effect. Considering $n = 0$, for example, where there is a one-to-one relation between the two, we get that for $\gamma_0 \sim 10^{-22}$ GeV the effect will be maximal for distances of the order $L \sim \mathcal{O}(10^3)$ km. This is the typical distance traveled by atmospheric neutrinos crossing the Earth and therefore the sensitivity of IceCube is maximized in this range. Conversely, for larger (smaller) values of γ_0, only neutrinos coming from the most horizontal (vertical) directions are affected, leading to a reduced impact on the χ^2.

From the comparison between the different panels in figure 5 we can see that the limits change considerably with the value of n, which parametrizes the energy

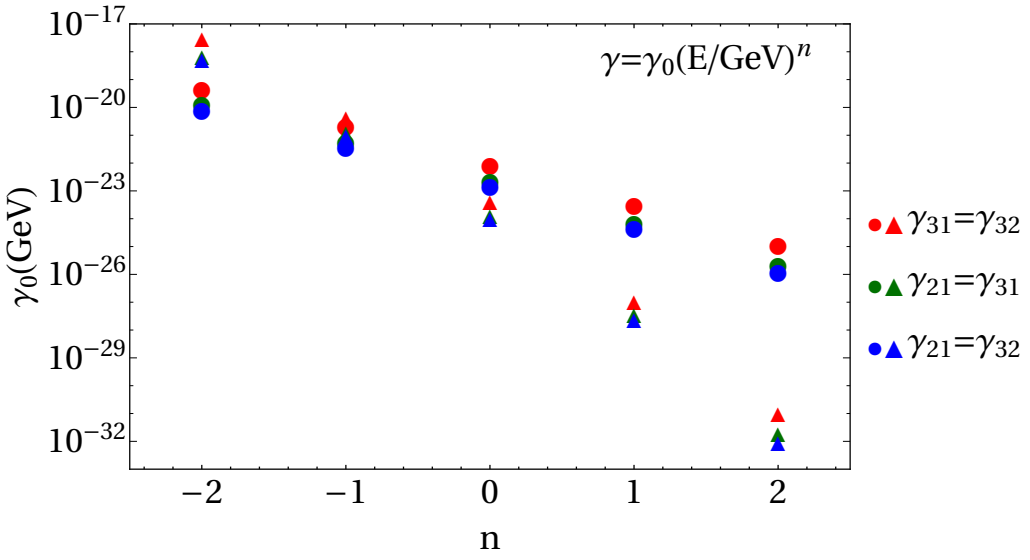

Figure 6: 95% CL bounds on the decoherence parameters γ_0, for NO, as a (discrete) function of the power-law index n for for the Atmospheric limit (red), Solar limit I (green) and Solar limit II (blue). The solid circles (triangles) correspond to the DeepCore (IceCube) analysis.

dependence of the decoherence parameters (see eq. (2.13)). In particular, we observe in figure 5 that the sensitivity improves as n is increased and that, as the vaule of n is increased, the results for IceCube improve much faster (compared to DeepCore) due to the higher neutrino energies considered. The behaviour of the sensitivities with the value of n is better appreciated in figure 6, where we show the bounds obtained at 95% CL (for 1 degree of freedom) as a (discrete) function of the power-law index n, for $n = -2, -1, 0, 1$ and 2. The DeepCore bounds are represented by solid circles while the IceCube constraints are given by the solid triangles. The results seem to follow the linear relation

$$\ln(\gamma_0/\text{GeV}) = \text{constant} - n \ln(E_0/\text{GeV}), \tag{5.1}$$

where $E_0 \simeq 2.5$ TeV (30 GeV) for IceCube (DeepCore). This can be understood as follows. Decoherence effects enter the oscillation probabilities only through the factor $\gamma L = \gamma_0 (E/\text{GeV})^n L$, for any value of n. Naively, we expect that the sensitivity limit is obtained for $\gamma L \sim \mathcal{O}(1)$ (although the precise value will eventually depend on the neutrino mass ordering, on the particular γ_{ij} which drives the sensitivity, and on the data set considered). Taking the logarithm of $\gamma_0 (E/\text{GeV})^n L = \text{constant}$, we reproduce eq. (5.1). At first approximation, the value of E_0 in eq. (5.1) can be estimated as the average energy of the IceCube and DeepCore event distributions,

$\langle E \rangle$, as

$$\langle E \rangle \equiv \frac{\int \frac{dN}{dE} E dE}{\int \frac{dN}{dE} dE} \,, \tag{5.2}$$

where dN/dE is the event number distribution. This leads to $\langle E \rangle \simeq 4$ TeV (40 GeV) for IceCube (DeepCore), which are in the right ballpark although somewhat different from the values of E_0 giving the best fit to the data shown in figure 6. Nevertheless, we find these to be in reasonable agreement, given our naive estimation of E_0 as the mean energy for each experiment.

6 Conclusions

NO	$n=-2$	$n=-1$	$n=0$	$n=1$	$n=2$
IceCube (this work)					
atmospheric ($\gamma_{31}=\gamma_{32}$)	$2.8\cdot10^{-18}$	$4.2\cdot10^{-21}$	$\mathbf{4.0\cdot10^{-24}}$	$\mathbf{1.0\cdot10^{-27}}$	$\mathbf{1.0\cdot10^{-31}}$
solar I ($\gamma_{31}=\gamma_{21}$)	$6.8\cdot10^{-19}$	$1.2\cdot10^{-21}$	$\mathbf{1.3\cdot10^{-24}}$	$\mathbf{3.5\cdot10^{-28}}$	$\mathbf{1.9\cdot10^{-32}}$
solar II ($\gamma_{32}=\gamma_{21}$)	$5.2\cdot10^{-19}$	$9.2\cdot10^{-22}$	$9.7\cdot10^{-25}$	$2.4\cdot10^{-28}$	$9.0\cdot10^{-33}$
DeepCore (this work)					
atmospheric ($\gamma_{31}=\gamma_{32}$)	$\mathbf{4.3\cdot10^{-20}}$	$2.0\cdot10^{-21}$	$8.2\cdot10^{-23}$	$3.0\cdot10^{-24}$	$1.1\cdot10^{-25}$
solar I ($\gamma_{31}=\gamma_{21}$)	$\mathbf{1.2\cdot10^{-20}}$	$5.4\cdot10^{-22}$	$2.1\cdot10^{-23}$	$6.6\cdot10^{-25}$	$2.0\cdot10^{-26}$
solar II ($\gamma_{32}=\gamma_{21}$)	$7.5\cdot10^{-21}$	$3.5\cdot10^{-22}$	$1.4\cdot10^{-23}$	$4.2\cdot10^{-25}$	$1.1\cdot10^{-26}$
Previous Bounds					
SK (two families) [7]		$2.4\cdot10^{-21}$	$4.2\cdot10^{-23}$		$1.1\cdot10^{-27}$
MINOS (γ_{31},γ_{32}) [29]		$\mathbf{2.5\cdot10^{-22}}$	$1.1\cdot10^{-22}$	$2\cdot10^{-24}$	
KamLAND (γ_{21}) [15]		$\mathbf{3.7\cdot10^{-24}}$	$6.8\cdot10^{-22}$	$1.5\cdot10^{-19}$	

Table 3: DeepCore/IceCube bounds on γ_{ij}^0 in GeV ($\gamma_{ij} = \gamma_{ij}^0 (E/\text{GeV})^n$), at the 95% CL (1 degree of freedom) and for NO. Previous constraints are also provided for comparison, and the dominant limit in each case is highlighted in bold face (notice that we considered the most conservative bound from the two solar limits).

In this work, we have derived strong limits on non-standard neutrino decoherence parameters in both the solar and atmospheric sectors from the analysis of IceCube and DeepCore atmospheric neutrino data. Our analysis includes matter effects in a consistent manner within a three-family oscillation framework, unlike most past literature on this topic. In Sec. 2 we have developed a general formalism, dividing the matter profile into layers of constant density, which permits to study decoherence effects in neutrino oscillations affected by matter effects in a non-adiabatic regime. Our analysis shows that the matter effects are extremely relevant for atmospheric neutrino oscillations and their importance in order to correctly interpret the two-family limits obtained previously in the literature, as outlined in Sec. 3.

We have found that the sensitivity to decoherence effects depends strongly on the neutrino mass ordering and on whether the sensitivity is dominated by the neutrino or antineutrino event rates. For neutrinos, the decoherence effects at high energies are mainly driven by γ_{21} (γ_{31}) for normal (inverted) ordering, while in the antineutrino case they are essentially controlled by γ_{32} (γ_{21}) for normal (inverted) ordering. This means that, considering a three-family framework including matter effects is essential when decoherence effects in atmospheric neutrino oscillations are studied. Our results are summarized in table 3 for normal ordering (NO) of neutrino masses, and in table 4 for inverted ordering (IO). The two tables summarize, together with the most relevant bounds present in the literature, the 95% CL bounds extracted from our analysis of DeepCore and IceCube atmospheric neutrino data, for the three limiting cases considered in this work: (A) atmospheric limit ($\gamma_{21} = 0$), (B) solar limit I ($\gamma_{32} = 0$) and (C) solar limit II ($\gamma_{31} = 0$). In Appendix B we show that the bounds derived in these limits correspond to the most conservative results that can be extracted in the general case.

In this work, we considered a general dependence of the decoherence parameters with the energy, as $\gamma_{ij} = \gamma_{ij}^0 \, (E/\mathrm{GeV})^n$ with $n = \pm 2, 0, \pm 2$. Our results improve over previous bounds for most of the cases studied, with the exception of the $n = -1$ case. For $n = -1$, KamLAND gives the dominant bound on γ_{21} while MINOS gives the strongest constraints on γ_{31} and γ_{32}. Indeed, both KamLAND and MINOS are also expected to give the strongest bound for $n = -2$, although to the best of our knowledge no analysis has been performed for this case yet. Our results show that, for $n = 0$ (which is the case most commonly considered in the literature), IceCube improves the bound on γ_{31} and γ_{32} in (more than) one order of magnitude with respect to the SK constraint, obtained in a simplified two-family approximation, and by more than one order (almost two orders) of magnitude for NO (IO) with respect to the KamLAND constraint on γ_{21}. In particular, we find that the reference value for γ_{23} considered in Ref. [17] to explain the small tension previously reported between NOvA and SK data is indeed already excluded by IceCube data. Regarding the cases with $n = 1, 2$, we find that the sensitivity of IceCube is particularly strong. For instance, IceCube improves the bound from KamLAND on γ_{21} by almost 9 (8) orders of magnitude for $n = 1$ and NO (IO), while for $n = 2$ the bound on γ_{31} and γ_{32} is improved in 4 (5) orders of magnitude with respect to the SK limit for NO (IO).

Acknowledgments

We thank C. González-García, M. Maltoni and J. Salvado for useful discussions. JLP, IMS and HN thank the hospitality of the Fermilab Theoretical Physics Department where this work was initiated. HN also thanks the hospitality of the CERN Theoretical Physics Department where the final part of this work was done. HN was supported

IO	$n=-2$	$n=-1$	$n=0$	$n=1$	$n=2$
IceCube (this work)					
atmospheric ($\gamma_{31}=\gamma_{32}$)	$6.8\cdot10^{-19}$	$1.2\cdot10^{-21}$	$\mathbf{1.3\cdot10^{-24}}$	$\mathbf{3.5\cdot10^{-28}}$	$\mathbf{1.9\cdot10^{-32}}$
solar I ($\gamma_{31}=\gamma_{21}$)	$5.2\cdot10^{-19}$	$9.2\cdot10^{-22}$	$9.8\cdot10^{-25}$	$2.4\cdot10^{-28}$	$9.0\cdot10^{-33}$
solar II ($\gamma_{32}=\gamma_{21}$)	$2.8\cdot10^{-18}$	$4.2\cdot10^{-21}$	$\mathbf{4.1\cdot10^{-24}}$	$\mathbf{1.0\cdot10^{-27}}$	$\mathbf{1.0\cdot10^{-31}}$
DeepCore (this work)					
atmospheric ($\gamma_{31}=\gamma_{32}$)	$\mathbf{1.4\cdot10^{-20}}$	$5.8\cdot10^{-22}$	$2.2\cdot10^{-23}$	$7.5\cdot10^{-25}$	$2.3\cdot10^{-26}$
solar I ($\gamma_{31}=\gamma_{21}$)	$8.3\cdot10^{-21}$	$3.6\cdot10^{-22}$	$1.4\cdot10^{-23}$	$4.7\cdot10^{-25}$	$1.3\cdot10^{-26}$
solar II ($\gamma_{32}=\gamma_{21}$)	$\mathbf{5.0\cdot10^{-20}}$	$2.3\cdot10^{-21}$	$9.4\cdot10^{-23}$	$3.3\cdot10^{-24}$	$1.2\cdot10^{-25}$
Previous Bounds					
SK (two families) [7]		$2.4\cdot10^{-21}$	$4.2\cdot10^{-23}$		$1.1\cdot10^{-27}$
MINOS (γ_{31},γ_{32}) [29]		$\mathbf{2.5\cdot10^{-22}}$	$1.1\cdot10^{-22}$	$2\cdot10^{-24}$	
KamLAND (γ_{21}) [15]		$\mathbf{3.7\cdot10^{-24}}$	$6.8\cdot10^{-22}$	$1.5\cdot10^{-19}$	

Table 4: Same as table 3, but assuming IO instead.

by the Brazilian funding agency, CNPq (Conselho Nacional de Desenvolvimento Cientıfico e Tecnológico), and by Fermilab Neutrino Physics Center. IMS acknowledges support from the Spanish grant FPA2015-65929-P (MINECO/FEDER, UE) and the Spanish Research Agency ("Agencia Estatal de Investigacion") grants IFT "Centro de Excelencia Severo Ochoa" SEV2012-0249 and SEV-2016-0597. This work was partially supported by the European projects H2020-MSCA-ITN-2015-674896-ELUSIVES and 690575-InvisiblesPlus-H2020-MSCA-RISE-2015. This manuscript has been authored by Fermi Research Alliance, LLC under Contract No. DE-AC02-07CH11359 with the U.S. Department of Energy, Office of Science, Office of High Energy Physics. The publisher, by accepting the article for publication, acknowledges that the United States Government retains a non-exclusive, paid-up, irrevocable, world-wide license to publish or reproduce the published form of this manuscript, or allow others to do so, for United States Government purposes.

A Computation of oscillation probabilities in three-layers

The simulation of atmospheric neutrino experiments is computationally demanding in the standard three-family scenario, and even more if decoherence effects are included in the analysis. Therefore, due to the cost of implementing a large number of layers for the PREM profile density, in this work we consider a simplified three-layer model for the Earth matter density profile assuming a core and Earth radii of 3321 km and 6371 km, respectively. The values of the matter densities of the inner layer (core) and the outer layer (mantle) are taken to be around $\rho = 12$ g/cm^3 and 4.6 g/cm^3, respectively. However, their values are slightly adjusted depending on the distance traveled by the neutrinos to match as close as possible the profile of

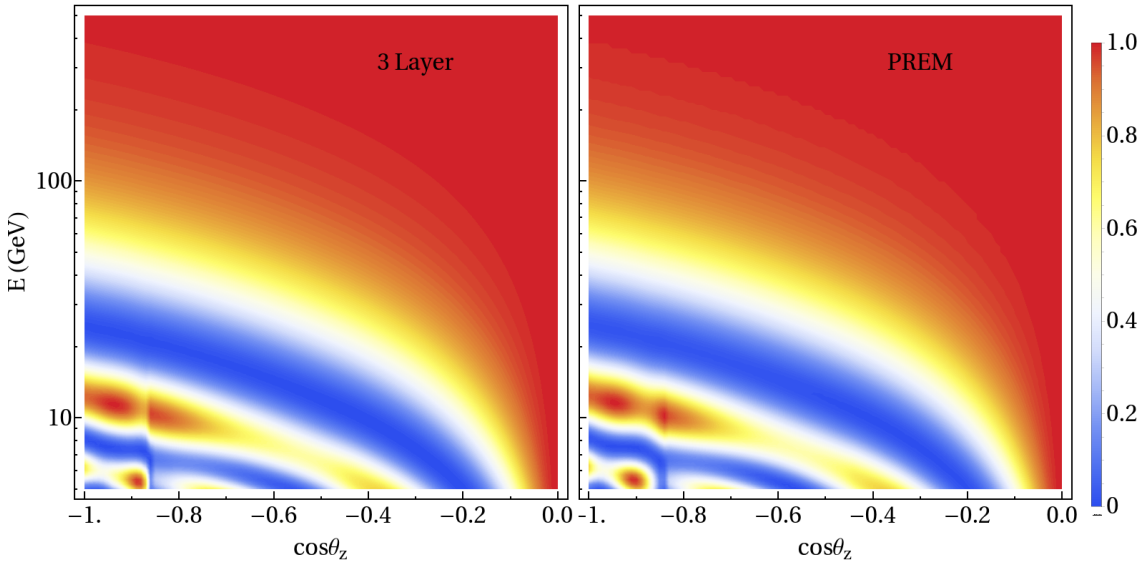

Figure 7: Oscillograms for $P_{\mu\mu}$ without decoherence considering our three layer approximation (left panel) and the PREM model (right panel) for the Earth matter density profile.

the PREM model [47]. Note that, in our simulations, we have not considered the atmosphere as an additional layer. This is a good approximation for neutrinos going upwards in the detector ($\cos\theta_z < 0$), but is not a valid approximation in the region $\cos\theta_z > 0$. Nevertheless, this has no impact in our analysis since for neutrinos with $\cos\theta_z > 0$ the distance travelled is very short and, therefore, they would only be sentive to extremely large values of the decoherence parameters which are already ruled out by other experiments.

In figure 7 we compare the results obtained for the oscillation probability for our modified three-layer approximation (left panel) against the exact numerical results using the full PREM profile [47] (right panel), which divides the Earth into eleven layers given by a polynomial function of the distance traveled. In this figure, the results are shown for the standard three-family scenario with no decoherence, in order to illustrate the accuracy of our three-layer approximation. The results are shown as a neutrino oscillogram, which represents the oscillation probability in the $P_{\mu\mu}$ channel in terms of energy and the zenith angle θ_z of the incoming neutrino. In this figure, a normal mass ordering was assumed, together with the following input values for the oscillation parameters [4, 5]: $\Delta m^2_{21} = 7.4{\cdot}10^{-5}$ eV^2, $\Delta m^2_{31} = 2.515{\cdot}10^{-3}$ eV^2, $\theta_{12} = 33.62°$, $\theta_{13} = 8.54°$, $\sin^2\theta_{23} = 0.51$, and $\delta = 234°$.

As can be seen from the comparison between the two panels, some differences take place but only for energies below the IceCube/DeepCore energy threshold $\sim \mathcal{O}(5\,\text{GeV})$. Therefore, we conclude that the agreement between the probabilities obtained using the exact PREM model (right) and our approximate three-layer

model (left) is sufficiently good for the purposes of this work. We have also checked that, using our simplified three-layer model applied to the standard case without decoherence, we are able to reproduce up to a very good approximation the DeepCore oscillation fit for the atmospheric parameters θ_{23} and Δm^2_{32} [37].

B Five-dimensional analysis

The γ_{ij} are not completely independent parameters as we have already pointed out (see eq. (2.7)). In order to simplify the analysis, in this work we have studied three different representative cases: (A) Atmospheric limit, $\gamma_{21} = 0$ ($\gamma_{32} = \gamma_{31}$); (B) Solar limit I, $\gamma_{32} = 0$ ($\gamma_{21} = \gamma_{31}$); and (C) Solar limit II, $\gamma_{31} = 0$ ($\gamma_{21} = \gamma_{32}$). Considering these one-γ_{ij} dominated cases is expected to be a very good approximation in view of equations (3.1)-(3.4). In any case, in this Appendix we will show that the results obtained in these simplified scenarios apply to the more general case in which the three γ_{ij} are different from zero.

Let us assume that just one D_m matrix contributes to the decoherence term of the evolution equations given by eq. (2.2). In such a case, one of the γ_{ij} parameters is a function of the other two γ_{ij}. Without loss of generality, we chose γ_{21} and γ_{31} as the free parameters and γ_{32} is then given by

$$\gamma_{32} = \left(\sqrt{\gamma_{21}} \pm \sqrt{\gamma_{31}}\right)^2 . \tag{B.1}$$

In order to understand how general are the results presented in sec. 5, we have performed a five-dimensional analysis varying γ_{21}, γ_{31}, θ_{23} and Δm^2_{32} in the fit, and imposing the constraint given by the equation above. In figure 8 we show the $\sqrt{\Delta\chi^2}$ obtained from the five-dimensional DeepCore analysis as a function of γ_{21} (dashed green curve) and γ_{31} (dashed red curve), marginalizing over the rest of the free parameters, for the $n = 0$ case (the same conclusions apply to the other cases studied in this work). For the sake of comparison, the $\sqrt{\Delta\chi^2}$ associated to the atmospheric (solid red curve), solar I (solid green curve) and solar II (solid blue curve) limits is also included in the same figure. NO was assumed but the results can be easily extrapolated to the IO case using the mapping given in eq. (3.8).

Figure 8 shows that the five-dimensional $\sqrt{\Delta\chi^2}$ distribution projected into γ_{31} coincides with the Atmospheric limit one, while when it is projected into γ_{21} resembles the most conservative of the two solar limits. This is due to the marginalization over the parameters which are not shown. For instance, in the case of γ_{21} the marginalization selects, between the two solar limits, the most conservative result. We conclude therefore that our analysis distinguishing the three limits (A), (B) and (C), provides the most conservative bounds that can be applied to the general case in which the three γ_{ij} are different from zero.

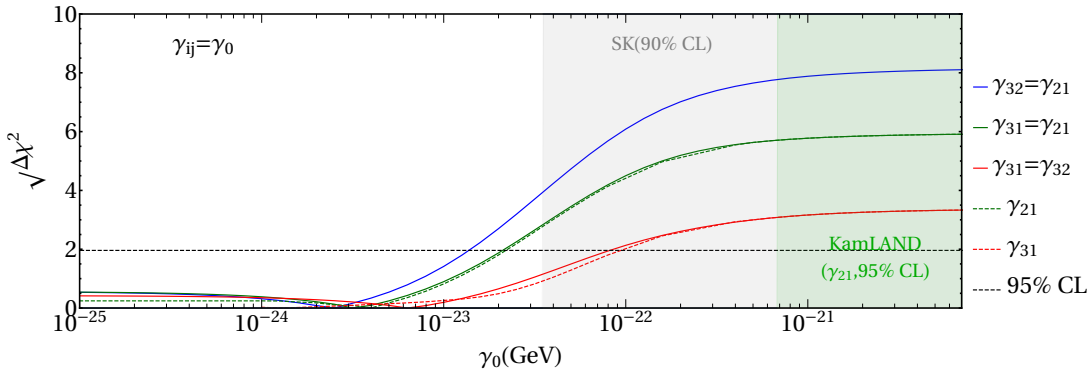

Figure 8: $\sqrt{\Delta\chi^2}$ obtained from the five-dimensional DeepCore analysis as a function of γ_{21} (dashed green curve) and γ_{31} (dashed red curve), marginalizing over the rest of the free parameters, for the $n = 0$ case and NO. The $\sqrt{\Delta\chi^2}$ for the Atmospheric (solid red curve), Solar I (solid green curve) and Solar II (solid blue curve) limits is also shown.

References

[1] Daya Bay collaboration, F. P. An et al., *New Measurement of Antineutrino Oscillation with the Full Detector Configuration at Daya Bay*, *Phys. Rev. Lett.* **115** (2015) 111802, [1505.03456].

[2] A. Izmaylov, ""T2K Neutrino Experiment. Recent Results and Plans." Talk given at the Flavour Physics Conference, Quy Nhon, Vietnam, August 13–19, 2017." http://v17flavour.in2p3.fr/ThursdayAfternoon/Izmaylov.pdf.

[3] Alexander Radovic, ""Results from NOvA", Fermilab Joint Experimental-Theoretical Physics Seminar, January 12, 2018.." http://theory.fnal.gov/events/event/results-from-nova/.

[4] "NuFIT 3.2 (2018)." Results available at: http://www.nu-fit.org.

[5] I. Esteban, M. C. Gonzalez-Garcia, M. Maltoni, I. Martinez-Soler and T. Schwetz, *Updated fit to three neutrino mixing: exploring the accelerator-reactor complementarity*, *JHEP* **01** (2017) 087, [1611.01514].

[6] F. Benatti and R. Floreanini, *Open system approach to neutrino oscillations*, *JHEP* **02** (2000) 032, [hep-ph/0002221].

[7] E. Lisi, A. Marrone and D. Montanino, *Probing possible decoherence effects in atmospheric neutrino oscillations*, *Phys. Rev. Lett.* **85** (2000) 1166–1169, [hep-ph/0002053].

[8] A. M. Gago, E. M. Santos, W. J. C. Teves and R. Zukanovich Funchal, *Quantum dissipative effects and neutrinos: Current constraints and future perspectives*, *Phys. Rev.* **D63** (2001) 073001, [hep-ph/0009222].

[9] A. M. Gago, E. M. Santos, W. J. C. Teves and R. Zukanovich Funchal, *A Study on*

quantum decoherence phenomena with three generations of neutrinos, hep-ph/0208166.

[10] D. Morgan, E. Winstanley, J. Brunner and L. F. Thompson, *Probing quantum decoherence in atmospheric neutrino oscillations with a neutrino telescope*, *Astropart. Phys.* **25** (2006) 311–327, [astro-ph/0412618].

[11] D. Hooper, D. Morgan and E. Winstanley, *Probing quantum decoherence with high-energy neutrinos*, *Phys. Lett.* **B609** (2005) 206–211, [hep-ph/0410094].

[12] G. L. Fogli, E. Lisi, A. Marrone, D. Montanino and A. Palazzo, *Probing non-standard decoherence effects with solar and KamLAND neutrinos*, *Phys. Rev.* **D76** (2007) 033006, [0704.2568].

[13] Y. Farzan, T. Schwetz and A. Y. Smirnov, *Reconciling results of LSND, MiniBooNE and other experiments with soft decoherence*, *JHEP* **07** (2008) 067, [0805.2098].

[14] P. Bakhti, Y. Farzan and T. Schwetz, *Revisiting the quantum decoherence scenario as an explanation for the LSND anomaly*, *JHEP* **05** (2015) 007, [1503.05374].

[15] G. Balieiro Gomes, M. M. Guzzo, P. C. de Holanda and R. L. N. Oliveira, *Parameter Limits for Neutrino Oscillation with Decoherence in KamLAND*, *Phys. Rev.* **D95** (2017) 113005, [1603.04126].

[16] R. L. N. Oliveira, *Dissipative Effect in Long Baseline Neutrino Experiments*, *Eur. Phys. J.* **C76** (2016) 417, [1603.08065].

[17] J. A. B. Coelho, W. A. Mann and S. S. Bashar, *Nonmaximal θ_{23} mixing at NOvA from neutrino decoherence*, *Phys. Rev. Lett.* **118** (2017) 221801, [1702.04738].

[18] J. a. A. B. Coelho and W. A. Mann, *Decoherence, matter effect, and neutrino hierarchy signature in long baseline experiments*, *Phys. Rev.* **D96** (2017) 093009, [1708.05495].

[19] J. A. Carpio, E. Massoni and A. M. Gago, *Revisiting quantum decoherence in the matter neutrino oscillation framework*, 1711.03680.

[20] C. Giunti and C. W. Kim, *Coherence of neutrino oscillations in the wave packet approach*, *Phys. Rev.* **D58** (1998) 017301, [hep-ph/9711363].

[21] S. W. Hawking, *Breakdown of Predictability in Gravitational Collapse*, *Phys. Rev.* **D14** (1976) 2460–2473.

[22] J. R. Ellis, J. S. Hagelin, D. V. Nanopoulos and M. Srednicki, *Search for Violations of Quantum Mechanics*, *Nucl. Phys.* **B241** (1984) 381. [,580(1983)].

[23] S. B. Giddings and A. Strominger, *Loss of Incoherence and Determination of Coupling Constants in Quantum Gravity*, *Nucl. Phys.* **B307** (1988) 854–866.

[24] Super-Kamiokande collaboration, Y. Fukuda et al., *Evidence for oscillation of atmospheric neutrinos*, *Phys. Rev. Lett.* **81** (1998) 1562–1567, [hep-ex/9807003].

[25] Super-Kamiokande collaboration, Y. Fukuda et al., *Measurement of a small*

atmospheric muon-neutrino / electron-neutrino ratio, *Phys. Lett.* **B433** (1998) 9–18, [hep-ex/9803006].

[26] Super-Kamiokande collaboration, Y. Fukuda et al., *Study of the atmospheric neutrino flux in the multi-GeV energy range*, *Phys. Lett.* **B436** (1998) 33–41, [hep-ex/9805006].

[27] Super-Kamiokande collaboration, Y. Fukuda et al., *Measurement of the flux and zenith angle distribution of upward through going muons by Super-Kamiokande*, *Phys. Rev. Lett.* **82** (1999) 2644–2648, [hep-ex/9812014].

[28] M. M. Guzzo, P. C. de Holanda and R. L. N. Oliveira, *Quantum Dissipation in a Neutrino System Propagating in Vacuum and in Matter*, *Nucl. Phys.* **B908** (2016) 408–422, [1408.0823].

[29] R. L. N. de Oliveira, M. M. Guzzo and P. C. de Holanda, *Quantum Dissipation and CP Violation in MINOS*, *Phys. Rev.* **D89** (2014) 053002, [1401.0033].

[30] G. Lindblad, *On the Generators of Quantum Dynamical Semigroups*, *Commun. Math. Phys.* **48** (1976) 119.

[31] T. Banks, L. Susskind and M. E. Peskin, *Difficulties for the Evolution of Pure States Into Mixed States*, *Nucl. Phys.* **B244** (1984) 125–134.

[32] M. C. Gonzalez-Garcia and M. Maltoni, *Status of Oscillation plus Decay of Atmospheric and Long-Baseline Neutrinos*, *Phys. Lett.* **B663** (2008) 405–409, [0802.3699].

[33] P. B. Denton, H. Minakata and S. J. Parke, *Compact Perturbative Expressions For Neutrino Oscillations in Matter*, *JHEP* **06** (2016) 051, [1604.08167].

[34] P. B. Denton, H. Minakata and S. J. Parke, *Addendum to "Compact Perturbative Expressions for Neutrino Oscillations in Matter"*, 1801.06514.

[35] E. K. Akhmedov, M. Maltoni and A. Yu. Smirnov, *1-3 leptonic mixing and the neutrino oscillograms of the Earth*, *JHEP* **05** (2007) 077, [hep-ph/0612285].

[36] IceCube collaboration, M. G. Aartsen et al., *The IceCube Neutrino Observatory: Instrumentation and Online Systems*, *JINST* **12** (2017) P03012, [1612.05093].

[37] IceCube collaboration, M. G. Aartsen et al., *Determining neutrino oscillation parameters from atmospheric muon neutrino disappearance with three years of IceCube DeepCore data*, *Phys. Rev.* **D91** (2015) 072004, [1410.7227].

[38] IceCube collaboration, M. G. Aartsen et al., *Searches for Sterile Neutrinos with the IceCube Detector*, *Phys. Rev. Lett.* **117** (2016) 071801, [1605.01990].

[39] B. J. P. Jones, *Sterile neutrinos in cold climates*. PhD thesis, Massachusetts Institute of Technology, 2015. available from http://hdl.handle.net/1721.1/101327.

[40] C. A. Argüelles, *New physics with atmospheric neutrinos*, 2015. PhD Thesis, available at https://docushare.icecube.wisc.edu/dsweb/Get/Document-75669/tesis.pdf.

[41] J. P. Yanez Garza, *Measurement of neutrino oscillations in atmospheric neutrinos with the IceCube DeepCore detector*, 2014. PhD thesis, available at: http://edoc.hu-berlin.de/dissertationen/yanez-garza-juan-pablo-2014-06-02/PDF/yanez-garza.pdf.

[42] IceCube collaboration, M. G. Aartsen et al., *Search for Astrophysical Tau Neutrinos in Three Years of IceCube Data*, *Phys. Rev.* **D93** (2016) 022001, [1509.06212].

[43] "IceCube collaboration webpage." https://icecube.wisc.edu/science/data.

[44] C. Weaver, *Evidence for astrophysical muon neutrinos from the northern sky*, 2015. PhD thesis, available at https://docushare.icecube.wisc.edu/dsweb/Get/Document-73829/weaver_thesis_2015.pdf.

[45] M. Honda, M. Sajjad Athar, T. Kajita, K. Kasahara and S. Midorikawa, *Atmospheric neutrino flux calculation using the NRLMSISE-00 atmospheric model*, *Phys. Rev.* **D92** (2015) 023004, [1502.03916].

[46] IceCube collaboration, M. G. Aartsen et al., *Measurement of Atmospheric Neutrino Oscillations at 6–56 GeV with IceCube DeepCore*, *Phys. Rev. Lett.* **120** (2018) 071801, [1707.07081].

[47] A. M. Dziewonski and D. L. Anderson, *Preliminary reference earth model*, *Phys. Earth Planet. Interiors* **25** (1981) 297–356.

Chapter6

Conclusions

The work developed in this thesis has been focused into the physics reach of the new generation of neutrino telescopes. In particular, we have concentrated on the scientific program developed by IceCube and DeepCore related to the measurement of flavor oscillation and the discovery of New Physics signals. This thesis can be framed within a broad research project, which aims the determination of the neutrino oscillation parameters, as well as to look for new physics signals by studying the present and future neutrino experiments.

The most simple scenario which explains the neutrino flavor oscillation observed by most of the neutrino experiments, consist of an oscillation between the three active neutrinos included the SM. In this theoretical model, I have collaborated in a global fit where all the neutrino oscillation data available up to 2016 have been combined. My contribution has consisted of studying the flavor oscillation measured by DeepCore in atmospheric neutrinos. DeepCore can identify muon neutrinos by looking for signals composed by a "track" and a "cascade". The low energy threshold of this experiment $E_\nu > 5$ GeV, allows the observation of ν_μ in an energy window where neutrino oscillations induce a sizeable effect. In the framework of three neutrino mixing, the flavor oscillation is determined by six parameters, DeepCore is mainly sensitive to Δm^2_{3l} and θ_{23}. The fit shows that θ_{23} is close to maximal mixing ($\sin^2\theta_{23} \sim 0.5$), and Δm^2_{3l} is a bit above ($\Delta m^2_{32} \sim 2.7 \times 10^{-3}\text{eV}^2$) the preferred values by long baseline experiments ($\Delta m^2_{3l} \sim 2.5 \times 10^{-3}\text{eV}^2$). The statistical significance of DeepCore over the global fit is very small, the precision over these two parameters is mainly due to long baseline experiments like T2K or NOνA. In the global fit, where those results were included, was discussed the complementary role played by atmospheric/accelerator (mainly sensitive to $\nu_\mu \to \nu_\mu$ disappearance channel) and the reactor data (mainly sensitive to $\nu_e \to \nu_e$ disappearance channel), on the determination of Δm^2_{3l}, showing how a consistent combination of both sets can modify the inferred value of the neutrino mass ordering.

IceCube can be used as a tool to look for New Physics. The simplest extension of the SM that account for the neutrino masses is known as "SeeSaw Type I", and predicts the existence of a sterile neutrino. The mass of this new fermion is not predicted by any model and can take any value over several orders of magnitude. Masses in the MeV to GeV range can be tested in DeepCore and IceCube by looking for "Double Cascades" signals. We have found two scenarios where that event topology can be created by sterile neutrinos:

- Heavy neutrino production via mixing with an active neutrino, and the Z boson. This process takes place via mixing of light and heavy (N) states. For ν_e and ν_μ, the coupling with the sterile fermion has been widely tested by

accelerator experiments, but for ν_τ the constraints are much weaker since the production of this neutrino flavor is much more complicated. For IceCube, ν_τ arrive at the detector by the oscillation of atmospheric ν_μ. In this scenario, the first cascade is created by the NC interaction of ν_τ with an ice nucleon (n) inside the detector $\nu_\tau n \to Nn$. The second shower is given by the decay of N into charged particles. Making a numerical estimation of the number of events in six years of data, it is shown that IceCube can increase the bounds by one or two orders of magnitude for masses of the heavy state around $m_N \sim 1$ GeV.

- Heavy neutrino production via a transition magnetic moment. In this scenario, both cascades are created by the interaction of the active neutrino with the heavy state through the magnetic moment operator. We have studied the transition between the two light states, ν_μ and ν_τ, and a heavy state. The sensitivity of the experiment has been obtained by making an estimation of the number of events for six years of data taking. The results show that IceCube can measure heavy states with masses from $\sim$ MeV up to $\sim$ GeV. About the transition magnetic moment, the greatest sensitivity over the current constrains is obtained for ν_τ.

Another scenario where we have looked for New Physics signals is the astrophysical neutrinos, which were recently discovered by IceCube. The energy of the events measured is in the range of 30 TeV to PeV. These particles arrive at the detector as an incoherent superposition of massive states, and the oscillation probability depends only on the mixing matrix elements. In the presence of non-standard interactions between neutrinos and ordinary matter, the matter potential can be generalized to a 3×3 complex matrix, where all the elements are different from zero. We have used the bounds over these new interactions to study the flavor modifications on the astrophysical neutrinos once they cross the Earth. The results show an oscillation of the flavor with the distance travel by the neutrino through the Earth. This oscillation allows to distinguish the New Physics effects from the uncertainties on the production source, which are translate as different final states at the detector. The size of the modifications depends on the initial flavor composition of the neutrino flux. In the cases where a flux is initially dominated by a specific flavor, the final state shows a wide range of values in flavor spectrum.

In addition to the existence of new interactions, the evolution of neutrinos through the Earth can be modified in the presence of decoherence effects created by New Physics. Those effects can be parametrized in terms of three real parameters $(\gamma_{21}, \gamma_{31}, \gamma_{32})$ associated to the three standard oscillations mass splittings. In another work, we have studied the effects of these parameters on the atmospheric neutrinos measured by IceCube and DeepCore. We have assumed a possible dependence of the with the neutrino energy, $\gamma_{ij} = \gamma_{ij}^0 (E/\text{GeV})^n$ with $n = 0, \pm 1, \pm 2$. We have derived strong limits over γ_{ij} in both the solar and the atmospheric sectors by making a fit of the atmospheric events measured by IceCube and DeepCore. To do so, we have developed a general formalism to study the decoherence in non-adiabatic regimes dividing the matter profile into layers of constant density. The results show a dependence of the decoherence effects with the neutrino mass ordering. The limits obtained on γ_{31} and γ_{32} shows that IceCube improve the current bounds by one order of magnitude for $n = 0$. For a higher energy dependence ($n \geq 1$), the constraints obtained for the three parameters are even stronger. For $n = -2$, DeepCore present the stronger constraints, but for $n = -1$ the bounds are still dominated by MINOS and KamLAND.

Conclusiones

El trabajo desarrollado en esta tesis se centra en el estudio de la física accesible por la nueva generación de telescopios de neutrinos. En particular, nos hemos centrado en el programa científico desarrollado por IceCube y DeepCore en física de neutrinos. Esta tesis puede ser enmarcada en un programa de investigación más ámplio, que tiene como objetivo determinar los paámetros de oscilación de los neutrinos, así como la busqueda de señales de nueva física en los experimentos actuales y futuros.

El escenario más simple en el que las oscilaciones de neutrinos en sabor pueden ser explicadas está formado únicamente por los tres neutrinos contenidos en el Modelo Estandar (MS). Usando este modelo como marco teórico, he colaborado en un análisis global que ha usado los datos disponibles en oscilaciones de neutrinos hasta 2016. Mi contribución, ha consistido en el estudio de las oscilaciones de neutrinos medidas por DeepCore en neutrinos atmosféricos. DeepCore puede identificar neutrinos muónicos a través de señales compuestas por una "traza" y una "cascada". La energía mínima para este experimento es de $E_\nu > 5$ GeV, lo que le permite la detección de neutrinos en un rango de energías donde aún las oscilaciones pueden ser observadas. En el modelo de tres neutrinos las oscilaciones vienen determinadas por seis parámetros, de los cuales DeepCore es sensible a Δm^2_{3l} y θ_{23}. Los resultados de este experimento indican que θ_{23} se ha de encontrar próximo a su máximo valor ($\sin^2\theta_{23} \sim 0.5$), y que el parámetro de masas ha de tomar un valor un poco superior (inferior) al preferido en experimentos de *long baseline*, asumiendo una jerarquía de las masas normar (invertida). La relevancia estadísica de los resultados de DeepCore sobre el análisis global es pequeño, la precisión con que se conocen esos dos parámetros se debe a T2K y NOνA. En el trabajo donde estos resultados fueron incluidos, se discutió la complementariedad entre experimentos atmosféricos/aceleradores (principalmente sensibles al canal $\nu_\mu \to \nu_\mu$) y los experimentos de reactores (principalmente sensibles al canal $\nu_e \to \nu_e$) en la medida de Δm^2_{3l}. Los resultados mostraron que una combinación consistente de ambos conjuntos de datos puede afectar significativamente al resultado obtenido.

El experimento IceCube puede ser usado en la búsqueda de nueva física. La mínima extensión del MS que permite explicar las masas de los neutrinos se conoce como "SeeSaw Type I", y predice la existencia de un nuevo fermión, denominado neutrino estéril. La masa de este fermión no se encuentra predicha por ningún modelo. Para masas comprendidas en el rango que va desde los MeV hasta GeV, en otro trabajo hemos encontrado que IceCube puede estudiar a este nuevo fermión buscando las señales conocidas como "Double-Cascade". Hemos encontrado dos escenarios donde estos eventos puede ser creados por neutrinos estériles:

- Un acoplo entre neutrinos activos, neutrinos pesados (N) y el bosón Z. Para neutrinos ν_e y ν_μ, las cotas sobre el acoplo establecidas por experimentos con

aceleradores son muy fuertes. Sin embargo, para ν_τ las cotas son más débiles ya que este tipo de neutrinos son mucho más difíciles de estudiar. Los ν_τ llegan a IceCube a través de la oscilación en sabor de los ν_μ producidos en la atmósfera. En este escenario, la primera cascada se produce a través de una corriente neutra (CN) creada en la interacción de ν_τ con los nucleones del hielo. La segunda cascada se produce en el decaimiento de N. A través de una integración numérica hemos obtenido el número de eventos que el detector puede observar en seis años. Los resultados muestran que IceCube puede aumentar los límites sobre el acoplo entre neutrinos activos y estériles en varios órdenes de magnitud, para masas al rededor de $m_N \sim 1$ GeV.

- La producción de neutrinos pesados a través de un momento magnético de transición. En este escenario ambas cascades se crean a través de la interacción entre neutrinos activos y neutrinos pesados mediante un momento magnético de transición. Hemos estudiado dos casos ν_μ y ν_τ. La sensitividad del experimento ha sido obtenida estimando el número de eventos medidos por el detector en seis años. Los resultados muestran que IceCube puede observar neutrinos estériles con masas comprendidas entre $\sim$ MeV hasta $\sim$ GeV. En cuanto al momento magnético, el mayor incremento de sensibilidad frente a los resultados actuales es obtenido para ν_τ.

Los neutrinos astrofísicos han sido recientemente descubiertos por IceCube. La energía de estos eventos está comprendida entre 30 TeV to PeV. La distancia recorrida por estas partículas hasta llegar a la Tierra las convierte en una superposición incoherente de estados masivos, y por tanto, la probabilidad de oscilación del estado $|\nu_\alpha\rangle$ en el estado $|\nu_\beta\rangle$ viene dada únicamente por los elementos de la matriz de mezcla. En presencia de nuevas interacciones entre los neutrinos y la materia ordinaria, el potencial que describe la evolución de los neutrinos a través de la Tierra puede ser generalizado a una matriz compleja 3×3, donde todos los elementos son distintos de cero. En otro trabajo, hemos usado los límites actuales sobre estas nuevas interacciones para estudiar las modificaciones que pueden introducir en el sabor de los neutrinos astrofísicos, una vez estos cruzan la Tierra. Los resultados muestran una oscilación en sabor en función de la dirección de la distancia recorrida por el neutrino a través de la Tierra. Este efecto ayuda a diferenciar a este modelo de nueva física y la incertidumbre acerca de la fuente de producción de estos neutrinos. Las desviaciones encontradas en el sabor dependen de la composición en sabor del flujo inicial. En los casos en que el flujo está dominado por un sabor específico, el estado final muestra un mayor espectro de posibilidades. La desviación en sabor introducida por la nueva física hace más difícil la identificación de la fuente de neutrinos.

Además de la existencia de nuevas interacciones, la evolución de neutrinos atmosféricos a través de la Tierra se puede ver afectada, en presencia de nueva física, por efectos adicionales de decoherencia. Estos efectos pueden ser descritos en términos de tres parámetros $(\gamma_{21}, \gamma_{31}, \gamma_{32})$, asociados a los tres parámetros de masas de las oscilaciones estándar. En otro trabajo hemos estudiado este escenario, considerando además la posibilidad de que los parámetros anteriores dependan de la energía del neutrino, $\gamma_{ij} = \gamma_{ij}^0 (E/\text{GeV})^n$ con $n = 0, \pm 1, \pm 2$. A través de un ajuste a los eventos atmosféricos medidos por IceCube y DeepCore hemos obtenido nuevos límites sobre γ_{ij}. Para ello, hemos desarrollado un nuevo formalismo que permite estudiar estos efectos en regímenes no adiabáticos. Los resultados muestran una dependencia con el orden de las masas de los neutrinos. Los límites obtenidos para

γ_{31} y γ_{32} y $n = 0$ en IceCube son un orden de magnitud mayores a los obtenidos por los experimentos actuales. Para una dependencia mayor en energía ($n \geq 1$), el incremento obtenido frente a los límites actuales, en este caso para los tres parámetros, es incluso mayor. Para $n = -2$, los límites más fuertes son obtenidos por DeepCore, pero para $n = -1$ todavía dominan los valores de MINOS y KamLAND.

Bibliography

[1] T. Kajita, *Nobel Lecture: Discovery of atmospheric neutrino oscillations*, *Rev. Mod. Phys.* **88** (2016) 030501.

[2] Kamiokande-II collaboration, K. S. Hirata et al., *Experimental Study of the Atmospheric Neutrino Flux*, *Phys. Lett.* **B205** (1988) 416. [,447(1988)].

[3] D. Casper et al., *Measurement of atmospheric neutrino composition with IMB-3*, *Phys. Rev. Lett.* **66** (1991) 2561–2564.

[4] Kamiokande, Super-Kamiokande collaboration, T. Kajita, *Atmospheric neutrino results from Super-Kamiokande and Kamiokande: Evidence for neutrino(mu) oscillations*, *Nucl. Phys. Proc. Suppl.* **77** (1999) 123–132, [hep-ex/9810001]. [,123(1998)].

[5] Super-Kamiokande collaboration, Y. Fukuda et al., *Evidence for oscillation of atmospheric neutrinos*, *Phys. Rev. Lett.* **81** (1998) 1562–1567, [hep-ex/9807003].

[6] MACRO collaboration, M. Ambrosio et al., *Measurement of the atmospheric neutrino induced upgoing muon flux using MACRO*, *Phys. Lett.* **B434** (1998) 451–457, [hep-ex/9807005].

[7] Soudan-2 collaboration, W. W. M. Allison et al., *The Atmospheric neutrino flavor ratio from a 3.9 fiducial kiloton year exposure of Soudan-2*, *Phys. Lett.* **B449** (1999) 137–144, [hep-ex/9901024].

[8] M. C. Gonzalez-Garcia and M. Maltoni, *Phenomenology with Massive Neutrinos*, *Phys. Rept.* **460** (2008) 1–129, [0704.1800].

[9] SLD Electroweak Group, DELPHI, ALEPH, SLD, SLD Heavy Flavour Group, OPAL, LEP Electroweak Working Group, L3 collaboration, S. Schael et al., *Precision electroweak measurements on the Z resonance*, *Phys. Rept.* **427** (2006) 257–454, [hep-ex/0509008].

[10] Particle Data Group collaboration, C. Patrignani et al., *Review of Particle Physics*, *Chin. Phys.* **C40** (2016) 100001.

[11] Planck collaboration, P. A. R. Ade et al., *Planck 2015 results. XIII. Cosmological parameters*, *Astron. Astrophys.* **594** (2016) A13, [1502.01589].

[12] C. Giunti and C. W. Kim, *Fundamentals of Neutrino Physics and Astrophysics*. 2007.

[13] L. Wolfenstein, *Neutrino Oscillations in Matter*, *Phys. Rev.* **D17** (1978) 2369–2374. [,294(1977)].

[14] S. P. Mikheev and A. Yu. Smirnov, *Resonance Amplification of Oscillations in Matter and Spectroscopy of Solar Neutrinos*, *Sov. J. Nucl. Phys.* **42** (1985) 913–917. [,305(1986)].

[15] T. K. Gaisser and M. Honda, *Flux of atmospheric neutrinos*, *Ann. Rev. Nucl. Part. Sci.* **52** (2002) 153–199, [hep-ph/0203272].

[16] C. V. Achar et al., *Detection of muons produced by cosmic ray neutrinos deep underground*, *Phys. Lett.* **18** (1965) 196–199.

[17] F. Reines, M. F. Crouch, T. L. Jenkins, W. R. Kropp, H. S. Gurr, G. R. Smith et al., *Evidence for high-energy cosmic ray neutrino interactions*, *Phys. Rev. Lett.* **15** (1965) 429–433.

[18] P. Lipari, *The Geometry of atmospheric neutrino production*, *Astropart. Phys.* **14** (2000) 153–170, [hep-ph/0002282].

[19] M. Honda, M. Sajjad Athar, T. Kajita, K. Kasahara and S. Midorikawa, *Atmospheric neutrino flux calculation using the NRLMSISE-00 atmospheric model*, *Phys. Rev.* **D92** (2015) 023004, [1502.03916].

[20] A. M. Dziewonski and D. L. Anderson, *Preliminary reference earth model*, *Phys. Earth Planet. Interiors* **25** (1981) 297–356.

[21] E. K. Akhmedov, A. Dighe, P. Lipari and A. Y. Smirnov, *Atmospheric neutrinos at Super-Kamiokande and parametric resonance in neutrino oscillations*, *Nucl. Phys.* **B542** (1999) 3–30, [hep-ph/9808270].

[22] "NuFIT 3.2 (2018)." Results available at: http://www.nu-fit.org.

[23] E. K. Akhmedov, M. Maltoni and A. Yu. Smirnov, *1-3 leptonic mixing and the neutrino oscillograms of the Earth*, *JHEP* **05** (2007) 077, [hep-ph/0612285].

[24] E. K. Akhmedov, M. Maltoni and A. Yu. Smirnov, *Neutrino oscillograms of the Earth: Effects of 1-2 mixing and CP-violation*, *JHEP* **06** (2008) 072, [0804.1466].

[25] IceCube collaboration, M. G. Aartsen et al., *Evidence for High-Energy Extraterrestrial Neutrinos at the IceCube Detector*, *Science* **342** (2013) 1242856, [1311.5238].

[26] F. Halzen, *High-energy neutrino astrophysics*, *Nature Phys.* **13** (2016) 232–238.

[27] IceCube collaboration, M. G. Aartsen et al., *The IceCube Neutrino Observatory: Instrumentation and Online Systems*, *JINST* **12** (2017) P03012, [1612.05093].

[28] IceCube collaboration, R. Abbasi et al., *The Design and Performance of IceCube DeepCore*, *Astropart. Phys.* **35** (2012) 615–624, [1109.6096].

[29] J. P. Yanez Garza, *Measurement of neutrino oscillations in atmospheric neutrinos with the IceCube DeepCore detector*. PhD thesis, Humboldt U., Berlin, 2014. PhD thesis, available at: http://edoc.hu-berlin.de/dissertationen/yanez-garza-juan-pablo-2014-06-02/PDF/yanez-garza.pdf.

[30] IceCube collaboration, M. G. Aartsen et al., *Measurement of Atmospheric Neutrino Oscillations at 656 GeV with IceCube DeepCore*, *Phys. Rev. Lett.* **120** (2018) 071801, [1707.07081].

[31] M. Dentler, A. Hernndez-Cabezudo, J. Kopp, P. Machado, M. Maltoni, I. Martinez-Soler et al., *Updated global analysis of neutrino oscillations in the presence of eV-scale sterile neutrinos*, 1803.10661.

[32] M. C. Gonzalez-Garcia, M. Maltoni and T. Schwetz, *Global Analyses of Neutrino Oscillation Experiments*, *Nucl. Phys.* **B908** (2016) 199–217, [1512.06856].

[33] S. Weinberg, *Baryon and Lepton Nonconserving Processes*, *Phys. Rev. Lett.* **43** (1979) 1566–1570.

[34] F. Bonnet, M. Hirsch, T. Ota and W. Winter, *Systematic study of the d=5 Weinberg operator at one-loop order*, *JHEP* **07** (2012) 153, [1204.5862].

[35] A. Abada, C. Biggio, F. Bonnet, M. B. Gavela and T. Hambye, *Low energy effects of neutrino masses*, *JHEP* **12** (2007) 061, [0707.4058].

[36] A. Zee, *A Theory of Lepton Number Violation, Neutrino Majorana Mass, and Oscillation*, *Phys. Lett.* **93B** (1980) 389. [Erratum: Phys. Lett.95B,461(1980)].

[37] V. De Romeri, E. Fernandez-Martinez, J. Gehrlein, P. A. N. Machado and V. Niro, *Dark Matter and the elusive Z in a dynamical Inverse Seesaw scenario*, *JHEP* **10** (2017) 169, [1707.08606].

[38] M. C. Gonzalez-Garcia and J. W. F. Valle, *Fast Decaying Neutrinos and Observable Flavor Violation in a New Class of Majoron Models*, *Phys. Lett.* **B216** (1989) 360–366.

[39] M.-C. Chen, A. de Gouvea and B. A. Dobrescu, *Gauge Trimming of Neutrino Masses*, *Phys. Rev.* **D75** (2007) 055009, [hep-ph/0612017].

[40] P. Coloma, P. B. Denton, M. C. Gonzalez-Garcia, M. Maltoni and T. Schwetz, *Curtailing the Dark Side in Non-Standard Neutrino Interactions*, *JHEP* **04** (2017) 116, [1701.04828].

[41] M. B. Gavela, D. Hernandez, T. Ota and W. Winter, *Large gauge invariant non-standard neutrino interactions*, *Phys. Rev.* **D79** (2009) 013007, [0809.3451].

[42] C. Biggio, M. Blennow and E. Fernandez-Martinez, *General bounds on non-standard neutrino interactions*, *JHEP* **08** (2009) 090, [0907.0097].

[43] S. Antusch, J. P. Baumann and E. Fernandez-Martinez, *Non-Standard Neutrino Interactions with Matter from Physics Beyond the Standard Model*, *Nucl. Phys.* **B810** (2009) 369–388, [0807.1003].

[44] C. Giunti, *Coherence and wave packets in neutrino oscillations*, *Found. Phys. Lett.* **17** (2004) 103–124, [hep-ph/0302026].

[45] E. Akhmedov, J. Kopp and M. Lindner, *Collective neutrino oscillations and neutrino wave packets*, *JCAP* **1709** (2017) 017, [1702.08338].